Universidade de Aveiro
2022

EDUARDO MARQUES E SILVA ROCHA DE OLIVEIRA

INTEGRAÇÃO DE DADOS DE DETEÇÃO REMOTA PARA FACILITAR AVALIAÇÕES MULTI-RISCO EM REGIÕES COSTEIRAS

INTEGRATION OF REMOTE SENSING DATA TO FACILITATE MULTI-HAZARDS RISK ASSESSMENTS IN COASTAL REGIONS

Universidade de Aveiro
2022

EDUARDO MARQUES E SILVA ROCHA DE OLIVEIRA

INTEGRATION OF REMOTE SENSING DATA TO FACILITATE MULTI-HAZARDS RISK ASSESSMENTS IN COASTAL REGIONS

Tese apresentada à Universidade de Aveiro para cumprimento dos requisitos necessários à obtenção do grau de Doutor em Ciências e Engenharia Do Ambiente, realizada sob a orientação científica do Doutor Maria de Fátima Lopes Alves, Professora Auxiliar com Agregação do Departamento de Ambiente e Ordenamento da Universidade de Aveiro e coorientação científica do Doutor Leonardo Disperati, Professor Auxiliar da Università degli Studi di Siena, Itália.

Apoio financeiro da FCT e do FSE no âmbito do III Quadro Comunitário de Apoio, através da Bolsa de Doutoramento com a referência SFRH/BD/104663/2014.

o júri

presidente

Professor Doutor Paulo Jorge de Melo Matias Faria de Vila Real
Professor Catedrático, Universidade de Aveiro

Professor Doutor José Luís Zêzere
Professor Catedrático, Universidade de Lisboa

Professor Doutor Salvatore G.P. Virdis
Professor Assistente, Asian Institute of Technology, Tailândia

Professora Doutora Luísa Maria Gomes Pereira
Professora Coordenadora, Universidade de Aveiro

Doutor Luca Cenci
Investigador de Pós-Doutoramento, Serco Italia S.p.A, Itália

Prof. Doutor Leonardo Disperati (Coorientador)
Professor Assistente, Università degli Studi di Siena, Itália

agradecimentos

Em primeiro lugar, um profundo agradecimento à Professora Fátima Alves, pelo incessante apoio, pela abertura ao mundo da investigação e pela partilha da sua experiência e visão em tantas ocasiões. Agradeço também ao Leonardo Disperati, pela amizade, acolhimento, as inúmeras horas em que ensinou a desenvolver espírito crítico, e pelo fermento que continuo a nutrir e a usar nas minhas pizzas.

Agradeço à FCT pela concessão da bolsa para produzir esta investigação.

A todos os colegas da 313 e à incrível COPING team, com os quais partilhei tão bons momentos, em especial à Maria da Luz, Lisa, Adriano, Márcia, Tereza, Cristina, Tanya, Sílvia, Fábio, Johnny, Isabel, André e Luiz. Obrigado à Professora Celeste Coelho, Sandra Valente e Cristina Ribeiro e a tantos outros que fazem do DAO um sítio melhor. Agradeço também ao Luca Cenci, pela colaboração em tantos trabalhos e boa disposição, e aos colegas da Universidade de Siena.

Um agradecimento especial à Carla, Rubi, Nuno e Luzinha, pela amizade, aventuras e por se terem tornado na minha família de Aveiro. Um muito obrigado também ao Ricardo e Jana, e aos vizinhos da Lagoa, Jörg, Inês, Rui, Júlio e Dulce, pela amizade e todo apoio sobretudo em tempos de pandemia.

Um agradecimento especial à minha família. À minha irmã Adriana, ao Nuno e Nina e aos meus pais Maria e Carlos, pelo incondicional apoio, carinho e amor.

Em especial, obrigado à Anita por estar sempre presente com a sua cumplicidade, incentivo, carinho e compreensão. Por último obrigado ao meu filho Xavier, que é também ele um resultado desta tese, e pelo constante desafio de crescermos juntos.

palavras-chave

Cheias, Inundações, Áreas ardidas, Incêndios, Cartografia, Monitorização, Imagens multiespectrais, Satélites, Deteção de mudanças.

resumo

Este trabalho foi desenvolvido no domínio da Geomática aplicado a avaliações de risco.O principal objetivo passa pelo desenvolvimento de metodologias de suporte a avaliações multi-risco, baseadas em técnicas de deteção remota por satélite.

Esta tese resultou no desenvolvimento de dois modelos, para a deteção de extensão de cheias e áreas ardidas. Apesar de constituirem dois tipos de perigo com características antagónicas, os dois modelos desenvolvidos partilham os mesmos princípios teóricos, consistindo em abordagens de deteção de alterações, a partir de multiplos índices obtidos a partir de imagens de satélite multiespectrais.
Os dois modelos foram desenvolvidos e implementados na Região de Aveiro (localizada no litoral oeste da região centro de Portugal Continental), que apresenta diversas pressões naturais e antropogénicas, e que, ao longo dos últimos anos, têm sido amplamente estudadas relativamente à vulnerabilidade e exposição a diversas fontes de perigo. De forma a avaliar a eficácia dos modelos, compararam-se os resultados da sua aplicação com métodos alternativos e dados de fontes oficiais.

As metodologias desenvolvidas ao longo desta tese demonstraram elevado potencial para incorporação em processos de avaliação de risco, com poucos recursos e num curto espaço de tempo, contribuindo para apoiar e facilitar o trabalho de planeadores do terriório e decisores, na adoção de práticas fundamentadas. Esta investigação vai ao encontro de diversas estratégias nacionais e europeias, contribuindo para o aumento da resiliência dos territórios face a perígos de origem meteorológica.

keywords

Flooding, Innundation, Burned areas, Wildfires, Cartography, Maping, Monitoring, Multispectral Images, Satellites, Change detection.

abstract

This research is a development in the field of Geomatics applied to risk assessment. The main objective is to provide methodologies to support multi-hazard assessments at regional scales, based on satellite remote sensing techniques.
This thesis resulted in the development of two models to detect both flood and wildfire burned extents. Despite the antagonic characteristics of such hazards, both models share the same theoretical principles, consisting in multi-index change detection approaches based on multispectral imagery.
Both models were developed and implemented to the Aveiro region (in the Northwest of Central Portugal), chosen because of its natural and anthropogenic pressures, which has been widely studied in terms of its vulnerabilities and exposure to several sources of hazards. The accuracy of these methods was obtained through comparison with other methods or oficial reference sources.

These models have shown great potential for incororation in the risk assessment process, with few requirements in terms of time and resources, supporting and facilitating territorial planners and decision makers to adopt more informed decisions. This research meets several national and European strategic goals, contributing to increase the resilience of territories to weather related hazards.

TABLE OF CONTENTS

LIST OF FIGURES

LIST OF TABLES

Appendix A:

Appendix B:

LIST OF ACRONYMS

AWEI – Automated Water Extraction Index

AWEI_NS – AWEI no shadow

AWEI_S – AWEI shadow

BAI - Burned Area Index

BrI – Burned related Indices

CLC – Corine Land Cover

HMc – High Magnitude change

HSBA – Hierarchical Split-Based Approach

ICNF – Portugal's Institute for Nature Conservation and Forests

LMc – Low Magnitude change

MHRA – Multi-Hazard Risk Assessment

MINDED – Multi-INDEx Differencing

MIRBI - Mid Infrared Burned Index

MNDWI – Modified Normalized Difference Water Index

NBR - Normalized Burn Ratio

Nc – No change

NDVI – Normalized Difference Vegetation Index

NDWI – Normalized Difference Water Index

NIR – Near InfraRed

RBA – Reference Burned Areas

RS – Remote Sensing

SAR – Synthetic Aperture Radar

SHRA – Single Hazard Risk Assessment

SWIR – Short Wave InfraRed

TCB – Tasseled Cap Brightness

TCW - Tasseled Cap Wetness

TOA – Top of Atmosphere

VIS - Visible

WrI – Water-related Indices

Chapter 1:
INTRODUCTION

1. Background

The coexistence of modern industrial societies together with fragile natural territories increases the vulnerabilities and exposure to both technological and natural risks, placing new challenges for risk-management at local and regional scales (de Souza Porto and de Freitas, 2003). The effects of global climate change are contributing to increase the frequency and intensity of weather related hazards (Deleu et al., 2011), requiring decision support information tools to establish effective disaster mitigation strategies (Grünthal et al., 2006).

According to the European 2020 Strategy (EC, 2010a), there is a global need to strengthen economies towards climate risks, disaster prevention and response. By 2014, the European Union Internal Security Strategy set a target to establish a risk management policy linking threat and risk assessments to decision making, where each member-State would have to proceed with risk assessment and cartography. Risk management is amongst the priorities of Portugal's national strategic policies and has been successively incorporated in regional and national spatial planning programmes (Fonseca et al., 2014). In 2019, Portugal's National Emergency and Civil Protection Authority published a national level risk assessment evaluation for natural, technological and mixed hazards, considering impact of climate change scenarios (ANEPC, 2019).

Experiences with decision makers show that a territorial perspective is desirable for spatial planning decisions and emergency strategies (Grünthal et al., 2006). Hazard-related maps are fundamental tools for the support of preventive measures, allowing decision makers to identify the spatial distribution and intensities of each hazard, exposed population and values, or expected losses.

The risk assessment process is usually composed by the following steps: 1) hazard identification; 2) hazard assessment; 3) elements-at-risk exposure analysis; 4) vulnerability assessment; and 5) risk

estimation (Van Westen, 2013). By definition, Single-Hazard Risk Assessments (SHRA) address only one hazard individually, being the most traditional approach. Nonetheless, most natural and anthropogenic risks are likely to occur at one same location and, not rarely, at the same time. Multi-Hazard Risk Assessments (MHRA) may address multiple hazardous sources and multiple variable elements overlapping in time and space, resembling more to the reality of spatial management of decision-makers (Carpignano et al., 2009). MHRAs allow establishing comparisons between several hazard types, contributing to raise awareness and develop tailor-made mitigation strategies (Carpignano et al., 2009; EC, 2010b).

The risk assessment process can be highly complex, in particular for MHRAs, requiring many sorts of data, which are often unavailable or may be extremely costly to obtain. Spatial and statistical data have different relevancies for each hazard type, although some of the most common include land use, vegetation, Earth surface slope, oceanographic and meteorological factors (Van Westen, 2013). Remote Sensing (RS) techniques have been used as either complementary or alternative sources to ground-based surveys, and may offer a synoptic perspective for many of these measurements, contributing for a wide range of disciplines (Tralli et al., 2005). Satellite earth observations are available at different spatial, spectral and temporal resolutions, and have been used to reconstruct recent-history catastrophic events, providing data for prediction and mitigation planning actions (e.g., Grünthal et al., 2006; Leifer et al., 2012; D Lu et al., 2004; Van Westen, 2013).

2. Objectives and Research questions

This thesis aims at developing methods to facilitate the characterization of weather-related events based on remote sensing data and techniques. The main objective is to develop RS methods that may be used to support and facilitate multi-hazard risk assessments, with particular focus on coastal regions. This work is targeted to regional scale applications, being in line with the requirements of national and European strategies and sectorial plans. It intends to provide spatial managers and decision-makers with reliable, cost-effective and facilitative tools, and to support private and public sectors in increasing territorial resilience to risk. With this in mind, the following research questions were formulated:

'How can RS data and methods be incorporated in multi-hazard risk assessments, in an effective and efficient way?'

‘What are the main advantages and limitations of using satellite remote sensing methods to monitor weather-related hazards in coastal regions?’

‘May RS techniques be exclusively used to reliably characterize multiple types of hazards in coastal regions?’

3. Thesis structure

The structure of this thesis is divided into five chapters:

- Chapter 1 - Introduction:
    - This chapter contains a general introduction of the thesis, objectives and research questions;
- Chapter 2 - Satellite remote sensing for single and multi-hazard risk assessments:
    - This chapter includes a literature review of methods used in the contexts of single and multi-hazard risk assessments. Particular focus was given to some of the most relevant weather-related hazards of the Mediterranean Biogeographical region and the application of satellite remotes sensing data and techniques;
- Chapter 3 - Multi-INDEx Differencing (MINDED) method for flood extent estimations:
    - This chapter presents MINDED, one of the most important outputs of this thesis, corresponding to an innovative remote sensing method for determining flooded area extents. The implementation of MINDED is demonstrated through a semi-automatic application in the Aveiro Region study area.
- Chapter 4 - A new method (MINDED-BA) for automatic detection of burned areas using remote sensing data:
    - Following the identification of several potential research developments (in the previous chapters), Chapter 4 presents MINDED-BA, a burned extent assessment model. MINDED-BA shares the same theoretical principles of the original MINDED, but is itself an advancement in respect to the original method. MINDED-BA includes several additional procedures specific to the detection of burned areas, but also for enhancing data processing, improve automatization and overall model performance.

- Chapter 5 - General conclusions and future research:
    - This chapter includes the general conclusions of this thesis, which are presented with an integrative perspective of all previous chapters. Key findings are identified and the research questions (from Chapter 1) are addressed. Future research lines are also pointed out.

4. Other considerations

Among the above-mentioned thesis structure, Chapter 3 has been published in an international peer-reviewed journal:

- Oliveira, E.R., Disperati, L., Cenci, L., Pereira, L.G., Alves, F.L., 2019. Multi-Index Image Differencing Method (MINDED) for flood extent estimations. Remote Sens 11:1–29. doi: 10.3390/rs11111305

Moreover, Chapter 2 and Chapter 4 will also be submitted for publication.

During the period of this thesis, other publications were produced in co-authorship, contributing for the characterization of multiple hazards and processes occurring in the study area considered in Chapters 3 and 4:

- Cenci L., Disperati L., Persichillo M.G., Oliveira E.R., Alves F.L., Phillips M. (2018) Integrating remote sensing and GIS techniques for monitoring and modelling shoreline evolution to support coastal risk management. GISCIENCE & REMOTE SENSING, 55, (3), 355-375.
- Azevedo A., Fortunato A.B., Epifanio B., den Boer S., Oliveira E.R., Alves F.L., de Jesus G., Gomes J.L., Oliveira A. (2017) An oil risk management system based on high-resolution hazard and vulnerability calculations. OCEAN & COASTAL MANAGEMENT, 136 1-18.
- Cenci L., Persichillo M.G., Disperati L., Oliveira E.R., Alves F.L., Pulvirenti L., Rebora N., Boni G., Phillips M. (2015) Remote Sensing for Coastal Risk Reduction Purposes: Optical and Microwave data fusion for shoreline evolution monitoring and Modelling. 2015 IEEE INTERNATIONAL GEOSCIENCE AND REMOTE SENSING SYMPOSIUM (IGARSS), 1417-1420. 978-1-4799-7929-5.

- Oliveira A., Jesus G., Gomes J.L., Rogeiro J., Azevedo A., Rodrigues M., Fortunato A.B., Dias J.M., Tomas L.M., Vaz L., Oliveira E.R., Alves F.L., den Boer S. (2014) An interactive WebGIS observatory platform for enhanced support of integrated coastal management. Journal Of Coastal Research, 507-512

REFERENCES

ANEPC, 2019. Avaliação nacional de risco, 1a Atualização - Julho de 2019. Lisboa, Portugal.

Carpignano, A., Golia, E., Di Mauro, C., Bouchon, S., Nordvik, J.-P., 2009. A methodological approach for the definition of multi-risk maps at regional level: first application. J. Risk Res. 12, 513–534. https://doi.org/10.1080/13669870903050269

de Souza Porto, M.F., de Freitas, C.M., 2003. Vulnerability and industrial hazards in industrializing countries: an integrative approach. Futures 35, 717–736. https://doi.org/10.1016/s0016-3287(03)00024-7

Deleu, J., Tambuyzer, H., Stephenne, N., 2011. Multi Risk preparedness supported by Earth Observation. Eurosense Gi4DM Conf. 3-8 May, Antalaya, Turkey.

EC, 2010a. Europe 2020 A European strategy for smart, sustainable and inclusive growth.

EC, 2010b. Risk Assessment and Mapping Guidelines for Disaster Management. Eur. Com. Staff Work. Pap. 21 December, Brussels, Belgium.

Fonseca, T.C., Costa, E.M., Zêzere, J.L., 2014. A Gestão Risco no Território, o Contributo dos Planos Regionais de Ordenamento do Território, in: VIII Encontro Nacional de Riscos.

Grünthal, G., Thieken, A.H., Schwarz, J., Radtke, K.S., 2006. Comparative Risk Assessments for the City of Cologne - Storms, Floods, Earthquakes. Nat. Hazards 38, 21–44. https://doi.org/10.1007/s11069-005-8598-0

Leifer, I., Lehr, W.J., Simecek-Beatty, D., Bradley, E., Clark, R., Dennison, P., Hu, Y., Matheson, S., Jones, C.E., Holt, B., Reif, M., Roberts, D.A., Svejkovsky, J., Swayze, G., Wozencraft, J., 2012. State of the art satellite and airborne marine oil spill remote sensing: Application to the BP Deepwater Horizon oil spill. Remote Sens. Environ. 124, 185–209. https://doi.org/10.1016/j.rse.2012.03.024

Lu, D., Li, G., Valladares, G.S., Batistella, M., 2004. Mapping soil erosion risk in Rondônia, Brazial Amazonia: Using RUSLE, Remote Sensing and GIS 512, 499–512.

Tralli, D.M., Blom, R.G., Zlotnicki, V., Donnellan, A., Evans, D.L., 2005. Satellite remote sensing of earthquake, volcano, flood, landslide and coastal inundation hazards. ISPRS J. Photogramm. Remote Sens. 59, 185–198. https://doi.org/10.1016/j.isprsjprs.2005.02.002

Van Westen, C.J., 2013. Remote Sensing and GIS for Natural Hazards Assessment and Disaster Risk Management, in: Schroder, J.F., Bishop, M.P. (Eds.), Treatise on Geomorphology. Elsevier Inc., San Diego, USA., pp. 259–298.

Chapter 2:
SATELLITE REMOTE SENSING FOR SINGLE AND MULTI-HAZARD RISK ASSESSMENTS

Abstract: Can satellite remote sensing data provide reliable alternatives to support multi-hazard assessments? For several years, the incorporation of such data has been growing in single-hazard risk assessments, but multi-hazard approaches, despite being attractive solutions, are still lacking developments in this area. This chapter provides a review of different approaches from single to multiple hazard risk assessments, with special focus on the incorporation of remote sensing data. This literature review addresses methods used for single weather-driven hazard assessments in Mediterranean regions, including wildfires, soil erosion and floods (fluvial and coastal), as well as multi-hazard approaches. Each method is analysed according to a set of pre-defined characteristics, to facilitate its analysis and enable comparisons. Despite being a relatively new field, the literature about multi-hazard risk assessments contains a wide diversity of approaches from diverse scientific fields. This chapter identifies the difficulties in interpreting and selecting such methods and presents its main advantages and disadvantages. It concludes that free satellite remote sensing data meets most data requirements for top-down approaches, from regional-scale studies and beyond.

Keywords: wildfire; flood; coastal; erosion; data aggregation; hazard interaction

1. Introduction

Traditional Single-Hazard Risk Assessment (SHRA) approaches include vulnerability and exposure analysis of any elements affected by one hazard. However, most natural and anthropogenic risks are likely to occur at the same location and, not rarely, at the same time (Carpignano et al., 2009). Multi-Hazard Risk Assessments (MHRA) have been highlighted as an ideal solution to deal with the combination of multiple hazardous sources and multiple variable elements overlapping in time and

space, which may prove to be extremely useful to support spatial planning decisions and emergency strategies.

Despite its apparent simplicity, multi-hazard risk assessments are complex tasks at various levels. Not only they address the possibility of occurrence of different types of events (by considering multiple hazard sources), but also the possibility of several hazards occurring at the same time (or within a certain time frame), according to different types of interactions, which may result in secondary hazards or secondary events. Rather than using a geographically based approach, i.e., with a territorial perspective, they can also be element-oriented, focusing on specific features (e.g., buildings, population, infrastructure) (Delmonaco et al., 2007).

Considering the complexity of risk assessments, a strong conceptual foundation is often described as being useful to understand cause-effect relationships of elements in hazard contexts. Some of the conceptual framework models derive from other environmental management fields but are often used in risk assessment contexts, allowing the integrating with other methods (Narayan et al., 2014).

In general, hazard assessments may be analysed qualitatively or quantitatively, with the second considering two types of approaches: data-driven or physically based methods. Data-driven approaches, which are also referred to as statistical or mathematical-statistical (e.g., Devi et al., 2015), rely on the study of hazard effects, which are usually obtained from historic records. Rather than focusing on the physics of processes, these methods act as a 'black-box', analysing the correlation among the effects and factors which are assumed to control of the effects of hazard events, using parametric or non-parametric methods to estimate their probabilities (Liu et al., 2016c). Instead, physically based methods focus on modelling processes using equations including spatial and temporal parameters. These parameters may be treated as deterministic or probabilistic, depending on the consideration of uncertainties (Schmidt et al., 2011). In any case, either quantitative approach should account for probabilities of occurrence. Marzocchi and Woo (2009) highlight the advantages of introducing the concept of probabilities in risk analysis, as a valuable contribution for further risk management and decision-making processes, by allowing immediate comparisons and gradation between different risks, to define "acceptable risk" levels, and perform cost-benefit analysis.

According to Liu et al. (2016a), geophysical environmental factors can be categorized into two types: stable factors and trigger factors. Stable factors are described as directly related to the pre-conditions before hazard events occur, while trigger factors are considered less stable, determining

the frequency and magnitude of hazards. Their corresponding variables may include primary variables (e.g., temperature, precipitation), synoptic variables (e.g., weather types, pressure), compound variables (e.g., humidity, evaporation), or proxy variables (i.e., soil moisture, river discharge or flow velocity) (Gallina et al., 2016; UKCIP, 2003).

One of the most important considerations concerns the availability of ready and reliable data, which depending on the working scale, can be expensive or inaccessible to risk assessment experts. Earth Observation (EO) using satellite Remote Sensing (RS) has been highlighted as groundbreaking, providing solutions to reduce efforts, costs and time in multi-hazard risk assessments.

2. Satellites

Spatial and statistical data have different relevancies depending on the type of hazard. Some of the most common include land use, vegetation, slope, oceanographic and meteorological factors (Van Westen, 2013). RS has provided a synoptic perspective for many of these measurements, with variable spatial (or geometric), spectral, radiometric and temporal resolutions, contributing for a wide range of disciplines (Tralli et al., 2005). Satellite EO has been used in several single hazard risk assessment contexts, enabling the possibility to reconstruct recent-history catastrophic events and providing data to predict and plan mitigation actions (e.g., Chuvieco et al., 2010; Grünthal et al., 2006; Harb and Acqua, 2017; D Lu et al., 2004).

Finding suitable spatial or geographical information requires a careful analysis of its specifications to satisfy methodological data requirements. This process may be even more challenging, since satellite remote sensing data and products often imply extremely high costs, for both commercial and non-commercial uses. However, in the recent past, this paradigm has been changing, as the access to free and open data is increasing. For example, the INSPIRE EU Directive (2007/2/EC) entered into force in the state-members in 2007, establishing a framework oriented to make spatial or geographical information more accessible and interoperable, for the European Community environmental policies and activities. In particular, low-to-medium spatial resolution imagery have started to be distributed without charging. The Landsat series, which dates back to the late ’70s, has become free to the public since 2008, representing the longest running enterprising of satellite EO. The ASTER dataset (Advanced Spaceborne Thermal Emission and Reflection Radiometer) also started by being freely available only for non-commercial educational uses, but this policy was extended to all users since 2016. Other examples of free access data include Meteosat (first and

second-generation), MODIS (Moderate Resolution Imaging Spectroradiometer), SRTM (Shuttle Radar Topography Mission) and more recently the Copernicus Program with several Sentinel series. Nevertheless, higher spatial resolution imagery continue to have significant costs to end-users, as are often managed by private-sector entities, e.g., Worldview, Quickbird, Pleiades or IKONOS. In 2016, the French Government announced that SPOT images older than 5 years old and dating back to 1986, would be freely released for research purposes.

Despite any eventual loss of commercial interest of older images, they continue being extremely valuable for research and investigation purposes, as they may be the only alternative for portraying certain events from the recent Earth's history. If private and public entities continue improving the distribution of free access data, the use of RS should become more massified and reach a broader public, contributing to the construction of the Global Earth Observation System of Systems (GEOSS) and the World Heritage program (Selding, 2014).

Table A.1 includes a summary of some of the main free-access satellites that are currently available for EO purposes.

Among passive satellites, the long-record Landsat series has been successively updated. At the time of writing, both Landsat 7 and 8 missions are still operational with an offset of 8 days (Landsat 7 is expected to be replaced by Landsat 9 after September 2021). Despite suffering from a failure of the Scan Line Corrector since 2003, Landsat 7 images can still be used thought processing techniques (e.g., Chen et al., 2011). EO-1 ALI and ASTER have been launched to provide comparable or improved alternatives, to map the land surface temperature, reflectance or elevation. Compared to the Landsat series, ASTER delivers increased spectral resolution at equivalent spatial resolution. Since both spectral and spatial resolutions control the detection capability, ASTER allows identifying features smaller than its spatial resolution (e.g., Disperati and Virdis, 2015). Besides, other than the usual Nadir looking bands, ASTER includes a backwards-looking band (3B), which provides stereo coverage, allowing for the generation of Digital Elevation Model(s) (DEM).

As for lower spatial resolutions, the Meteosat first generation (Meteosat-1 to -7) was initiated in 1972 by a predecessor of the European Space Agency (ESA), consisting in a group of meteorological geosynchronous satellites for continuous and reliable meteorological observations. These were gradually replaced by a second-generation series (Meteosat-8 to 11), which are still active (eventually being replaced by a third generation). The MODIS series, composed by two sensors on-board of Terra and Aqua satellites (both part of the National Aeronautics and Space Administration (NASA) Earth Observing System) is capable of providing short revisit times (1-2 days depending on

the latitudes) along with 36 multispectral bands which can have a wide range of uses: the identification of land/cloud/aerosols boundaries; ocean colour, phytoplankton and biogeochemistry; atmospheric water vapour; surface and cloud temperature; atmospheric temperature; cirrus clouds water vapour; cloud properties; ozone; and cloud top altitude (NASA, n.d.). VIIRS is another multi-disciplinary sensor providing data for ocean, land, aerosol, and cloud purposes, capable of twice the coverage of MODIS with 750m resolution.

Regarding high-resolution data, SPOT-5 delivers panchromatic images with 5m of spatial resolution, but with only three multispectral bands and one short wave infrared band, respectively with a spatial resolution of 10m and 20m.

In terms of active satellites, NASA's Shuttle Radar Topography Mission (SRTM), was initially released with 3 arc-seconds (or about 90 m) resolution for regions outside the United States of America, but by late 2015, the public release was updated to a resolution of 1 arc-second (about 30m). Regarding ESA's missions, the first European Remote Sensing (ERS-1) included a synthetic aperture imaging radar, radar altimeter and instruments to measure ocean surface temperature and wind fields, which was later complemented by ERS-2, with an additional sensor for atmospheric ozone monitoring. ENVISAT was the successor to ERS, having a more advanced imaging radar, radar altimeter and temperature-measuring radiometer. More recently, starting in 2015, Japan Aerospace Exploration Agency (JAXA) has released several a freely available world digital surface model, the ALOS World 3D, with a horizontal resolution of approx. 30-meter mesh (1 arcsec) and 5-meter vertical mesh, derived from the Advanced Land Observing Satellite "DAICHI" (ALOS). This dataset is comparable to the SRTM, with additional benefits, such as wider coverage (including Antarctica).

In the last years, ESA has been responsible for an ambitious initiative, the Copernicus programme, aiming to release upwards to 30 satellites, which include Sentinel-1 missions, capable of proving day and night radar images and Sentinel-2 missions, designed for high-resolution optical images for land services. At the time of writing, Sentinel-3 services are also operational, being relevant for ocean and land monitoring. Sentinel 4 and 5 are still being prepared and are expected to contribute for atmospheric composition monitoring from geostationary and polar orbits, while Sentinel-6 will carry a radar altimeter to measure global sea-surface height, primarily for operational oceanography and climate studies (ESA, n.d.).

The access to some of the above-mentioned data may be found in several web platforms that often distribute freely available information, including raw data and products with different levels

of processing. Amongst the most important, is the USGS Earth Explorer(USGS, 2020a) which offers worldwide coverage and includes the most important Landsat catalogue (with multiple processing levels), as well as ASTER, SRTM, MODIS or NOAA's AVHRR. The European Space Agency also created a specific data hub for the Copernicus series (ESA, 2021), including Sentinel's 1, 2 and 3 products. NASA's Earthdata Search (NASA, 2020a) is another valuable portal, containing a wide range of data (e.g., Aqua, Terra, Aura, TRMM, Calipso, NASA DC, JASON, ENVISAT, ALOS, METEOSAT, GOES, ICESAT, GMS, Landsat, NIMBUS, SMAP, RADARSAT, NOAA satellites, GPS satellites). The equivalent Earth Observation Link (EOLi) (ESA, 2020) allows to browse and preview EO images from Envisat, ERS, IKONOS, DMC, ALOS, SPOT, Kompsat, Proba, IRS, SCISAT. Moreover, several other platforms are offering final products with particular interest for natural hazard-related studies, including the Atmosphere Archive & Distribution System (LAADS) Distributed Active Archive Center (DAAC) (NASA, 2020b), Joint Research Centre European Forest Fire Information System (JRC/EC, 2020), HydroSHEDS (WWF, 2020), and Earth Observation Data with several near-real-time products, including MODIS and VIIRS(NASA, 2020c).

Free-access RS data has become a valuable source for several applications, including research purposes. The catalogue of available RS data will likely increase, not only from future satellite missions, but also if the industry continues promoting the dissemination of older datasets. Besides, aerial remote sensing databases should not be forgotten, particularly for local scale studies (e.g., Manzo et al., 2015). In some cases, these can report to periods before satellite EO data, and depending on the study area or purpose of the application, may be freely available.

3. Weather-related hazards in temperate Mediterranean regions

Weather-related natural hazards have been accounted for major losses worldwide, as a consequence of meteorological, hydrological or climatological events (Hoeppe, 2016). Even relatively mild climates can be affected by such occurrences. For example, the European temperate Mediterranean zone (Figure 2.1), where Portugal is included, is generally characterized by hot summers and mild winters, yet presenting pronounced climatic differences within short distances, depending on altitude, continental landmasses, or maritime influence (Condé et al., 2002). This is the case of locations on the border with the Atlantic biogeographical region, where the annual temperature amplitude is lower and the annual precipitation is higher, resulting in mild rainy winters and not excessively dry summers. Still, extreme events are amongst the main causes of weather-related natural hazards affecting this region, a tendency which will likely increase,

according to the latest climate change records and projections. The 5th assessment report of the Intergovernmental Panel on Climate Change (R. S. Kovats et al., 2014) highlights that since 1950, in parts of Southern Europe, high-temperature extremes have become more frequent, while low-temperature extremes and annual precipitation have been decreasing (Condé et al., 2002). Extreme sea levels have also increased due to mean sea level rise. In terms of projected climate changes, Southern Europe is likely to be affected by a strong warming in summer, while the annual precipitation should decrease. Projections also indicate a marked increase of extremes in Europe, in particular heatwaves, droughts and heavy precipitation events.

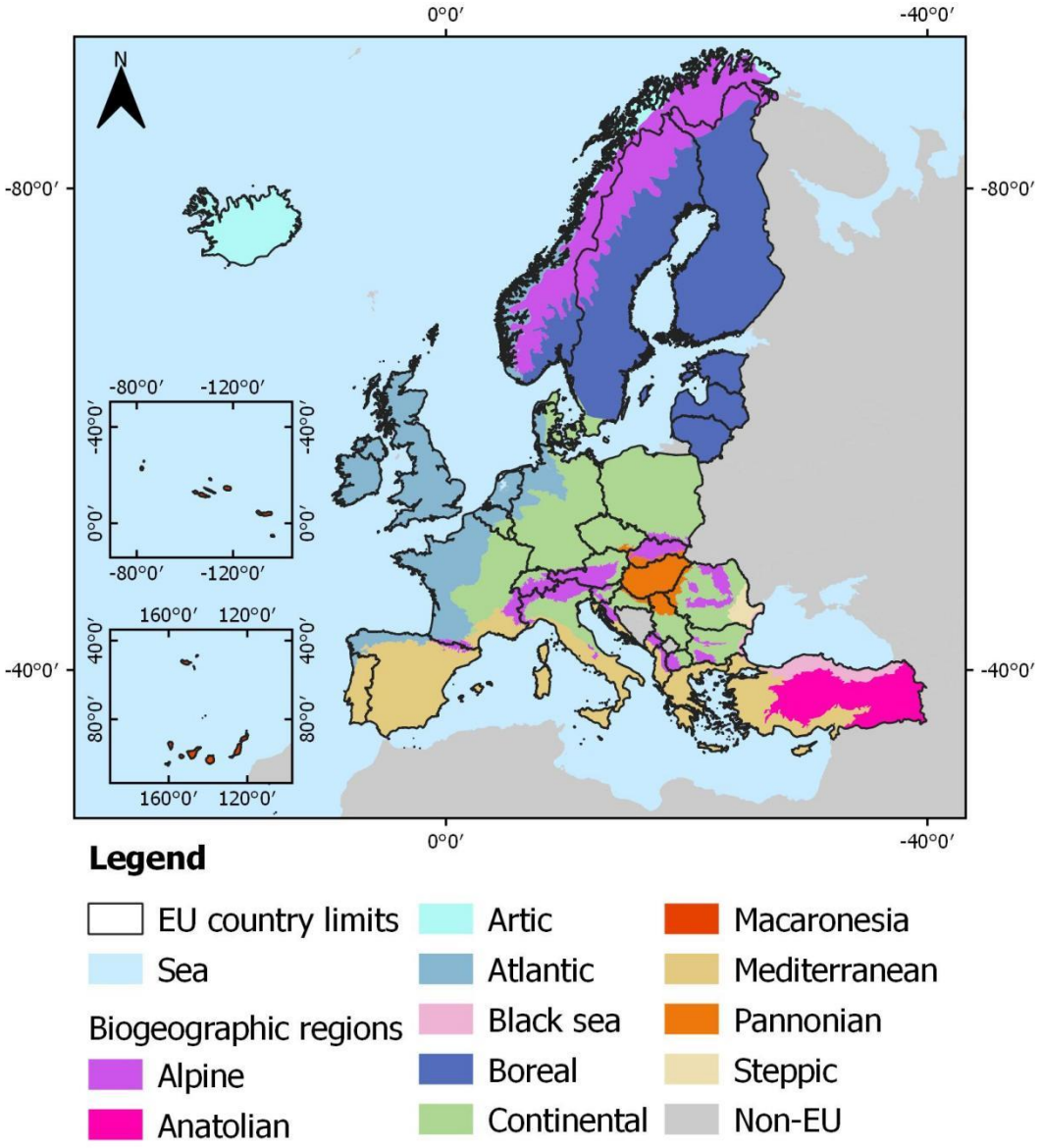

Figure 2.1 – Biogeographic regions within the European Union (EU) (Sources: European Commission, Eurostat, GISCO; EEA) (Coordinate system: WGS84 Pseudo-Mercator).

According to Condé et al. (2002), more than half of the Mediterranean Biogeographical region is already affected by soil erosion risk, as a consequence of dry climate periods and exposed slopes, which are amplified by overgrazing, deforestation and surface disturbance. Wildfires, both natural but especially human-induced, are another major problem in southern European countries, with an annual average of 48.940 fires and 454.104 ha burned areas, in the last 35 years (Schmuck et al., 2015). Besides the multi-aspect damages of wildfires which have consequences to human lives, socio-economy and biodiversity, they also contribute for soil erosion and desertification. Deep burned soils which loose the binding protection of vegetation or litter, suffer from the altered hydrological response, reducing resistance to erosion and increasing runoff during post-fire rainstorms (Esteves et al., 2012).

Flood disasters are amongst the most important natural hazards of Europe in terms of economic losses (EEA, 2010). The degree of such losses is often dependent on a combination of societal and hydro-meteorological factors, being usually higher whenever hydrological floods (i.e. riverine, coastal and flash floods) occur in populated areas. According to the EM-DAT records (which date back to 1926), some of the most deadly flood events in Europe have occurred in Southern Europe, although the number of fatalities has been decreasing in the last decades. Still, between 1998 and 2009, the Mediterranean Region was affected by some of the most significant disasters in Europe, with Italy amongst the countries with the largest economic losses (EEA, 2010).

Storms are described as natural events that combine strong winds with heavy precipitation. Along with floods, storms are amongst the most significant natural hazards affecting Europe. Between 1998 and 2009, storms were the deadliest natural hazard, resulting in 729 fatalities (EEA, 2010). In Europe, these phenomena are typically associated with extra-tropical cyclones, mostly occurring between October and April, and can affect parts of the Mediterranean Region, as storms sweep from the Atlantic to the northern Iberian Peninsula and southern France. Coastal regions are particularly affected by such events, not only because they are hubs for growing population and activities, but also because they are already suffering from climate change effects (e.g., sea-level rise, increased cyclone intensity, rotation of the average wave direction), aggravating already existing coastal erosion processes. Moreover, when storm events occur under particular tidal characteristics (e.g., spring tides), their effects tend to be amplified, contributing to increase damages resulting from wave overtopping and coastal flooding.

Temperature extremes may refer to both sides of the scale and are associated with changes in inter-annual temperature variability. According to EEA (2010), most cold waves (or cold spells) in

Europe are associated with damages to agriculture, infrastructure and property, although they can also contribute to increased mortality rates. Still, heat waves (or heat spells) are those responsible for most deaths in Europe, with a particular incidence in the Mediterranean geophysical region. For example, during the hot summer of 2003, over than 70.000 fatalities were registered throughout Europe. In addition, during 2006 and 2007 there was increased mortality due to heat waves (EM-DAT). Climate change is affecting heatwaves, which have been increasing twice as fast over the last 25 years (EEA, 2010).

The following section consists of a review of methods used for analysing weather-related natural hazards, including different types of approaches for the assessment of exposure, vulnerability and risk, with special focus on RS applications.

4. A review of methods

Risk assessments are often based on conceptual frameworks, which may help to identify and illustrate the relations inherent to hazards. The Source-Pathway-Receptor concept (SPR-concept) is one of such frameworks, being originally developed within the context of environmental sciences to describe pollution movements, and have later applied for risk assessment purposes (Holdgate, 1979). The SPR-concept and its variation, the Source-Pathway-Receptor-Consequence concept (SPRC-concept) (Gouldby et al., 2005), allow to quickly translate the components of risk estimation and are particularly well established in flood risk assessments (e.g., Oumeraci et al., 2015). The Drivers, Pressures, State, Impact and Response framework (DPSIR) was originally developed as an adaptive management tool for the analysis of environmental problems, establishing cause-effect relations, between society and the environment, being also applied in risk assessment contexts (Gari et al., 2015; Juan Pablo Lozoya et al., 2011). The DPSIR conceptual framework was later adapted and defined as the Pathways of Effects by J.P. Lozoya et al. (2011), allowing to establish relations between hazards and ecosystem services. Conceptual frameworks have been referred to contribute for hazard understanding and communication between researchers, stakeholders and the public, and allow integration with other methods (Gari et al., 2015). Nevertheless, conceptual frameworks tend to suffer from subjectivity issues, not only in terms of the used terminology, but also in the assignment of variables according to each class, which may vary even for studies about the same subjects. Besides, if multi-hazard interactions are to be considered, to avoid double-counting issues, it would be necessary to use nested schematization to include element interactions and feedback loops, which makes the analysis very complex (Gari et al., 2015).

4.1. Single hazard methods

In general, RS data and methods may be used in different stages of the risk assessment process (Harb and Acqua, 2017; Van Westen, 2013). The most direct and immediate approach is to monitor the occurrence of hazardous events and to determine the extent of their effects. For example, digital imagery processing techniques may be used to identify ongoing processes (e.g., active fires, flooding), to determine the extent of hazard occurrences (e.g., annual wildfires, flooded extents), or to distinguish areas undergoing different processes (e.g., erosion and accumulation zones of coastal areas, landslides or from other soil erosion processes) (Cenci et al., 2015; Joyce et al., 2009; Sala et al., 2016; Vilar et al., 2015a). However, RS may also be used in more indirect approaches, incorporating parameters applied in hazard modelling or further stages of the risk assessment process. This section includes examples of different types of single-hazard approaches, addressing some of the most prominent weather-related hazards affecting the Mediterranean biogeographical region. Considering the focus of this thesis on RS applications, the selection of hazards was focused on those having direct interactions with two of the most easily identifiable hazard-driving elements - water and vegetation. The selected hazards include wildfires, soil erosion, and floods (both fluvial and coastal).

For summarization purposes, the information about each method has been organized and synthetized into tables (Table A.2 to Table A.4), which include a short description, data requirements, the scale of application, geographical scope, main advantages and disadvantages (highlighted or not, by the authors of each method). Moreover, these tables also contain references about the authors of each method and case study applications. Finally, each table entry is checked about the incorporation of RS data.

4.1.1. Wildfires

Wildfire risk assessments have been around for several decades and have been consistently implemented globally. The Fire Weather Index (FWI), based on the empirical Canadian model (Van Wagner, 1987) has been adopted by many national government agencies to provide wildfire risk assessments on a daily base. One of the major advantages of the FWI is the fact that it combines two other indices, the Initial Spread Index and the Buildup Index, allowing obtaining uniform results solely from weather variables. In addition, by being built around equations, the FWI may be readily

implemented through computer processing. Despite not being originally developed for such purposes, the incorporation of RS data has been introduced in further developments of the FWI, with current satellite data and derived products capable of fulfilling most of its data requirements. Bedia et al. (2015) applied the FWI at a global scale for both present and future climate projections. The later authors used MODIS products (to create 'non-burned' and 'burned' masks), together with publicly available climate data from the WATCH Forcing Dataset-ERA Interim and the Global Map of Terrestrial Ecoregions (freely distributed by the World Wildlife Fund). The European Forest Fire Information System (EFFIS) has also been used as an alternative source of fire data, providing updated information on current, long-term forecasts and fire history in Europe and in the Mediterranean Area, using both MODIS and VIIRS data to create updated maps of hotspots and fire perimeters (Vilar et al., 2015a).

As recognized by Coelho et al. (2007), most FWI data requirements include meteorological inputs, which may not always be available at the desired spatial and temporal resolutions. The same study proposes an alternative methodology to assess wildfire risk, considering the lack of public fully available meteorological data, composed of four intermediate indices. The fire detection probability consists in identifying "blind zones" for fire detection, considering terrain elevation, watchtowers network, proximity to roads and other build-up areas. The ignition risk is determined considering the number of ignitions per administrative unit, land uses, and built-up areas proximity. The propagation risk index relies on elevation, land use and built-up areas proximity, adding available forest fuel management strips networks. Finally, the suppression probability index combines the information about firefighting operative distribution and arrival time, obtained from the available road network and elevation. Despite considering mostly GIS variables, the Wildfire risk method (Coelho et al. 2007) has potential for further integration of RS data and procedures (e.g., land cover classification, burned extent masking, fire frequency), which would allow improving its automatization levels.

Amongst the forest fire literature, the most extended method for measuring plant moisture content is the Fuel Moisture Content (FMC). This is one of the critical factors affecting fire ignition and fire propagation. The FMC is defined as a simple proportion of fresh weight and dry weight, being originally dependent on intensive fieldwork sampling (e.g., Chuvieco et al., 2002; Van Wagner, 1987). RS methods have been tested to provide significantly better cost-effective alternatives, capable of temporal and spatial coverage derived directly from the vegetation cover. Chuvieco et al. (2002) tested the correlation of FMC obtained from plot areas with several indices

obtained from Landsat TM, obtaining promising results with variable correlation levels depending on the vegetation cover. Based on such experience, Chuvieco et al. (2010) developed a framework for fire risk assessment using GIS and RS technologies, which was implemented in several Spanish regions. This study considers several variables to estimate fire hazard danger, including the Ignition Danger (obtained from the estimation of FMC and contributions from lightning and human causes), Propagation Danger and several Vulnerability components (including Socio-economic value, Degradation potential and Landscape value). Since it covers several aspects of fire risk assessment, it presents some disadvantages inherent to its extensive requirements of data usage, in particular from the socio-economic realm.

From point of view of RS, finding suitable indicators for vulnerability purposes is one of the biggest challenges. Tedim et al. (2014) provide a complete set of vulnerability indicators for forest fires and coastal erosion, applied in two Portuguese study sites. Many of these indicators may be obtained using satellite data. For example, the 'wildland-urban interface', or the 'number of buildings', are considered to be indicators of forest fire exposure characteristics, which can be acquired from digital imagery classification. DEMs could also provide data for the indicator 'forest areas slope', which is associated to the physical dimension of Susceptibility/Fragility Indicators. Nevertheless, most of these indicators are related to the social and economic dimensions (e.g., GDP, population age, employment, etc.), being heavily dependent on statistical databases.

4.1.2.Soil Erosion

Soil erosion is a long studied for phenomena, contributing to soil degradation and desertification processes, with consequences for agriculture production, water quality, and derived socio-economic and environmental problems. Several biophysical factors affect these processes, including climate, land cover, soil type and topography. However, those resulting from human activities are generally the most challenging to estimate.

The Universal Soil Loss Equation (USLE) has been one of the most studied methods to determine annual soil loss. Originally developed to be applied in gently sloping croplands in the USA (Wischmeier and Smith, 1978), it has since been tested and upgraded, having worldwide application. The USLE has been applied in Mediterranean climates, considering a wide diversity of land covers, topographies and soil management practices. The Revised Universal Soil Loss Equation (RUSLE) maintains some of the empirical structure of its previous version, but with improved erosion prediction capabilities, including sub-factors from process-based concepts and encompassing a wider variety of situations, including forest, rangeland and disturbed areas (Renard et al., 1997, 1994). Despite being considerably data demanding, (Lu et al., 2004a) were able to apply the RUSLE in the Brazilian Amazonia using only RS and GIS data. This achievement was made through a series of parameter developments and simplifications, such as the assumption of equal climatic conditions throughout the study area and absence of support practices implementation, eliminating two parameters from the overall equation, Rainfall-Runoff Erosivity (R) and Support Practice (P). The remaining factors, Soil Erodibility (S), Topographic Factor (LS) and Cover Management Factor (C) were obtained from soil maps and survey data, a DEM and other parameters obtained from Landsat TM+ imagery.

The Morgan-Morgan-Finney (MMF) is a semi-empirical model used in the prediction of annual soil loss by water (Morgan, 2001). Compared to USLE or RUSLE, it contains a more consolidated physical structure, providing better estimates of soil loss. Vieira et al. (2014) highlight the importance of wildfires as a major cause of increased runoff and soil erosion in Mediterranean forests and woodlands, using a revised version of MMF to model runoff and erosion in burned areas and their mitigation. Nevertheless, due its increased complexity and data requirements, the MMF model is also heavily dependent on field measurements, which would present significant constrains for further integration of RS data.

In respect to post-fire erosion scenarios, the Erosion Risk Management Tool (ERMiT) was created to assess the risk of damaging runoff and erosion events occurring after a fire, providing a

distribution of rain event erosion rates with a probability of occurrence (Robichaud et al., 2007). This software can be particularly useful for land managers to plan mitigation treatments, using the Water Erosion Prediction Project (WEPP) to estimate erosion and runoff on burned sites, and stochastic weather files generated by CLImate GENerator (CLIGEN). Its application includes burned and recovering forest, rangeland and chaparrals, with or without the application of mitigation treatments. Considering its simplicity and relatively few data requirements, it demonstrates a potential for incorporating (at least partially) RS data. Nevertheless, despite delivering reasonable estimates of sediment delivery in most post-fire monitored sites, the few exceptions, i.e., over predicted sediment delivery, were precisely in two southern California sites with Mediterranean Climate (Robichaud et al., 2016). In order to apply ERMit outside the US, formatted input files (CLIGEN format) are already provided, including for southern European countries. However, Robichaud et al. (2016) refer that key field-measured input parameters are likely to be different, depending on soil types and previous land uses, such as less erodible heavily used lands in southern Mediterranean countries.

The Pan European Erosion Risk Assessment (PESERA) is a physically-based model, designed to estimate average long-term erosion rates, which has been applied across Europe at 1km resolution (Kirkby et al., 2008). The model is constructed around a central water balance, separating precipitation into possible pathways, including interception losses, evapotranspiration, overland flow, runoff and infiltration. Esteves et al. (2012) applied the PESERA model in fire-affected sites in Portugal, considering a 50-year climate historical time-series. Compared to field data, PESERA over-estimated post-fire erosion in thin stony soils, which occur in much of the fire-prone terrain in central Portugal. Despite being considered as a consistent and objective model, capable of providing long-term average values according to scenarios (past or future), it is more complex than other empirical models, and substantially more demanding on data requirements, in particular of rainfall data, which in many countries is of particularly difficult access.

4.1.3.Floods

According to the Floods Directive (2007/60/EC), 'flood' is defined as the temporary covering by water of land not normally covered by water, including rivers, mountain torrents, Mediterranean ephemeral watercourses, and floods from the sea in coastal areas. Flood risk is described as a combination of the probability of a flood event and its potential of causing adverse consequences for human health, the environment, cultural heritage and economic activity.

Flood hazard related studies in large study areas are often ambitious undertakings, presenting high spatial variability interactions (Rathjens et al., 2016). Large hydrological systems present a wide diversity of boundary conditions, depending on where a given catchment area joins a waterbody (i.e. rivers, estuaries, coastal lagoons, sea, or the ocean). Amongst the selected hazards considered in this chapter, those related to floods have the widest variety of approaches. Different methods are available for specific contexts, from one-dimensional modelling and beyond, using physically based or data-driven approaches. However, many are too complex or data demanding to consider the use of RS data, and were not included in this review.

4.1.3.1.Fluvial

Fluvial flood hazard maps are usually built after the collection of historical information about past flood events, using news reports, questionnaires, flood marks surveys (e.g., Coelho et al., 2007) or satellite RS data. The modelling chain usually starts with hydrologic modelling to obtain hydrographs for assigned return periods (e.g., the 100-year flow), which are consequently incorporated in hydraulic flow propagation models to estimate water surface elevations and corresponding inundation areas (Degiorgis et al., 2012; Sangwan and Merwade, 2015).

Most hydrological models are built around the assumption that flows can be affected by up-stream diversion and storage (USDA, 2012), therefore relying on the availability of relevant time series of rainfall data and drainage area to identify flood-prone areas. Hydraulic analyses are built around river channel geometry and other variables, such as surface roughness and boundary conditions to determine flood inundation areas under different return period-flood events (Degiorgis et al., 2012). In sum, meteorological, hydrological and hydraulic investigations are needed to define and estimate flooding impact, which together with vulnerability assessments, can be combined in final risk analysis (Apel et al., 2009).

The estimation of flood discharges can be assumed with different levels of detail. The most basic approaches are usually based on the statistics of extremes, yet they lack higher spatial differentiation and detail on dynamic aspects (Büchele et al., 2006). Different types of hydrological models can provide such estimates. Some authors (e.g., Gunasekera et al., 2015), divide them into deterministic vs stochastic models, depending whether or not they produce the same output from a set of input values. Others (e.g., Martini and Loat, 2007), classify them as static vs dynamic, depending on their temporal factor. According to Devi et al. (2015), the most important classifications include empirical, conceptual (or parametric) and physically-based models. While physically based models try to represent the real physical processes, conceptual models rely on

semi-empirical equations, field data and calibrations. Instead, empirical models entirely ignore the features and processes of hydrological systems. Whenever gauge data for flood frequency and base flood analyses is unavailable (e.g., in remote locations), probabilistic methods can be used as alternatives (Bates and De Roo, 2000; Gall et al., 2007). Choosing the right model is usually a compromise between input data requirements and result accuracy, in which simplified models tend to produce less accurate outputs.

One of the most popular hydrological models is the Soil & Water Assessment Tool (SWAT) (Gassman et al., 2007). It allows simulating long-term river watershed conditions, being very popular for agriculture production and management purposes, as well as flood hazard assessments. Nevertheless, the continuous simulation characteristics of this physical model are rather complex and time-consuming, being highly dependent on the availability of water level gauges and precipitation data.

Runoff models are typically built around equations that estimate runoff as a function of other watershed-related parameters (Devi et al., 2015). Some of these methods have been around for several decades (e.g., Empirical curve number, HBV, TOPMODEL, WEPP) and have been consecutively developed throughout several versions and modifications. Despite not being originally designed to incorporate such data, RS has been consistently used in many case study applications, particularly DEMs, which are used for characterizing topography catchments.

The Topographic Index (Manfreda et al., 2014, 2011, 2008) and the Topographic Wetness Index (TWI) (Jalayer et al., 2014; Qin et al., 2011) are modified versions of the TOPMODEL. These methods have been applied in the delineation of flood-prone areas based on topography, relying mostly on DEMs obtained from satellite RS. In many cases, the quality of such datasets is not consistent, especially towards the extremes of the vertical axes, such as in mountain areas (e.g., Kolecka and Kozak, 2014) and low relief areas (e.g., Gall et al., 2007). Although the main goal of such models not including flood risk assessments, as they allow continuous monitoring of entire river basins (or certain sections). By providing complete representations of the hydrologic dynamics, they have also been used for flood extension and water-depth estimations (e.g., Grillakis et al., 2010; Manfreda et al., 2011). Devi et al. (2015) describe TOPMODEL as a semi-distributed model, while reffering that other authors consider it to be a physically-based model, since its parameters can be theoretically measured.

Al-Abadi et al. (2016) included the TWI together with other six factors obtained from GIS and RS data to delineated flood-prone areas in an arid region. Catastrophe theory models were used to

derive weights from a linear combination technique, and the Analytical Hierarchy Process (AHP) allowed obtaining normalized ranks according to the classes of each factor. A sensitivity analysis was used to define flood susceptibility maps based on the highest variation indices, which included 'distance to streams', 'curve-numbers', 'elevation', and 'TWI'.

The LISFLOOD model (Bates and De Roo, 2000) has been described as a simple raster-based model for flood inundation simulation, relying on uniform flow formulae (Manning equation). This physically-based hydrological rainfall-runoff model consists of three sub-models: a catchment water balance model, a catchment flood simulation model and a high-resolution floodplain inundation model, which are embedded in a dynamical GIS environment (Lavalle et al., 2005). The main inputs consist of a DEM and land use maps, being suitable for RS based studies. LISFLOOD and subsequent modified versions have been applied to simulate floods in river channels and floodplains. Van der Sande (2001) compared different image classification techniques and data sources, including an IKONOS-2 image, to derive land use in a river floodplain in the Netherlands. By assuming different Manning roughness coefficients settings, the LISFLOOD model was used to generate several flood extent maps. Damage estimation was calculated by using stage-damage curves provided by official public sources, which were used to create damage loss maps.

In relatively low relief areas, DEMs can identify morphological breaks in slopes, distinguishing upland and floodplain areas (Rathjens et al., 2016). A fast approach to create static flood inundation maps is to simply overlay a DEM with a surface corresponding to the water level during a flood event, assuming the water surface to be flat and everything below it to be flooded (e.g., Priestnall et al., 2000; Sangwan and Merwade, 2015; Wang et al., 2002)). Nevertheless, when considering global scale DEMs (with lower accuracy and resolutions) such approaches should be used with caution when used for flood inundation modelling (Karlsson and Arnberg, 2011).

Alternatively, hydraulic or hydrodynamic models can be used to obtain more detailed information about flood inundation extents, while hydrographs, produced by hydrologic models, may be used as inputs to establish upstream or downstream boundary conditions.

One-dimensional hydraulic finite difference models, such as the HEC-RAS (Brunner, 2016; Samarasinghe et al., 2010; Sangwan and Merwade, 2015), are capable of providing flood extent and depth estimates with relatively few data requirements. River channels and floodplains are described as a series of cross sections perpendicular to flow direction, defined by a series of lateral and elevation coordinates which are typically obtained from DEMs. RS methods can also be applied to determine Manning's friction coefficients derived from land use.

Onana et al. (2008) presented a RS approach to assess flood hazard risk maps in an urban growth context, where SAR images and Normalized Difference Vegetation Index (NDVI) measurements were used for vulnerability mapping. Hazard exposure was determined with a linear dispersion flow model, requiring three parameters obtained with RS data: velocity flow for lateral translation, the distance from the source of flow, and the coefficient of dispersion.

Other 2D approaches such as Mike 21, rely on structured or unstructured grids, for flood depth and extent. However, with such increased complexity there are also further data requirements. Besides, as it is not always easy to represent the location of cross-sections, it may often be the case when such added efforts do not represent an increased predictive ability, when compared to simpler models (Bates and De Roo, 2000).

3D hydrodynamic models such as ELCIRC (e.g., Baptista, 1987; Dias et al., 2014) or SELFE (e.g., Fortunato et al., 2013; Zhang and Baptista, 2008) provide even more complete simulations of water circulation and dynamics, but are consecutively more complex and dependent on exhaustive bathymetric grids and computational time, which go beyond the scope of this review.

From the perspective of a predominant use of RS data, the simplest and best likely approach for fluvial flood hazard assessments seems to consist in morphometric analysis based on DEMs, instead of considering higher complexity discharge hydrologic models. However, systematic multi-temporal analysis should be crucial for determining the return periods of each event.

Regarding the vulnerability component of flood-related risk analysis, the typical approach consists in establishing a correspondence between flood depth and extension maps with exposed assets (e.g., land use or cover, population, buildings, infrastructures, vehicles, etc.). Depth damage functions can be used to estimate the damages per square meter or exposed elements, by considering their characteristics (number of floors, materials, type of property, etc.) (Meyer and Messner, 2005; Van der Sande, 2001). Other demographic variables can also be used to characterize the vulnerability of the exposed population (e.g., GDP distribution, age, or employment rates) (Samarasinghe et al., 2010).

4.1.3.2.Coastal

According to Fortunato et al. (2013), coastal flood studies usually involve one of the following approaches: 1) the analysis of inundation marks and other testimonies of previous events; 2) the statistical analysis of data from tide gauges; 3) the use of process-based models that reproduce the main physical processes involved; or 4) the combination of various approaches. Whenever there is

a lack of consistent records of data, the use of RS technologies can be considered for identifying marks of previous events. However, there are some shortcomings, such as the inability to properly identify inundation depths below 50 cm (Fortunato et al., 2013; Ramsey et al., 2012).

From the perspective of RS techniques, one of the most common approaches is to perform studies to estimate the shoreline position, for calculating erosion or accretion rates. Despite being a straightforward concept, the extraction of shoreline position can be a challenging task, due to its highly dynamic characteristics, on both temporal and spatial scales. RS is theoretically an ideal source for registering fast-changing processes (natural or anthropogenic). Boak and Turner (2005) describe a list of proxies which may be used for establishing more functional definitions of shoreline. Some of these proxies may be extracted from satellite images, exclusively or in a combination with other methods (Virdis et al., 2012). Cenci et al. (2013) used one of these proxies, 'the stable dune vegetation line', to perform a multitemporal shoreline analysis of a NW-Portuguese coast stretch, through a radiometric analysis of the Landsat imagery dataset, and later with Sentinel-1 data (Cenci et al., 2017b, 2015). The estimation of erosion and accretion rates was obtained with the Digital Shoreline Analysis System (DSAS) a freely available GIS based software which computes rate-of-change statistics for a time series of shoreline vector data (Himmelstoss, 2009). However, such rates are not considered valid for characterising urban coastal settlements, since those areas are often protected by engineering infrastructures, therefore not being representative of the natural shoreline evolution process.

Joint probability analysis are used for determining the chance of relevant sources taking high values simultaneously (Oumeraci et al., 2015). When applied to variables such as water levels or wave height, they can be used for flood risk purposes, to estimate the probability of storm surge affecting open coasts or estuaries. Hawkes (2008) summarizes the terminology and compares three types of joint probability analysis, including the JOIN-SEA approach, a group of freely available computer programs designed for joint probability extremes analysis. Such approaches rely on extensive independent records (e.g., significant wave height, mean wave period and sea level), which may be achieved using generators (e.g., the stochastic storm surge generator).

A Coastal Vulnerability Index has been described by Thieler and Hammar-Klose (2000) and further developed by Pendleton et al. (2005), in order to map the relative vulnerability of the coast to future sea level. It consists on ranking six physical variables contributing to sea-level rise: geomorphology, regional coastal slope, rate of relative sea-level rise, historical shoreline change rates, mean tidal range, and mean significant wave height. Based on this methodology, Kumar et al. (2010)

introduced some developments, which this number to eight risk variables. Some of these parameters can be directly obtained from RS methods, while others were derived from software modelling tools. RS methods were used to extract elevation (SRTM) and to estimate shoreline change rate (using DSAS). The software Mike 21 SW, a wind-wave model which simulates the growths, decay and transformation of wind-generated waves and swells in offshore and coastal areas, was used to obtain significant wave height (Danish Hydraulic Institute, 2015). The WXTide software was used to predict the maximum annual amplitudes of tides, which are derived from a worldwide network of stations.

Appelquist (2013) presented a simple framework to assess multiple climate change hazards in coastal environments, covering the aspects of ecosystem disruption, gradual inundation, saltwater intrusion, erosion and flooding. The methodology is illustrated in a wheel shaped diagram, starting in the centre, and following a route of different options according to coastal classification features: geological layout, wave exposure, tidal range, flora/fauna, sediment balance and storm climate. A short description is provided to classify each feature according to classes, using simple quantitative and qualitative methods. Depending on the classification of coastal features, 565 individual results may be achieved, each corresponding to different levels according to each coastal hazard. The use of RS is briefly mentioned, to determine the geologic layout and sediment balance (through Google Earth), but has the potential of being extensively developed in order to improve the accuracy of the inherent hazard estimations (as described in Appelquist and Balstrøm (2015), a later application of the same methodology).

The integration of different types of data, models and resources are often complex and challenging tasks. The DIVA (Hinkel and Klein, 2009), THESEUS (Simcic et al., 2014) or CERA (Narra et al., 2017) are examples of GIS-based tools which facilitate this processes in coastal flooding risk assessment contexts. One of their main advantages is the inclusion of graphical interfaces that guide the user throughout the process of data and modelling integration, including direct access to pre-defined global databases, which become more accessible to users with different backgrounds and levels of experience. Some of these tools are built in open software platforms, which increase the potential for further incorporation of RS data.

As previously mentioned in section 4.1.1, Tedim et al. (2014) includes a set of coastal erosion vulnerability indicators. An index of coastal erosion exposure and fragility is defined as the percentage of land uses being affected by erosion (associated to three functions: Agriculture, Urban and Ecological), relative to the total surface of a given parish. Indicators of coastal erosion resilience

are divided into five types: Physical, Environmental, Economic, Social and Institutional. Moreover, it considers the type of coastline geology and geomorphology, including the presence of dunes, as an indicator of physical resilience to erosion. The Environmental resilience is evaluated in terms of the ecosystems adaptability/endemism. The Economy component, is divided into 'Economic status' (available funds for protection works, GDP), 'Empowerment' (citizen economic dependence to community, and community dependence in respect to the state), 'Companies' (financial resources, insurance rates, insurance and sate compensations), 'Social' (population age, education, socialization/sense of community) and 'Institutional' (Landscape planning regulation). Several of these indicators are ambiguous and lack further descriptions, likely requiring extensive fieldwork and interviews. Others have the potential of being extracted from RS methods, in particularly those related to the physical realm of vulnerability.

4.2. Multi-hazard methods

This section includes a review of some of the most important methodologies addressing Multi-Hazard Risk Assessments (MHRA) (complemented with Table A.5).

We started by performing a preliminary literature survey, using the Scopus database (Elsevier, 2020). Our search was limited to documents including the following terms in their titles, abstract or keywords: Query 1- "multi-hazard AND risk"; and Query 2 - "multi-hazard AND risk AND remote sensing". Moreover, and given purpose of this work, we considered excluding entries corresponding to those within the fields of "Materials Science", "Energy", "Medicine", "Business, Management and Accounting", "Arts and Humanities", "Chemistry", "Chemical Engineering", "Economics, Econometrics and Finance", "Health Professions", "Psychology", "Biochemistry, Genetics and Molecular Biology", "Dentistry" and "Nursing". This literature survey resulted in 501 entries for Query 1 and 18 entries for Query 2. In Figure 2.2, we can verify the annual distribution of these results, in which those corresponding to Query 1 have been consistently increasing since the early 2000's, while those referring to Query 2 are much more recent and still very scarce. The distribution of results per subject area is shown in Figure 2.3, where Query 1 is distributed by 11 categories, while Query 2 is limited to only 7 subject areas, with "Earth and Planetary Sciences" being the most representative of both.

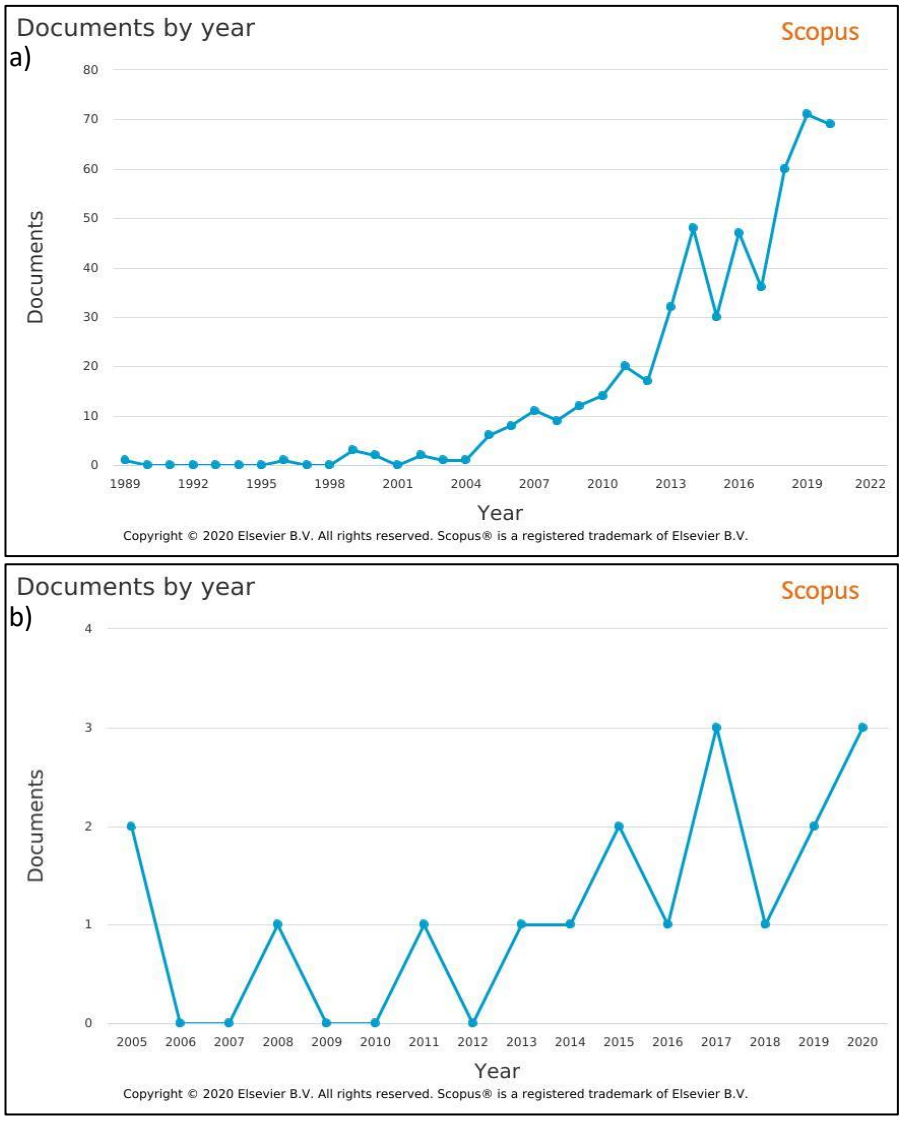

Figure 2.2 – Document distribution by year, according to Scopus (Elsevier, 2020)*, for:* ***a)*** *Query 1 - "multi-hazard AND risk";* ***b)*** *Query 2 - "multi-hazard AND risk AND remote sensing" (Source: Scopus, Elsevier 2020).*

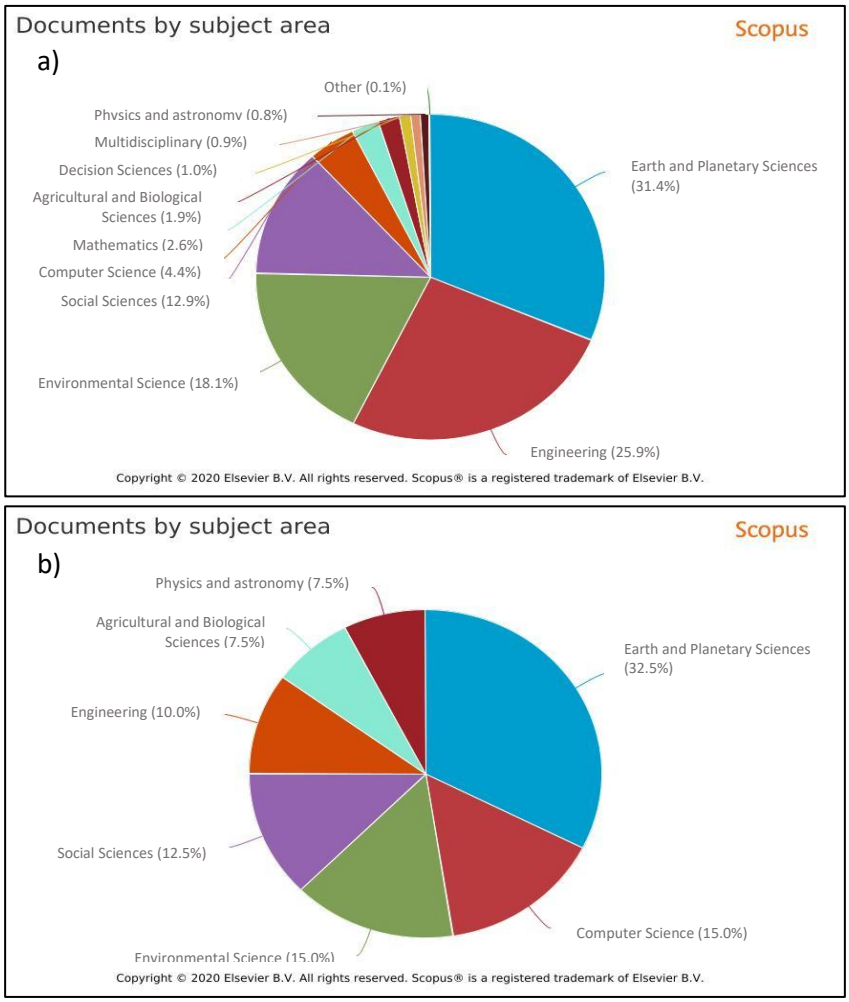

Figure 2.3 - Documents by subject area, according to Scopus (Elsevier, 2020)*, for:* ***a)*** *Query 1 - "multi-hazard AND risk";* ***b)*** *Query 2 - "multi-hazard AND risk AND remote sensing" (Source: Scopus, Elsevier 2020).*

Considering the results of the above mentioned literature survey and since MHRA still corresponds to an emerging field with few dedicated methods, the following review includes examples beyond the context of temperate Mediterranean regions.

For comparison purposes, special attention was given to the following characteristics:

1. Model Type: similarly to single-hazard approaches, multi-hazard methods can either be determined with physically-based models, data-driven methods applied to observed features and events, or a combination of both;
2. Type of results: typically divided into generic or element-oriented (focusing on certain features, e.g., loss of human life, economic losses, or buildings);

3. Aggregation: whenever any combined multi-hazard risk index is provided, aggregation processing is usually required. The most common include the sum of individual hazard exposures and vulnerabilities, or the assignment of weights for each individual hazard risk;
4. Hazard Interactions: some approaches account multiple hazards individually, while others address hazard relationships (e.g., parallel, series or independent interactions);
5. Incorporation of RS data.

One of the first references regarding multi-hazard approaches is the composite vulnerability analysis presented by UNDRO (1979), which describes some of the terminology and methods to be applied in a pilot project within the Metro Manila Area (Philippines). However, the biggest advances in MHRA have been conducted after the year 2000.

The Community Risk approach developed by Granger et al. (1999) is one of the first concrete approaches towards multi-hazard risk assessments. It includes a characterization of the elements at risk and their relative vulnerability to a group of different hazards. Instead of determining specific vulnerabilities for each hazard, an overall community vulnerability rank, based on five themes, is determined with a set of demography-based indicators, determined for each suburb. Hazard exposures regarding earthquakes, landslides, floods and cyclones (wind and storm tide) were determined using probability and process models, fed by a local monitoring system, without any direct incorporation of RS methods. These models were later used to establish scenarios according to the annual exceedance probability of occurrence. Exposure rankings were based on scenarios that match or exceed the threshold values defined by the levels of community acceptance regarding each hazard. The total risk of each hazard was established for every suburb according to four classes, depending on the suburb rank distribution, regarding their vulnerability and exposure to each hazard. In sum, this study represents a collection of normalized single hazard assessments, using a common vulnerability index, without any sorts of aggregation.

The methodology used by the Munich Reinsurance Company (2003) is another example of the first multi-hazard approaches, this time aiming for an absolute approach and by considering all relevant hazards at once. It was developed for the specific context of megacities, embracing a total risk index obtained from three main components: hazard exposure, vulnerability and exposed values. The exposure analysis was obtained from extensive historic records to provide average

annual losses for earthquakes, windstorms and floods. In addition to allocating average annual losses, the study includes a factor for long return periods catastrophes (1000-year-loss), based on the World Map of Natural Hazards (Berz et al., 2001) and the analysis of environmental factors. The vulnerability component comprises building classifications (hazard related and general) and preparedness levels (e.g., existing regulations, planning, or protection measures). Exposed values where determined from building material values and a global significance classification about the role of the urban area in the individual economic network. Each main component was standardized and combined in the total risk index using direct multiplication (equal weighting).

Other worldwide element-oriented publications include the Disaster Risk Index (UNDP, 2004) and the World Bank global multi-hazard analysis (Dilley et al., 2005), both relying on worldwide databases to determine the risk to loss of life/economic losses of multiple hazards.

The HAZUZ-MH, developed by (FEMA, 2004), is included in the category of one-tool software for MHRA. By granting access to its own databases, it provides a step-by-set guide to determine aggregated loss estimation from floods, hurricanes and earthquakes. The software flexibility allows the use of different levels of detail and incorporation of additional data from other sources. It has increased customization capabilities, including the evaluation of other hazards, applications outside the USA and incorporation of RS data.

Lavalle et al. (2005) developed a multiple (or integrated) weather-related risk assessment for the EU, combining RS data and available institutional databases. Single hazard maps are presented for floods (using DEMs and LISFLOOD model), forest fires (using EFFIS database), drought (combining LISFLOOD and EFAS framework) and heat waves (using temperature and humidity related indicators). The vulnerability components are also presented for each hazard, mostly based on general statistics (e.g., GDP per capita, age groups) and land cover. Instead of combining the multiple hazards in a unique representation, single risk maps are presented individually, in a non-exhaustive overview.

As part of the ESPON Hazards Project, Schmidt-Thomé et al. (2006) collected information of several single hazard assessments, including the first integrated hazard and risk overview on European territory. The Delphi method is used for multi-hazard weighting and assessment of overall risk, which was tested in the Dresden Region (Germany) and Centre Region of Portugal. The Delphi method was considered to offer limited and subjective information for inner-regional risk profiles.

At a closer scale, Khatsu and Van Westen (2005) implemented an element-oriented methodology, focused on urban-building to derive the population at risk, in a rapidly developing city in North-eastern India. Given the limited availability of existing data, the methodology used to create a multi-hazard map incorporates RS data, complemented with field mapping and historical data. The study is based on a building inventory, used to establish susceptibility categories for landslides (using a bivariate statistical method integrating EO field data), urban fires (multi-criteria evaluation) and earthquake damage (considering three scenarios of earthquake intensity). The multi-hazard loss estimation combines the occurrence of the highest category of each hazard for each building, which is later used to estimate the corresponding population at risk according to the different wards. The results of this study are presented as independent categories of cumulative hazard occurrence, without considering any type of aggregation or hazard interaction.

Grünthal et al. (2006) presented another methodology for multi-hazard risk assessments at a local scale. The study refers to the hazard from windstorms, flooding and earthquakes affecting the city of Cologne in Germany, using a common economic assessment for their comparison. The paper presents a stepwise methodological framework, including hazard assessment, asset inventory, vulnerability assessment, loss estimation and synthesis. Mathematical distribution functions were used to extrapolate time series of recorded data (i.e. wind speed, river discharge and seismic parameters), which were complemented with additional topographic-cartographic information (including a DEM). Official data was used to determine the spatial distribution of economic assets per land use. Damage functions were applied to a set of scenarios with different probabilities for each hazard to obtain their corresponding loss estimation. The risk curves for the three hazards (i.e. annual probability of exceedance vs monetary losses) are plotted together without considering any further aggregation or hazard interaction.

Wipulanusat et al. (2009) is an example of a multi-hazard risk assessment using RS methods at a regional scale. Individual hazard rankings were determined by weighting and ranking several empirical factors associated with floods and droughts. A multi-hazard map was created by aggregating the ranks for individual hazards, population density and land use type. Given its simple deterministic and empirical approach, this methodology presents several limitations, considering its subjectivity, lack of uncertainty analysis and no consideration of hazard interactions (even though floods and droughts are not mutually exclusive events).

Within the scope of the project Regional RiskScape, Schmidt et al., (2011) developed a software with a generic framework for modelling risks from different natural hazards and for various

elements at risk. A software prototype was tested in urban centres and small communities in New Zealand. It contains spatially explicit modules for hazard models, asset datasets and vulnerability (fragility functions), which were used to simulate the potential impacts of extreme events. It allows calculating damage ratios and losses, and establishing comparisons of each risk profile, without including any type of hazard interactions.

Van Westen (2013) is one of the most significant frameworks for understanding single and multi-hazard risk assessments, considering GIS and EO products and introducing some of the benefits of satellite-based monitoring systems. It provides a conceptual framework model for cause-effect relationships between triggering events, primary and secondary hazards. It is suited for multi-hazard risk studies, which can be an alternative to other models, such as the SPRC or the DPSIR. Nevertheless, it fails to distinguish the specific parameters that should be used to characterize each variable. It includes an overview of the various forms of available spatial data and their relevance for different hazards, including earthquakes, volcanic hazards, drought, windstorms, floods, coastal, landslides and wildfire. In addition, it includes another framework about the integration of GIS data for multi-hazard assessments, which is organized into eight components (i.e. input data, susceptibility, hazard, vulnerability, risk, quantitative/qualitative approaches, and disaster risk management).

Marzocchi et al. (2012) discuss the principles of multi-risk assessments and describes a general procedure, along with a simple real case example. After calculating the ranks for each individual risk (Marzocchi et al., 2009), they consider a long-term scenario triggering events, in which the result of a secondary risk has a higher probability than the individual risk by itself. The authors recognized the relevance of the event tree structure to analyse hazard interactions, and refer the importance of Bayesian methods, which provide a probability density function instead of a single value for the probability at each node. In other words, the procedure provides the posterior probability distribution that integrates the prior probability distribution (Grezio et al., 2010). The method allows weighting and merging of all components, providing estimates of the absolute probability of any possible event, with associated aleatory and epistemic uncertainties.

The work of Mignan et al. (2014) and Liu et al. (2015) are examples of two different theoretical frameworks for multi-risk assessment, developed within the MATRIX project. The first one (Mignan et al., 2014), is a generic framework based on the Sequential Monte Carlo Method, which considers hazard interactions, such as conjoint and cascading events. A set of time series (each representing one risk scenario) is generated from sampling events from a Poisson distribution, allowing the

probabilistic assessment of losses and recognition of more or less probable risk paths. It accounts for time-variant vulnerability and exposure, which consider the evolution of assets value with time, due to socioeconomic factors or occurrence of previous losses. The complexity of the method depends on the number of considered perils and interactions. Instead, the work of Liu et al. (2015), is a three-level method for multi-risk assessment, based on Bayesian networks. It requires a pre-existing assessment of single hazards (e.g., occurrence rates, intensities, pathways), dynamic vulnerabilities (time-variant) and consequences. The first level consists of a decision-making flowchart about the necessity of a multi-type assessment approach. The second level addresses hazards interactions and dynamic vulnerability using a matrix approach for a semi-quantitative assessment. The third level is a quantitative multi-risk assessment model, using Bayesian networks to estimate the probability of triggering /cascade events and model the time-variant vulnerability of a system exposed to multiple hazards. Both Mignan et al. (2014) and Liu et al. (2015) are exemplified using a theoretical application to a virtual city, assuming the same generic database which includes typical engineering values. Despite the lack of real-world applications, both methods seem to be potential candidates for incorporating RS data.

Agapiou et al. (2016) offer an alternative method to deal with multi-hazard aggregation. The paper includes an assessment of the risk of natural and anthropogenic hazards for cultural heritage in Cyprus, based on satellite imagery and GIS (developed throughout previous studies in the area). It starts by clustering monuments according to spatial constraint factors (i.e. elevation, tectonic activity, salinity, road network proximity, vicinity of urban areas, soil erosion and fire occurrence), resulting in five homogenous classes. The AHP is applied for each group, assigning different weights for each standardized factor (except for elevation). The overall risk hazard and corresponding map were obtained by summing all weighted factors for each class. Despite the simplicity of this approach, the use of clustering combined with AHP constitutes a more objective alternative compared to other methods (e.g., empirical, Delphi method). Unfortunately, it does not discriminate information about the types of hazard interactions and is unable of addressing data uncertainty.

Liu et al. (2016a) explore the conceptual relationship behind multi-hazard interactions, including a general analysis of the hazard-forming environments. Stable factors are used to identify which kinds of natural hazards influence a given area and to calculate susceptibility. Trigger factors are used to calculate the probability and magnitude, according to a systematic classification of hazards interactions (including independent, mutually exclusive, parallel and series relationships). The

paper describes a simple case study analysis focused on typhoon, flood and landslides in China's Yangtze River Delta. A basic framework of multi-hazard risk assessment for two consecutive typhoons is also presented.

In Liu et al. (2016b) a Bayesian Network (BN) method was used to develop the MmhRisk-HI, a quantitative model, approaching hazard interactions which is applied in a Chinese region. The model is divided into two main components: 1) Calculation of exceedance probability of multiple hazards occurring together, focusing on triggering factors relationships; and 2) Calculation of possible loss, including an exposure analysis and loss ratio assessment. The exposure analysis determines the spatial distribution of exposed elements, incorporating environmental data (daily meteorological records), disaster data (type, time and place) and socioeconomic data (general city statistics). The loss ratio assessment is calculated from a BN structure, which is used to select vulnerability-related indicators (independent variables) and hazard related indicators (trigger factors with different relationships). The multi-hazard risk assessment can be later integrated in a GIS environment to map possible loss caused with different exceedance probabilities. The case study addresses the most common multi-hazard scenario in the region, which is to be affected by two consecutive typhoons. This scenario is treated has a multi-hazard group, with corresponding hazard and vulnerability indicators. The model is almost entirely constructed on statistical data, and RS data is briefly referred to determine the spatial distribution of elements at risk.

In another publication, Liu et al. (2016c) compare two types of approaches in MHRA: the risk index, and the mathematical-statistical (i.e., data-driven) method. Both were applied to China's provinces, using simplified methods. The compared analysis resulted in significant inconsistencies but highlighted some of each relative merits.

Harb and Acqua (2017) discuss about the relevancy of RS technologies to analyse the components of multi-risk assessments and during different phases of the disaster management cycle. They highlight the benefits of both SHRA and MHRA approaches, concluding that they should not to be considered as alternatives to each other. Multi-hazard maps may not have the same level of detail of single-risk maps, but can address aggregation and integration of hazard dependencies, which may result in more generic and flexible products. Instead, SHRA are described to benefit from a unified risk metrics and reduced ambiguity when establishing common units of hazard intensity and vulnerability.

5. Conclusions

This chapter highlights the lack of publications with explicit incorporation of Remote Sensing (RS) data in both single and Multi-Hazard Risk Assessments (MHRA). As MHRA are still part of a relatively new field, there is a lack of agreement about the best way of dealing with aggregation, weighting and interactions between the multiple hazards. This is in part a consequence of the complexity in handling temporal and spatial scales of different hazard types, and their potential interactions. Besides, multi-hazard approaches often encompass a wide variety of scientific domains, with different terminologies and ways of cataloguing data and methods, which represents an added challenge.

Several publications highlight the benefits of using conceptual frameworks for risk assessment purposes. However, for MHRA, the simple task of assigning interactions is subjective because different elements may be classified differently depending on the type of hazard. Still, there are stepwise frameworks (e.g., FEMA, 2004; Liu et al., 2016b; Marzocchi et al., 2012; Schmidt et al., 2011; Van Westen, 2013) which can be useful in MHRA. Most, highlight the importance of defining the timeframe, study area, or scale of application, which should be amongst the first considerations of any methodological selection. The choice of methods should favour the simplicity and capability of providing the required information.

The lack of consistent historic records of disaster events is a limitation for determining hazard exceedance probabilities. Considering the lifetime of the satellite EO era, which has been gradually growing in number and sophistication, there is a collection of over 40 years of data, which is currently available throughout several databases. Given the current investments and plans to launch further missions, multiple science fields should expect a growth in RS data incorporation. Weather-related hazard assessments should be no exception.

Several studies highlight the importance of determining RS uncertainties and the awareness of incorporating such data, which may be affected by artefacts, errors, and questionable accuracy. Nevertheless, given the high costs of implementation and maintenance of exhaustive field monitoring campaigns and surveys, free RS data is already a valuable source of information, particularly from regional-to-global scales. Such top-down approaches contribute to overview and identify potential risk areas in need of more detailed local studies (Kappes et al., 2010).

The ultimate challenge of hazard assessments concerns the representation of results to increase the acknowledgment levels of visualization for decision-making purposes, including land-use planning and disaster risk management.

REFERENCES

Agapiou, A., Lysandrou, V., Themistocleous, K., Hadjimitsis, D.G., 2016. Risk assessment of cultural heritage sites clusters using satellite imagery and GIS: the case study of Paphos District, Cyprus. Nat. Hazards. https://doi.org/10.1007/s11069-016-2211-6

Al-Abadi, A.M., Shahid, S., Al-Ali, A.K., 2016. A GIS-based integration of catastrophe theory and analytical hierarchy process for mapping flood susceptibility: a case study of Teeb area, Southern Iraq. Environ. Earth Sci. 75, 687. https://doi.org/10.1007/s12665-016-5523-7

Apel, H., Aronica, G.T., Kreibich, H., Thieken, A.H., 2009. Flood risk analyses - How detailed do we need to be? Nat. Hazards 49, 79–98. https://doi.org/10.1007/s11069-008-9277-8

Appelquist, L.R., 2013. Generic framework for meso-scale assessment of climate change hazards in coastal environments. J. Coast. Conserv. 17, 59–74. https://doi.org/10.1007/s11852-012-0218-z

Appelquist, L.R., Balstrøm, T., 2015. Application of a new methodology for coastal multi-hazard-assessment & management on the state of Karnataka , India. J. Environ. Manage. 152, 1–10. https://doi.org/10.1016/j.jenvman.2014.12.017

Baptista, A.M., 1987. Solution of advection-dominated transport by Eulerian–Lagrangian Methods using the backwards method of char- acteristics. Massachusetts Institute of Technology.

Bates, P.D., De Roo, A.P.J., 2000. A simple raster-based model for flood inundation simulation. J. Hydrol. 236, 54–77. https://doi.org/10.1016/S0022-1694(00)00278-X

Bedia, J., Herrera, S., Gutiérrez, J.M., Benali, A., Brands, S., Mota, B., Moreno, J.M., 2015. Global patterns in the sensitivity of burned area to fire-weather: Implications for climate change. Agric. For. Meteorol. 214–215, 369–379. https://doi.org/10.1016/j.agrformet.2015.09.002

Berz, G., Kron, W., Loster, T., Rauch, E., Schimetschek, J., Schmieder, J., Siebert, A., Smolka, A., Wirtz, A., 2001. World map of natural hazards - a global view of the distribution and intensity of significant exposures. Nat. Hazards 23, 443–465. https://doi.org/10.1023/A:1011193724026

Boak, E.H., Turner, I.L., 2005. Shoreline Definition and Detection: A Review. J. Coast. Res. 214, 688–703. https://doi.org/10.2112/03-0071.1

Brunner, G.W., 2016. HEC-RAS River Analysis System : User's Manual.

Büchele, B., Kreibich, H., Kron, A., Thieken, A., Ihringer, J., Oberle, P., Merz, B., Nestmann, F., 2006. Flood-risk mapping: Contributions towards an enhanced assessment of extreme events and associated risks. Nat. Hazards Earth Syst. Sci. 6, 483–503. https://doi.org/10.5194/nhess-6-485-2006

Carpignano, A., Golia, E., Di Mauro, C., Bouchon, S., Nordvik, J.-P., 2009. A methodological approach for the definition of multi-risk maps at regional level: first application. J. Risk Res. 12, 513–534. https://doi.org/10.1080/13669870903050269

Cenci, L., Disperati, L., Persichillo, M.G., Oliveira, E.R., Alves, F.L., Phillips, M., 2017. Integrating remote sensing and GIS techniques for monitoring and modeling shoreline evolution to support coastal risk management. GIScience Remote Sens. 00, 1–21. https://doi.org/10.1080/15481603.2017.1376370

Cenci, L., Disperati, L., Sousa, L.P., Phillips, M., Alves, F.L., 2013. Geomatics for Integrated Coastal Zone Management : multitemporal shoreline analysis and future regional perspective for the Portuguese Central Region Radiometric Co-Registration 1349–1354. https://doi.org/10.2112/SI65-228.1

Cenci, L., Persichillo, M.G., Disperati, L., Oliveira, E.R., Alves, F.L., Pulvirenti, L., Rebora, N., Boni, G., Phillips, M., 2015. Remote sensing for coastal risk reduction purposes: Optical and microwave data fusion for shoreline evolution monitoring and modelling. 2015 IEEE Int. Geosci. Remote Sens. Symp. 1417–1420. https://doi.org/10.1109/IGARSS.2015.7326043

Chen, J., Zhu, X., Vogelmann, J.E., Gao, F., Jin, S., 2011. A simple and effective method for filling gaps in Landsat ETM+ SLC-off images. Remote Sens. Environ. 115, 1053–1064. https://doi.org/10.1016/j.rse.2010.12.010

Chuvieco, E., Aguado, I., Yebra, M., Nieto, H., Salas, J., Martín, M.P., Vilar, L., Martínez, J., Martín, S., Ibarra, P., de la Riva, J., Baeza, J., Rodríguez, F., Molina, J.R., Herrera, M.A., Zamora, R., 2010. Development of a framework for fire risk assessment using remote sensing and geographic information system technologies. Ecol. Modell. 221, 46–58. https://doi.org/10.1016/j.ecolmodel.2008.11.017

Chuvieco, E., Riaño, D., Aguado, I., Cocero, D., 2002. Estimation of fuel moisture content from multitemporal analysis of Landsat Thematic Mapper reflectance data: applications in fire danger assessment. Int. J. Remote Sens. 23, 2145–2162.

https://doi.org/10.1080/01431160110069818

Coelho, C.A., Alves, F.L., Ferreira, R.V., Valente, S., Teixeira, T., Ribeiro, C., Ferreira, A., Castanheira, E., Esteves, T., Coelho, C., Pinto, P., Silva, F., 2007. Relatório Final Risco de Cheia (No. Volume I), Definição das Condições de Risco de Cheia, Incêndios Florestais, Erosão Costeira e Industriais na Área de Intervenção da AMRIA. Aveiro, Portugal.

Coelho, C.O.A., Alves, F.L., Ferreira, A., Castanheira, E., Esteves, T.C., 2007. Relatório Final Risco de Incêndio Florestal, Definição das condições de risco de cheia, incêndios florestais, erosão costeira e industriais na área de intervenção da AMRIA. Aveiro, Portugal.

Condé, S., Richard, D., Liamine, N., 2002. European Environment Agency Europe ' s biodiversity The Mediterranean biogeographical region. EEA 54.

Danish Hydraulic Institute, 2015. Mike 21 Wave Modelling. Hørsholm, Denmark.

Degiorgis, M., Gnecco, G., Gorni, S., Roth, G., Sanguineti, M., Taramasso, A.C., 2012. Classifiers for the detection of flood-prone areas using remote sensed elevation data. J. Hydrol. 470–471, 302–315. https://doi.org/10.1016/j.jhydrol.2012.09.006

Delmonaco, G., Margottini, C., Spizzichino, D., 2007. ARMONIA methodology for multi-risk assessment and the harmonisation of different natural risk map. Armon. Proj. Appl. Multi-Risk Mapp. Nat. Hazards Impact assessment, Deliv. 3.1.1, Rome, Italy.

Devi, G.K., Ganasri, B.P., Dwarakish, G.S., 2015. A Review on Hydrological Models. Int. Conf. Water Resour. Coast. Ocean Eng. 4, 1001–1007. https://doi.org/10.1016/j.aqpro.2015.02.126

Dias, J.M., Lopes, C.L., Coelho, C., Pereira, C., Alves, F.L., Sousa, L.P., Inês, C., Fernandes, L., Phil, M.R., 2014. Influence of climate change on the Ria de Aveiro littoral : adaptation strategies for flooding events and shoreline retreat 320–325. https://doi.org/10.2112/SI70-054.1

Dilley, M., Chen, R.S., Deichmann, U., Lerner-Lam, A.L., Arnold, M., 2005. Natural Disasyer Hotspots. A Global Risk Analysis, Disaster Risk Management Series. https://doi.org/10.1080/01944360902967228

Disperati, L., Virdis, S.G.P., 2015. Assessment of land-use and land-cover changes from 1965 to 2014 in Tam Giang-Cau Hai Lagoon, central Vietnam. Appl. Geogr. 58, 48–64. https://doi.org/10.1016/j.apgeog.2014.12.012

EEA, 2010. Mapping the impacts of recent natural disasters and technological accidents in Europe -

An overview of the last decade, EEA Technical report. Copenhagen, Denmark. https://doi.org/10.2800/62638

Elsevier, 2020. Scopus [WWW Document]. URL www.scopus.com

ESA, 2021. Copernicus Open Access Hub [WWW Document]. URL https://scihub.copernicus.eu/dhus/ (accessed 12.11.20).

ESA, 2020. EOLi [WWW Document]. URL https://earth.esa.int/web/guest/eoli (accessed 11.9.20).

ESA, n.d. Overview of Copernicus - observing the earth [WWW Document]. URL http://www.esa.int/Our_Activities/Observing_the_Earth/Copernicus/Overview3 (accessed 5.22.21).

Esteves, T.C.J., Kirkby, M.J., Shakesby, R. a., Ferreira, a. J.D., Soares, J. a. a., Irvine, B.J., Ferreira, C.S.S., Coelho, C.O. a., Bento, C.P.M., Carreiras, M. a., 2012. Mitigating land degradation caused by wildfire: Application of the PESERA model to fire-affected sites in central Portugal. Geoderma 191, 40–50. https://doi.org/10.1016/j.geoderma.2012.01.001

FEMA, 2004. Using HAZUS-MH for Risk Assessment.

Fortunato, A., Rodrigues, M., Dias, J., Lopes, C., Oliveira, A., 2013. Generating inundation maps for a coastal lagoon: A case study in the Ria de Aveiro (Portugal). Ocean Eng. 64, 60–71. https://doi.org/10.1016/j.oceaneng.2013.02.020

Gall, M., Boruff, B.J., Cutter, S.L., 2007. Assessing Flood Hazard Zones in the Absence of Digital Floodplain Maps: Comparison of Alternative Approaches. Nat. Hazards Rev. 8, 1–12. https://doi.org/10.1061/(ASCE)1527-6988(2007)8:1(1)

Gallina, V., Torresan, S., Critto, A., Sperotto, A., Glade, T., Marcomini, A., 2016. A review of multi-risk methodologies for natural hazards: Consequences and challenges for a climate change impact assessment. J. Environ. Manage. 168, 123–132. https://doi.org/10.1016/j.jenvman.2015.11.011

Gari, S.R., Newton, A., Icely, J.D., 2015. A review of the application and evolution of the DPSIR framework with an emphasis on coastal social-ecological systems. Ocean Coast. Manag. 103, 63–77. https://doi.org/10.1016/j.ocecoaman.2014.11.013

Gassman, P.W., Reyes, M.R., Green, C.H., Arnold, J.G., 2007. The Soil and Water Assessment Tool: Historical Development, Applications and Future Research Directions. Am. Soc. Agric. Biol.

Eng. 50, 1211–1250.

Gouldby, B., Samuels, P., Klijn, F., Messner, F., Os, A. Van, Sayers, P., Samuels, P., Samuels, P., 2005. Language of Risk. Wallingford, UK.

Granger, K., Jones, T., Leiba, M., Scott, G., 1999. Community Risk in Cairns - A muliti-hazard risk assessment.

Grezio, A., Marzocchi, W., Sandri, L., Gasparini, P., 2010. A Bayesian procedure for Probabilistic Tsunami Hazard Assessment. Nat. Hazards 53, 159–174. https://doi.org/10.1007/s11069-009-9418-8

Grillakis, M.G., Tsanis, I.K., Koutroulis, A.G., 2010. Application of the HBV hydrological model in a flash flood case in Slovenia. Nat. Hazards Earth Syst. Sci. 10, 2713–2725. https://doi.org/10.5194/nhess-10-2713-2010

Grünthal, G., Thieken, A.H., Schwarz, J., Radtke, K.S., 2006. Comparative Risk Assessments for the City of Cologne - Storms, Floods, Earthquakes. Nat. Hazards 38, 21–44. https://doi.org/10.1007/s11069-005-8598-0

Gunasekera, R., Ishizawa, O., Aubrecht, C., Blankespoor, B., Murray, S., Pomonis, A., Daniell, J., 2015. Developing an adaptive global exposure model to support the generation of country disaster risk profiles. Earth-Science Rev. 150, 594–608. https://doi.org/10.1016/j.earscirev.2015.08.012

Harb, M., Acqua, F.D., 2017. Remote Sensing in Multirisk Assessment 53–65. https://doi.org/10.1109/MGRS.2016.2625100

Hawkes, P.J., 2008. Joint probability analysis for estimation of extremes. J. Hydraul. Res. 46, 246–256. https://doi.org/10.1080/00221686.2008.9521958

Himmelstoss, E.A., 2009. DSAS 4.0 - Installation Instructions and User Guide, Digital Sh. ed. USGS.

Hinkel, J., Klein, R.J.T., 2009. Integrating knowledge to assess coastal vulnerability to sea-level rise: The development of the DIVA tool. Glob. Environ. Chang. 19, 384–395. https://doi.org/10.1016/j.gloenvcha.2009.03.002

Hoeppe, P., 2016. Trends in weather related disasters - Consequences for insurers and society. Weather Clim. Extrem. 11, 70–79. https://doi.org/10.1016/j.wace.2015.10.002

Holdgate, M.W., 1979. A perspective of environmental pollution, Cambridge. ed. Cambridge; New York.

Jalayer, F., De Risi, R., De Paola, F., Giugni, M., Manfredi, G., Gasparini, P., Topa, M.E., Yonas, N., Yeshitela, K., Nebebe, A., Cavan, G., Lindley, S., Printz, A., Renner, F., 2014. Probabilistic GIS-based method for delineation of urban flooding risk hotspots. Nat. Hazards 73, 975–1001. https://doi.org/10.1007/s11069-014-1119-2

Joyce, K.E., Belliss, S.E., Samsonov, S. V., McNeill, S.J., Glassey, P.J., 2009. A review of the status of satellite remote sensing and image processing techniques for mapping natural hazards and disasters. Prog. Phys. Geogr. 33, 183–207. https://doi.org/10.1177/0309133309339563

JRC/EC, 2020. EFFIS [WWW Document]. URL http://effis.jrc.ec.europa.eu/ (accessed 11.9.20).

Kappes, M.., Keiler, M., Glade, T., 2010. From Single- to multi-hazard risk analyses: a concept addressing emerging challenges. Mt. Risks Bringing Sci. to Soc. 351–356.

Karlsson, J.M., Arnberg, W., 2011. Quality analysis of SRTM and HYDRO1K: a case study of flood inundation in Mozambique. Int. J. Remote Sens. 32, 267–285. https://doi.org/10.1080/01431160903464112

Khatsu, P., Van Westen, C.J., 2005. Urban multi-hazard risk analysis using GIS and Remote Sensing : A case study from Kohima Town , Nagaland , India . Petevilie Khatsu, in: Methodology.

Kirkby, M.J., Irvine, B.J., Jones, R.J.A., Govers, G., 2008. The PESERA coarse scale erosion model for Europe. I. - Model rationale and implementation. Eur. J. Soil Sci. 59, 1293–1306. https://doi.org/10.1111/j.1365-2389.2008.01072.x

Kolecka, N., Kozak, J., 2014. Assessment of the Accuracy of SRTM C- and X-Band High Mountain Elevation Data: A Case Study of the Polish Tatra Mountains. Pure Appl. Geophys. 171, 897–912. https://doi.org/10.1007/s00024-013-0695-5

Kumar, T.S., Mahendra, R.S., Nayak, S., Radhakrishnan, K., Sahu, K.C., 2010. Coastal Vulnerability Assessment for Orissa State, East Coast of India. J. Coast. Res. 263, 523–534. https://doi.org/10.2112/09-1186.1

Lavalle, C., Barredo, J.I., De Roo, A., Niemeyer, S., San Miguel-Ayanz, J., Genovese, E., Camia, A., 2005. Towards an European integrated map of risk from weather driven events, Reproduction.

Liu, B., Siu, Y.L., Mitchell, G., 2016a. Hazard interaction analysis for multi-hazard risk assessment: A

systematic classification based on hazard-forming environment. Nat. Hazards Earth Syst. Sci. 16, 629–642. https://doi.org/10.5194/nhess-16-629-2016

Liu, B., Siu, Y.L., Mitchell, G., 2016b. A quantitative model for estimating risk from multiple interacting natural hazards: an application to northeast Zhejiang, China. Stoch. Environ. Res. Risk Assess. https://doi.org/10.1007/s00477-016-1250-6

Liu, B., Siu, Y.L., Mitchell, G., Xu, W., 2016c. The danger of mapping risk from multiple natural hazards. Nat. Hazards 82, 139–153. https://doi.org/10.1007/s11069-016-2184-5

Liu, Z., Nadim, F., Garcia-Aristizabal, A., Mignan, A., Fleming, K., Luna, B.Q., 2015. A three-level framework for multi-risk assessment. Georisk 9, 59–74. https://doi.org/10.1080/17499518.2015.1041989

Lozoya, Juan Pablo, Sardá, R., Jiménez, J.A., 2011. A methodological framework for multi-hazard risk assessment in beaches. Environ. Sci. Policy 14, 685–696. https://doi.org/10.1016/j.envsci.2011.05.002

Lozoya, J.P., Sardá, R., Jiménez, J.A., 2011. Beach Multi-Risk Assessment in the Costa Brava (Spain). J. Coast. Res. 61, 408–4014. https://doi.org/10.2112/SI61-001.1

Lu, D., Li, G., Valladares, G.S., Batistella, M., 2004. Mapping soil erosion risk in Rondônia, Brazial Amazonia: Using RUSLE, Remote Sensing and GIS 512, 499–512.

Manfreda, S., Di Leo, M., Sole, A., 2011. Detection of Flood-Prone Areas Usins Digital Elevation Models. J. Hydrol. Eng. 16, 781–790. https://doi.org/10.1061/(ASCE)HE.1943-5584 .0000367

Manfreda, S., Nardi, F., Samela, C., Grimaldi, S., Taramasso, A.C., Roth, G., Sole, A., 2014. Investigation on the use of geomorphic approaches for the delineation of flood prone areas. J. Hydrol. 517, 863–876. https://doi.org/10.1016/j.jhydrol.2014.06.009

Manfreda, S., Sole, A., Fiorentino, M., 2008. Can the basin morphology alone provide an insight into floodplain delineation. WIT Trans. Ecol. Environ. 118, 47–56. https://doi.org/10.2495/FRIAR080051

Manzo, C., Valentini, E., Taramelli, A., Filipponi, F., Disperati, L., 2015. Spectral characterization of coastal sediments using Field Spectral Libraries, Airborne Hyperspectral Images and Topographic LiDAR Data (FHyL). Int. J. Appl. Earth Obs. Geoinf. 36, 54–68. https://doi.org/10.1016/j.jag.2014.11.003

Martini, F., Loat, R., 2007. Handbook on good practices for flood mapping in Europe. Eur. Exch. Circ. flood Mapp. 60.

Marzocchi, M., Mastellone, M.L., Ruocco, A. Di, Novelli, P., Romeo, E., Gasparini, P., 2009. Principles of multi-risk assessment - Interation amongst natual and man-induced risks. Proj. Report, Eur. Comm. Dir. Res. Dir. I — Environ. Unit I.5—Climate Chang. Environ. Risks.

Marzocchi, W., Garcia-Aristizabal, A., Gasparini, P., Mastellone, M.L., Di Ruocco, A., 2012. Basic principles of multi-risk assessment: a case study in Italy. Nat. Hazards 62, 551–573. https://doi.org/10.1007/s11069-012-0092-x

Marzocchi, W., Woo, G., 2009. Principles of volcanic risk metrics: Theory and the case study of Mount Vesuvius and Campi Flegrei, Italy. J. Geophys. Res. 114, 1–12. https://doi.org/10.1029/2008JB005908

Meyer, V., Messner, F., 2005. National Flood Damage Evaluation Methods - A Review of Applied Methods in Negland, the Netherlands, the Czech Republic and Germany. FLOODsite.

Mignan, A., Wiemer, S., Giardini, D., 2014. The quantification of low-probability-high-consequences events: Part I. A generic multi-risk approach. Nat. Hazards 73, 1999–2022. https://doi.org/10.1007/s11069-014-1178-4

Morgan, R.P.C., 2001. A simple approach to soil loss prediction: A revised Morgan-Morgan-Finney model. Catena 44, 305–322. https://doi.org/10.1016/S0341-8162(00)00171-5

Munich Reinsurance Company, 2003. Annual review: Natural catastrophes 2002. Munich, Germany.

Narayan, S., Nicholls, R.J., Clarke, D., Hanson, S., Reeve, D., Horrillo-caraballo, J., Hissel, F., Kowalska, B., Parda, R., Willems, P., Ohle, N., Zanuttigh, B., Losada, I., Ge, J., Trifonova, E., Penning-rowsell, E., Paul, J., 2014. The SPR systems model as a conceptual foundation for rapid integrated risk appraisals : Lessons from Europe. Coast. Eng. 87, 15–31. https://doi.org/10.1016/j.coastaleng.2013.10.021

Narra, P., Coelho, C., Sancho, F., Palalane, J., 2017. CERA: An open-source tool for coastal erosion risk assessment. Ocean Coast. Manag. 142, 1–14. https://doi.org/10.1016/j.ocecoaman.2017.03.013

NASA, 2020a. Earthdata Search [WWW Document]. URL https://search.earthdata.nasa.gov/search (accessed 11.9.20).

NASA, 2020b. LAADS DAAC [WWW Document]. URL https://ladsweb.modaps.eosdis.nasa.gov/ (accessed 11.12.20).

NASA, 2020c. Earth Observation Data [WWW Document]. URL https://earthdata.nasa.gov/earth-observation-data (accessed 11.12.20).

NASA, n.d. MODIS Specifications [WWW Document]. URL http://modis.gsfc.nasa.gov/about/specifications.php (accessed 8.22.16).

Onana, V.P., Rudant, J.P., Trouvé, E., Mauris, G., Laporte, N.T., Walker, W., 2008. A flood hazard risk assessment map in growing urban areas by integrating remote sensing and dem data. Int. Geosci. Remote Sens. Symp. 3, 1268–1271. https://doi.org/10.1109/IGARSS.2008.4779589

Oumeraci, H., Kortenhaus, A., Burzel, A., Naulin, M., Dassanayake, D.R., Jensen, J., Wahl, T., Mudersbach, C., Gönnert, G., Gerkensmeier, B., Fröhle, P., Ujeyl, G., 2015. XtremRisK — Integrated Flood Risk Analysis for Extreme Storm Surges at Open Coasts and in Estuaries: Methodology, Key Results and Lessons Learned. Coast. Eng. J. 57, 1540001. https://doi.org/10.1142/S057856341540001X

Pendleton, B.E.A., Thieler, E.R., Williams, S.J., Norton, G.A., Survey, U.S.G., Beavers, R., 2005. Coastal Vulnerability Assessment of Golden Gate National Recreation Area to Sea-Level Rise Open-File Report 2005-1058 U . S . Department of the Interior.

Priestnall, G., Jaafar, J., Duncan, A., 2000. Extracting urban features from LiDAR digital surface models. Comput. Environ. Urban Syst. 24, 65–78. https://doi.org/10.1016/S0198-9715(99)00047-2

Qin, C.Z., Zhu, A.X., Pei, T., Li, B.L., Scholten, T., Behrens, T., Zhou, C.H., 2011. An approach to computing topographic wetness index based on maximum downslope gradient. Precis. Agric. 12, 32–43. https://doi.org/10.1007/s11119-009-9152-y

R. S. Kovats, Valentini, R., Bouwer, L.M., Georgopoulou, E., Jacob, D., Martin, E., Rounsevell, M., Soussana, J., 2014. Europe, in: Climate Change 2014: Impacts, Adaptation, and Vulnerability. Part B: Regional Aspects. Contribution of Working Group II to the Fifth Assessment Report of the Intergovernmental Panel on Climate Change. Cambridge, United Kingdom and New York, NY, USA, pp. 1267–1326.

Ramsey, E., Werle, D., Suzuoki, Y., Rangoonwala, A., Lu, Z., 2012. Limitations and Potential of Satellite Imagery to Monitor Environmental Response to Coastal Flooding. J. Coast. Res. 280,

457–476. https://doi.org/10.2112/JCOASTRES-D-11-00052.1

Rathjens, H., Bieger, K., Chaubey, I., Arnold, J.G., Allen, P.M., Srinivasan, R., Bosch, D.D., Volk, M., 2016. Delineating floodplain and upland areas for hydrologic models: a comparison of methods. Hydrol. Process. 30, 4367–4383. https://doi.org/10.1002/hyp.10918

Renard, K.G., Foster, G.R., Weesies, G.A., McCool, D.K., Yoder, D.C., 1997. Predicting Soil Erosion by Water: A Guide to Conservation Planning With the Revised Universal Soil Loss Equation (RUSLE).

Renard, K.G., Foster, G.R., Yoder, D.C., McCool, D.K., 1994. RUSLE revisited: status, questions, answers, and the future. J. Soil Water Conserv. 49, 213–220.

Robichaud, P.R., Elliot, W.J., Lewis, S.A., Miller, M.E., 2016. Validation of a probabilistic post-fire erosion model. Int. J. Wildl. Fire 25, 337–350. https://doi.org/10.1071/WF14171

Robichaud, P.R., Elliot, W.J., Pierson, F.B., Hall, D.E., Moffet, C. a., 2007. Predicting postfire erosion and mitigation effectiveness with a web-based probabilistic erosion model. Catena 71, 229–241. https://doi.org/10.1016/j.catena.2007.03.003

Sala, J., Lopez, A., Romero, L., Koudogbo, F., 2016. A Sentinel-1 Flood map generation QGIS plugin. EGU Gen. Assem. 2016, held 17-22 April. 2016 Vienna Austria, p.14693 18, 14693.

Samarasinghe, S., Nandalal, H., Weliwitiya, D., Fowze, J., Harazika, M., Samarakoon, L., 2010. Aplication of Remote Sensing and GIS for Flood Risk Analysis:A Case Study at Kalu - Ganga River, Sri Lanka. Int. Arch. Photogramm. Remote Sens. Spat. Inf. Sci. XXXVIII, 110–115.

Sangwan, N., Merwade, V., 2015. A Faster and Economical Approach to Floodplain Mapping Using Soil Information. J. Am. Water Resour. Assoc. 51, 1286–1304. https://doi.org/10.1111/1752-1688.12306

Schmidt-Thomé, P., Kallio, H., Jarva, J., Tarvainen, T., Greiving, S., Fleischhauer, M., Peltonen, L., Kumpulainen, S., Olfert, A., Bärring, L., Persson, G., Relvão, A.M., Batista, M.J., 2006. The Spatial Effects and Management of Natural and Technological Hazards in Europe ESPON 1.3.1. https://doi.org/951-690-918-3

Schmidt, J., Matcham, I., Reese, S., King, A., Bell, R., Henderson, R., Smart, G., Cousins, J., Smith, W., Heron, D., 2011. Quantitative multi-risk analysis for natural hazards: A framework for multi-risk modelling. Nat. Hazards 58, 1169–1192. https://doi.org/10.1007/s11069-011-9721-z

Schmuck, G., San-Miguel-Ayanz, J., Durrant, T., Boca, R., Libertà, G., Petroliagkis, T., Di Leo, M., Rodrigues, D., Boccacci, F., Schulte, E., 2015. Forest fires in Europe, Middle East and North Africa 2014, Scientific and Technical Research series. https://doi.org/10.2788/1082

Selding, P.B., 2014. France To Make Older Spot Images Available to Researchers for Free [WWW Document]. SpaceNews. URL http://spacenews.com/39234france-to-make-older-spot-images-available-to-researchers-for-free/

Simcic, D., Bagli, S., Bozzeda, F., Pietrantoni, L., Zagonari, F., Hoggart, S., Nicholls, R.J., 2014. THESEUS decision support system for coastal risk management. Coast. Eng. 87, 218–239. https://doi.org/10.1016/j.coastaleng.2013.11.013

Tedim, F., Gardin, M., Vinchon, C., Carvalho, S., Desramaut, N., Rohmer, J., 2014. Assessment of Vulnerability to Natural Hazards - A European Perspective, in: Birkmann, J., Kienberger, S., Alexander, D. (Eds.), Comprehensive Vulnerability Assessment of Forest Fires and Coastal Erosion: Evidences from Case-Study Analysis in Portugal. Elsevier, Amserdam, Boston, Heildelberg, London, New York, Oxford, San Diego, San Francisco, Singapore, Sydney, Tokyo. https://doi.org/10.1016/B978-0-12-410528-7.00007-2

Thieler, E.R., Hammar-Klose, E.S., 2000. National Assessment of Coastal Vulnerability to Sea-Level Rise. Open-File Rep. 00-179 1.

Tralli, D.M., Blom, R.G., Zlotnicki, V., Donnellan, A., Evans, D.L., 2005. Satellite remote sensing of earthquake, volcano, flood, landslide and coastal inundation hazards. ISPRS J. Photogramm. Remote Sens. 59, 185–198. https://doi.org/10.1016/j.isprsjprs.2005.02.002

UKCIP, 2003. Climate adaptation: Risk, uncertainty and decision-making, Policy. Oxford, UK. https://doi.org/10.1016/j.molcel.2011.04.017

UNDP, 2004. Reducing Disaster Risk - A Challenge for Development. New York, USA.

UNDRO, 1979. Office of the United Nations Disaster Relief Co-ordinator (UNDRO).

USDA, 2012. Chapter 18: Selected Statistical Methods, in: United States Department of Agriculture, Natural Resources Conservation Service (Eds.), National Engineering Handbook.

USGS, 2020. Earth Explorer [WWW Document]. URL https://earthexplorer.usgs.gov/ (accessed 11.12.20).

Van der Sande, C.J., 2001. River Flood Damage Assessment using IKONOS Imagery.

Van Wagner, C.E., 1987. Development and structure of the Canadian forest fire weather index system, Forestry, Forestry Technical Report 35. Ontario, Canada. https://doi.org/19927

Van Westen, C.J., 2013. Remote Sensing and GIS for Natural Hazards Assessment and Disaster Risk Management, in: Schroder, J.F., Bishop, M.P. (Eds.), Treatise on Geomorphology. Elsevier Inc., San Diego, USA., pp. 259–298.

Vieira, D.C.S., Prats, S. a., Nunes, J.P., Shakesby, R. a., Coelho, C.O. a., Keizer, J.J., 2014. Modelling runoff and erosion, and their mitigation, in burned Portuguese forest using the revised Morgan–Morgan–Finney model. For. Ecol. Manage. 314, 150–165. https://doi.org/10.1016/j.foreco.2013.12.006

Vilar, L., Camia, A., San-Miguel-Ayanz, J., 2015. A comparison of remote sensing products and forest fire statistics for improving fire information in mediterranean Europe. Eur. J. Remote Sens. 48, 345–364. https://doi.org/10.5721/EuJRS20154820

Virdis, S.G.P., Oggiano, G., Disperati, L., 2012. A Geomatics Approach to Multitemporal Shoreline Analysis in Western Mediterranean: The Case of Platamona-Maritza Beach (Northwest Sardinia, Italy). J. Coast. Res. 282, 624–640. https://doi.org/10.2112/JCOASTRES-D-11-00078.1

Wang, Y., Colby, J.D., Mulcahy, K.A., 2002. An efficient method for mapping flood extent in a coastal floodplain using Landsat TM and DEM data. Int. J. Remote Sens. 23, 3681–3696. https://doi.org/10.1080/01431160110114484

Wipulanusat, W., Nakrod, S., Prabnarong, P., 2009. Multi-hazard Risk Assessment Using GIS and RS Applications : A Case Study of Pak Phanang Basin. Walailak J. Sci. Technol. 6, 109–125.

Wischmeier, W.H., Smith, D.D., 1978. Predicting rainfall erosion losses. Agric. Handb. no. 537 285–291. https://doi.org/10.1029/TR039i002p00285

WWF, 2020. HydroSHEDS [WWW Document]. URL http://www.hydrosheds.org/ (accessed 11.12.20).

Zhang, Y., Baptista, A.M., 2008. SELFE: A semi-implicit Eulerian-Lagrangian finite-element model for cross-scale ocean circulation. Ocean Model. 21, 71–96. https://doi.org/10.1016/j.ocemod.2007.11.005

Chapter 3:
MULTI-INDEX IMAGE DIFFERENCING METHOD (MINDED) FOR FLOOD EXTENT ESTIMATIONS

Abstract: Satellite remote sensing data are often used to extract water surfaces related to extreme events like floods. This study presents the Multi-INDEx Differencing (MINDED) method, an innovative procedure to estimate flood extents, aiming at improving the robustness of single water-related indices and threshold-based approaches. MINDED consists of a change detection approach integrating specific sensitivities of several indices. Moreover, the method also allows quantifying the uncertainty of the Overall flood map, based on both the agreement level of the stack of classifications and the weight of every index obtained from the literature. Assuming the lack of ground truths to be the most common condition in flood mapping, MINDED also integrates a procedure to reduce the subjectivity of thresholds extraction focused on the analysis of water-related indices frequency distribution. The results of the MINDED application to a case study using Landsat images are compared with an alternative change detection method using Sentinel-1A data, and demonstrate consistency with local fluvial flood records.

Keywords: remote sensing; optical satellites; Landsat; change detection; flood mapping; Portugal

1. Introduction

Floods are amongst the most important weather-driven hazards, being capable of inducing considerable damage, including economic losses, and threatening of human lives (EEA, 2010). The effects of floods are dependent on several factors, including flow velocity and depth. Even standing water can produce damage, depending on the persistence time and land cover affected (e.g., damages to crops). Floods may result from heavy or persistent rainfall, flooding by water bodies, water tables rising, snowmelt, or they may originate from artificial sources (Liu, 2016). Mapping flood extent is, thus, important for several scientific (e.g., better understating of

hydrological and, more generally, earth system science processes) and operational (e.g., emergency management; risk and damage assessment, insurance claims) applications.

Flood hazard modelling chains usually start with hydrologic modelling to obtain hydrographs for assigned return periods (e.g., the 100-year flow), which are consequently incorporated into hydraulic flow propagation models to estimate water surface elevations and corresponding inundation areas (Allen and Pavelsky, 2018; Nardi et al., 2019; Pekel et al., 2016). Therefore, knowing the extent of flood events is one of the main requirements of the whole modelling process. The use of remote sensing methods to extract water bodies from optical and microwave satellite data has been widely studied; the same principles generally apply for mapping flooded areas. Multispectral optical data may be used to identify distinctive spectral signatures of water features. Surface water is characterized by relatively higher reflectance values (ca. 0.1 or lower) in the visible region of the electromagnetic spectrum, with peaks occurring in the blue-green range, with respect to red and near-short (NIR-SWIR) wave infrared (Campbell and Wynne, 2011; Lillesand et al., 2015; McFeeters, 1996; Xie et al., 2016). However, such responses tend to vary in the visible and NIR regions, depending on the water column depth, turbidity, dissolved organic compounds and eutrophication (Gómez-Palacios et al., 2016; Richards, 2013). In the SWIR part of the spectrum, the absorption is very high (i.e., effectively black) independently of the water column characteristics. Moreover, this spectral interval shows better aerosol penetration capability, these conditions being particularly useful for implementing atmospheric correction methods for coastal and inland water-related studies (Shi and Wang, 2007; Stark et al., 2015; Vanhellemont and Ruddick, 2015). Nevertheless, a strong limitation of optical sensors is their dependence on both sunlight and cloud conditions, which may reduce the possibility to acquire data during a flood event. However, the increasing availability of free moderate spatial resolution optical data (e.g., Landsat series and Sentinel 2 constellations) augments the number of possible acquisitions related to a given event under favourable weather conditions. Indeed, there are several operational remote sensing flood detection tools and services based on optical satellites (e.g., Brakenridge et al., 2017; Dao and Liou, 2015; Kugler et al., 2007; Revilla-Romero et al., 2015).

Concerning microwave data, due to their almost all-weather, day and night imaging capabilities, active synthetic aperture radar (SAR) sensors (e.g., Cosmo SkyMed-CSK, Terra SAR-X, Sentinel 1 constellations) are the most employed tool for water extraction and mapping of flooded areas (e.g., Ding et al., 2015; Oberstadler and Ho, 1997; Smith, 1997; Wang et al., 2017; Yesou et al., 2007), as well as for operational purposes (e.g., Bates et al., 2006; Boni et al., 2016; Martinis et al., 2015; Pulvirenti et al., 2014, 2011). In SAR images, flooded areas can be easily

detected because their backscattering signal intensity is significantly lower compared to other surface features (e.g., non-flooded areas) imaged by the sensors. While smooth water surfaces reflect the incident radar signal with a specular scattering mechanism, non-flooded areas scatter the radar signal in multiple directions (Chini et al., 2017; Ulaby and Dobson, 1989). However, as discussed in Matgen et al. (2011), SAR applications suffer from several limitations. The delineation of flood areas can be complicated in transient shallow water areas, which produce gradual signal variation between flooded and non-flooded areas. Both wind and precipitation may cause the roughening of water surfaces, producing pulse returns, which make difficult to delineate flooded areas correctly. Furthermore, the accurate extraction of flooded areas in urban environments can be affected by double bounce reflection of buildings. Moreover, it has been shown that X-band instruments (e.g., CSK and Terra SAR-X) can fail in discriminating flooded areas from the microwave radar signature of rain because of the attenuation of the radar signal by heavy precipitation events (Pulvirenti et al., 2014). Surface absorption/attenuation due to snow or very dry sand surfaces can also produce low backscatter values (i.e., dark areas) that can be erroneously classified as flooded areas, thus generating false alarms (Pulvirenti et al., 2014; Schlaffer et al., 2015). Finally, also data processing of shadowing effects in areas characterized by complex topography may result in the occurrence of low backscatter values. In addition to all of this, SAR images are affected by speckle noise that complicates their interpretation, due to the coherent nature of the signal, if compared with optical images of the same target (Chini et al., 2017).

The main objective of this study is to improve the estimation of flood extent by means of a satellite remote sensing method, integrating several water-related indices in a change detection method. The method, hereinafter referred as Multi INDEx Differencing (MINDED), was developed to be applied to multispectral satellite data acquired from different optical sensors, characterized by the presence of VIS, NIR SWIR bands, including the freely available entire Landsat series, the Advanced Spaceborne Thermal Emission and Reflection Radiometer (ASTER) and Sentinel-2. In order to reach as many users as possible, the procedure has been implemented through open-source software. MINDED was applied to a study area in North-western Portugal, and the results were compared with flooding maps obtained by the Hierarchical Split-Based Approach (HSBA) (Boni et al., 2016), a flood detection algorithm provided by the GPOD HASARD Sentinel-1 service.

1.1. Flood Extent Estimation Methods Based on Remote Sensing Imagery

The definition of flood, e.g., "temporary covering by water of land not normally covered by water" (EU, 2007), conceptually implies the occurrence of a certain type of change over time. Digital change detection techniques based on remote sensing imagery are capable of providing both long-term and short-term solutions (Coppin et al., 2004; Disperati and Virdis, 2015). Long-term change detection approaches consist of temporal trajectory analysis (also referred as trends), using long series of observation data, which can be used to detect subtle anomalies in annual variability of climatic variables, such as those resulting from climate change (Cenci et al., 2017b). However, that is not the case of floods, which can happen within a few days or hours. Bi-temporal change detection analysis includes several methods capable of dealing with such short-term phenomena (Coppin et al., 2004; Ji et al., 2009; Li et al., 2016; Lu et al., 2004b) (as summarized in Table 3.1).

Table 3.1 - Advantages and disadvantages of bi-temporal change detection methods.

Method	Advantages	Disadvantages
Post classification comparisons	Wide application (Coppin et al., 2004). Implemented by processing either single or multiple bands (including spectral relationships) (Coppin et al., 2004).	Not ideal for analysing the process of flooding and post-flooding events, due to the spatially continuous variation of soil wetness (Ji et al., 2009).
Multi-temporal spectral unmixing	Makes it possible to determine the water proportion changes in every pixel (flood detection) (Coppin et al., 2004).	More complex and less straightforward for mapping purposes (compared to other hard classification techniques). Difficulty in defining classes of change. Requires a priori information about the study area and end-members (Li et al., 2016).
Data transformation	Transformations are capable of sorting modifications of state according to different orders (including those resulting from water-related conditions) (Lu et al., 2004b).	Finding the meaning for each order of change is often a complex task and requires a deep knowledge of the study area (scene-dependent) (Lu et al., 2004b).
Change vector	Multivariate technique, capable of simultaneously incorporating multiple layers. Great potential to recognize and analyse the amount and type of changes (Coppin et al., 2004).	Selection of different thresholds is in practice very complex (Coppin et al., 2004).
Image ratioing	Pixel-by-pixel based analysis of either two-date images or image transformations (Coppin et al., 2004; Singh, 1989).	The non-normal distribution of results has been criticized for being statistically invalid, preventing the computation of thresholds based on standard deviation functions (Coppin et al., 2004; Singh, 1989)
Univariate image differencing	Wide application (Coppin et al., 2004). Despite its simplicity, it can achieve better performances compared to other methods (Singh, 1989).	Unable to directly specify the type of change (Singh, 1989).

Univariate image differencing is the most widely applied bi-temporal approach. It consists of subtracting spectral or transformed data (e.g., using water-related indices), producing positive and negative values, depending on the type of change (Coppin et al., 2004). In theoretical and ideal conditions, no-change areas should result in zero values; however, in real conditions, this is not the case as an effect of spatial and spectral co-registration errors, as well as natural time-

dependent changes. One or more thresholds may be required to define two or more classes of change (density-slicing), which may provide hints about amounts and types of change (Singh, 1989).

Both optical and SAR data can be used to detect floods using bi-temporal change detection methods, which consist of comparing images acquired before and after a certain event. In principle, the images pre-dating the event should be the most recent from the available dataset, while the post-event the oldest. Regarding the pre-event images, a wide period between acquisition and the event will also imply natural changes resulting from phenological cycles as well as seasonal water body variations (Gómez-Palacios et al., 2016). As for the post-event images, the corresponding time span should be as short as possible in order to record the most accurate picture of the flooded area. However, it can be difficult to obtain optical satellite imagery approximately coeval to flood occurrence, since hydro-meteorological events are typically associated with clouds and long periods of adverse weather conditions. Concerning SAR data instead, when applying change detection methods, particular attention must be paid for taking into account all the differences between the image changes occurred to the image's targets (e.g., a comparison between images acquired by the same sensor but with different orbit/geometry of acquisitions).

1.1.1. Optical Water-Related Indices

Many optical Water-related Indices (WrI) have been defined and applied in the literature to detect surface water from remote sensing imagery. This section introduces those most commonly found in flood-related literature.

The Normalized Difference Vegetation Index (NDVI) (Rouse et al., 1973), is obtained with spectral bands corresponding to Red and NIR regions. Without being specific for water detection purposes, it has a theoretical threshold of zero, being the negative values generally associated with water occurrence.

The Normalized Difference Water Index (NDWI) (McFeeters, 1996) is one of the first specific indices to detect water, considering Green and NIR bands in a similar structure to the NDVI. The NDWI includes the same theoretical threshold of zero, but with positive values being interpreted as water. The Modified Normalized Difference Water Index (MNDWI) was proposed by Xu (2006), as an alternative to the NDWI, using SWIR (e.g., band 5 of Landsat TM) instead of the NIR

band. The MNDWI has become one of the most popular water detection indices (Zhai et al., 2015).

The Automated Water Extraction Index (AWEI) (Feyisa et al., 2014) was conceived for sensors covering the visible to SWIR electromagnetic spectrum range and consists of multiple subtractions and additions of bands through several empirically based coefficients, developed to maximize the separability between water and non-water pixels. It was developed to improve classification accuracy in areas including shadow and dark surfaces, where most other indices tend to fail. It includes two versions: the 'AWEI no shadow' (AWEI_NS) for situations where shadows are not major problems and the 'AWEI shadow' (AWEI_S) intended to effectively eliminate shadows or other dark surfaces (Zhai et al., 2015). Both versions were developed for a theoretical imposed threshold of zero, with water pixels corresponding to positive values. Nevertheless, as with other indices, in practice, the optimal threshold is usually scene-dependent.

The Tasseled Cap method was first developed by (Kauth and Thomas, 1976) for Landsat MSS sensor and then applied to Landsat TM (Crist and Cicone, 1984). It consists of a multispectral sensor-based transformation, which makes it possible to obtain new outputs such as Brightness, Greenness, and Wetness. Tasseled Cap Wetness (TCW) (Crist, 1985) can be used to identify water, using a theoretical value of zero to separate water (positive values) from non-water pixels (Fisher et al., 2016). TCW is usually obtained with sensor-specific coefficients applied to either Top of Atmosphere (TOA) (e.g., Baig et al., 2014; Huang et al., 2002) or ground reflectance (Devries et al., 2016).

Table 3.2 summarizes the main advantages and disadvantages of each of the previous WrI as resulting from the literature. Despite the overall advantages, there are additional challenges for flood detection purposes. Suitability and accuracies of each index are affected by local conditions, which, depending on the study area heterogeneity, may vary within short distances (e.g., land cover type, topography, atmospheric conditions).

Table 3.2 - Advantages and disadvantages of optical Water-related Indices (WrI).

WrI Name	Advantages	Disadvantages	Equation
NDVI (Rouse et al., 1973)	Improved detection capacity with mixed water and vegetation (Fang-fang et al., 2011)	Less suited for water detection (Ji et al., 2009; McFeeters, 1996)	NDVI = (NIR − RED) / (NIR + RED)
NDWI (McFeeters, 1996)	Good performance in mountain shadow areas (Gao et al., 2016) Good overall accuracy (Rokni et al., 2014; Zhou et al., 2017) Good performance in large urban areas with cloud-free conditions (Fisher et al., 2016)	Weaker abilities to extract water bodies (Gao et al., 2016) Sensitive to built-up land signals, which often results in an overestimation of water bodies (Zhou et al., 2017)	MNDWI = (GREEN – SWIR1) / (GREEN + SWIR1)
MNDWI (Xu, 2006)	The capacity of removing interferences of built-up feature signals (Rokni et al., 2014; Zhou et al., 2017) Better suited for open water mapping (Zhou et al., 2017)	High variability of optimal thresholds (Zhou et al., 2017) Unable to remove certain shadow noises effectively (Zhou et al., 2017)	NDWI = (GREEN − NIR) / (GREEN + NIR)
AWEI (Feyisa et al., 2014)	Good performance in large urban areas (Fisher et al., 2016)	Difficulty in finding optimal thresholds (Li et al., 2016) Unable of totally removing mountain shadows (Li et al., 2016) May misclassify high albedo surfaces (Feyisa et al., 2014; Zhai et al., 2015; Zhou et al., 2017)	AWEI_NS = 4 × (GREEN − SWIR1) − (0.25 × NIR + 2.75 × SWIR1)
TCW (Crist, 1985)	Good ability to extract water bodies (Gao et al., 2016)	Fails to suppress mountain shadow (Gao et al., 2016)	TCW = aB1 + bB2 + …. + iBj *

** Sensor dependent (examples given in Table 3.3).*

Table 3.3 - Examples of Tasseled Cap Wetness (TCW) coefficients for different optical satellite sensors.

Sensor	Data	TCW Coefficients	Reference
Landsat 4 TM; Landsat 5 TM	Reflectance Factor	0.0315 B1 + 0.2021 B2 + 0.3102 B3 + 0.1594 B4 + 0.6806 B5 − 0.6109 B7	(Crist, 1985)
Landsat 7 ETM+	At-satellite reflectance	0.2626 B1 + 0.2141 B2 + 0.0926 B3 + 0.0656B4 − 0.7629 B5 − 0.5388 B7	(Huang et al., 2002)
ASTER	At-satellite reflectance	0.166 B1 − 0.087 B2 − 0.703 B3 + 0.187B4 + 0.040 B5 + 0.500 B6 − 0.287 B7 + 0.030 B8 − 0.318 B9	(Yarbrough et al., 2005)
SPOT-5	At-satellite reflectance	0.397 B1 + 0.260 B2 + 0.118 B3 − 0.872 B4	(Ivits et al., 2008)
Landsat 8 OLI	At-satellite reflectance	0.1511 B2 + 0.1973 B3 + 0.3283 B4 + 0.3407 B5 − 0.7117 B6 − 0.4559 B7	(Baig et al., 2014)
Sentinel-2	At-satellite reflectance	0.0649 B1 + 0.1363 B2 + 0.2802 B3 + 0.3072 B4 + 0.5288 B5 + 0.1379 B6 − 0.0001 B7 − 0.0807 B8 − 0.0302 B9 + 0.0003 B10 − 0.4064 B11 − 0.5602 B12 − 0.1389 B8A	(Nedkov, 2017)

Regardless of the method chosen, mixed pixels are a common problem affecting remote sensing applications, particularly those resulting from moderate spatial resolution (e.g., 30 m)

satellite images (Feng et al., 2015). As referred by Fisher et al. (2016), another limitation of water classification methods concerning the handling of the variability of reflectance spectra which changes according to water properties (e.g., concentrations of phytoplankton and sediments, depth, or substratum type). Another difficulty relates to the discrimination between shadows cast and clouds, and the steep topography, quarries and tall buildings, which may produce signals similar to those of water. In the case of flood analysis, the presence of clouds and cloud shadows are very common, and one of the first steps should be masking such features (e.g., Memon et al., 2015; Xiao et al., 2014).

For reproducibility reasons, when analysing different epochs and locations, the simplest approach would be to use single global thresholds for each WrI. Finding an optimal scene-dependent threshold may provide better accuracy, even though this can be a difficult task due to high temporal and spatial variability (Ji et al., 2009).

1.1.2.Flood-Related Synthetic Aperture Radar Applications

According to Chini et al. (2017), the use of a simple global threshold is the most frequent approach in flood delineation from SAR imagery. Although this approach can be easily implemented, and thus, is particularly suitable for operational applications related to flood risk emergency management, the criteria used for defining the threshold value affect drastically flood mapping results (Chini et al., 2017). Such approaches for image thresholding can be based on the visual inspection of the grey-scale frequency histogram (Bartsch et al., 2008; Brivio et al., 2002; Smith et al., 1996, 1995), or automatic algorithms (e.g., Hess et al., 1994; Otsu, 1979). Given the recently increased availability of SAR images, in the last years, several thresholding methods for flood detection have been developed (Boni et al., 2016; Chini et al., 2017; Giustarini et al., 2013; Martinis et al., 2015b, 2009). These methods exploit the characteristics of SAR systems to produce image histograms which are characterized by a bimodal distribution (representative of the classes flooded/non-flooded) that can be used to define an optimal threshold for detecting inundated areas (Boni et al., 2016; Chini et al., 2017; Giustarini et al., 2013; Martinis et al., 2015a; Pulvirenti et al., 2014). Such rational can be applied both to a multitemporal dataset (change detection methods), or to a single-event image. In the first case, the flood mapping algorithm can be represented as a binary classification problem in which the “change” class (i.e., the flooded area) must be resolved from the “no change” class (which represents the “background” dominant class of the image) (Chini et al., 2017). In the second case, instead, the water/flooded pixels correspond to the darker areas of the image that must

be discriminated from the other (surrounding) land cover classes which are characterized by higher backscattering values (Cenci et al., 2017a).

2. Proposed Method

2.1. MINDED: the Multi-INDEx Differencing approach

The Multi-INDEx Differencing (MINDED) method for flood areas detection, illustrated in Figure 3.1, combines several WrI in a change detection approach, as an alternative to the single WrI analysis commonly found in the literature. This method has the objective of integrating the strengths of each index and considers the agreement level among outputs obtained by different indices as an indicator of overall uncertainty. The structure of MINDED is demonstrated using six of the most common WrI found in the literature. Nevertheless, the same theoretical principles of the method should apply if other indices are to be considered.

In order to define the study area and the imagery dataset to process, as a preliminary step, we assume that a certain area could have experienced a flooding event within a certain period. If historical flood records are not available, other indirect data sources may be considered (e.g., precipitation measurements, river water levels, local news).

For flooded areas, WrI variation occurs between the epochs *t1* and *t2* (respectively prior and after the given flood event). For a change detection method based on image differencing, no-change areas (Nc) are theoretically represented by the digital value zero. Assuming the time span ($t2 - t1$) is reasonably short, in principle, Nc should be the majority of the pixel image distribution, corresponding to the modal value of the frequency distribution. In contrast, digital values different to zero represent change areas, and they tend to be located toward both tails of the frequency distribution. When WrI differencing (ΔWrI) is used, we expect to locate flooded areas changes in only one of the tails, either positive (e.g., ΔNDWI, ΔMNDWI, ΔTCW, ΔAWEI), or negative (e.g., ΔNDVI) (Figure 3.2). The higher the distance from the modal ΔWrI value, the higher the magnitude of change, until a complete change of state from dry to flooded surface. If only such kind of flood changes occur, this results in an ideal bi-modal distribution of the function (*f*) where the discrimination between Nc and flooded areas is unambiguous (thresholding interval-Figure 3.2a). In practice, different flooding conditions (water thickness and suspended materials, water surface roughness), as well as different initial conditions (land cover, substrate properties, surface roughness and wetness, and their spatial distribution in respect to pixel size), imply a continuous distribution of ΔWrI values beyond Nc (Figure 3.2b).

Moreover, when analysing the frequency distribution, one should also take into account the effect of the spatial-spectral misregistration between *t1* and *t2* imagery, changes resulting from phenomena other than flooding, and finally the effective sensitivity of WrI to detect surface water. The main consequence of these conditions is that the real distribution of Nc is represented by a bell-shaped range of ΔWrI values located around zero (Figure 3.2c, Figure 3.2d).

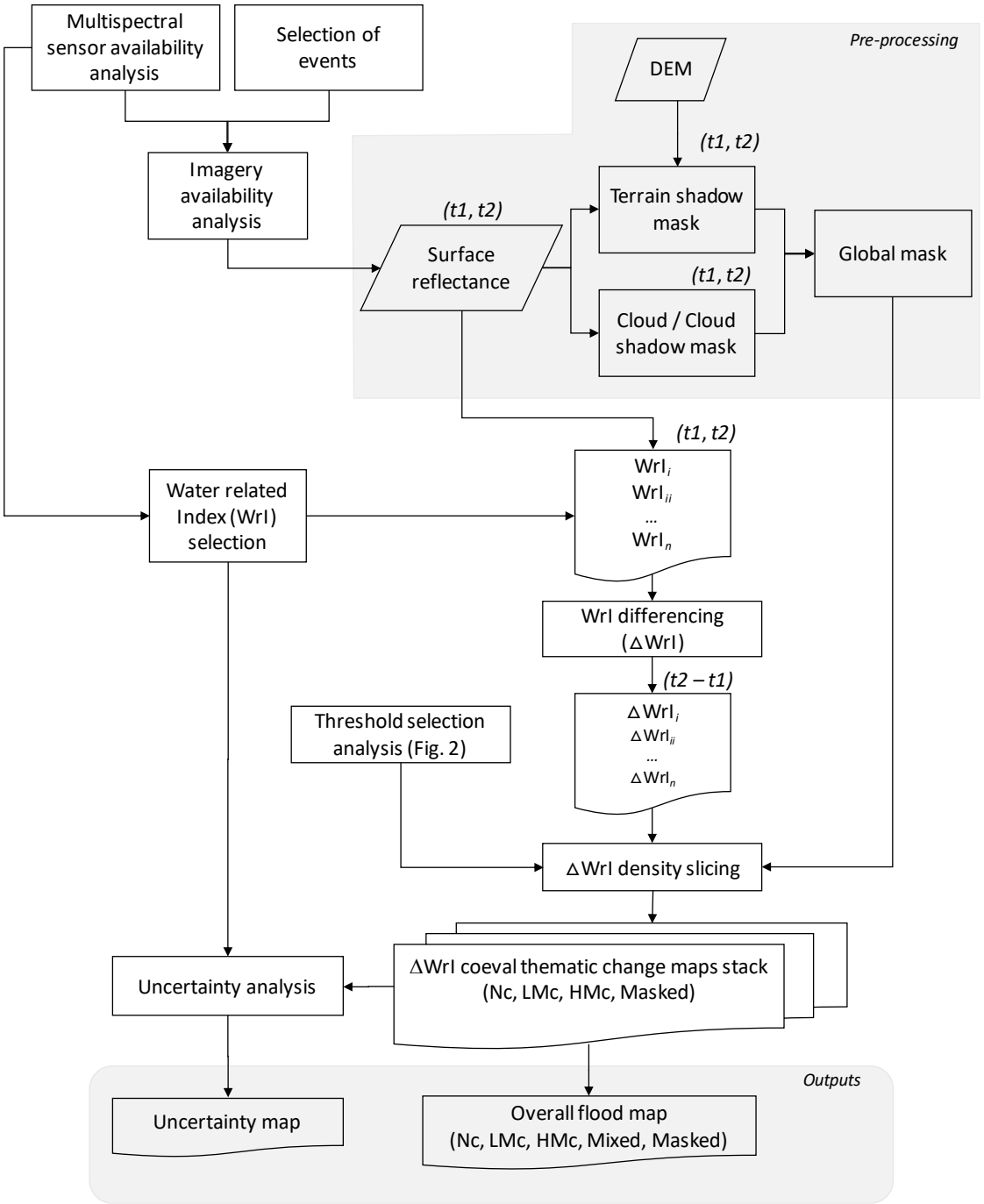

Figure 3.1 - The Multi-INDEx Differencing (MINDED) method workflow.

Given the above considerations and the fact that image differencing prevents discriminating among the types of change, but only change signal and intensity, we assume to classify flooded areas into the categories Low-Magnitude change (LMc) and High-Magnitude change (HMc) as a function of the ΔWrI value (Figure 3.2b–d). This assumption requires the definition of two thresholds, between Nc-LMc (TL) and LMc-HMc (TH), which are then used to apply density slicing (Campbell and Wynne, 2011; Singh, 1989) to the multitemporal imagery. These thresholds should be ideally defined with analysis of ground truth data. If such information is not available, thresholds may be obtained by only analysing the frequency distribution of data. The latter approach is a key point of MINDED, allowing us to perform semi-automatic remote sensing procedures to extract flooded area extent from satellite imagery. We assume that these thresholds correspond to a sudden variation of ΔWrI frequency, which is a consequence of the effects that the appearance of water-related conditions may induce on sets of pixels. The variation may be more (Figure 3.2c) or less (Figure 3.2d) pronounced depending on the occurrence of change-related secondary modal values. In the first case, the first order derivative of the function (*df*) is a useful tool to define the thresholds, which are assumed to be located where the change of signs of *df* occurs. In other cases (Figure 3.2d), *df* continuously approaches zero without reaching it. Therefore, we chose as a threshold the ΔWrI value where the second order derivative function (*d2f*) reaches a local maximum, corresponding to a sudden variation of both *f* and *df*. In this approach, we assumed that this option would ensure the reproducibility of the method while reducing its subjectivity. In practice, for a given scene differencing, the distribution of ΔWrI may follow both the conditions of Figure 3.2c,d around either TL or TH.

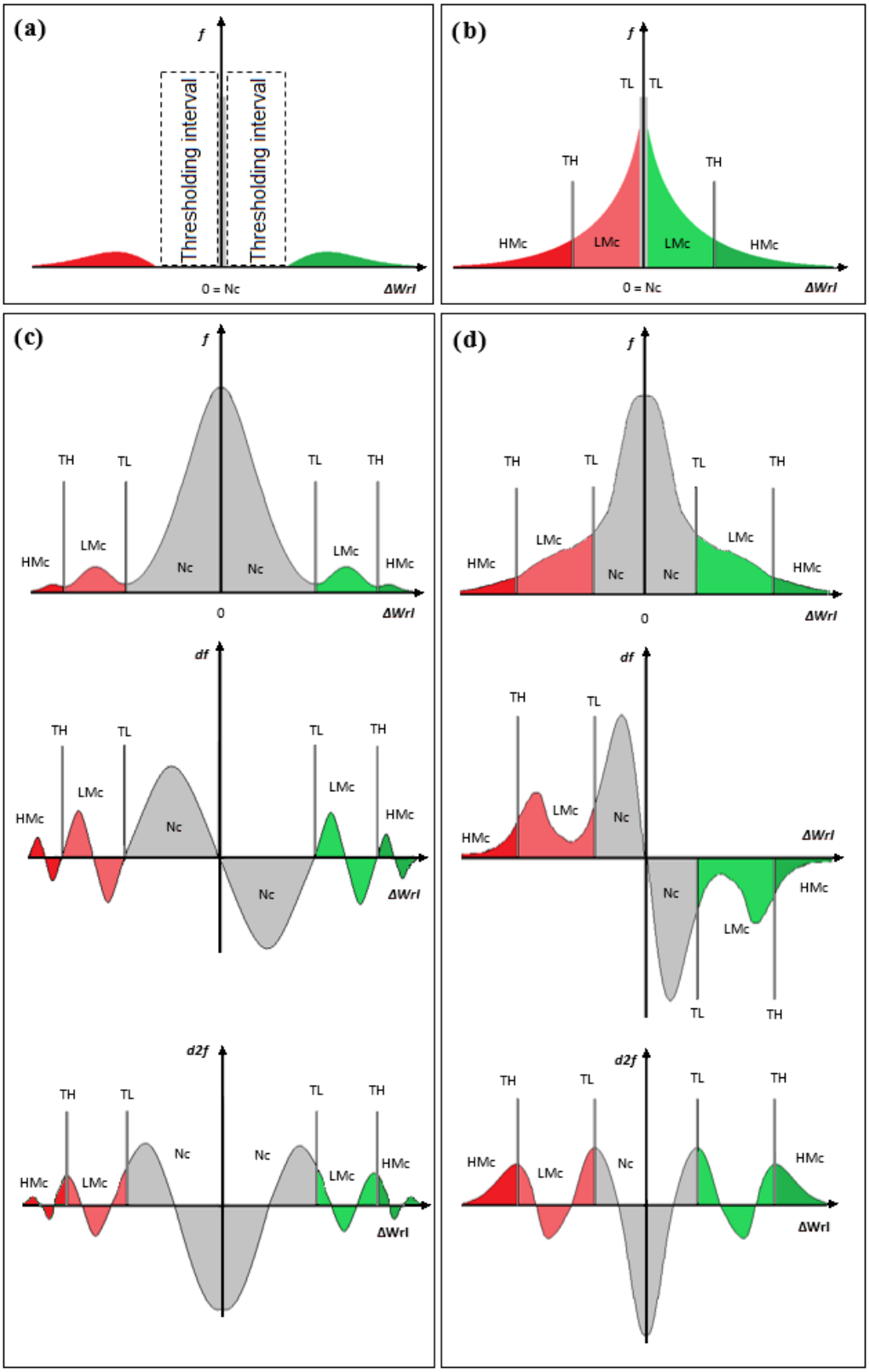

*Figure 3.2 - Density slicing classification (Nc—No change; LMc—Low-Magnitude change; HMc—High-Magnitude change) and threshold selections (TL—threshold between Nc-LMc; TH—threshold between LMc-HMc) for different types of frequency (f) distribution histograms of ΔWrI: (**a**) Ideal perfect distribution: no misregistration effects, perfect separation between Nc and change areas; (**b**) Ideal distribution: no misregistration effects, gradual transition from Nc to change; (**c**) Real distribution 1: misregistration effects, gradual well separated transition from Nc to change, and corresponding first (df) and second order (d2f) derivatives; (**d**) Real distribution 2: misregistration effects, gradual change from Nc to change, and corresponding first and second order derivatives.*

Without ground truth information, the interpretation of HMc may be nonetheless considered obvious, because it should represent a complete change of state from dry land to water surface. However, the same does not apply to LMc, which may be expected to represent pixels changing from dry to wet/saturated surfaces, as well as wet/saturated to water surfaces. Moreover, depending on the duration of the time span (*t2* − *t1*), LMc may also correspond to those flooded areas that underwent drying/drainage processes after the flooding event. This is particularly interesting for those situations whenever it is impossible to obtain cloud-free satellite images immediately after a flood event. Finally, Nc areas are expected to include permanent water bodies, continuously wet/saturated surfaces, as well as any other kind of permanently dry surfaces.

WrI are determined for *t1* and *t2* using the corresponding spectral bands (Table 3.2). As for TCW the equation and parameters of transformation are sensor-dependent (examples are given inTable 3.3).

After calculating ΔWrI, we perform density slicing based on TL and TH, to obtain a stack of six coeval thematic change maps. These maps represent changes caused by flooding according to each WrI specific sensitivity. The stack is then analysed to extract two outputs, the Overall flood map and the Uncertainty map.

The Overall flood map integrates the information from each WrI and is obtained by picking the absolute majority among the frequency of the change classes Nc, LMc, HMc (at least four consistent classifications over six). If an absolute majority does not occur, pixels are classified as 'Mixed'.

The Uncertainty map is obtained by Equation (1) which integrates pixel statistics of change classes within the stack, together with WrI specific average a priori accuracies (Acc_{WrI}) obtained from literature values (Table 3.4),

$$\rho_i = \sum Acc_{WrI} - max\begin{cases} \sum_{WrI=\mathrm{Nc}} Acc_{WrI} \\ \sum_{WrI=\mathrm{LMc}} Acc_{WrI} \\ \sum_{WrI=\mathrm{HMc}} Acc_{WrI} \end{cases}, \quad (1)$$

where *i* is a given pixel and ρ_i its uncertainty of change classification. This implies that the parameter Acc_{WrI} is a weighting factor for change classification statistics (count), while $\sum Acc_{WrI}$ is the limiting value for the definition of the uncertainty scale range. The expected range of ρ_i is 0 - ≈ 3.8, where ρ_i = 0 represents the lowest uncertainty corresponding to six each other coherent

change classes. This approach also handles pixel statistical ties, by choosing the combination of indices that provides the highest cumulative Acc_{WrI}.

Table 3.4 - Average a priori WrI accuracies for water detection, obtained from the literature, in percentage (Sources: Fisher et al., 2016; Rokni et al., 2014; Zhai et al., 2015; Zhou et al., 2017).

Index	Literature Accuracies				Average A Priori Accuracy (Acc_{WrI})
	(Zhai et al., 2015)	(Fisher et al., 2016)	(Zhou et al., 2017)	(Rokni et al., 2014)	
NDWI	0.938	0.946	0.950	0.995	0.957
MNDWI	0.968	0.967	0.934	0.920	0.947
NDVI	0.933	-	-	0.990	0.961
TCW	-	0.966	0.918	-	0.942
AWEI_NS	0.967	0.975	0.941	0.953	0.959
AWEI_S	0.967	0.984	0.943	0.953	0.962
				$\sum Acc_{WrI}$	5.728

2.2. Pre-Processing Considerations

As with any change-detection methods, geometrically corrected surface reflectance data should be used as inputs to implement the MINDED method correctly. When these products are not available, additional pre-processing steps are required, i.e., geometric co-registration and radiometric calibrations (Campbell and Wynne, 2011; Schowengerdt, 2007).

In principle, the implementation of MINDED should be applied to cloud-free areas, while minimizing the time span ($t2 - t1$), in order to reduce the influence of other changes than those caused by flooding (e.g., phenological cycles, land cover modifications) (Coppin et al., 2004). This is made by choosing the newest image pre-dating and the oldest post-dating the flood event. In practice, a trade-off between time span duration and cloud coverage has to be applied.

Regardless, considering the characteristics of optical satellite imagery and the sensitivity of water detection indices, before implementing MINDED, pre-processing is necessary to extract a global mask including clouds, cloud shadows, and topographic shadows. Both cloud and topographic shadows are dark areas with very low reflectance values in the same bands, where the water spectral signature is also characterized by low values (Hughes and Hayes, 2014; Schowengerdt, 2007; Zhu and Woodcock, 2012). For this reason, most WrI are susceptible to collect such features as water, and it is necessary to mask such pixels.

Regarding clouds and cloud shadows, several options can be applied. Whenever available, sensors providing products containing cloud cover and shadow cover data can be used directly to perform masking (e.g., Landsat 4-7 and 8 Level-2, or Sentinel-2 Level-1C). Otherwise, sensor specific procedures may be used, particularly single-epoch-based methods (e.g., Braaten et al., 2015; Fisher, 2014; Hughes and Hayes, 2014; Hulley and Hook, 2008; Irish et al., 2006;

Scaramuzza et al., 2012; Zhu and Woodcock, 2012), which may be applied to pre-process both *t1* and *t2* images before implementing MINDED.

Topographic shadows can be deduced from sun elevation and azimuth parameters that are usually included in satellite products metadata. In order to perform topographic shadows masking, these parameters are integrated with a Digital Elevation Model (DEM), e.g., the Shuttle Radar Topography Mission (SRTM) Version 3.0 1-arc-sec DEM (NASA, 2015), the Advanced Spaceborne Thermal Emission and Reflection Radiometer (ASTER) GDEM (NASA, 2004), the ALOS World 3D (AW3D30) Global DEM (JAXA, 2015), or the Multi-Error-Removed Improved-Terrain DEM (MERIT) (Yamazaki et al., 2017).

3. Study Area: The Aveiro Region (Portugal)

The Aveiro Region was chosen due to its context of recurrent floods and non-complex topography, presenting a favourable context for remote sensing-based flood detection. It is located on the north-western part of continental Portugal (Figure 3.3), being part of the Mediterranean Biogeographical region, nearby the border with the Atlantic zone. It is characterized by a temperate Mediterranean climate under maritime influence (EEA, 2010).

The study area includes the 11 municipalities of the Baixo Vouga Sub region (NUTS III), corresponding to the lower section of the Vouga River Watershed. This river is the main fluvial course draining into the Aveiro Lagoon, a shallow coastal lagoon, with a length of 45 km (N-S direction) and a maximum width of 10 km (W-E direction) (Azevedo et al., 2017). The lagoon and adjacent areas are recognized as a complex system, integrating urban areas and a wide range of natural and semi-natural habitats, classified as a Special Protection Area (Natura 2000 Network) and Site of Community Importance (Sousa et al., 2016).

Moreover, the study area includes another shallow natural lagoon, the Pateira de Fermentelos. It is classified as a Ramsar Site and is a part of the lowland area of the Cértima River, immediately located on the confluence with the Águeda River (an affluent of the Volga River). Due to its relatively compact and elongated catchment area, the Águeda River induces inflow to the Pateira de Fermentelos, producing floods during heavy rain events (Sena and C. Melo, 2012). At about 2.5 km to the east, is located Águeda, one of the largest cities of the study area, which, despite successive efforts of authorities, it is known for being regularly affected by urban floods.

Within the study area, the following municipalities are recurrently affected by floods due to intense precipitations: Aveiro, Estarreja, Oliveira do Bairro, Sever do Vouga, Vagos, and Mira. Besides, considering the coastal influence of this territory, there are also reports of recurring floods due to spring tides in Estarreja, Ílhavo, and Murtosa (Alves et al., 2010; CMI, 2016).

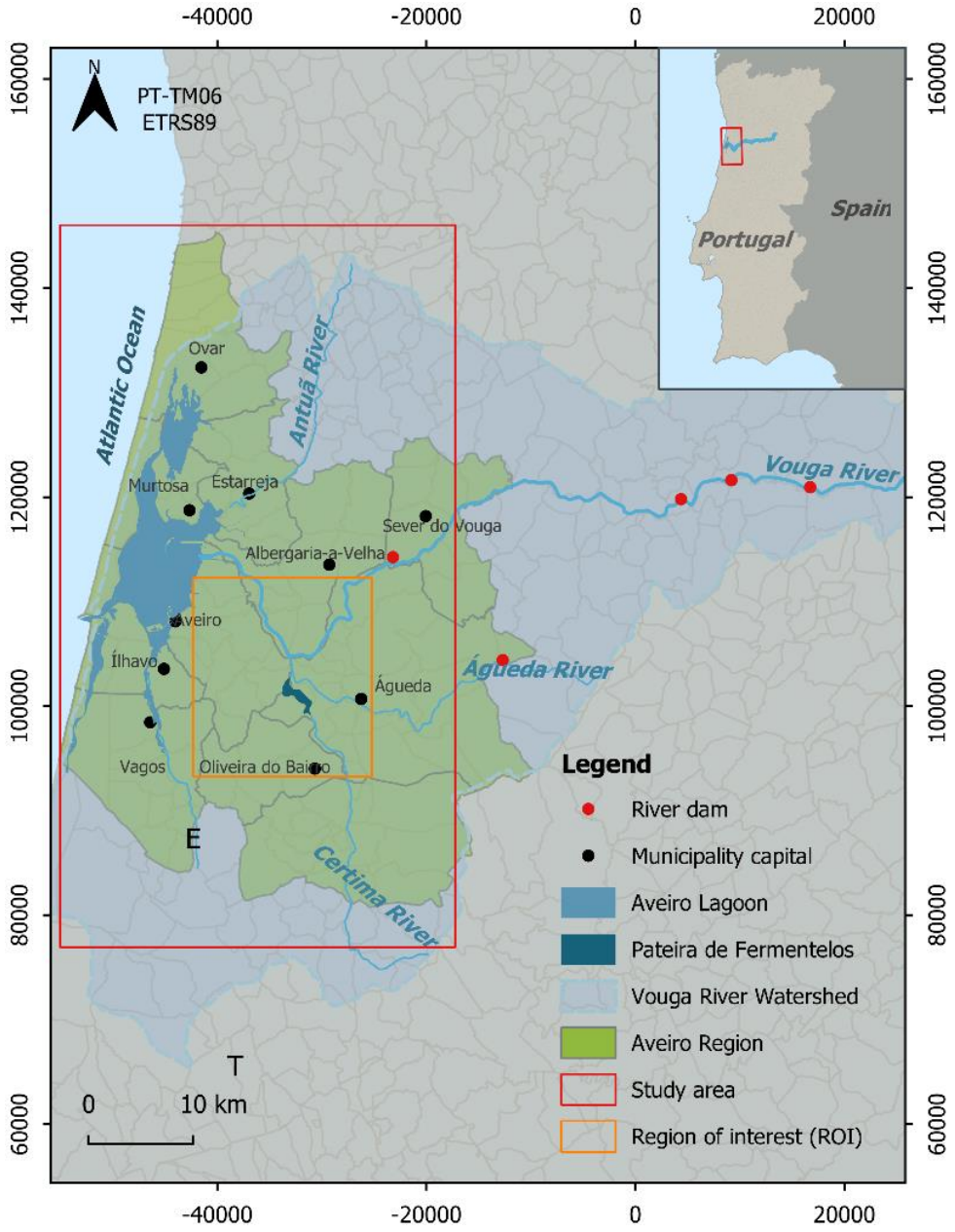

Figure 3.3 - Study area location (Source: CAOP, Atlas do Ambiente, DQA, OpenMaps). Meteorological stations Estrada (E) and Tentugal (T) used for wind speed monitoring (Coordinate system: PT-TM06/ETRS89).

4. Results

Herein, we illustrate the MINDED method for flood extent estimation through an application to the Aveiro Region study area. In order to preserve the use of free software only, all image-

processing tasks were performed with GRASS GIS (v7.2.2), while map compositions were made with QGIS (v2.18.15).

4.1. Selection of Events

Considering the lack of a long-term systematic record of floods in the Aveiro region, the selection of events was based on an indirect method. Daily precipitation data were extracted from a monitoring database portal (APA, 2018), corresponding to 23 meteorological stations located inside the Vouga river catchment area (between 30 December 1979 and 12 September 2017). Maximum daily precipitation records were ranked from largest to smallest, for every meteorological station. Return periods were calculated from Equation (2), derived from a Weibull distribution (Equation (3), where, *Tx* is the period expressed in number of years, P_x is the probability of exceedance, *n* is the number of observations and *r* is the rank number (RAES, 2013).

$$T_x = \frac{1}{P_x}, \tag{2}$$

$$P_x = \frac{r}{(n+1)} 100\,, \tag{3}$$

Table B1 resumes the 50 largest daily precipitation events, providing maximum daily precipitations and maximum return periods (calculated independently for each of the 23 meteorological stations). The highest record corresponds to a return period of 32.7 years and maximum daily precipitation of 180.0 mm. We used this list in order to search for usable couples (*t1* and *t2*) of imagery to be processed (see Section 4.2).

4.2. Satellite Data Selection

In order to maintain the simplicity of this methodological application, the selection of satellite data was restricted to freely available orthorectified products of multispectral surface reflectance. Landsat Level-2 products (from Landsat 4 to 8) are accessible 'On-demand' (i.e., usually requiring few hours between the order and delivery of the products) in the NASA's EarthExplorer portal (https://earthexplorer.usgs.gov/). Landsat 5 TM, 7 ETM+, and 8 OLI have the same spatial resolution (30 m in the visible, NIR and SWIR bands) and temporal resolution (16 days, which decrease if more satellites are accounted for a multitemporal analysis). Sentinel 2 Level-2A products, instead, can be downloaded from the Copernicus Open Access Hub website (https://scihub.copernicus.eu/). Sentinel 2 are acquired by the same sensor carried by a

constellation of two satellites (Sentinel 2A and 2B). Sentinel 2 data have a spatial resolution that varies from 10 m to 60 m in the visible, NIR, SWIR range (10 m to 20 m for the exploited bands) and a constellation temporal resolution of 5 days at equator (Drusch et al., 2012).

From the list of the 50 largest precipitation events (Table B1), we searched images matching the methodological requirements of this study, i.e., cloud-free conditions and a reasonably short time span between *t1* and *t2* (we assumed approximately 1 month prior and 15 days after each event). This process resulted in four suitable events to be analysed (Table 3.5). Amongst these, only two events match reports of flood occurrences. This is likely the consequence of flooding not being dependent from daily precipitation only, since other factors, such as precipitation intensity, dam breach/discharges, etc. may be relevant. Besides, flood records may be incomplete, since they are more focused on recent years. In addition, we observe data discontinuities from several meteorological stations, indicating that some of them did not acquire date continuously. Finally, as with most Portuguese rivers, those within the study area are densely dammed, contributing to regulate water levels during intense precipitation periods (especially during drier months).

Table 3.5 - Selected precipitation events, available satellite images (LS—Landsat; S—Sentinel) and flood event records. For a complete list, consult Table A1 (Supplementary Materials).

Date	Maximum Daily Precipitation (mm)	Maximum Return Period (Years)	Available Satellite Images		Flood Event Records
			t1	t2	
19 January 2003	80.6	26.5	LS7 (07 December 2002)	LS7 (24 January 2003)	Estarreja, Oliveira do Bairro, Vagos, Murtosa
13 February 2016	128.9	16.4	S1 (6 February 2016); LS8 (5 February 2016)	LS7 (29 February 2016)	Águeda
12 March 2004	78.5	11.8	LS7 (12 February 2004)	LS7 (15 March 2004)	-
7 October2009	119.0	6.8	LS7 (21 September 2009)	LS5 (15 October 2009)	-

The major selectable precipitation event matching flood records occurred in 2003 (19 January 2003), with a return period of 26.5 years (the third largest of all records). The available satellite images include two Landsat 7 TM scenes, with *t2* being acquired 5 days after the event (RGB composites are compared in Figure 3.4). Records mention the floods of January 2003, which affected the municipalities of Estarreja, Mira, Murtosa, Oliveira do Bairro and Vagos (affecting infrastructures and agriculture fields in Sosa, nearby the Boco River) (Alves et al., 2010; CMI, 2016). The second largest, occurred in 2016 (13 February 2016), ranking 12th, with a return period of 19.2 years. This event affected mostly the municipality of Águeda, causing multiple material damages and one mortal victim. The remaining selected events occurred in 2004 (12

March 2004) and 2009 (7 October 2009), with considerably smaller return periods and without any reports of flooding within the study area.

Those selected events were analysed with MINDED, using available Landsat 5, 7 and 8 data. Landsat 7 images acquired after 31 May 2003 have data gaps caused by a failure in the Scan Line Corrector (SLC). Nevertheless, we decided to include such images in our analysis by excluding the corresponding faulty pixels in both epochs (*t1* and *t2*). The list of all available images is reported in Table B1.

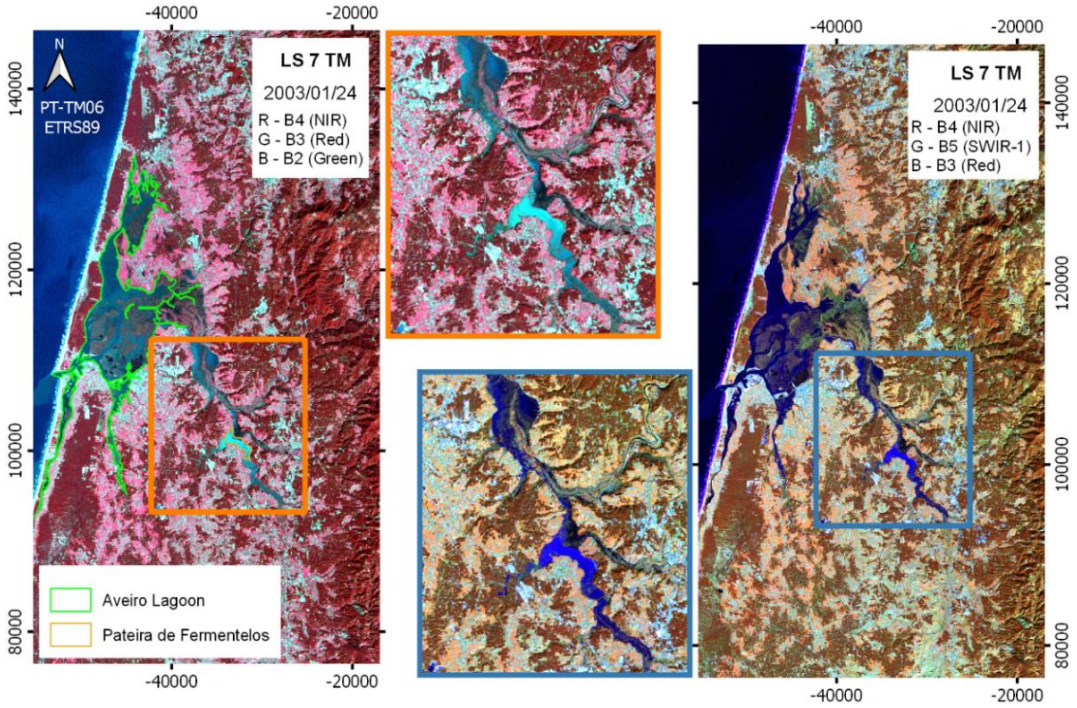

Figure 3.4 - False-colour RGB composites of Landsat 7 (LS7) TM bands, acquired 5 days after the 19/01/2003 flood event (26.5 return period). (Coordinate system: PT-TM06/ETRS89).

4.3. Pre-Processing

In order to perform masking of topographic shadows using only free available data, we decided to use the ALOS World 3D–30 m (AW3D30) Global DEM provided by the Japan Aerospace Exploitation Agency (JAXA at http://www.eorc.jaxa.jp/ALOS/en/aw3d30/data/index.htm), due to its horizontal resolution and improved vertical accuracy (Purinton and Bookhagen, 2017; Santillan and Makinano-Santinano-Santillan, 2016). Shaded relief maps, where produced for *t1* and *t2* (using the *r.relief* command of GRASSGIS).

Regarding clouds and cloud shadows, we decided to use the quality assessment bands of Landsat Level-2 products, which provides probabilities of occurrence of such features. Using the information of 'pixel_qa' band, we selected those matching the following attributes in order to extract cloud-related masks: 'Cloud Shadows', 'Snow/Ice', 'Cloud', 'Low cloud confidence', 'Medium cloud confidence' and 'High cloud confidence' (USGS, 2018). Note that we assumed a conservative approach by including the lowest levels of confidence.

Topographic shadows and cloud-related masks were merged into a global mask (using GRASSGIS command *r.mapcalc*).

4.4. Index Calculation and Differencing

As introduced in Section 2, we first determined the WrI and ΔWrI imagery. Then, we obtained the ΔWrI frequency distribution histograms (*f*) and corresponding first and second order derivatives (respectively *df* and *d2f*). Given the difference of scales between normalized and non-normalized ΔWrI, we used different binning ranges to obtain frequency functions, respectively based on 255 and 5000 classes. Moreover, smoothing of *f* (by means of moving averages) was useful to aid the interpretation of *df* and *d2f* in order to extract thresholds.

The threshold extraction procedure is exemplified in Figure 3.5 for ΔNDWI, ΔNDVI and ΔTCW using the same flooding event of 2003. The different shape of the ΔTCW distribution (as well as the other non-normalized ΔWrI), compared to ΔNDWI and ΔNDVI (Figure 3.5a), is due to the compression of scale caused by the high magnitude of the extreme values of the parameter. As the *f* distribution does not show secondary modal values beyond the Nc mode, these ΔWrI frequency functions are interpreted as being representative of the example in Figure 3.2d. For these reasons, instead of interpreting *df* (Figure 3.5b), we analysed *d2f* to obtain TL and TH (Figure 3.5c). Since NDVI detects water as negative values, threshold selection analysis was focused on the negative side of the ΔNDVI frequency distribution histogram, unlike the other indices. Following the theoretical premises of Figure 3.2d, the selection of TL corresponds to the absolute modal value of *d2f*, which identification was straightforward for the entire dataset under analysis. Instead, the selection of TH required further statistical processing due to a less favourable signal to noise ratio conditions caused by the lower frequency of pixels having ΔWrI larger than the TH. For this reason, we performed a series of smoothing procedures by using unweighted moving averages, until finding the setup which provided the best delineation of the following local maximum (TH) of *d2f*.

Finally, the application of TL and TH allowed us to obtain the thematic spatial representations shown in Figure 3.5c. Table 3.6 includes the threshold list for all ΔWrI and for every selected event.

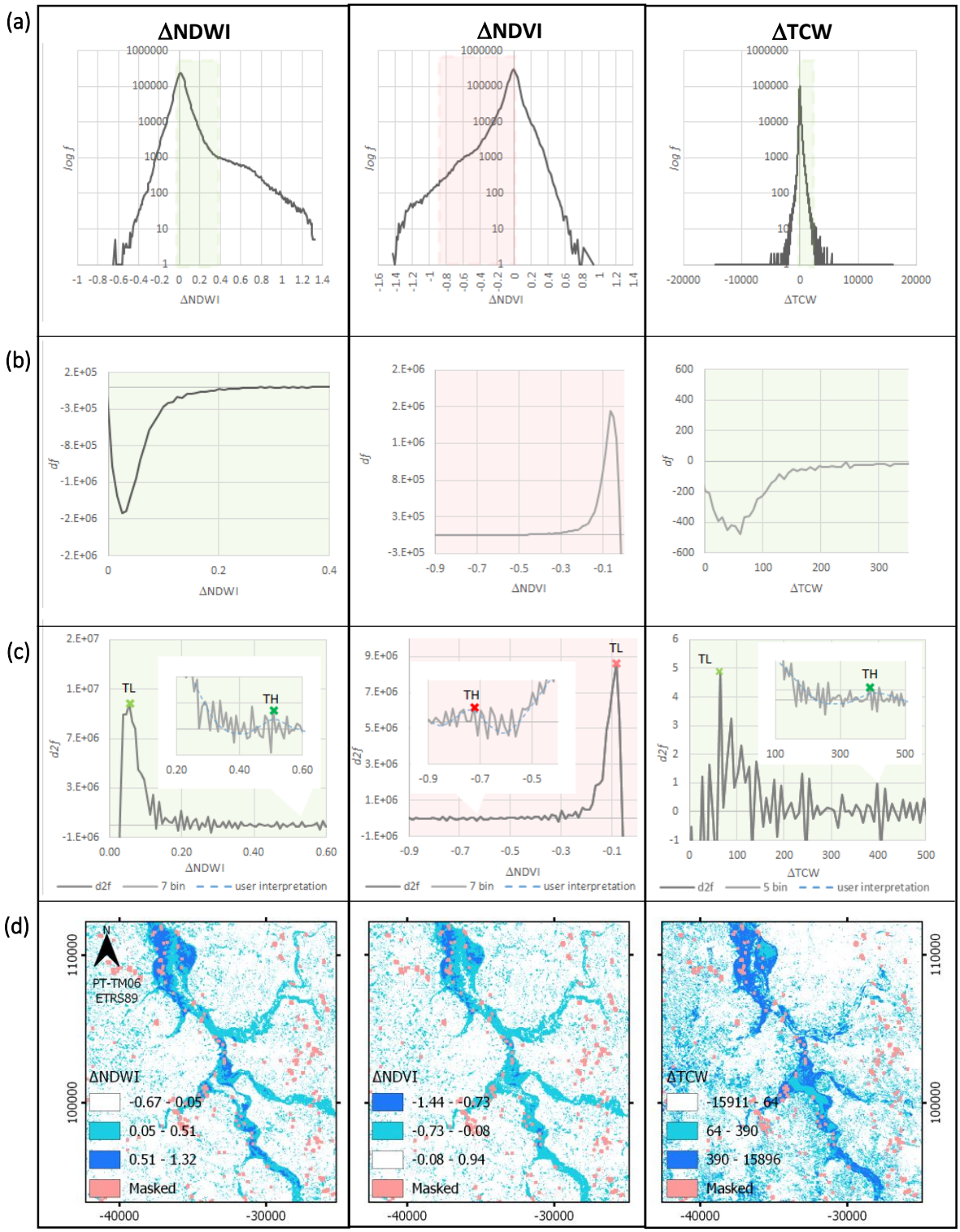

*Figure 3.5 - Examples of threshold extraction (TL and TH) analysis from ΔNDWI, ΔNDVI and ΔTCW (for the event of 2003, within the region of interest): (**a**) frequency distribution functions; (**b**) first order derivatives (df); (**c**) second order derivatives (d2f); (**d**) spatial representation of ΔWrI after thresholding (Coordinate System: PT-TM06/ETRS89).*

Table 3.6 - Thresholds of each ΔWrI, for every selected event.

	2003		2004		2009		2016	
	TL	**TH**	**TL**	**TH**	**TL**	**TH**	**TL**	**TH**
I	0.05	0.51	0.02	0.32	0.00	0.58	0.10	0.42
ΔMNDWI	0.07	0.62	0.00	0.20	0.00	0.48	0.08	0.35
ΔNDVI	−0.80	−0.73	−0.06	−0.44	−0.02	−0.49	−0.13	−0.32
ΔTCW	64	390	12	250	132	513	43	318
ΔAWEI_NS	322	2604	138	2332	333	2442	1476	4566
ΔAWEI_S	388	1173	143	668	94	1419	876	2974

4.5. Flood Extent Estimation Results

After the selection of the thresholds, we performed density slicing (Campbell and Wynne, 2011; Singh, 1989) for each ΔWrI, resulting in a stack of six thematic maps for each of the four events. The overall flood extent map is produced using mathematical operators that assign each pixel to pick the class that corresponds to the majority within the stack of coeval thematic classifications (i.e., at least four consistent classifications). Whenever the condition of a majority is not met, pixels are classified as 'Mixed'.

Taking the largest precipitation event (19 January 2003) as an example, we compared each ΔWrI coeval thematic map (Figure 3.6). In every map, a noticeable concentration of LMc and HMc areas along both the Pateira de Fermentelos lagoon and the major riverbeds of the region of interest (ROI) may be observed. In particular, HMc areas are concentrated to the north-western part of the ROI (towards both sides of the Vouga River section). Another array of HMc areas is located towards the north-eastern side of the Pateira de Fermentelos lagoon, near the confluence with the Águeda River. As for the half-southern part of the ROI (along the Águeda river, the Cértima river and its confluence with the Pateira de Fermentelos), HMc change areas are generally detected except for ΔNDVI, which detect them as LMc. In general, with respect to maps obtained by normalized indices, those from non-normalized indices are characterized by larger extents of randomly distributed change pixels located away from fluvial areas. Table 3.7 summarizes the information about the extent of the coeval thematic classes obtained within the ROI from each ΔWrI, for the 2003 event. Most LMc areas are detected by ΔAWEI_NS and ΔTCW (respectively 24.2%, and 21.8%), while most HMc areas are detected by ΔAWEI_S, ΔAWEI_S and ΔTCW (respectively 9.3%, 7.8%, and 3.8%). Amongst all indices, normalized indices are overall less sensitive to detect HMc areas, with ΔNDVI being the least one (1.2% of the ROI).

Table 3.7 - Coeval class results, obtained within the ROI from each ΔWrI, for the 2003 flood event.

	Nc		LMc		HMc	
	Area (ha)	%	Area (ha)	%	Area (ha)	%
ΔNDWI	25,138	75.8	5870	17.8	872	2.6
ΔMNDWI	27,369	82.6	3578	10.8	933	2.8
ΔNDVI	26,895	81.1	4579	13.8	404	1.2
ΔTCW	22,166	66.9	7238	21.8	1267	3.8
ΔAWEI_NS	21,255	64.1	8029	24.2	2594	7.8
ΔAWEI_S	24,799	74.8	3988	12.0	3092	9.3

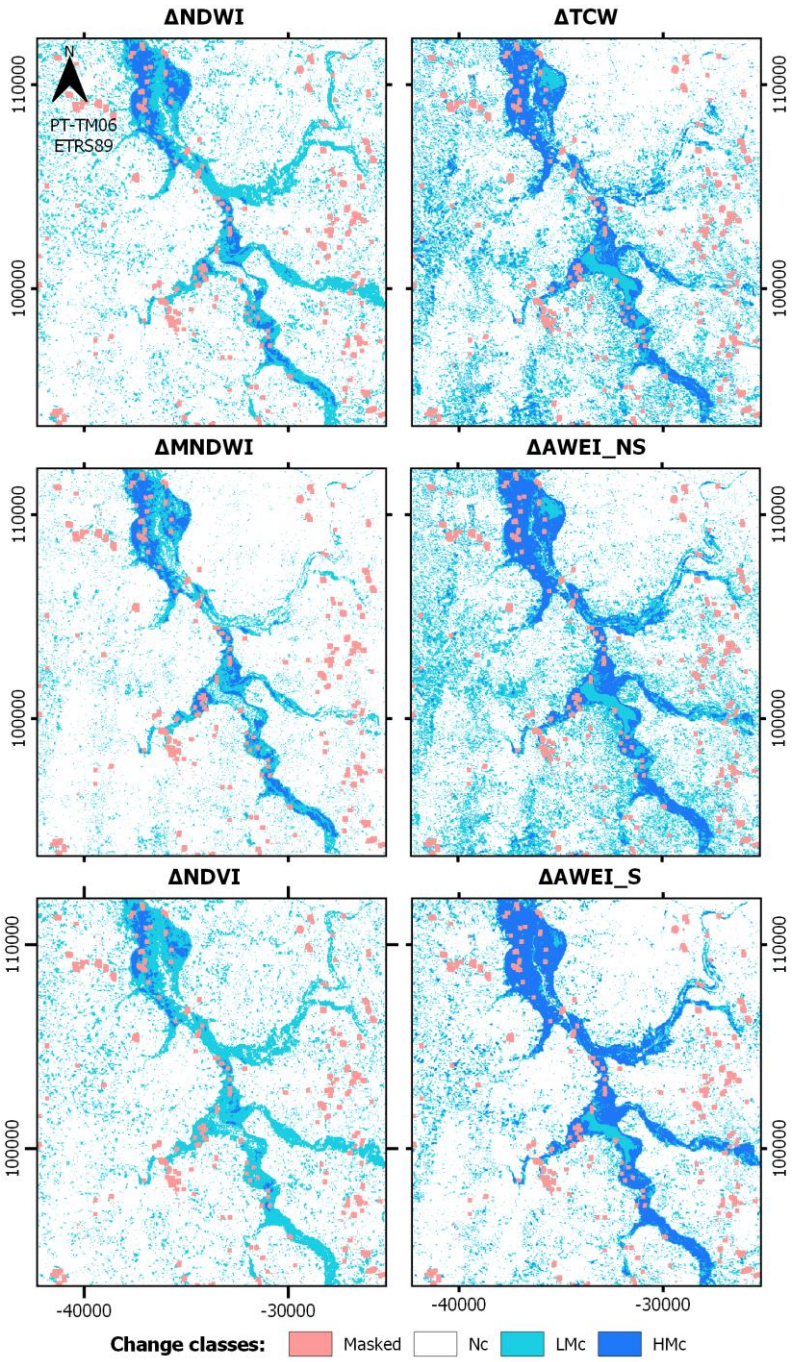

Figure 3.6 - Coeval thematic maps for each ΔWrI, at the region of interest, for the event of 19 January 2003 (Coordinate System: PT-TM06/ETRS89).

The Overall flood map (Figure 3.7a) and the Uncertainty map (Figure 3.7b) are obtained by a procedure based on stacking the six coeval ΔWrI thematic maps (Section 2.1). We observe that the frequency of 'Mixed' pixels (9.1% of the ROI) is smaller than the sum of the remaining classes (Nc + LMc + HMc = 87.1%). Moreover, 'Mixed' pixels are also clearly less widespread than the randomly distributed change pixels located away from fluvial areas (Figure 3.7a vs. Figure 3.6). Larger regions of 'Mixed' pixels mostly make a rim between Nc-LMc and LMc-HMc. The quantitative uncertainty map makes it possible to perform a spatial analysis of classification consistencies. Low uncertainty values are predominant (0 to 2 − 81.9% of the ROI), whereas the highest uncertainties (3 to ≈ 4 − 0.9% of the ROI and 0.4% of the whole study area) are concentrated around areas of change, with special incidence into the major riverbeds.

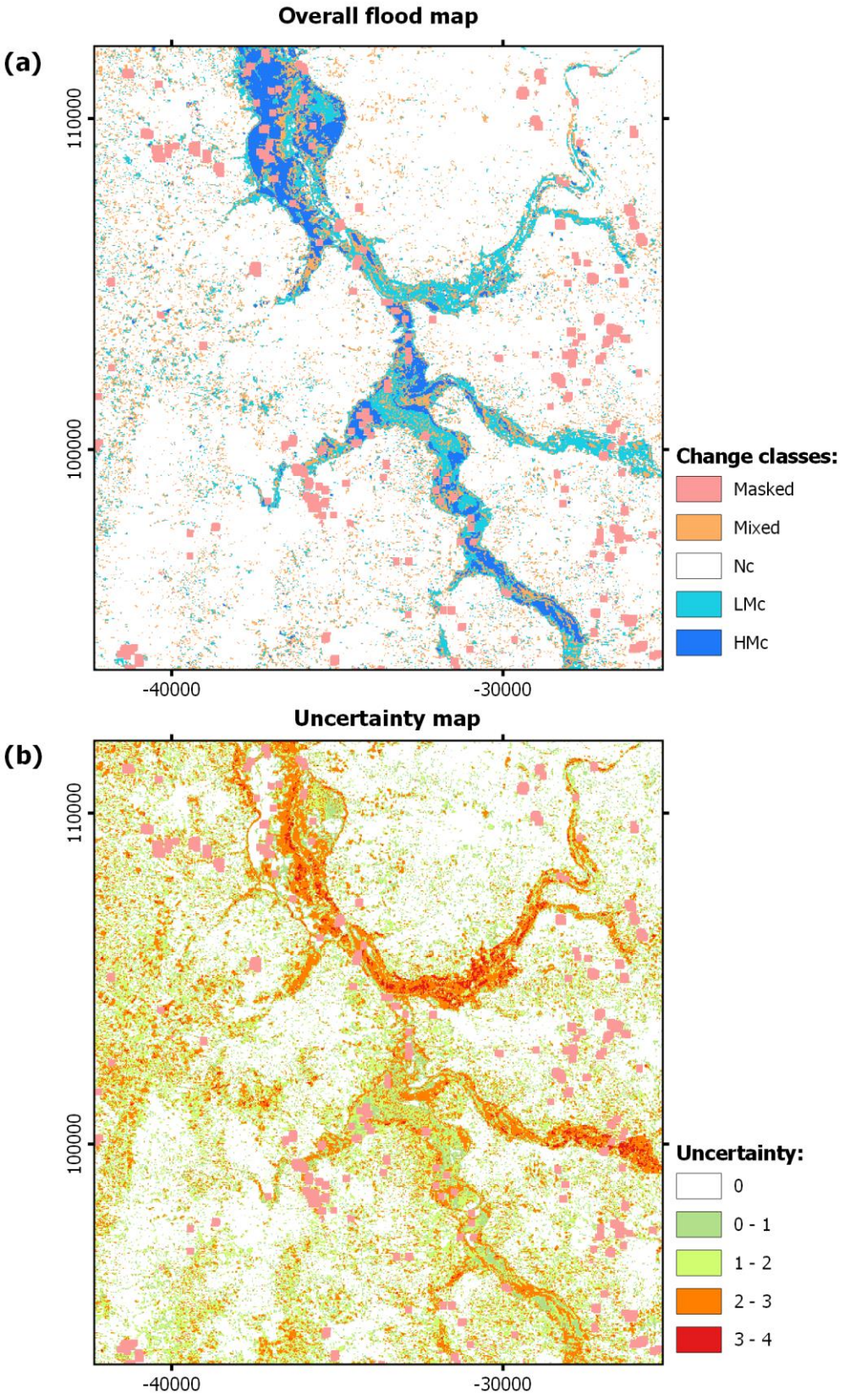

*Figure 3.7 - MINDED results for the 19 January 2003 event, at the region of interest: (**a**) Overall flood map; (**b**) Uncertainty map (Coordinate System: PT-TM06/ETRS89).*

Table 3.8. For the event of 2004, we detected almost only Nc areas. In 2009, only few LMc (4.4%) and HMc (0.4%) areas were detected by MINDED, most of them corresponding to saltmarshes and mudflat areas located inside the Aveiro lagoon. As for the ROI, the few LMc and HMc areas are located within the Pateira de Fermentelos lagoon. Most LMc and HMc areas that appear in the maps of Figure 3.8 are related to the two largest precipitation events. In 2016, the lower parts of the Vouga (Albergaria-a-Velha) and Antuã rivers (Estarreja) a large extent of LMc and HMc areas is mapped. Most changes are located around the Pateira de Fermentelos lagoon, along the Cértima and Águeda rivers (the second in a smaller extent), intersecting Águeda and Oliveira do Bairro municipalities. Regarding the event of 2003, which is characterized by the largest return period (26.5 years–Table 3.5), we detected the largest extent of change pixels, a total of 23,660 ha (corresponding to 8.2% of the whole study area). For this largest event, change areas are consistent with the records of fluvial flood occurrences (see Section 4.2) which were detected in all the reported municipalities. Once more, several change areas within the Aveiro Lagoon correspond to intertidal saltmarshes and mudflat areas.

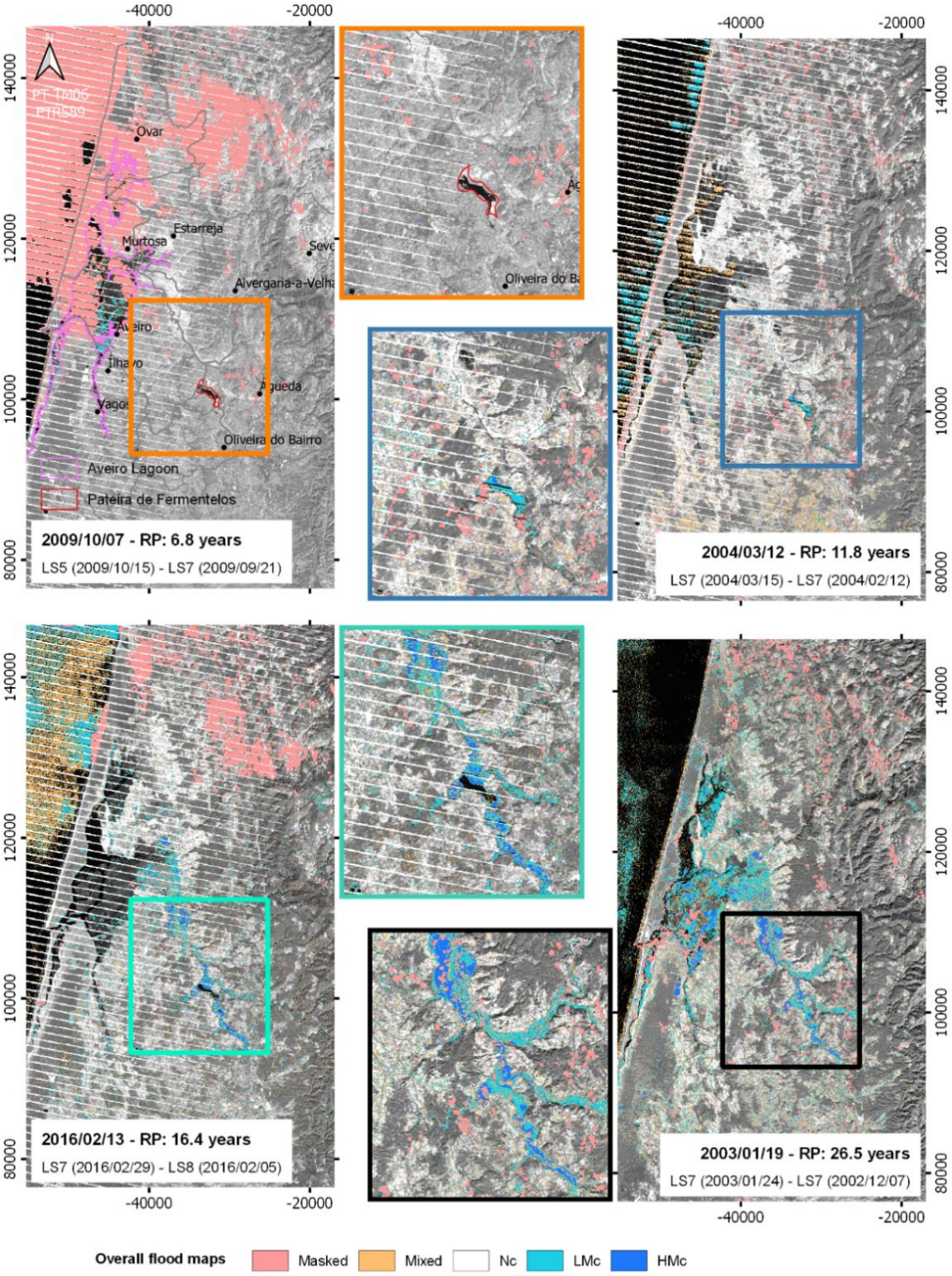

Figure 3.8 - Overall flood maps obtained with MINDED, for each selected event (the corresponding NIR band of t2 is displayed in grayscale as the background of Nc pixels) within both the study area and ROI (Coordinate System: PT-TM06/ ETRS89).

Table 3.8 - Overall flood map results for the whole study area in terms of extent (ha and %) and corresponding class mean uncertainties (MU), for every selected event.

Overall Flood Results	2003			2004			2009			2016		
	Area		MU	Area		MU	Area		MU	Area		MU
	ha	%		ha	%		ha	%		ha	%	
Mixed	26,814	9.3	2.8	13,873	4.8	2.9	3561	10.7	2.8	35,408	12.3	2.9
Nc	229,067	79.5	0.6	187,508	65.1	0.4	24,835	74.9	1.0	181,247	62.9	0.8
LMc	20,214	7.0	2.2	14,238	1.5	2.6	1639	4.4	2.4	17,399	6.0	2.7
HMc	3446	1.2	1.9	377	0.1	2.6	130	0.4	2.8	3381	1.2	2.2

4.6. Comparison with SAR Data

Given SAR potentialities for mapping water bodies and the environmental characteristics of the study area (i.e., an absence of complex topography, snow and dry sand surface, relevant urban areas), Sentinel 1 images can be considered as a reliable source of data to perform comparisons with the MINDED outputs. Hence, we compared our results with flooding maps obtained by the Hierarchical Split-Based Approach (HSBA) (Chini et al., 2017). This is a straightforward automatic change detection method based on Sentinel-1 imagery differencing.

Considering the availability of Sentinel 1A data, the HSBA algorithm was implemented to analyse the event of 2016 (13 February 2016), using three Sentinel 1A images, one for a period before the event, and two for a period after. Thus, we selected the same reference image from 6 February 2016 (7 days before the event), and two others, one from 18 February 2016 (5 days after the event) and another from 1 March 2016 (1 day after the LS7 image used as *t2*, 16 days after the event) as post-event images.

Each Sentinel 1A scene was obtained in IWS (interferometric wide swath) mode, as ESA GRDH products (20 × 22 m resolution, resampled to 10 × 10 pixels). All selected Sentinel-1A products have been acquired with the same relative orbit (125). The algorithm was applied using the following options: Lee Sigma speckle filter (3 × 3), SRTM 1 arc sec geocoding, 5 minimum levels for HSBA, 2.4 Ashman coefficient, a minimum number of 1.000 pixels for the image tiles to process, and by considering eliminating objects below 10 pixels.

Wind conditions during the acquisition affect water surface roughness, and therefore, the accuracy of both water surface and flood extent mapping. According to meteorological data of 'Estrada' and 'Tentugal' stations (APA, 2018), the wind speed at the acquisition times of all the considered images was less than 2.0 m/s, which has no effects in inland waters (RMS, 2015).

The comparison between MINDED and HSBA results for the event of 2016 is illustrated in Figure 3.9.

From the analysis of Figure 3.9b and Figure 3.9c, it is possible to observe that the extent of flooded areas detected by the HSBA algorithm reduced over time (i.e., from 18 February 2016 to 1 March 2016), with particular incidence to North and West of the Pateira de Fermentelos lagoon (along the Águeda and Vouga rivers). This is confirmed by the multi-temporal Sentinel 1A RGB composite (Figure 3.9d), which highlights in purple those areas flooded by 18 February 2016, but recovered toward the initial conditions on 1 March 2016. Those areas still flooded by 1 March 2016 (dark blue) are mostly concentrated to Southwest of the Pateira de Fermentelos lagoon (along the Cértima River).

A quantitative pixel location comparison of MINDED is presented within the form of confusion matrixes (Table 3.9) (Congalton, 1991), using MINDED as reference data (although neither method provides ground truth reference). For comparison purposes, HSBA results were reprojected and resampled to the same grid of MINDED (i.e., the resolution of Landsat images, 30 × 30m), using bilinear interpolation. Class accuracies, commission errors (i.e., overestimation), omission errors (i.e., underestimation) and overall accuracies are provided.

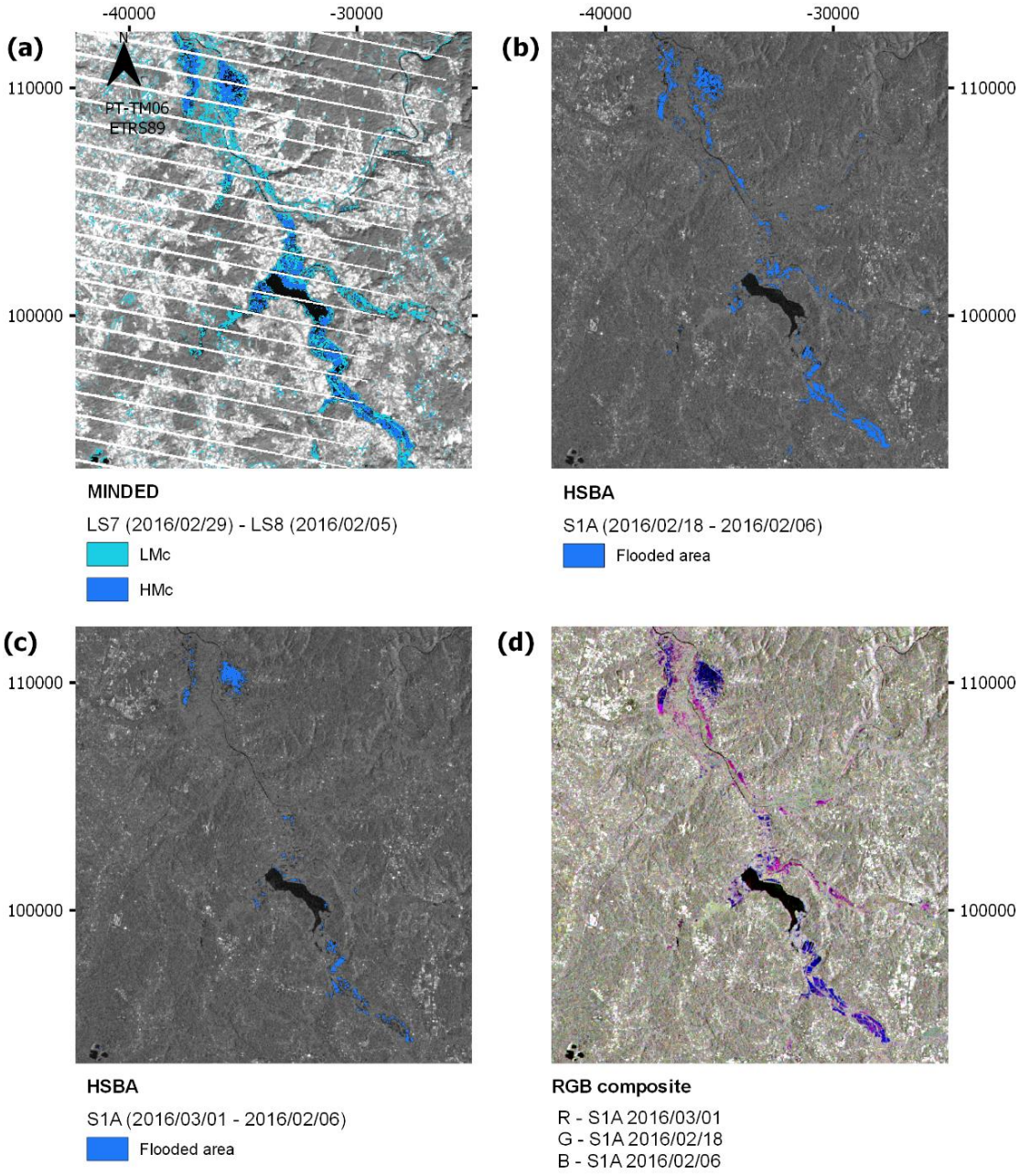

*Figure 3.9 - Comparison of flooded areas results for the 2016 event (13 February 2016) within the ROI, obtained with: (**a**) MINDED (NIR band of LS7 29 February 2016 in the background); (**b**,**c**) the HSBA algorithm-considering two different post-event images (S1A IW GRDH from 18 February 2016 and 1 March 2016 respectively, represented in the backgrounds); (**d**) False colour RGB composite: R-S1A obtained 16 days after the event (1 March 2016), G-S1A obtained 5 days after the event (18 February 2016), B-S1A reference image 7 days prior to the event (6 February 2016) (Coordinate System: PT-TM06/ETRS89).*

Table 3.9 - Confusion matrix between results of MINDED and HSBA methods, analysed in terms of No Change (Nc) and Flooded areas (LMc + HMc), for the event of 13 February 2016, within the region of interest.

		MINDED-LS7 29 February 2016			
		Nc	**Change (LMc + HMc)**	**Total**	**Commission Error (%)**
HSBA-S1A 18/02/2016	Non-Flooded	273,516	43,198	316,714	13.64
	Flooded	245	4688	4933	4.97
	Total	273,761	47,886	321,647	
	Class agreement (%)	99.91	9.79		
	Omission error (%)	0.09	90.21		
	Overall agreement (%)			86.49	
HSBA-S1A 01/03/2016	Non-Flooded	273,685	46,231	319,916	14.45
	Flooded	76	1655	1731	4.39
	Total	273,761	47,886	321,647	
	Class agreement (%)	99.97	3.46		
	Omission error (%)	0.03	96.54		
	Overall agreement (%)	85.60			

Despite the temporal proximity between the post-event images Landsat 7 (29 February 2016) and Sentinel 1A (1 March 2016), the match between MINDED change classifications (i.e., LMc + HMc) and HSBA flooded areas is only 1635 pixels (149 ha), corresponding to a class agreement of 3.46%. Instead, the match with the Sentinel 1A image closer to the flood event (18 February 2016) is 4688 pixels (422 ha), corresponding to a class agreement of 9.79%. In both periods, HSBA underestimates flooded areas in comparison to MINDED, which is more noticeable for 1 March 2016 (omission error of 97%), and less for 18 February 2016 (omission error of 90%). The commission errors of flooded areas for both HSBA periods are significantly low, 4.97% for 18 February 2016 and 4.39% for 1 March 2016, resulting from conflicting classifications of Non-Flooded (HSBA) and Change areas (MINDED). Regardless of the date of post-event HSBA images, we verify overall agreement levels around 86%. The clear majority of concordant Non-flooded-Nc classifications influences the high overall agreement levels.

5. Discussion

We performed a Multi-INDEx Differencing (MINDED) method to detect flooded areas aimed at improving the robustness of single-index approaches. It benefits from the sensitivities of individual indices for detecting water with different characteristics, to mitigate their specific limitations, and to assess the consistency among flood detection results within the so-called Overall flood map.

In digital change detection approaches, thresholds control the results of image differencing, which may be a critical undertaking when no ground truth data is available (Coppin et al., 2004). In practice, missing ground truth is the typical condition when analysing archive data, and in

particular when studying extreme events like floods, for which systematic collection of field data may be problematic. For these reasons, MINDED includes an expedited procedure aimed at reducing subjectivity for thresholds selection. The procedure is based on the analysis of the frequency distribution of water-related index differencing (ΔWrI) data, as well as the corresponding first and second order derivatives. Different thresholds may be selected to discriminate between No change (Nc) areas and different types of change, based on both magnitude and sign of ΔWrI values. Nc areas are expected to include any type of permanently dry surfaces, as well as permanent water bodies and stable wet/saturated surfaces. High Magnitude change (HMc) areas represent a complete change of state from dry land to water surfaces. Low Magnitude change (LMc) areas may include different conditions of subtle change like either areas changing from dry to wet/saturated, or from wet/saturated to water surfaces. Moreover, when post-event (*t2*) images are acquired several days after the flood, LMc may also include areas that were initially flooded, and then underwent the process of recovering toward their original status. For this reason, we consider that MINDED widens the period in which to obtain usable images to extract maximum flood extents. This is particularly relevant for optical satellite imagery, due to their heavy dependence on cloud-free conditions, which tend to be less frequent immediately after heavy precipitation periods. The multi-index approach also makes it possible to extract a 'Mixed' class resulting from a majority analysis implemented within MINDED, as well as an Uncertainty map (Equation (1)) which quantitatively represents the spatial distribution of coherence among the different WrI results. The determination of uncertainty is also based on accuracies known from the literature (Table 3.4), which are used as weighting factors. Consequently, MINDED incorporates the assumed performance of single WrI, even though such accuracies may have been obtained by different methods, assumptions, and sensors, as well as environmental conditions.

As for the implementation of MINDED in the study area, further conclusions may be drawn. Regarding the selection of events to perform the analysis, it is necessary to acknowledge the importance of acquisition time for both pre- and post-event images (respectively *t1* and *t2*). When working with archive imagery related to past events, for which details about spatiotemporal flooding evolution are unknown, the reference image *t1* may represent already altered conditions, due to either previous flooding or high water discharge levels. In these cases, the outputs of MINDED will result in underestimation of the overall flooded area. As for *t2*, the detection capabilities could vary depending on surface permeability, drainage behaviour, and post-event anthropic management, which may limit the available time for usable post-event image acquisition. This is particularly relevant for the 13/02/2016 flood, which was studied with

a Landsat (LS) 7 image acquired 16 days after the event. In this case, MINDED was able to detect tracks of floods in naturalized areas (e.g., mostly HMc areas nearby the Pateira de Fermentelos lagoon), even though only LMc areas were detected in the Águeda city centre, where several streets were reported to be previously inundated. It is important to highlight that the effects of flooding on impervious surfaces, like those of urban areas, are ephemeral and few hours/days may be enough to return to the pre-event surface reflectivity conditions. Thus, we can expect the more *t2* is acquired later than the event, the lower is the accuracy of MINDED to map the maximum flood extent. Moreover, it is expected to observe a progressive transition from HMc to LMc classes. MINDED cannot solve these issues related to the dynamics of post-flood processes, without the integration of ground truths and/or ancillary data.

As a general condition, flood water characteristics may affect the results obtained by indices based on different wavelength ranges of the electromagnetic spectrum (e.g., NIR or SWIR) (Fisher et al., 2016; Wang et al., 2011; Xu, 2006). This issue can be relevant for those events lacking information collected in the field (as the ones considered within this chapter). Nevertheless, concerning the 2003 event, no relevant differences may be identified between the post-event (*t2*) NIR and SWIR bands (Figure 3.4). Such similarities are consequently reflected in ΔMNDWI and ΔNDWI results (Table 3.7). In this case, the characteristics of floodwater produced similar effects on both the NIR and SWIR bands, which can be interpreted as an indicator of low turbidity. In fact, the *t2* image was acquired 5 days after the flood event, allowing time for sedimentation to take place in slow-moving or standing water areas. Among all indices, ΔNDVI was the one detecting fewest HMc areas, confirming its weaker capabilities for recognizing water surfaces (Ji et al., 2009; McFeeters, 1996).

Regarding the statistics of the ΔWrI, when using different sensors for *t1* and *t2*, we can expect to observe the occurrence of non-zero centred modal values. This should not be interpreted as a shortcoming since we can still assume the whole distribution, as well as the Nc condition, to be centred with the main modal value. This is verified for the 2009 and 2016 events, for which, considering the limited availability of cloud-free images during the flood periods, we decided to use different sensors for *t1* and *t2*. The width of the "bell" shape of each histogram is expected to be input-data related and variable according to the distribution of both Nc and LMc/HMc areas, spatial and radiometric co-registration between *t1* and *t2* images, and natural time-depending changes of features (e.g., phenology changes in natural or agricultural areas). However, other sudden changes rather than flooding may also occur, which could be detected as false alarms (e.g., land cover conversions from agricultural practices, effects of fires). The latest represent intrinsic errors of any image-differencing methods, such as MINDED, which

nonetheless may be recognized if such changes occur in places falling out of potentially floodable areas (e.g., by analysing DEM).

Considering that neither of the analysed events resulted in an ideal multi-modal histogram (Figure 3.2c), in order to extract the thresholds, we could not use the first order derivative (*df*), so we analysed the second order derivative (*d2f*) instead. While the extraction of TL, between Nc and LMc, was a straightforward procedure, the extraction of TH, between LMc and HMc, required further statistical processing that is aimed at improving the signal-to-noise ratio in the considered ΔWrI range. This last task is more prone to user-subjectivity, so TH should be more reasonably considered as a range of values, which spatial effects have to be verified at map scale. Being a typical expert-dependent analysis, this segment of MINDED may be hardly implemented as a fully automatic tool procedure.

An advantage of MINDED, resulting from the approach of combining results from different WrI, is the possibility to recognize eventually erratic classifications from a certain index in respect to the others. As observed for the 2003 event, all the ΔWrI maps are characterized by apparently random distributed change pixels located away from fluvial areas (Figure 3.6). In a single-index flood detection approach, these pixels represent a false alarm condition that reduces the quality of the flooding map. This is particularly relevant for the non-normalized ΔWrI maps, which may result from ineffective cloud masking. In addition, higher sensitivities to terrain shadowing caused by local relief (Table 3.2) may produce similar effects, due to rough masking from global-scale DEM. A more detailed analysis of such areas highlights the fact that the spatial distributions of such pixels are mainly non-overlapping amongst the ΔWrI maps. Consequently, the process of stacking implemented within MINDED efficiently handles these false alarms by classifying most of them as Nc, or 'Mixed' in a smaller degree (e.g., 9.3% of the ROI for the 2003 event-Figure 3.7). This observation highlights the benefit of MINDED approach with respect to the standard single-index alternatives. The 'Mixed' class is mostly located nearby the transition areas between Nc-LMc and LMc-HMc, suggesting that they result from the occurrence of subtle changes that are differently recognized by each WrI. Furthermore, it also shows that the combined results from every ΔWrI are each other consistent. Another indication of the effectiveness of MINDED is the analysis of the spatial distribution of uncertainty. Highest uncertainty values are concentrated around the major riverbeds and areas of change, and their frequency is low (ρ = 3 to ≈ 4 − 0.4% of the study area). This suggests that, even though every WrI may provide different results about change, MINDED integrates these results giving a more robust representation of changes.

As expected, we observed larger extents of flooded areas with higher return period events. However, in some cases (2009, 2004 and 2003), several intertidal areas were classified as being flooded (mostly as LMc). This is a consequence of differences of tidal states between *t1* and *t2*, meaning that *t1* image likely was acquired during lower tide. Besides, we have to assume that MINDED might detect false alarms within permanent water bodies, such as the Pateira de Fermentelos lagoon, due to variations of water thickness/composition or floating debris/vegetation that might be classified as LMc or even HMc areas.

Regarding the comparison between MINDED and HSBA methods, results show that the location of Flooded and HMc classes areas are coherent. MINDED is more sensitive to detect tracks from recent flood events, particularly in LMc areas, which implies detection of larger flooded areas. On the other hand, despite the apparent improved spatial resolution of Sentinel 1A imagery (which is not directly comparable with the spatial resolution of optical data Kumar et al., 2010), the HSBA algorithm seems to be less sensitive to discriminate between water 'saturated' areas and drier surfaces during the days following a flood event (resulting in higher commission errors). We consider that the low agreement level between Change and Flooded classes (Table 3.9), is likely related to the unavailability of Sentinel 1 images acquired during the flood event (or immediately after), as well as to the HSBA procedure which eliminates change clusters smaller than 10 pixels.

6. Conclusions

This study presents an innovative method based on the integration of change-detection concepts that are known from the literature. MINDED makes it possible to detect the extent of past and future flood events, combining multiple water-related indices derived from optical satellite data within a change detection approach, and benefiting from long-term image catalogues.

The method implements image differencing and provides a consistent procedure to analyse the frequency distribution of water-related indices for the extraction of different thresholds depending on the magnitude of changes, as a reproducible alternative to ground-truthing. Then, types of change are discriminated considering the sign of difference and applying density slicing based on thresholds.

High magnitude changes include surfaces changing from 'dry' to 'flooded' state, while low magnitude changes correspond to surfaces changing from 'dry' to 'saturated', or 'saturated' to

'flooded' states. Unchanged areas do not discriminate between permanent water bodies and permanent dry surfaces, which is not a limitation for flood hazard analysis. By integrating different water-related indices with different sensitivities to water characteristics, and considering the agreement among the resulting classifications, the method is capable of obtaining both an Overall flood map and an Uncertainty map, estimating uncertainty bounds for flooded areas. This approach increases the robustness of results, particularly in the transition areas between flooded and non-flooded surfaces, as well as where randomly distributed changes not related to water might occur. Moreover, the possibility of analysing flood events by comparing imagery acquired by different sensors may help to widen the temporal window for obtaining suitable optical satellite images. For these reasons, we consider MINDED being a new valid method to be integrated along with others, including SAR-based approaches (e.g., data-fusion methods), to obtain the best representation of flooded areas.

The performance of MINDED was tested with an application to a study area in north-western Portugal, using Landsat imagery to perform flood detection analyses for several events. The results are consistent with known historical flood records. When processing images acquired several days after a triggering precipitation event, MINDED showed the capability of detecting tracks of floods both in naturalized and agricultural areas.

Since no ground truth data was available, we compared results from the same event with those obtained by processing multi-date post-event Sentinel-1A scenes using the Hierarchical Split-Based Approach algorithm. The best agreement between methods was obtained by processing the earliest post-event Sentinel-1A image, supporting the idea that MINDED provides a close representation of the maximum flood extent.

The current implementation of MINDED has the potential for automatization improvement, which would contribute to its use as a more expedite method for operational purposes. Further developments of MINDED should be tested in other regions and contexts, as well as by integrating more water-related indices and a different number of indices. Moreover, there is potential to implement MINDED using data obtained from other sensors, including improved spatial resolution alternatives (e.g., Sentinel-2), without requiring relevant adjustments to the procedures, still providing an evaluation of uncertainty. Finally, we highlight that the threshold selection procedure developed in this chapter, when applied to either other indices or data, has the potential to be applied to change detection studies other than flooding.

Allen, G.H., Pavelsky, T.M., 2018. Global extent of rivers and streams. Science (80-.). 361, 585–588. https://doi.org/10.1126/science.aat0636

Alves, F.L., Sousa, L.P., Silva, J.V., Dias, J.M., Lopes, C., Coelho, C., Pereira, C., 2010. Tarefa 2. Revisão do estado-da-arte, recolha e análise de dados, ADAPTARia - Modelação das Alterações Climáticas no Litoral da Ria de Aveiro Estratégias de Adaptaçãp para Cheias Costeiras e Fluviais. Aveiro, Portugal.

APA, 2018. SNIRH [WWW Document]. URL http://snirh.pt/

Azevedo, A., Fortunato, A.B., Epifânio, B., den Boer, S., Oliveira, E.R., Alves, F.L., de Jesus, G., Gomes, J.L., Oliveira, A., 2017. An oil risk management system based on high-resolution hazard and vulnerability calculations. Ocean Coast. Manag. 136, 1–18. https://doi.org/10.1016/j.ocecoaman.2016.11.014

Baig, M.H.A., Zhang, L., Shuai, T., Tong, Q., 2014. Derivation of a tasselled cap transformation based on Landsat 8 at-satellite reflectance. Remote Sens. Lett. 5, 423–431. https://doi.org/10.1080/2150704X.2014.915434

Bartsch, A., Pathe, C., Wagner, W., Scipal, K., 2008. Detection of permanent open water surfaces in central Siberia with ENVISAT ASAR wide swath data with special emphasis on the estimation of methane fluxes from tundra wetlands. Hydrol. Res. 39, 89. https://doi.org/10.2166/nh.2008.041

Bates, P.D., Wilson, M.D., Horritt, M.S., Mason, D.C., Holden, N., Currie, A., 2006. Reach scale floodplain inundation dynamics observed using airborne synthetic aperture radar imagery: Data analysis and modelling. J. Hydrol. 328, 306–318. https://doi.org/10.1016/j.jhydrol.2005.12.028

Boni, G., Ferraris, L., Pulvirenti, L., Squicciarino, G., Pierdicca, N., Candela, L., Pisani, A.R., Zoffoli, S., Onori, R., Proietti, C., Pagliara, P., 2016. A Prototype System for Flood Monitoring Based on Flood Forecast Combined with COSMO-SkyMed and Sentinel-1 Data. IEEE J. Sel. Top. Appl. Earth Obs. Remote Sens. 9, 2794–2805. https://doi.org/10.1109/JSTARS.2016.2514402

Braaten, J.D., Cohen, W.B., Yang, Z., 2015. Remote Sensing of Environment Automated cloud and cloud shadow identi fi cation in Landsat MSS imagery for temperate ecosystems. Remote Sens. Environ. 169, 128–138. https://doi.org/10.1016/j.rse.2015.08.006

Brakenridge, G.R., Syvitski, J.P.M., Niebuhr, E., Overeem, I., Higgins, S.A., Kettner, A.J., Prades, L., 2017. Design with nature: Causation and avoidance of catastrophic flooding, Myanmar. Earth-Science Rev. 165, 81–109. https://doi.org/10.1016/j.earscirev.2016.12.009

Brivio, P.A., Colombo, R., Maggi, M., Tomasoni, R., 2002. Integration of remote sensing data and GIS for accurate mapping of flooded areas. Int. J. Remote Sens. ISSN 23, 429–441. https://doi.org/10.1080/01431160010014729

Campbell, J.B., Wynne, R.H., 2011. Introduction to Remote Sensing, Fifth Edition, 5th ed, introduction to remote sensing fifth edition.

Cenci, L., Boni, G., Pulvirenti, L., Squicciarino, G., Gabellani, S., Gardella, F., Pierdicca, N., Chini, M., 2017a. Monitoring reservoirs' water level from space for flood control applications. A case study in the Italian Alpine region. 2017 IEEE Int. Geosci. Remote Sens. Symp. (IGARSS), Fort Worth, TX, 2017 5617–5620. https://doi.org/10.1109/IGARSS.2017.8128279

Cenci, L., Disperati, L., Persichillo, M.G., Oliveira, E.R., Alves, F.L., Phillips, M., 2017b. Integrating remote sensing and GIS techniques for monitoring and modeling shoreline evolution to support coastal risk management. GIScience Remote Sens. 00, 1–21. https://doi.org/10.1080/15481603.2017.1376370

Chini, M., Hostache, R., Giustarini, L., Matgen, P., 2017. A Hierarchical Split-Based Approach for Parametric Thresholding of SAR Images: Flood Inundation as a Test Case. IEEE Trans. Geosci. Remote Sens. 1–14. https://doi.org/10.1109/TGRS.2017.2737664

CMI, 2016. Estratégia Municipal de Adaptação às Alterações Climáticas no Município de Ílhavo.

Congalton, R.G., 1991. A review of assessing the accuracy of classifications of remotely sensed data. Remote Sens. Environ. 37, 35–46. https://doi.org/10.1016/0034-4257(91)90048-B

Coppin, P., Jonckheere, I., Nackaerts, K., Muys, B., Lambin, E., 2004. Digital change detection methods in ecosystem monitoring: A review. Int. J. Remote Sens. 25, 1565–1596. https://doi.org/10.1080/0143116031000101675

Crist, E.P., 1985. A TM Tasseled Cap equivalent transformation for reflectance factor data. Remote Sens. Environ. 17, 301–306. https://doi.org/10.1016/0034-4257(85)90102-6

Crist, E.P., Cicone, R.C., 1984. A Phisically-Based Transformation of Thematic Mapper Data - The Tasseled Cap. Ieee Trans. Geosci. Remote Sens. 22, 256–263. https://doi.org/10.1109/TGRS.1984.350619

Dao, P.D., Liou, Y.A., 2015. Object-based flood mapping and affected rice field estimation with landsat 8 OLI and MODIS data. Remote Sens. 7, 5077–5097. https://doi.org/10.3390/rs70505077

Devries, B., Pratihast, A.K., Verbesselt, J., Kooistra, L., Herold, M., 2016. Characterizing forest change using community-based monitoring data and landsat time series. PLoS One 11, 1–25. https://doi.org/10.1371/journal.pone.0147121

Ding, X., Nunziata, F., Li, X., Migliaccio, M., 2015. Performance Analysis and Validation of Waterline Extraction Approaches Using Single- and Dual-Polarimetric SAR Data. IEEE J. Sel. Top. Appl. Earth Obs. Remote Sens. 8, 1019–1027. https://doi.org/10.1109/JSTARS.2014.2362511

Disperati, L., Virdis, S.G.P., 2015. Assessment of land-use and land-cover changes from 1965 to 2014 in Tam Giang-Cau Hai Lagoon, central Vietnam. Appl. Geogr. 58, 48–64. https://doi.org/10.1016/j.apgeog.2014.12.012

Drusch, M., Bello, U. Del, Carlier, S., Colin, O., Fernandez, V., Gascon, F., Hoersch, B., Isola, C., Laberinti, P., Martimort, P., Meygret, A., Spoto, F., Sy, O., Marchese, F., Bargellini, P., 2012. Remote Sensing of Environment Sentinel-2 : ESA ' s Optical High-Resolution Mission for GMES Operational Services 120, 25–36. https://doi.org/10.1016/j.rse.2011.11.026

EEA, 2010. Mapping the impacts of recent natural disasters and technological accidents in Europe - An overview of the last decade, EEA Technical report. Copenhagen, Denmark. https://doi.org/10.2800/62638

EU, 2007. DIRECTIVE 2007/60/EC OF THE EUROPEAN PARLIAMENT AND OF THE COUNCIL of 23 October 2007 on the assessment and management of flood risks. Off. J. Eur. Union L 288, 2007.

Fang-fang, Z., Bing, Z., Jun-sheng, L., Qian, S., Yuanfeng, W., Yang, S., 2011. Comparative Analysis of Automatic Water Identification Method Based on Multispectral Remote Sensing. Procedia Environ. Sci. 11, 1482–1487. https://doi.org/10.1016/j.proenv.2011.12.223

Feng, Q., Gong, J., Liu, J., Li, Y., 2015. Flood mapping based on multiple endmember spectral mixture analysis and random forest classifier-the case of yuyao, China. Remote Sens. 7, 12539–12562. https://doi.org/10.3390/rs70912539

Feyisa, G.L., Meilby, H., Fensholt, R., Proud, S.R., 2014. Automated Water Extraction Index: A new technique for surface water mapping using Landsat imagery. Remote Sens. Environ.

140, 23–35. https://doi.org/10.1016/j.rse.2013.08.029

Fisher, A., 2014. Cloud and Cloud-Shadow Detection in SPOT5 HRG Imagery with Automated Morphological Feature Extraction 776–800. https://doi.org/10.3390/rs6010776

Fisher, A., Flood, N., Danaher, T., 2016. Comparing Landsat water index methods for automated water classification in eastern Australia. Remote Sens. Environ. 175, 167–182. https://doi.org/10.1016/j.rse.2015.12.055

Gao, H., Wang, L., Jing, L., Xu, J., 2016. An effective modified water extraction method for Landsat-8 OLI imagery of mountainous plateau regions. IOP Conf. Ser. Earth Environ. Sci. 34, 012010. https://doi.org/10.1088/1755-1315/34/1/012010

Giustarini, L., Hostache, R., Matgen, P., Schumann, G.J., Bates, P.D., Mason, D.C., 2013. A Change Detection Approach to Flood Mapping in Urban Areas Using TerraSAR-X. IEEE Trans. Geosci. Remote Sens. 51, 2417–2430. https://doi.org/10.1109/TGRS.2012.2210901

Gómez-Palacios, D., Torres, M.A., Reinoso, E., 2016. Flood mapping through principal component analysis of multitemporal satellite imagery considering the alteration of water spectral properties due to turbidity conditions. Geomatics, Nat. Hazards Risk 0, 1–17. https://doi.org/10.1080/19475705.2016.1250115

Hess, L.L., Melack, J.M., Davis, F.W., 1994. Mapping of Floodplain Inundation with Multi-Frequency Polarimetric SAR: Use of a Tree-Based Model. Int. J. Ecol. Environ. Sci. 11, 1072–1073.

Huang, C., Wylie, B., Homer, C., Yang, L., Zylstra, G., 2002. Derivation of a Tasseled cap transformation based on Landsat 7 at-satellite reflectance. Int. J. Remote Sens. 23, 1741–1748. https://doi.org/10.1080/01431160110106113

Hughes, M.J., Hayes, D.J., 2014. Automated Detection of Cloud and Cloud Shadow in 4907–4926. https://doi.org/10.3390/rs6064907

Hulley, G.C., Hook, S.J., 2008. A new methodology for cloud detection and classification with ASTER data 35, 1–6. https://doi.org/10.1029/2008GL034644

Irish, R.R., Barker, J.L., Goward, S.N., Arvidson, T., 2006. Characterization of the Landsat-7 ETM ƨ Automated Cloud-Cover Assessment (ACCA) Algorithm 72, 1179–1188.

Ivits, E., Lamb, A., Langar, F., Hemphill, S., Koch, B., 2008. Orthogonal Transformation of Segmented SPOT5 Images : Seasonal and Geographical Dependence of the Tasselled Cap

Parameters 74, 1351–1364.

JAXA, 2015. ALOS Global Digital Surface Model “ALOS World 3D - 30m (AW3D30)” [WWW Document]. URL https://www.eorc.jaxa.jp/ALOS/en/aw3d30/

Ji, L., Zhang, L., Wylie, B., 2009. Analysis of Dynamic Thresholds for the Normalized Difference Water Index. Photogramm. Eng. Remote Sens. 75, 1307–1317. https://doi.org/10.14358/PERS.75.11.1307

Kauth, R.J., Thomas, G.S., 1976. The tasselled cap - A graphic description of the spectral-temporal development of agricultural crops as seen by Landsat. Proc. Symp. Mach. Process. Remote. Sensed Data, West Lafayette, Indiana, U.S.A, 29 June-1 July 1976 41–51.

Kugler, Z., De Groeve, T., Groeve, T. De, 2007. The global flood detection system. Off. Off. Publ. … 45.

Kumar, T.S., Mahendra, R.S., Nayak, S., Radhakrishnan, K., Sahu, K.C., 2010. Coastal Vulnerability Assessment for Orissa State, East Coast of India. J. Coast. Res. 263, 523–534. https://doi.org/10.2112/09-1186.1

Li, Y., Gong, X., Guo, Z., Xu, K., Hu, D., Zhou, H., 2016. An index and approach for water extraction using Landsat–OLI data. Int. J. Remote Sens. 37, 3611–3635. https://doi.org/10.1080/01431161.2016.1201228

Lillesand, T.M., Kiefer, R.W., Chipman, J.W., 2015. Remote Sensing and Image Interpretation, 7th ed. New York, USA.

Liu, C., 2016. Analysis of Sentinel-1 SAR data for mapping standing water in the Twente region 37.

Lu, D., Mausel, P., Brondízio, E., Moran, E., 2004. Change detection techniques. Int. J. Remote Sens. 25, 2365–2407. https://doi.org/10.1080/0143116031000139863

Martinis, S., Kersten, J., Twele, A., 2015a. A fully automated TerraSAR-X based flood service. ISPRS J. Photogramm. Remote Sens. 104, 203–212. https://doi.org/10.1016/j.isprsjprs.2014.07.014

Martinis, S., Kuenzer, C., Wendleder, A., Huth, J., Twele, A., Roth, A., Dech, S., 2015b. Comparing four operational SAR-based water and flood detection approaches. Int. J. Remote Sens. 36, 3519–3543. https://doi.org/10.1080/01431161.2015.1060647

Martinis, S., Twele, A., Voigt, S., 2009. Towards operational near real-time flood detection using

a split-based automatic thresholding procedure on high resolution TerraSAR-X data. Nat. Hazards Earth Syst. Sci. 9, 303–314. https://doi.org/10.5194/nhess-9-303-2009

Matgen, P., Hostache, R., Schumann, G., Pfister, L., Hoffmann, L., Savenije, H.H.G., 2011. Towards an automated SAR-based flood monitoring system: Lessons learned from two case studies. Phys. Chem. Earth 36, 241–252. https://doi.org/10.1016/j.pce.2010.12.009

McFeeters, S.K., 1996. The use of the Normalized Difference Water Index (NDWI) in the delineation of open water features. Int. J. Remote Sens. 17, 1425–1432. https://doi.org/10.1080/01431169608948714

Memon, A.A., Muhammad, S., Rahman, S., Haq, M., 2015. Flood monitoring and damage assessment using water indices: A case study of Pakistan flood-2012. Egypt. J. Remote Sens. Sp. Sci. 18, 99–106. https://doi.org/10.1016/j.ejrs.2015.03.003

Nardi, F., Annis, A., Baldassarre, G. Di, Vivoni, E.R., Grimaldi, S., 2019. GFPLAIN 250 m , a global high-resolution dataset of Earth ' s floodplains. Nat. Publ. Gr. 6, 1–6. https://doi.org/10.1038/sdata.2018.309

NASA, 2015. Shuttle Radar Topography Mission (SRTM) [WWW Document]. URL https://www2.jpl.nasa.gov/srtm/

NASA, 2004. Advanced Spaceborne Thermal Emission and Reflection Radiometer (ASTER) [WWW Document]. URL https://asterweb.jpl.nasa.gov/gdem.asp

Nedkov, R., 2017. Orthogonal transformation of segmented images from the satellite sentinel-2. Comptes Rendus L'Academie Bulg. des Sci. 70, 687–692.

Oberstadler, R., Ho, Ã.H., 1997. ASSESSMENT OF THE MAPPING CAPABILITIES OF ERS-1 SAR DATA FOR FLOOD MAPPING : A CASE STUDY IN GERMANY 11.

Otsu, N., 1979. A Threshold Selection Method from Gray-Level Histograms. IEEE Trans. Syst. Man. Cybern. 9, 62–66. https://doi.org/10.1109/TSMC.1979.4310076

Pekel, J., Cottam, A., Gorelick, N., Belward, A.S., 2016. High-resolution mapping of global surface water and its long-term changes. Nature 540, 418–422. https://doi.org/10.1038/nature20584

Pulvirenti, L., Marzano, F.S., Pierdicca, N., Mori, S., Chini, M., 2014. Discrimination of water surfaces, heavy rainfall, and wet snow using COSMO-SkyMed observations of severe weather events. IEEE Trans. Geosci. Remote Sens. 52, 858–869.

https://doi.org/10.1109/TGRS.2013.2244606

Pulvirenti, L., Pierdicca, N., Chini, M., Guerriero, L., 2011. An algorithm for operational flood mapping from Synthetic Aperture Radar (SAR) data using fuzzy logic. Nat. Hazards Earth Syst. Sci. 11, 529–540. https://doi.org/10.5194/nhess-11-529-2011

Purinton, B., Bookhagen, B., 2017. Validation of digital elevation models (DEMs) and comparison of geomorphic metrics on the southern Central Andean Plateau 211–237. https://doi.org/10.5194/esurf-5-211-2017

RAES, D., 2013. Frequency analysis of rainfall data. Coll. Soil Phys. 30th Anniv. (1983 - 2013) 42. https://doi.org/10.1051/matecconf/20165703013

Revilla-Romero, B., Hirpa, F.A., Pozo, J.T. del, Salamon, P., Brakenridge, R., Pappenberger, F., de Groeve, T., 2015. On the use of global flood forecasts and satellite-derived inundation maps for flood monitoring in data-sparse regions. Remote Sens. 7, 15702–15728. https://doi.org/10.3390/rs71115702

Richards, J.A., 2013. Remote Sensing Digital Image Analysis An Introduction.

RMS, 2015. Beaufort Scale for Land Areas. Reading, U.K.

Rokni, K., Ahmad, A., Selamat, A., Hazini, S., 2014. Water feature extraction and change detection using multitemporal landsat imagery. Remote Sens. 6, 4173–4189. https://doi.org/10.3390/rs6054173

Rouse, J.W., Hass, R.H., Schell, J.A., Deering, D.W., 1973. Monitoring vegetation systems in the great plains with ERTS. Third Earth Resour. Technol. Satell. Symp. 1, 309–317.

Santillan, J.R., Makinano-Santinano-Santillan, M., 2016. Vertical Accuracy Assessment of 30-M Resolution ALOS, ASTER, and SRTM Global DEMS over Northeastern Mindanao, Philippines, in: The International Archives of the Photogrammetry, Remote Sensing and Spatial Information Sciences. Prague, Czech Republic, pp. 12–19. https://doi.org/10.5194/isprsarchives-XLI-B4-149-2016

Scaramuzza, P.L., Bouchard, M.A., Dwyer, J.L., 2012. Development of the Landsat Data Continuity Mission Cloud-Cover Assessment Algorithms 50, 1140–1154.

Schlaffer, S., Matgen, P., Hollaus, M., Wagner, W., 2015. Flood detection from multi-temporal SAR data using harmonic analysis and change detection. Int. J. Appl. Earth Obs. Geoinf. 38, 15–24. https://doi.org/10.1016/j.jag.2014.12.001

Schowengerdt, R.A., 2007. Remote Sensing: Models and Methods for Image Processing, Third Edit. ed. Academic Press.

Sena, C., C. Melo, M.., 2012. Groundwater–surface water interactions in a freshwater lagoon vulnerable to anthropogenic pressures (Pateira de Fermentelos, Portugal). J. Hydrol. 466–467, 88–102. https://doi.org/https://doi.org/10.1016/j.jhydrol.2012.08.006

Shi, W., Wang, M., 2007. Detection of turbid waters and absorbing aerosols for the MODIS ocean color data processing 110, 149–161. https://doi.org/10.1016/j.rse.2007.02.013

Singh, A., 1989. Review Articlel: Digital change detection techniques using remotely-sensed data. Int. J. Remote Sens. 10, 989–1003. https://doi.org/10.1080/01431168908903939

Smith, L.C., 1997. Sattelite Remote Sensing of River Inundation Area, Stage, and Discharge: A Review. Hydrol. Process. 11, 1427–1439.

Smith, L.C., Isacks, B.L., Forster, R., Bloom, A.L., Preuss, I., 1995. Estimation of Discharge From Braided Glacial Rivers Using ERS 1 Synthetic Aperture Radar : First Results. Water Resour. Res. 31, 1325–1329. https://doi.org/10.1029/95WR00145

Smith, L.C., Isacks, B.L., Murray, A.B., Smith, L.C., Isacks, B.L., Bloom, A.L., Murray, A.B., 1996. Estimation of Discharge From Three Braided Rivers Using Synthetic Aperture Radar Satellite Imagery : Potential Application to Ungaged Basins. Water Resour. Res. 32, 2021–2034. https://doi.org/10.1029/96WR00752

Sousa, L.P., Sousa, A.I., Alves, F.L., Lillebø, A.I., 2016. Ecosystem services provided by a complex coastal region: Challenges of classification and mapping. Sci. Rep. 6, 1–14. https://doi.org/10.1038/srep22782

Stark, B., Member, Student, Mcgee, M., Member, Student, Chen, Y., Member, Senior, 2015. Short Wave Infrared (SWIR) Imaging Systems Using Small Unmanned Aerial Systems (sUAS). 2015 Int. Conf. Unmanned Aircr. Syst. 495–501. https://doi.org/10.1109/ICUAS.2015.7152328

Ulaby, F.T., Dobson, M.C., 1989. Handbook of Radar Scattering Statistics for Terrain, Artech Hou. ed.

USGS, 2018. Landsat Surface Reflectance Quality Assessment [WWW Document]. URL https://landsat.usgs.gov/landsat-surface-reflectance-quality-assessment

Vanhellemont, Q., Ruddick, K., 2015. Remote Sensing of Environment Advantages of high quality

SWIR bands for ocean colour processing : Examples from Landsat-8. Remote Sens. Environ. 161, 89–106. https://doi.org/10.1016/j.rse.2015.02.007

Wang, M., Shi, W., Tang, J., 2011. Remote Sensing of Environment Water property monitoring and assessment for China ' s inland Lake Taihu from MODIS-Aqua measurements. Remote Sens. Environ. 115, 841–854. https://doi.org/10.1016/j.rse.2010.11.012

Wang, W., Yang, X., Li, X., Chen, K., Liu, G., Li, Z., Gade, M., 2017. A Fully Polarimetric SAR Imagery Classification Scheme for Mud and Sand Flats in Intertidal Zones. IEEE Trans. Geosci. Remote Sens. 55, 1734–1742. https://doi.org/10.1109/TGRS.2016.2631632

Xiao, X., Wdowinski, S., Wu, Y., 2014. Improved water classification using an application-oriented processing of landsat ETM+ and ALOS PALSAR. Int. J. Control Autom. 7, 373–388. https://doi.org/10.14257/ijca.2014.7.11.35

Xie, H., Luo, X., Xu, X., Pan, H., Tong, X., 2016. Evaluation of Landsat 8 OLI imagery for unsupervised inland water extraction. Int. J. Remote Sens. 37, 1826–1844. https://doi.org/10.1080/01431161.2016.1168948

Xu, H., 2006. Modification of normalised difference water index (NDWI) to enhance open water features in remotely sensed imagery. Int. J. Remote Sens. 27, 3025–3033. https://doi.org/10.1080/01431160600589179

Yamazaki, D., Ikeshima, D., Tawatari, R., Yamaguchi, T. O'Loughlin, F., Neal, J.C., Sampson, C.C., Kanae, C., Bates, P.D., 2017. MERIT DEM: Multi-Error-Removed Improved-Terrain DEM [WWW Document]. Geophys. Res. Lett. vol.44. https://doi.org/10.1002/2017GL072874

Yarbrough, L.D., Easson, G., Kuszmaul, J.S., 2005. Using at-sensor radiance and reflectance Tasseled Cap transforms applied to change detection for the ASTER sensor. Proc. Third Int. Work. Anal. Multi-Temporal Remote Sens. Images 2005 2005, 141–145. https://doi.org/10.1109/AMTRSI.2005.1469857

Yesou, H., Andreoli, R., Fellah, K., Tholey, N., Clandillon, S., Bastiton, S., Allenbach, B., Meyer, C., Bestault, C., Fraipont, P., 2007. Large plain flood mapping and monitoring based on EO data. IGARRSS. https://doi.org/10.1109/IGARSS.2007.4423008

Zhai, K., Wu, X., Qin, Y., Du, P., 2015. Comparison of surface water extraction performances of different classic water indices using OLI and TM imageries in different situations. Geo-Spatial Inf. Sci. 18, 32–42. https://doi.org/10.1080/10095020.2015.1017911

Zhou, Y., Dong, J., Xiao, X., Xiao, T., Yang, Z., Zhao, G., Zou, Z., Qin, Y., 2017. Open surface water mapping algorithms: A comparison of water-related spectral indices and sensors. Water (Switzerland) 9. https://doi.org/10.3390/w9040256

Zhu, Z., Woodcock, C.E., 2012. Remote Sensing of Environment Object-based cloud and cloud shadow detection in Landsat imagery. Remote Sens. Environ. 118, 83–94. https://doi.org/10.1016/j.rse.2011.10.028

Chapter 4:
A NEW METHOD (MINDED-BA) FOR AUTOMATIC DETECTION OF BURNED AREAS USING REMOTE SENSING DATA

Abstract: This work presents a change detection method (MINDED-BA) for determining burned extents from multispectral remote sensing imagery. It consists in the development of a previous model (MINDED), originally created to estimate flood extents, combining a multi-index image differencing approach and the analysis of magnitudes of the image differencing statistics. The method was implemented, using Landsat data, to estimate yearly-burn extents within a study area located on northwest central Portugal, from 2000-2018. The modelling workflow includes several innovations, like preprocessing steps to adress some of the most important sources of error mentioned in the literature, and an optimal bin number selection procedure, the latter being the basis for the threshold selection for the classification of burn-related changes. The results of the model have been compared to an official yearly-burn extent database and allow verifying the significant improvements introduced by both the pre-processing procedures and the multi-index approach. The high overall accuracies of the model and its levels of automatization (thanks to an open-source Python script) indicates potential of being a reliable method for systematic unsupervised classification of burned areas.

Keywords: optical multispectral imagery; Landsat; digital change detection; multi-index; univariate image differencing; threshold selection; wildfires; image histogram binning; highly reflective surfaces; Portugal**.**

1. Introduction

Fire has played an important role throughout human history, allowing men to transform ecosystems worldwide (Chuvieco et al., 2014). Wildfires can be described has biomass burning, with potential impacts on human life, property and ecosystems (Chuvieco et al., 2014).

Remote Sensing (RS) methods have been widely applied to incorporate data in fire risk assessment studies. The application of RS methods usually falls into three categories: forecasting systems that predict favourable conditions before fire occurrences; monitoring systems for active fire detection; and monitoring of post-fire conditions, such as burned extent (e.g., burn scar maps) or fire severity (Abdollahi et al., 2018; Leblon et al., 2016).

Wildfire forecasting systems usually focus on addressing probabilities of ignition and propagation (see Section 4.1.1 of Chapter 2). Such models often combine dynamic variables (e.g., wind, temperature, or moisture) and static variables (e.g., slope, land cover or proximity to specific features), which may be derived from RS techniques (Adab et al., 2015; Liu et al., 2016a).

The detection of active fires through RS can be inferred from thermal anomalies, which may be detected from multiple sensors (e.g., MODIS, VIIRS, Landsat series). Rapid Burned area estimations may be obtained from short-revisiting time sensors, although such higher temporal resolutions usually come at the detriment of decreased spatial resolutions (e.g., Matin et al., 2017; Schroeder et al., 2016; Vilar et al., 2015b).

Multispectral indices obtained from optical sensors are amongst the most widely used to obtain variables to evaluate fire hazard (using time series) and to monitor fire-induced changes on vegetation, including burn severity and regeneration (Emilio Chuvieco et al., 2002; Kavzoglu et al., 2014). Such indices, which may, or may not have been developed specifically for the identification of burned areas, often result from a combination of two or more bands, from visible to short-wave infrared ranges (Bastarrika et al., 2011) (some examples are included in Table 4.1). Such combinations include Visible (VIS) and Near Infrared (NIR) couples, e.g., the Burned Area Index (BAI) (Emilio Chuvieco et al., 2002) which has been developed specifically for burned area discrimination, or the Normalized Difference Vegetation Index (NDVI) (Rouse et al., 1973; Satir et al., 2016) and the Normalized Difference Water Index (NDWI) (McFeeters, 1996; Satir et al., 2016). Other combinations consist in grouping Short Wave Infrared (SWIRs) (such as the SWIR1 bands from Landsat sensors) with VIS or NIR bands, e.g., the improved version of BAI (BAIMs) (Martin 2006), or the Normalized Burn Ratio (NBRs) (Key and Benson 1999), the latter allowing discriminating different levels of fire severity. Finally. Finally, other indices include longer short wave infrared bands (SWIRl) (such as the SWIR2 from Landsat sensors), e.g., the alternative versions of both BAI (BAIMl) and NBR (NBRl), the Mid Infrared Burned Index (MIRBI) (Trigg and Flasse, 2001), or the Normalized Burned Ratio 2 (NBR2) combining both SWIRs and SWIRl (USGS, 2020b).

Multispectral indices can be used for uni-temporal classifications (post-fire) or bi-temporal (pre to post fire difference) approaches (Escuin et al., 2008; Kavzoglu et al., 2014). Among bi-temporal change detections, the Differenced Normalized Burn Ratio (dNBR) is among those with the best performances (Sahana and Ganaie, 2017), demonstrating significant correlations with field measurements using images captured within ca.30 days after fire events (Parker et al., 2015). However, as with other indices, it shows poor discrimination between burned areas and other surfaces, such as water, bare soil or areas with little vegetation (Escuin et al., 2008). According to Bastarrika et al. (2011), the use of indices including SWIRs and SWIRl, has demonstrated to mitigate errors, particularly commission errors, such as false assignments of clouds, cloud shadows, topographic shadows and water. Such improvements have been explained by the distinctive spectral signatures of water and burned areas beyond the NIR region, where water tends to absorb longer wavelengths almost completely, while burned forest reflectance remains fairly constant or with a slightly growing trend (e.g., Pereira et al., 1999).

Table 4.1- Burned related Indices (BrI) and corresponding formulas.

Name	Equation	Reference
NDVI	$NDVI = \frac{NIR-Red}{NIR+Red}$ (1)	(Rouse et al., 1973)
NDWI	$NDWI = \frac{Green-SWIRs}{Green+SWIRs}$ (2)	(McFeeters, 1996)
NBRs	$NBRs = \frac{NIR-SWIRs}{NIR+SWIRs}$ (3)	(Key and Benson, 1999)
NBRl	$NBRl = \frac{NIR-SWIRl}{NIR+SWIRl}$ (4)	(Key and Benson, 1999)
NBR2	$NBR2 = \frac{SWIRs-SWIRl}{SWIRs+SWIRl}$ (5)	(USGS, 2020b)
MIRBI	$MIRBI = 10SWIRl + 2 - 9.8SWIRs$ (6)	(Trigg and Flasse, 2001)
BAI	$BAI = \frac{1}{(0.1-Red)^2+(0.6-NIR)^2}$ (7)	(E. Chuvieco et al., 2002)
BAIMs	$BAIMs = \frac{1}{(0.05-NIR)^2+(0.2-SWIRs)^2}$ (8)	(Martín et al., 2006)
BAIMl	$BAIMl = \frac{1}{(0.05-NIR)^2+(0.2-SWIRl)^2}$ (9)	(Martín et al., 2006)

The extraction of thematic information from spectral indices is usually carried out using one or more thresholds, which may be used to define two or more classes (density slicing) (Campbell and Wynne, 2011; Lillesand et al., 2015; Singh, 1989). However, as with any spectral index, finding optimal thresholds is often a difficult task, since they are usually scene-dependent (Cenci et al., 2017b; Oliveira et al., 2019). Besides, the characteristics and spectral reflectance of burned areas may also be highly variable, depending on fire severity, or the density of pre-fire vegetation (E. Chuvieco et al., 2002; de Luca et al., 2021).

One of the main objectives of this study is to develop and implement a method based on satellite RS imagery and GIS techniques, using an integrated multi-index image differencing approach aimed at determining burned areas, representing an advancement in respect to the applications of the single indices listed in Table 1. The method develops from the work of Oliveira et al. (2019) and it consists on the analysis of the distribution of a set of index differencing statistics, as well as the combination of different single-index classifications by means of a spatial majority analysis. The method was implemented in a fully automatic procedure and tested for a study area in north-western Portugal.

2. Methods

The method developed in this study consists of an adaptation of the Multi-INDEx Differencing (MINDED) method (Oliveira et al., 2019), which has been originally developed to estimate flood extents. For this work, we have incorporated the same methodological principles, yet with a different purpose: the detection of burned areas. The assembly the Multi-INDEx Differencing method for Burned Areas (MINDED-BA) follows the workflow illustrated in Figure 4.1, incorporating Burned related Indices (BrI). Non-normalized indices introduce data magnitude disparities, which may be exacerbated both in multitemporal analysis contexts and by mathematical derivative operations, potentially requiring additional computational processing and leading to threshold selection issues (Oliveira et al., 2019; Zongyi Ma et al., 2011). For these reasons, we decided to implement the MINDED-BA by using the following normalized indices: NBRs, NBRl, NBR2, NDVI and NDWI.

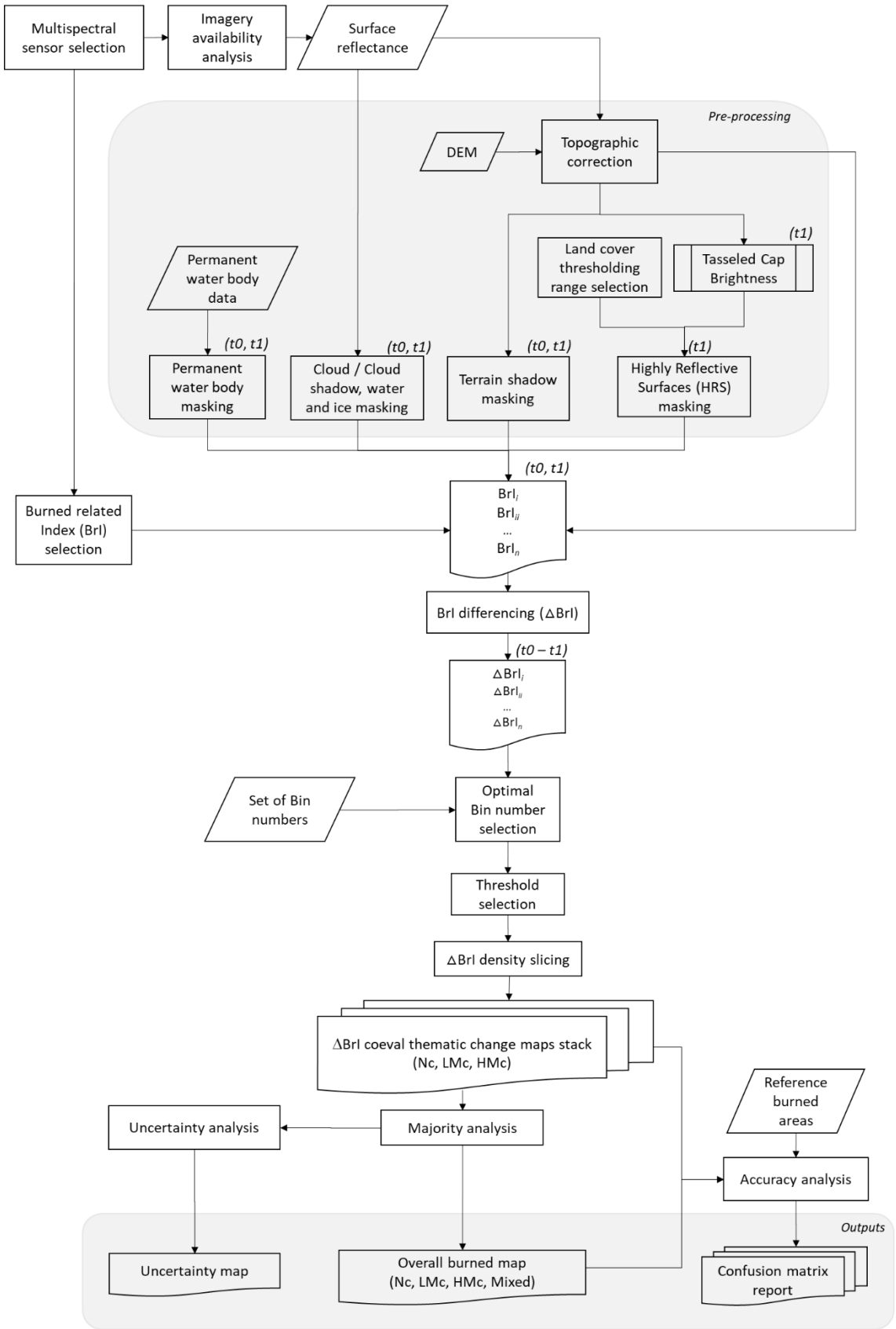

Figure 4.1 – The Multi-Index Differencing method for Burned Areas (MINDED-BA) workflow (adapted from (Oliveira et al., 2019).

Given the specificities of MINDED-BA, particular considerations should be drawn for defining the requirements of the satellite images dataset. Firstly, we should perform an analysis to identify the typical fire season period of the study area. In the case of the study area selected to test MINDED-BA (north-western Portugal), the temperate Mediterranean climate fire season spreads from boreal spring to late boreal summer, particularly during the highest temperature months (i.e., July, August and September) (EEA, 2010). This means that the estimation of yearly burned extents, may be assumed to be detectable from images acquired prior (*t0*) and after (*t1*) each year fire season. Moreover, in order to minimize false change detections associated with different phenological cycle stages, *t0* may be acquired after the end of the previous fire season. This also means that, in a context of a multi-year analysis, every *t1* scene may be used as *t0* for the following year. The calculation of the BrI should be performed using surface reflectance values, which may be readily available for some kinds of sensors (e.g., Landsat series Level 2). Another important issue is to address either *t0* or t1 conditions which may result in false detection of burned areas. These might include the occurrence of features such as clouds, cloud shadows, topographic shadows, as well as water-related changes (e.g., surface water bodies, soil and vegetation water content). Ideally, to minimize such errors, images should include none of these cases. In practice, additional conventional pre-processing steps may be performed in order to minimize the effects of the above conditions (e.g., Hantson and Chuvieco, 2011; Hughes and Hayes, 2014; Ihlen and USGS, 2019; Schowengerdt, 2007; Song et al., 2001; U.S. Geological Survey, 2019a; Zhu and Woodcock, 2012). Moreover, certain land cover changes (e.g., conversion and/or modifications due to clear-cuts, cropland harvesting or other soil mobilization practices) may produce index-differencing results similar to those from burning. In order to address these cases, specific pre-processing analyses should be performed using remote sensing techniques or other GIS operations based on ancillary information. These analyses represent one of the focuses of the methods developed in this research, and they will be later addressed in Section 4.2.

After the pre-processing phase, the following step of MINDED-BA is to calculate every BrI. This task should be performed (e.g., using the equations of Table 4.1) for both *t0* and *t1*.

Then, each corresponding ΔBrI may be calculated using Eq. 10:

$$\Delta BrI = BrI_{t0} - BrI_{t1} \quad (10)$$

Considering each BrI specific spectral reflectance bands and the arrangement of Eq.10 (i.e., with *t0* as the minuend and *t1* as the subtrahend), the following task is to identify the range of values of ΔBrI which are expected to correspond to burn-related changes. For example,

considering NDVI, burned areas are usually found as negative and near-zero values, while green vigorous vegetation is characterized by positive values. Hence, according to Eq.10, those changes from green vegetation to burned result in positive ΔNDVI values. In fact, every other BrI considered in this study performs in a similar way, with recently burned areas corresponding to positive ΔBrI values, whereas longer-term post-fire vegetation regrowth areas are detected as negative values (e.g., Keeley, 2009).

Then, thematic classification of changes are obtained applying thresholding techniques to every ΔBrI. To this aim, we considered an analogous procedure to (Oliveira et al., 2019), consisting in analysing each ΔBrI data distribution function (*f*), and corresponding first and second-order derivative functions, *d1f* and *d2f* respectively. Whenever the shape of *f* allows separating no-changes to changes (multi-modal shaped functions), thresholds may be directly extracted from this distribution curve. In practice, depending on how much gradual is the transition between no-change to change conditions, this threshold has to be estimated using either *d1f* or *d2f*.

Similarly to Oliveira et al. (2019), we also chose to select two thresholds, T1 and T2, to obtain two classes of magnitude of change, Low Magnitude Change (LMc) and High Magnitude Change (HMc).). With this, we expect to respectively detect respectively light burning conditions, such as partially burned canopy, or severe burning conditions, such as complete burning of initially vigorous green vegetation (e.g., forests with high leaf chlorophyll concentrations).

The MINDED-BA workflow continues with the combination of the coeval classifications obtained from the single ΔBrI images. Following the same procedures used with MINDED, we performed a spatial majority analysis, allowing us to obtain the overall burn classifications and to estimate uncertainties.

The final step of the model consists in quantifying accuracies, which may be performed by comparison with either ground truth data or reference ancillary spatial information. In the case of our study area, we compared the MINDED-BA outputs with the official dataset of yearly burned extents by Portugal's Institute for Nature Conservation and Forests (ICNF, 2020), which were used as our reference burned areas (RBA).

All the above steps of the MINDED-BA (Figure 4.1) were conceptualized also with the aim of developing a fully automatic processing tool for rapid and replicable extraction of burned areas from large multitemporal RS imagery datasets. The model was implemented a GRASSGIS Python

script, while the map outputs were obtained with QGIS, both being free and open-source software.

3. Study area

The study area considered in this study corresponds to the Aveiro Region, a set of 11 municipalities of the Baixo Vouga Sub region (NUTS III), located in the north-western part of continental Portugal (Figure 4.2). This region is characterized by a temperate Mediterranean climate under maritime influence (EEA, 2010).

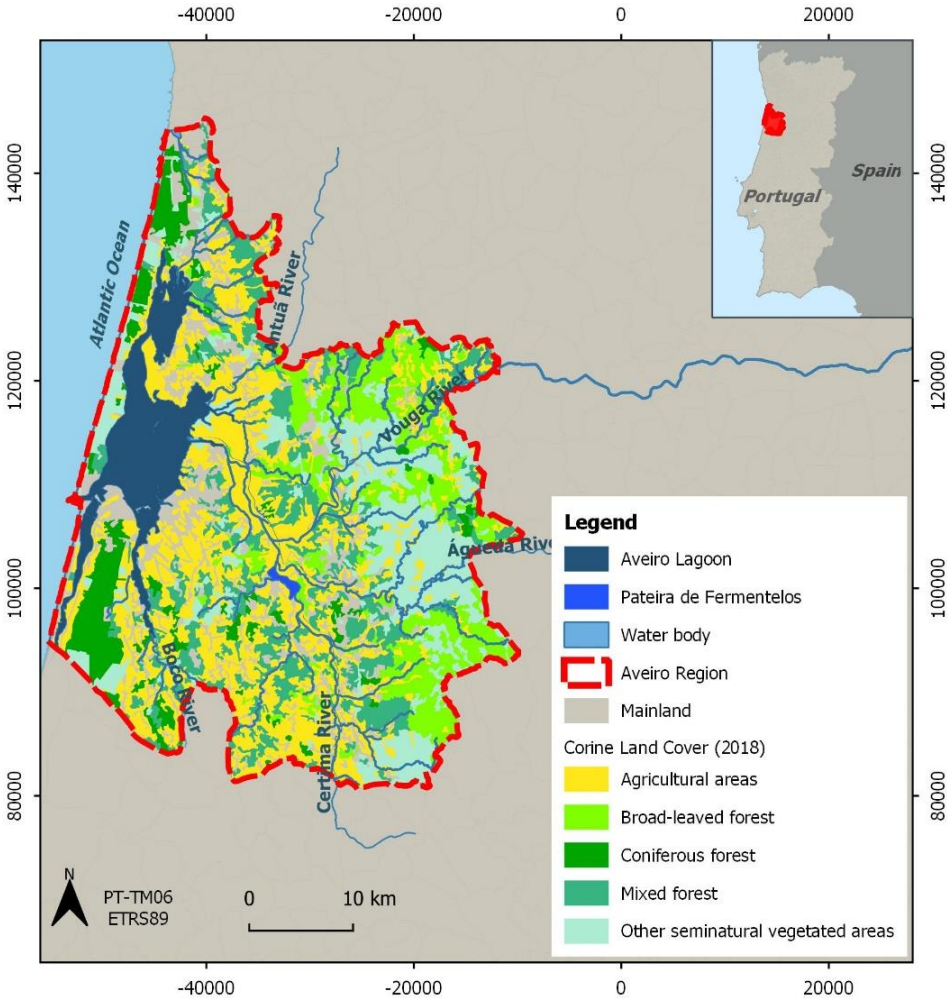

Figure 4.2 - Study area location map (Coordinate System: PT-TM06/ETRS89).

The total area covers about 169,286 ha, corresponding to the lower section of the Vouga River Watershed, which is the main freshwater inlet of a wide coastal lagoon, the Aveiro Lagoon. In Figure 4.2, we can identify other water bodies, including rivers and the Pateira de Fermentelos freshwater lagoon. The choice of this study area is justified by the recurrence of wildfires and

the coexistence of populated territory, along with several important ecological and socioeconomic resources (C. O. A. Coelho et al., 2007). Besides, the non-complex topography presents a favourable context for RS methods, such as the application of water-related indices (Oliveira et al., 2019). However, the wide extent and density of water bodies, wetlands and floodplains, represent an additional challenge to test the performance of a wildfire detection method such as MINDED-BA.

According to the Corine Land Cover survey from 2018, Forest and semi natural areas occupy 49% of the study area, consisting of Coniferous forest (13%), mostly *Pinus pinaster* concentrated in flat coastal municipalities, Broadleaved forest (26%), mostly of *Eucalyptus globulus* stands located to the more inland and hilly municipalities, and Mixed forest (30%). Regarding Agricultural areas, they occupy 29% of the study area, among which Permanently irrigated land is the most representative land cover class (27%). According to the Regional Forest Plan (National Ordinance n. 58/2019 of February 11), climate change scenarios confirm the tendency for increasing forest fire factors (ICNF, 2019).

4. Results

4.1. Satellite data selection

According to the above-described methodological principles of MINDED-BA, the main input of the method consists in multispectral satellite data acquired after the end of each fire season. We used the USGS EarthExplorer portal (USGS, 2020a) to search and select multispectral data from the Landsat (LS) series. Nevertheless, the MINDED-BA may be implemented considering any other optical multispectral sensors, for either *t0* or *t1*. In order to analyse the yearly-burned extents of our study area from 2000 to 2018, we have selected the multispectral images listed in Table 4.2. This list also includes one image from 1999, which has been used as *t0* for determining the annually burned extent of the year 2000. . As introduced in Section 2, each *t1* has been used as *t0* for the following reference year, which also allowed to facilitate the implementation of the Python script and reduced both computing storage and processing time. Considering the requirements to calculate each BrI, the multispectral data used as input for MINDED-BA have to correspond to surface reflectance values. For this research, we decided to use Landsat Collection 1 Level-2 products. In addition, to mitigate the adverse effects of non-burn related changes, our imagery dataset was generally chosen from autumn-winter periods, preferably during low cloud cover and non-flooded conditions.

Table 4.2– Landsat level-2 products selected for MINDED-BA (LS5 – Landsat 5; LS7 – Landsat 7; LS8 – Landsat 8).

Fire season - *t1* (year)	Image acquisition date	Sensor
1999	04/10/1999	LS5
2000	22/10/2000	LS5
2001	12/12/2001	LS5
2002	07/12/2002	LS7
2003	10/12/2003	LS7
2004	21/01/2005	LS5
2005	15/12/2005	LS7
2006	27/01/2007	LS5
2007	22/01/2008	LS7
2008	26/09/2008	LS5
2009	27/01/2010	LS7
2010	13/12/2010	LS7
2011	06/11/2011	LS5
2012	03/01/2013	LS7
2013	10/10/2013	LS8
2014	08/12/2014	LS7
2015	05/02/2016	LS8
2016	06/01/2017	LS8
2017	06/11/2017	LS8
2018	24/10/2018	LS8

4.2. Pre-processing

MINDED-BA is a change detection method that is susceptible to detect, as side effects, other types of change besides burning. As an index differencing based approach, the modal values of the data frequency functions are assumed to represent the condition of no-change, while different types of changes might be inferred depending on which side they are located in the frequency distribution curve (positive or negative sign). Even though MINDED-BA combines multiple indices, which are obtained from different spectral reflectance bands, other types of change (as those described in Section 2) may have the same sign of burned areas. If not addressed properly, these conditions will result in the occurrence of false positive errors. Pre-processing is therefore advised, which may be implemented from different types of data, including satellite imagery/products, ancillary geographic information, or reference literature values.

For this reason, we performed masking of clouds, cloud shadows, water and snow features using the 'pixel_qa' band of the Landsat level-2 products (U.S. Geological Survey, 2019a, 2019b).

Moreover, considering the susceptibility of permanent water bodies to produce false positive errors and the fact that their spatial position should be relatively stable and well known, we created an additional mask within a buffer of 30m around water bodies, using official thematic ancillary data (DGT, 2020).

Topographic corrections were performed for every spectral band, using the cosine method (Riaño et al., 2003; Schowengerdt, 2007). Firstly, an illumination model was created for each

scene, using the ALOSWorld 3D–30 m (AW3D30) Global DEM provided by the Japan Aerospace Exploitation Agency (JAXA, 2020), along with the sun elevation and azimuth acquisition conditions (according to the Landsat level-2 metadata). Secondly, we applied the illumination models of each scene, allowing to mask the shadowed areas, as well as to correct those original reflectance values for pixels directly illuminated from sunlight.

Both burned, bare soil, rock outcrops and artificial impervious areas are characterized by an absence of chlorophyll, which is otherwise present in green vegetation (Escuin et al., 2008). When comparing *t1* to *t0* images, any conversion towards the above-mentioned classes may result in false positive errors. For example, within the study area, corn is one of the most important agriculture crops, which during wintertime (i.e., for most of Table 4.2 scenes) may show a great variety of spectral signal reflectance, depending on different stages of growth, crop harvesting, or even soil mobilizations prior to new plantings. Some of these conditions result in the conversion of land cover from green vegetation to bare soil, which implies false positive errors. In order to mitigate these error conditions, we analysed the land cover spectral signatures literature, and we verified that, with the exception of NIR, the reflectance of burned areas, vegetation, wetlands and water is predominantly lower than other highly reflective surfaces (HRS), such as bare soil, rock outcrops and artificial impervious areas (e.g., Campbell and Wynne, 2011; Escuin et al., 2008; Lillesand et al., 2015; Pereira et al., 1999). With such considerations in mind, a thresholding range was determined from Pereira et al. (1999), with the objective of masking HRS in *t1*. However, since the original reference land cover values are given in top-of-atmosphere (TOA) reflectance, we determined the corresponding ground surface reflectance values, using the 22/10/2000 scene (Table 4.2). Both the TOA and surface reflectance were obtained from the image DN (Landsat 5 Level 1 and Level 2 respectively), using the band-specific factors provided in the metadata. Then, we sampled clusters of pixels within the range of TOA reflectance values, in order to calculate corresponding average TOA and surface reflectance, allowing determining their correlations and obtaining the surface reflectance signatures of the different land cover types (Figure 4.3). Considering the amplitude of the HRS masking thresholding range, which is maximum for bands TM2, TM3, TM5 and TM7, we integrated this multispectral information calculating the at-satellite Tasseled Cap Brightness (TCB) transformation based on these four bands only (Table 4.3). Different TCB values were calculated for a series of four increments of the thresholding range (M1-M4; Figure 4.3). Even though the diagram of Figure 4.3 refers to Landsat 5, we considered the same spectral signatures regardless the sensor, as these latter have a good spectral correspondence (e.g., Chander et al., 2013; Giuseppe Mancino, Agostino Ferrara, 2020). The four TCB increments were used to mask

the *t1* dataset. In principle, we expected M2 and M3 to maximize the separation between burned areas and HRS. However, as verified in Figure 4.4, in comparison to the false colour composite of Landsat 8 bands 654 (in RBG), we found M1 to produce slight improvements in masking HRS, without compromising the detection of burned areas, so justifying its use in the further steps of MINDED-BA

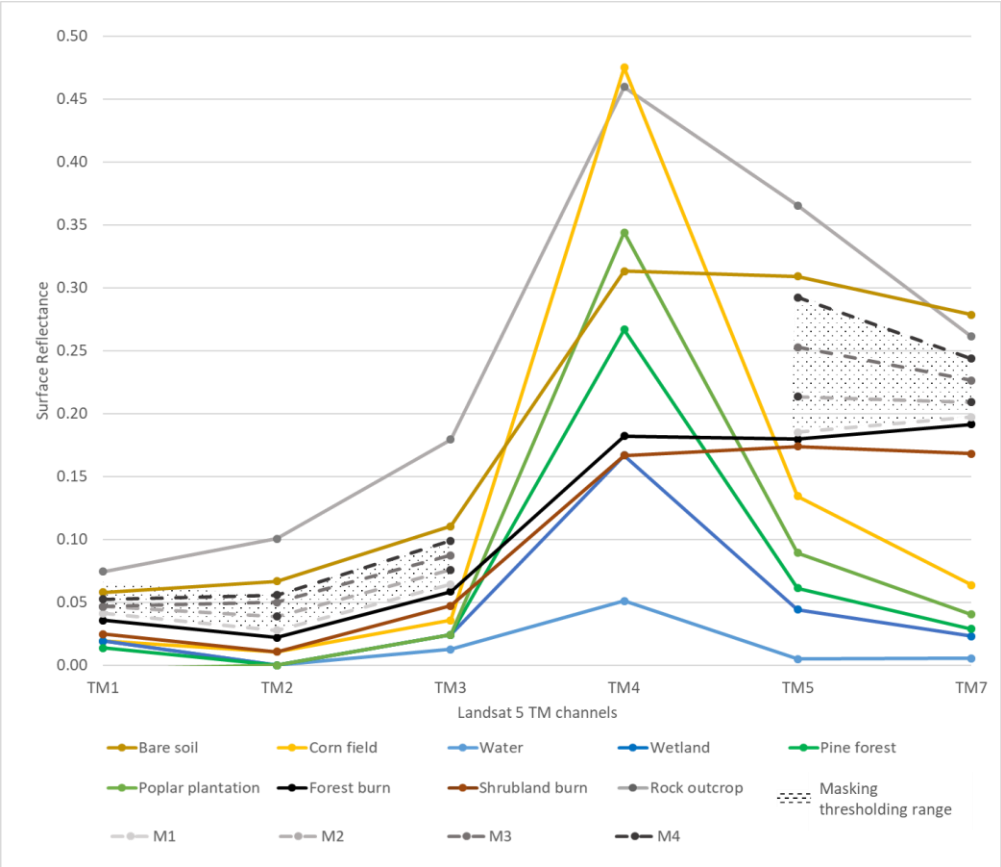

Figure 4.3 – Surface reflectance signatures of different land cover types and their correspondence to Landsat 5 TM (adapted from Pereira et al., 1999), along with different increments of a thresholding range (M1-M4) aimed for masking highly reflective surfaces (HRS).

Table 4.3 – Tasseled Cap Brightness (TCB) at-satellite reflectance coefficients for the red, swir1 and swir2 of Landsat sensors, along with the resulting TCB values for different increments of the thresholding range (M1-M4) for masking highly reflective surfaces (HRS).

Landsat sensor	Tasseled Cap Brightness (TCB) coefficients	Masking thresholds (TCB)			
		M1	M2	M3	M4
LS5 (TM)	0.4158 B2+0.5524 B3+0.3124 B5+0.2303 B7 [1]	0.1503	0.1728	0.2002	0.2252
LS7 (TM+)	0.3972 B2+0.3904 B3 + 0.2286 B5+ 0.1596 B7 [2]	0.1099	0.1272	0.1479	0.1664
LS8 (OLI)	0.278 B3+0.4733 B4 + 0.5080 B6+ 0.1872 B7 [3]	0.1692	0.1942	0.2261	0.2564

[1] Crist, 1985

[2] Huang et al., 2002

[3] Baig et al., 2014

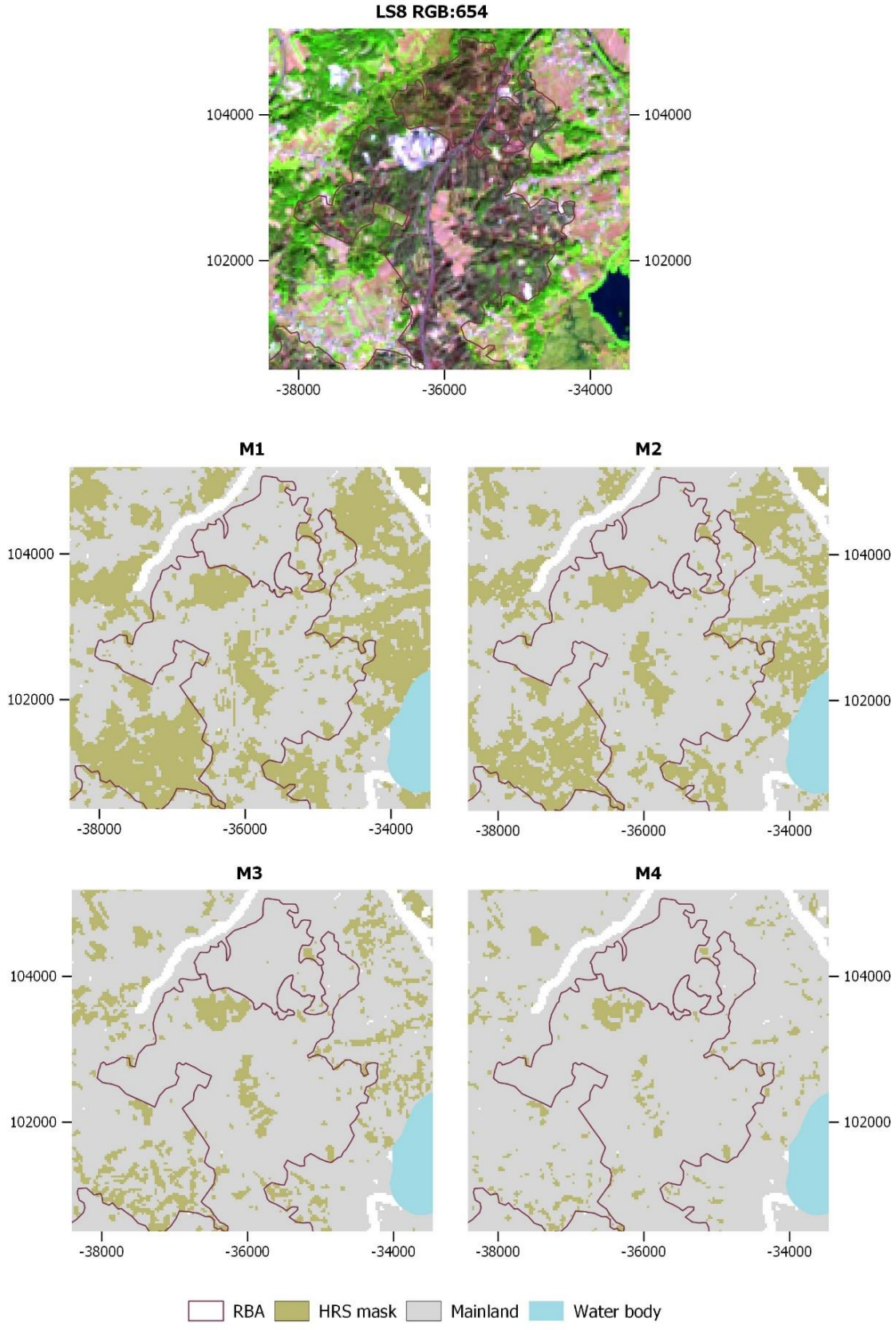

Figure 4.4 – Example of highly reflective surfaces (HRS) masks, obtained from different increments of the reference thresholding range (M1-M4, in Figure 4.3), compared to the corresponding false colour composite of a Landsat 8 OLI scene (from 06/11/2017) and the reference burned areas (RBA) (Coordinate System: PT-TM06/ETRS89).

4.3. Index calculation and differencing

After pre-processing every multispectral band, we calculated all BrI for each scene, i.e. for both *t0* and *t1*, using the equations of Table 4.1. As expected, the scale of results obtained ranges from -1 up to 1, as normalized indices (i.e., NBRs, NBRl, NBR2, NDVI and NDWI) were used.

Then, considering Equation 10, we calculated each ΔBrI, using the BrI values for *t0* and *t1*. As verified in the example of Figure 4.5, the scale of every ΔBrI ranges between -2 and 2.

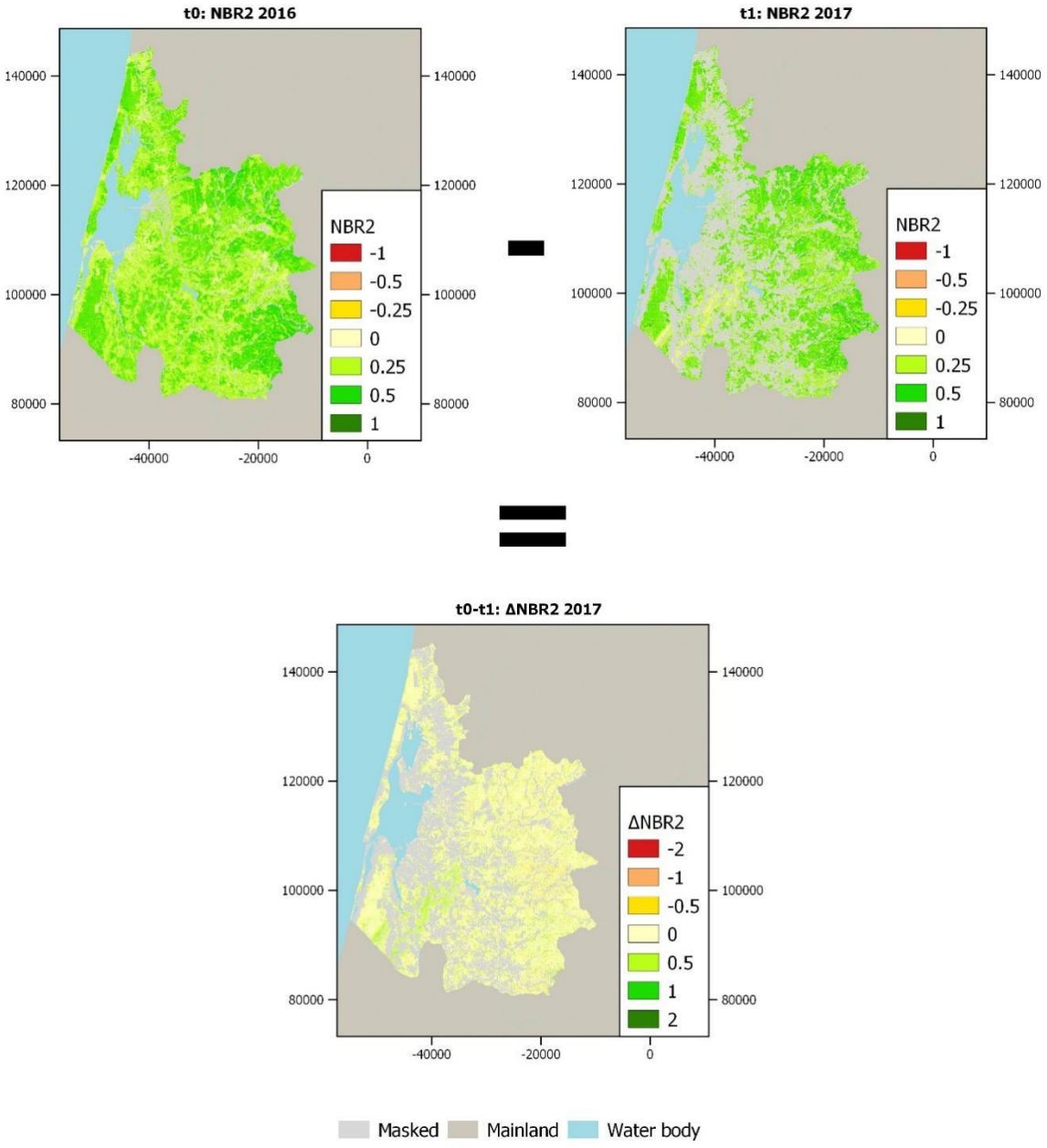

Figure 4.5 – Example of a single index differencing calculation, corresponding to the ΔNBR2 of the year 2017 (Coordinate System: PT-TM06/ETRS89).

4.3.1.Selection of optimal number of bins and threshold selection

For the threshold selection procedure of MINDED-BA, we calculated both first-order derivatives (*d1f*) and second-order derivatives (*d2f*) from the ΔBrI frequency distributions. The computational processing was performed considering the effect of data binning. In fact, we verified that by considering different binning intervals, we were experiencing significantly different results. Within a range of higher bins, we observed higher frequency oscillations, while, using smaller bins would substantially reduce this effect, until reaching a point where d1f and d2f start losing local extrema, consequently preventing any threshold selection. We also found that by using smoothing techniques based on mobile averaging (according to [30]), we could reduce local noise, but also reducing the overall signal of the functions. Besides, smoothing seemed to affect the shape of *d1f* and *d2f*, resulting in shifting of modal values in the horizontal axis, eventually causing the signal to become flat, which would have a negative effect in the threshold selection procedure. For these reasons, we developed a new approach to better address which number of bins would provide the best signal to noise combination, for both *d1f* and *d2f*.

We started by defining a representative set of numbers of bins to be analyzed. Equa-tion 11 allows extracting any amount (j) of numbers of bins (n) equally spaced in a base 10 logarithmic scale by a constant factor (a):

$$Bin_n = \begin{cases} 10^n, n = 1 \\ 10^{1+a(n-1)}, n \neq 1 \end{cases}, 1 \leq n \leq j, (j,n) \in \mathbb{N}, (a > 0) \in \mathbb{R} \quad (11)$$

Using Equation 11, we extracted a sample of 15 numbers of bins (i.e., *j*=15 and *n* from 1 to 15), equally spaced by a constant *a*=0.15, resulting in the following set: 10, 14, 20, 28, 40, 56, 79, 112, 158, 224, 316, 447, 631, 891, and 1259.

Afterwards, the optimal bin number selection was implemented for each ΔBrI *d1f* and *d2f*. This procedure was empirically performed considering Equation 12, which is based on the assumption that statistical noise is associated with erratic oscillations of these functions:

$$Bin\_ratio = \frac{total\_cs}{\#_{(>mv)}} \quad (12)$$

where $\#_{(>mv)}$ is the number of values of the variable greater than the modal value of the ΔBrI frequency distribution and *total_cs* is the total number of consecutive ΔBrI values with the same slope sign, including both consecutive positive and negative slopes. We calculated the *Bin_ratio* of Equation 12 for each number of bins of every ΔBrI *d1f* and *d2f*. The highest *Bin_ratio* is

assumed to correspond to the number of bins providing the optimal signal-to-noise combination.

Figure 4.6 illustrates an example of the *Bin_ratio* distribution of the *d1f* of every ΔBrI corresponding to the image difference of 2017. In this case, we verify that for every ΔBrI, an optimal number of bins may be selected corresponding to the modal value of the *Bin_ratio* distribution. We also found that the distribution functions achieve minimum stable values after ca. 447, further justifying the representability of both the selected sample size and numbers of bins.

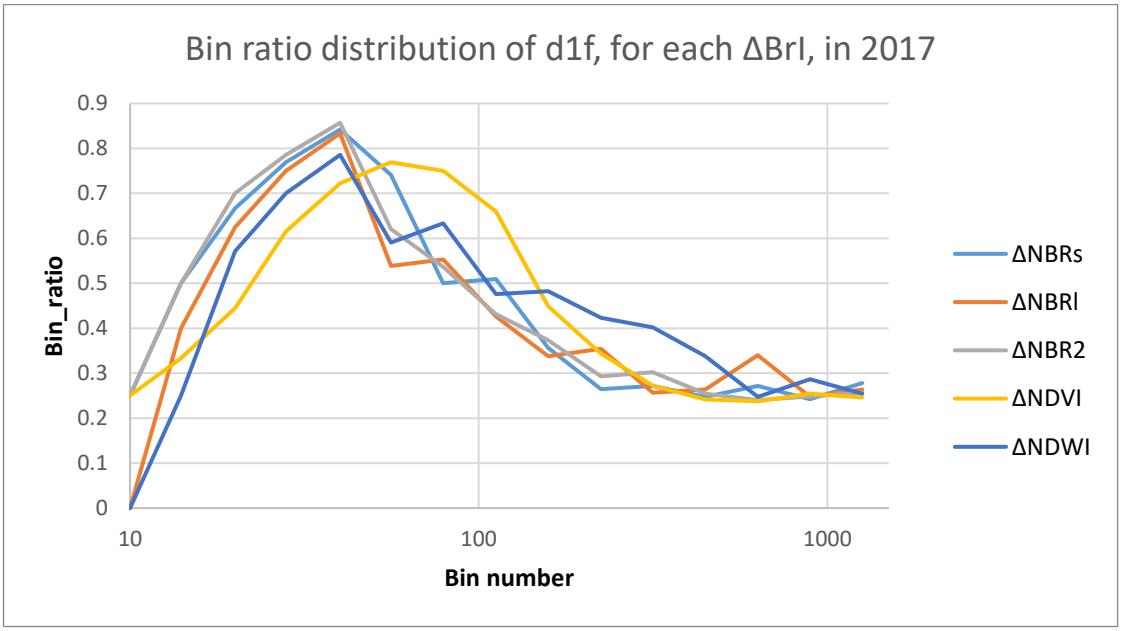

Figure 4.6 –Example of a Bin_ratio distribution of d1f, for each ΔBrI, in 2017.

The entire set of values for the optimal number of bins per year, ΔBrI and derivative order (*d1f* and *d2f*) is shown in Table 4.4. In Figure 4.7, the same data are represented as box-plot diagrams. We found the optimal number of bins to vary depending on the ΔBrI, derivative order, and scene. In general, the *d1f* of ΔNBRs appears to be less variable and, together with the ΔNDWI, is handled better with lower numbers of bins. For ΔNBR2 and ΔNDVI, the optimal numbers of bins of *d2f* are generally lower than those of *d1f*, with ΔNBR2 showing the highest variability for *d1f*. Despite having analyzed a wide range of numbers of bins (10-1259), we highlight that inter-quartile range of the entire set of optimal numbers of bins is concentrated into a very small range (28-56). This suggests the occurrence of a common tendency to stability of the optimal numbers of bins independently of the ΔBrI considered.

Table 4.4 – Optimal numbers of bins, for each ΔBrI d1f and d2f.

	df1					*df2*				
	ΔNBRs	**ΔNBRI**	**ΔNBR2**	**ΔNDVI**	**ΔNDWI**	**ΔNBRs**	**ΔNBRI**	**ΔNBR2**	**ΔNDVI**	**ΔNDWI**
2000	40	40	40	40	20	28	28	28	40	56
2001	40	40	14	40	56	40	28	20	28	40
2002	40	56	20	28	28	28	40	28	40	28
2003	40	40	28	40	40	28	40	28	28	28
2004	28	40	28	56	40	28	40	28	28	28
2005	40	56	28	56	28	28	28	28	40	28
2006	28	28	40	28	40	28	56	40	28	28
2007	28	40	56	40	28	28	40	40	28	28
2008	40	40	40	40	28	40	28	28	40	28
2009	40	40	20	40	28	40	28	28	40	56
2010	20	40	20	56	28	28	28	28	28	28
2011	40	56	56	40	28	28	28	56	40	28
2012	28	56	28	40	28	40	28	20	40	40
2013	40	40	79	56	79	40	28	56	40	20
2014	40	40	112	40	28	40	56	56	28	40
2015	40	40	79	56	28	28	28	56	28	28
2016	56	56	28	56	40	28	40	28	79	28
2017	40	40	40	56	40	28	40	40	40	40
2018	56	40	56	28	20	40	28	56	40	28
Average	38.1	43.6	42.7	44.0	34.5	32.4	34.7	36.4	37.0	33.1

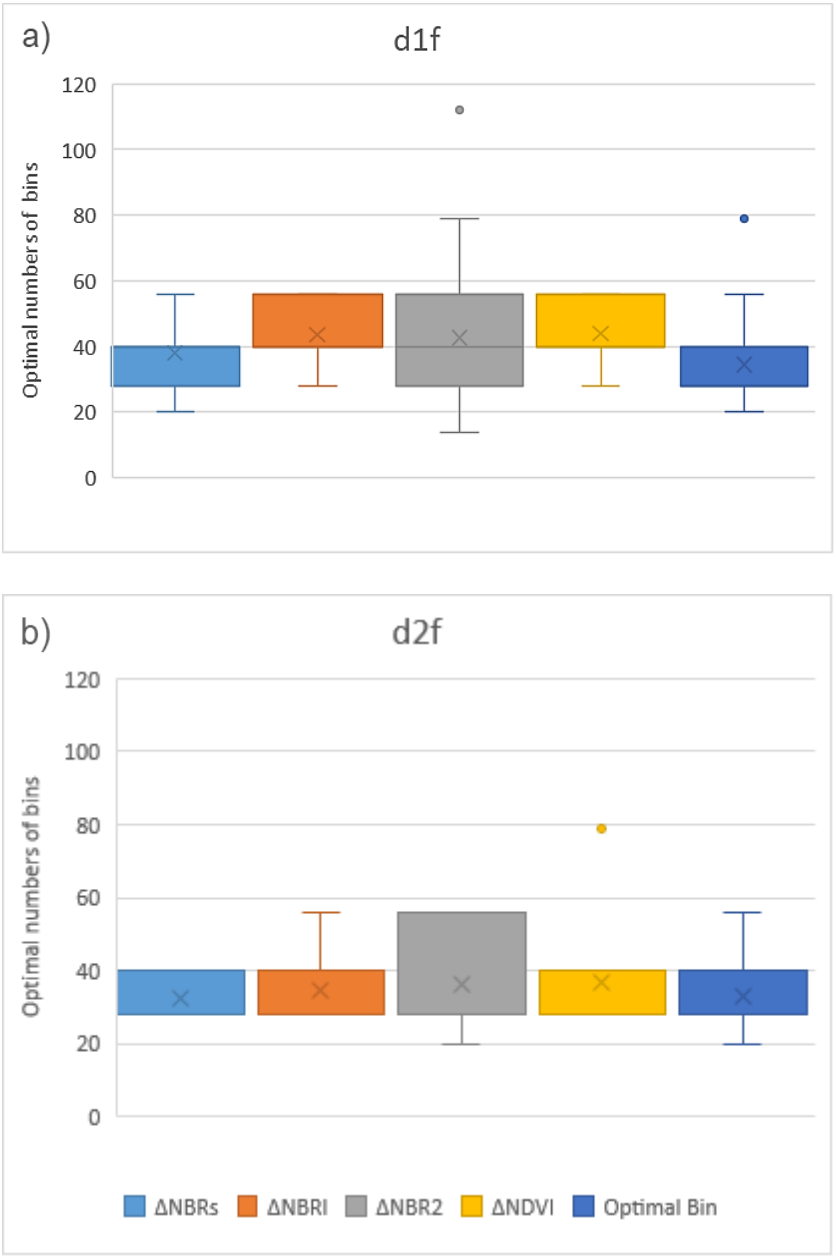

Figure 4.7 – Distribution of yearly optimal numbes of bins, per ΔBrI and derivative order: (a) d1f; (b) d2f.

Figure 4.8, illustrates the *d1f* and *d2f* functions obtained from different numbers of bins. This example corresponds to the ΔNBR2 of 2007, in which we can observe the optimal numbers of bins (i.e., 56 for *d1f* and 40 for *d2f*), alongside with other consecutive non-optimal values. Considering the example of Figure 4.8a, where thresholds may be identified as changes to positive *d1f* values, the representation for 79 bins seems to have the highest apparent signal, as the result of a lower compression of the ΔNBR2 frequency statistics. However, it also shows the highest oscillations, compared to other representations implying the detection of additional thresholds with lower ΔNBR2 values. The latter would potentially lead to increase false positive

detection (overestimation of changes). Also, in Figure 4.8a, due to the downsampling effect of numbers of bins 28 and 40, no thresholds could be extracted from *d1f,* which would potentially increase false negative errors (underestimation of changes). Regarding Figure 4.8b, where thresholds correspond to local maximums after a change to positive *d2f*, we also verify that higher bin numbers imply lower threshold values. However, higher numbers of bins also increase local noise, increasing the number of local maximums and consequent thresholds (e.g., 79 numbers of bins from ΔNBR2 0.4 to 0.9). In both cases, the optimal numbers of bins seem to provide the best apparent compromise between signal and noise.

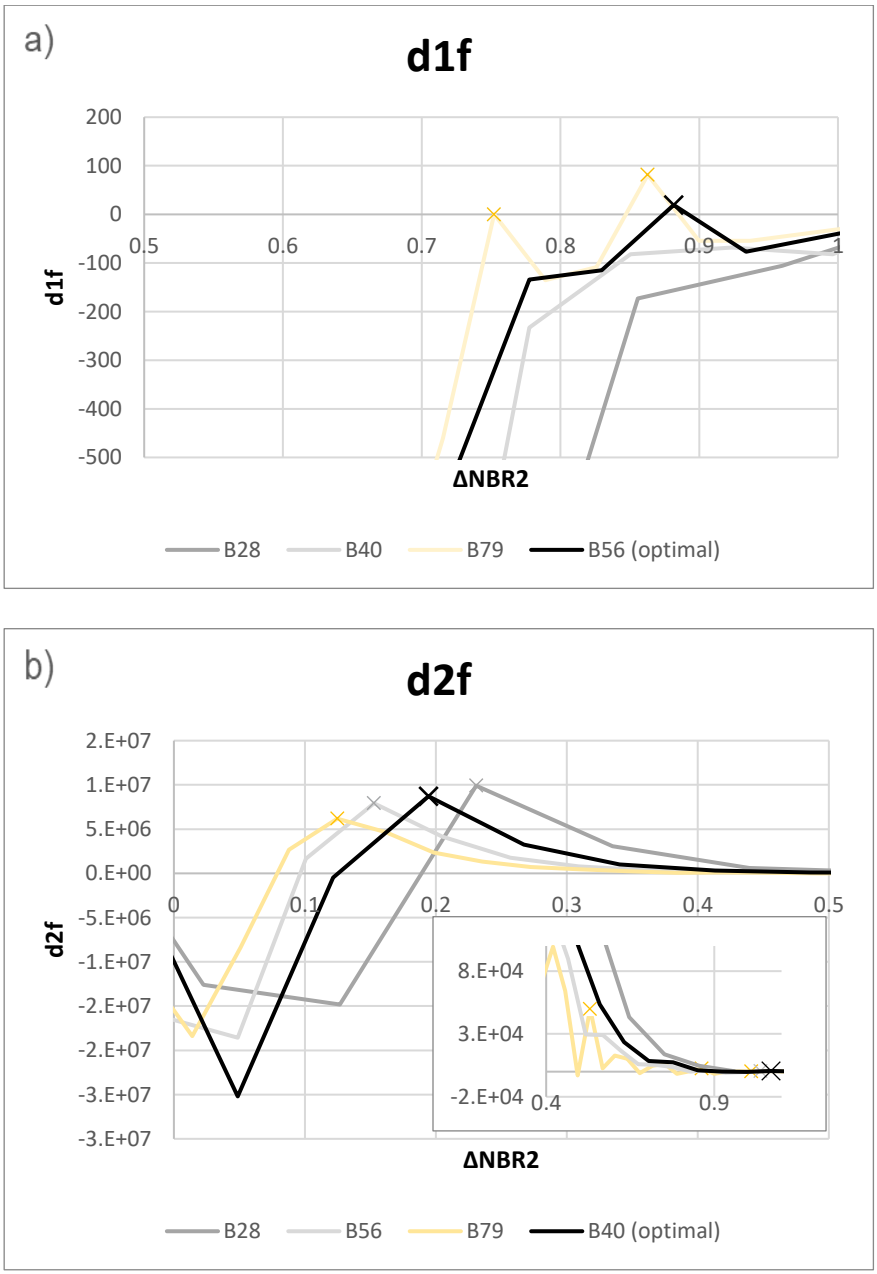

Figure 4.8 – Comparative example of different statistical data binning intervals of ΔNBR2 from 2007, with the corresponding thresholds (×) for d1f (a) and d2f (b).

The thresholds extracted from each optimal number of bins are listed in Table 4.5 and represented in Figure 4.9 as box-plot diagrams. For the threshold selection we chose the lowest threshold values, for *T1* and *T2,* independently of *d1f* and *d2f*. In some cases, only one threshold could be extracted, while in others, more than two thresholds could be found. This means that, in the example of Figure 4.8, *T1* was obtained by *d2f* (0.19), while *T2* by *d1f* (0.88). Table 4.5 and Figure 4.9 show that *T1* values are less variable in comparison to *T2*, with the exception of ΔNDVI, which are distributed in equivalent short ranges. Besides, the ΔNDVI T2 values are also significantly lower than the remaining ΔBrI. The ΔNDWI was among the most variable, for both *T1* and *T2*.

Table 4.5 –Thresholds T1 and T2 (if any), obtained from each ΔBrI.

	ΔNBRs		**ΔNBRl**		**ΔNBR2**		**ΔNDVI**		**ΔNDWI**	
	T1	**T2**	**T1**	**T2**	**T1**	**T2**	**T1**	**T2**	**T1**	**T2**
2000	0.09	0.56	0.14	-	0.20	-	0.11	-	0.06	0.50
2001	0.10	0.63	0.21	0.97	0.34	-	0.14	-	0.22	-
2002	0.16	-	0.24	0.90	0.27	-	0.09	0.45	0.23	-
2003	0.14	-	0.16	0.77	0.25	1.13	0.16	-	0.17	-
2004	0.30	-	0.33	0.94	0.31	-	0.20	-	0.43	-
2005	0.22	0.85	0.31	0.60	0.25	-	0.14	0.43	0.19	-
2006	0.22	0.89	0.20	0.66	0.19	0.96	0.17	-	0.34	-
2007	0.10	0.63	0.16	0.86	0.19	0.88	0.21	-	0.04	-
2008	0.24	0.48	0.33	-	0.24	-	0.10	0.42	0.45	-
2009	0.10	0.35	0.12	-	0.19	0.88	0.12	0.43	0.08	0.52
2010	0.12	-	0.21	-	0.22	1.07	0.21	-	0.15	-
2011	0.21	-	0.24	-	0.23	-	0.09	0.48	0.36	-
2012	0.11	0.56	0.18	0.66	0.26	-	0.06	-	0.18	0.71
2013	0.27	0.84	0.37	-	0.22	0.46	0.12	0.40	0.37	0.97
2014	0.05	0.60	0.08	0.56	0.12	0.40	0.15	-	0.09	-
2015	0.28	-	0.29	-	0.20	0.73	0.17	-	0.36	1.05
2016	0.06	0.19	0.10	0.75	0.09	0.72	0.05	0.50	0.20	-
2017	0.33	0.77	0.21	0.74	0.16	0.92	0.16	0.47	0.15	-
2018	0.15	0.82	0.17	-	0.11	0.50	0.11	0.49	0.13	0.93

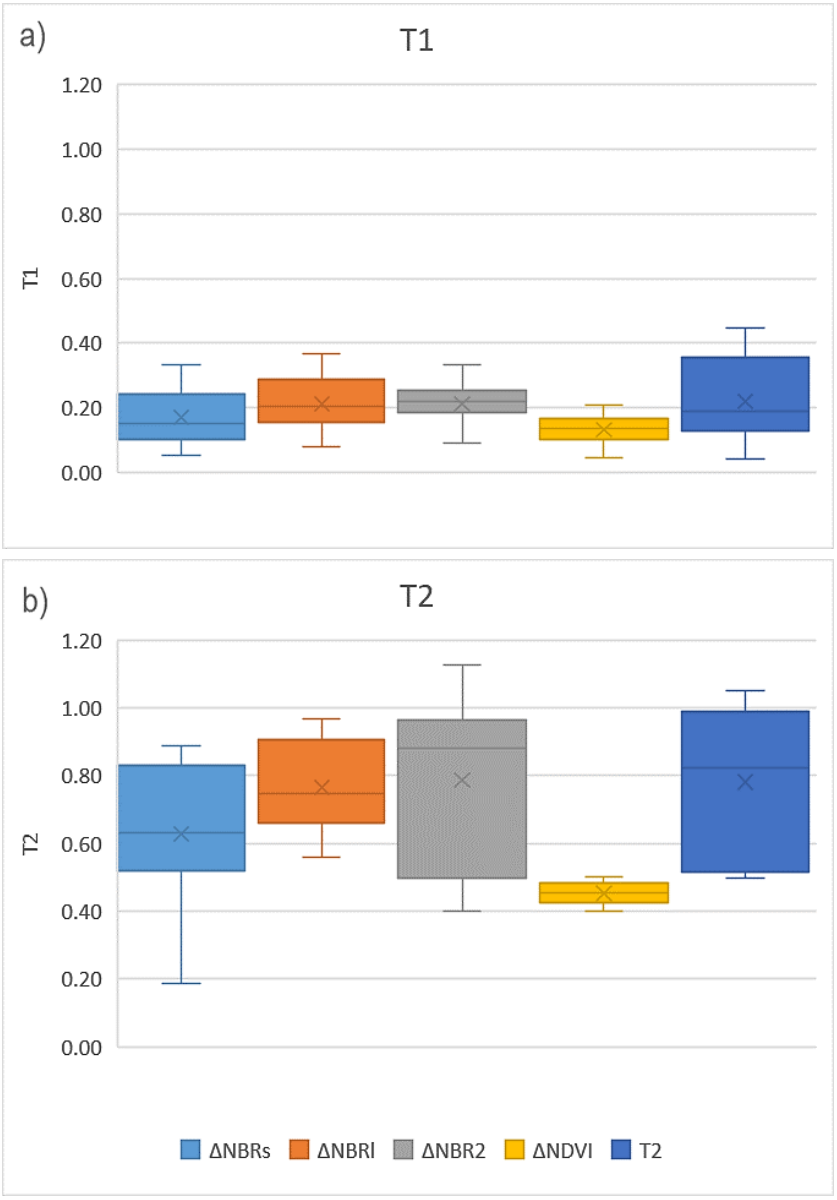

Figure 4.9 – Distribution of the thresholds obtained for each ΔBrI: (a) T1; (b) T2 (if any).

4.3.2.Single ΔBrI results

After extracting one or two thresholds for each ΔBrI, we performed density slicing to classify different burned related change magnitudes, which are summarized in Table 4.6. Following the approach of (Oliveira et al., 2019), every pixel lower than *T1* was classified as No change (Nc). Those in between *T1* and *T2* were classified as Low Magnitude change (LMc), while pixels above *T2* were classified as High Magnitude change (HMc). From Table 4.6, we can verify the consistency of Nc areas as the clear majority, followed by LMc areas, and finally HMc areas, the latter being always dependent on the detection of a *T2*.

The yearly burn-related maps from each ΔBrI are exemplified in Figure 4.10, for 2006 and 2016, where the single index classifications are compared to the RBA (ICNF, 2020).

Table 4.6 – Summary of single ΔBrI results, given as area (in hectares,) for each class (Nc – No change; LMc – Low Magnitude change; HMc – High Magnitude change).

	ΔNBRs			ΔNBRl			ΔNBR2			ΔNDVI			ΔNDWI		
Year	**Nc**	**LMc**	**HMc**	**Nc**	**LMc**	**HMc**	**Nc**	**LMc**	**HMc**	**Nc**	**LMc**	**HMc**	**Nc**	**LMc**	**HMc**
2000	96 808	7 463	33	99 907	4 509	-	103 706	577	-	97 821	6 483	-	102 063	2 357	2
2001	86 634	10 534	19	91 396	4 624	1	94 736	1 279	-	90 757	6 492	-	96 001	1 186	-
2002	111 021	5 431	-	111 939	2 263	3	111 647	2 555	-	112 082	4 395	44	112 189	4 262	-
2003	112 256	5 838	-	110 062	5 061	2	112 376	2 751	3	113 760	4 373	-	113 439	4 655	-
2004	96 583	6 735	-	95 041	5 831	5	97 697	3 184	-	98 810	4 554	-	98 604	4 694	-
2005	84 091	7 736	26	85 004	3 411	2 142	85 706	4 848	-	82 453	7 832	1 768	91 206	629	-
2006	91 977	6 718	10	88 952	8 326	464	92 817	4 923	1	95 200	3 514	-	93 914	4 790	-
2007	86 524	6 971	14	88 631	4 547	0	90 837	2 339	1	89 682	3 832	-	92 397	1 111	-
2008	81 004	3 726	308	83 051	1 931	-	83 446	1 537	-	82 734	2 301	4	81 591	3 447	-
2009	87 619	7 898	871	87 989	7 986	-	94 680	1 291	3	88 142	8 019	256	94 586	1 801	1
2010	85 104	6 177	-	87 502	2 748	-	87 723	2 522	3	87 596	3 696	-	89 881	1 400	-
2011	86 086	9 829	-	86 266	8 867	-	90 874	4 256	-	86 598	9 310	137	89 617	6 298	-
2012	98 776	8 283	570	101 703	4 176	497	104 778	1 592	-	98 752	8 919	-	105 730	1 897	2
2013	77 805	8 076	134	80 015	4 774	-	77 684	6 777	321	78 779	6 208	319	80 392	5 442	170
2014	93 499	8 934	7	95 621	5 672	27	98 429	2 512	367	97 234	5 281	-	101 763	672	-
2015	96 771	4 487	-	95 594	4 553	-	93 186	6 949	0	98 529	2 792	-	96 918	4 300	24
2016	89 787	10 910	10 277	94 283	16 451	239	102 827	8 145	1	88 387	22 322	68	110 191	739	-
2017	85 835	6 853	298	77 007	14 692	1 287	78 300	14 677	9	81 918	9 378	131	89 001	3 945	-
2018	82 016	6 090	0	86 110	2 023	-	79 445	8 686	2	84 716	3 392	32	87 716	397	0
Average	91063.0	7299.5	661.4	91898.6	5918.3	245.7	93731.2	4284.2	37.5	92313.1	6478.6	145.2	96168.4	2843.3	10.5

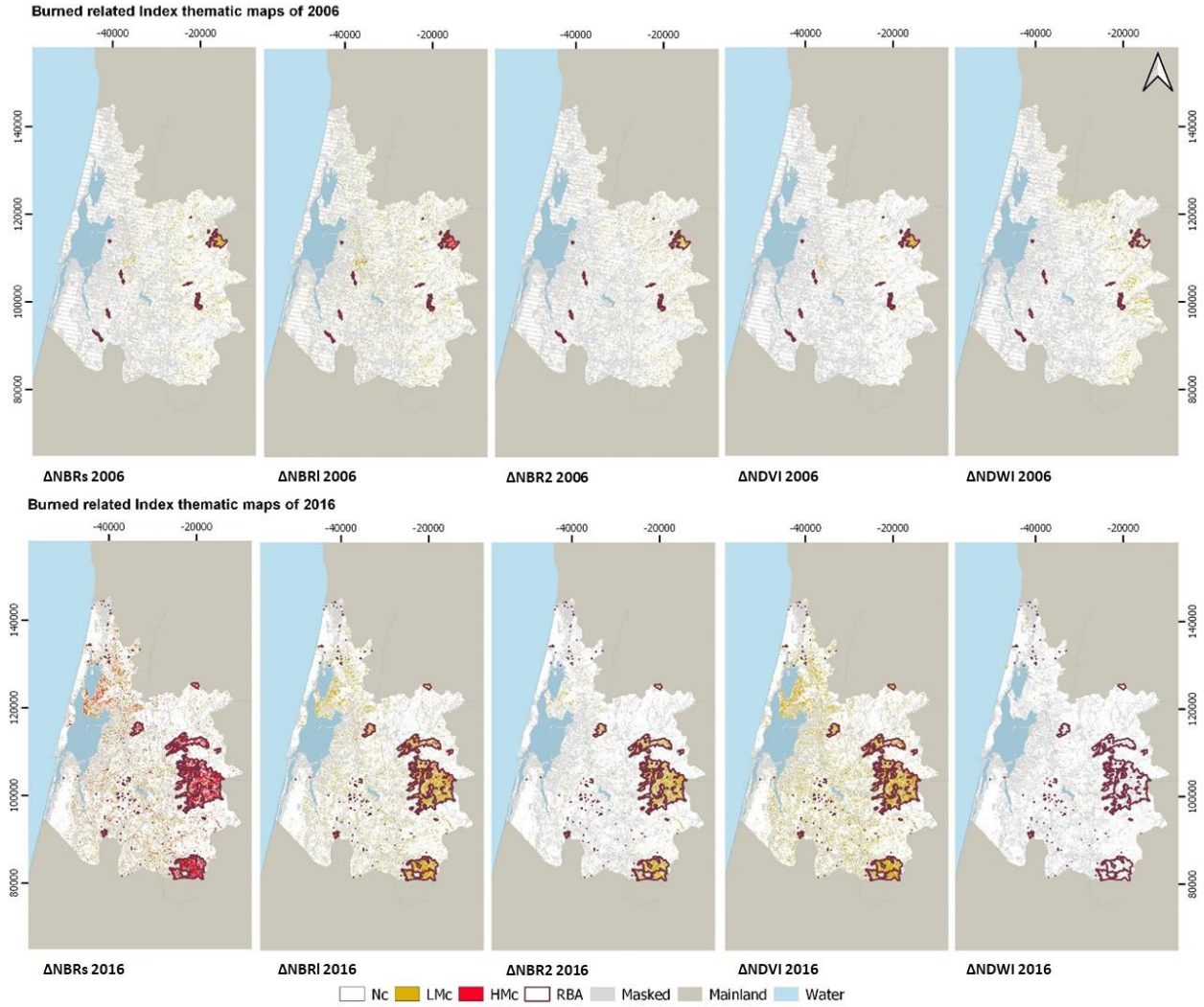

Figure 4.10 – Examples of coeval thematic maps from each ΔBrI, for 2006 and 2016, compared to the reference burned areas (RBA) (Coordinate System: PT-TM06/ETRS89).

From Table 4.6, we can verify that ΔNDWI tends to detect the least changes, both in terms of LMc and HMc areas. Moreover, and as verified in the examples of Figure 4.10, such changes tend to be clearly outside the limits of the RBA. Considering these discrepancies and the overall purpose of MINDED-BA, we decided to exclude ΔNDWI from further steps of the model. As for the remaining ΔBrI, we verify that ΔNBRs seems to be the most sensitive to detect both magnitudes of change, particularly in comparison to ΔNBR2. In Figure 4.10, most HMc areas were detected by ΔNBRs and ΔNBRl, with the clear majority occurring within the limits of the RBA. However, these same indices also seem to be more affected by image noise (i.e., apparently random distributed pixels), particularly for LMc areas. In 2006, several LMc pixels have been detected along the lower Vouga River by ΔNBRs, ΔNBRl and ΔNDVI. As for 2016, we also verify the occurrence of several change pixels outside the RBA (mostly LMc areas), which, based on visual inspection of imagery and ancillary data (EEA, 2020), are particularly incident in corn plantations, on the banks of the northern branch of the Aveiro Lagoon.

4.3.3.Combined overall burn maps

After performing density slicing for each ΔBrI, we combined the yearly classifications of ΔNBRs, ΔNBRl, ΔNBR2 and ΔNDVI through a majority analysis. This means that the overall burn maps classes Nc, LMc or HMc, were given whenever there was a majority among the coeval ΔBrI maps. For every non-majority combination, pixels were classified as 'Mixed'. Nevertheless, two particular conditions have been addressed. The first one corresponds to the case of 2LMc+2HMc coeval classifications, which were considered to likely describe burn related change, and therefore they were classified as LMc areas. The second condition corresponds to 2Nc+LMc+HMc. Despite the relative majority of Nc class, these were classified as Mixed, as the overall combination consists in a tie between no-change and change.

The overall results from the majority analysis procedure are shown in Table 4.7. In general, we observe Nc to be the most representative class (mostly above 90%), while HMc areas are the clear minority. LMc areas tend to be the second largest, which are sporadically exceeded by the Mixed class. From this entire set, 2016 was the year with the largest changes, particularly LMc areas, followed by 2017 and 2011. In contrast with the above results, we observe that Mixed areas remain relatively constant throughout the entire dataset, never exceeding 5% of the overall area.

Table 4.7 – Overall burn maps results, from 2000 to 2018.

year	Nc		LMc		HMc		Mixed	
	area (ha)	%	area (ha)	%	area (ha)	%	area (ha)	%
2000	98621	94.6	3645	3.5	-	0.0	2017	1.9
2001	90116	93.9	2774	2.9	-	0.0	3097	3.2
2002	111044	97.3	1573	1.4	0	0.0	1551	1.4
2003	110206	95.8	2232	1.9	-	0.0	2651	2.3
2004	95484	94.7	2572	2.6	-	0.0	2791	2.8
2005	83683	92.4	4678	5.2	403	0.4	1777	2.0
2006	90709	92.8	3186	3.3	3	0.0	3832	3.9
2007	88350	94.8	2235	2.4	0	0.0	2590	2.8
2008	82556	97.1	1349	1.6	1	0.0	1077	1.3
2009	87895	91.6	5074	5.3	49	0.1	2956	3.1
2010	86722	96.1	1787	2.0	-	0.0	1736	1.9
2011	86074	90.5	5741	6.0	-	0.0	3312	3.5
2012	99896	93.9	3618	3.4	191	0.2	2630	2.5
2013	78493	92.6	4329	5.1	52	0.1	1863	2.2
2014	94917	93.7	3253	3.2	1	0.0	3084	3.0
2015	95741	95.7	2397	2.4	-	0.0	1934	1.9
2016	91456	82.4	15974	14.4	112	0.1	3390	3.1
2017	79573	85.6	8897	9.6	287	0.3	4197	4.5
2018	85244	96.7	1921	2.2	-	0.0	953	1.1

Figure 4.11, shows the combined overall burn maps obtained with MINDED-BA, from 2000 to 2018. The thematic classifications obtained from the model are displayed along with the RBA, indicating a good correspondence between both datasets. These maps allow to observe that Mixed pixels tend to be located within burned areas.

Nevertheless, we also verify the occurrence of several LMc areas outside the RBA extents. In Figure 4.12, the false colour composites allow to identify flooded or highly water-saturated areas in brown, bare soil areas as light pink, whereas burned areas, as obtained by the RBA, correspond to tones similar to the above classes. The overall burn maps detect LMc areas, either around water bodies (e.g., 2000, 2009 and 2014), or in presumably non-burned agriculture fields (e.g., 2016) such as corn plantations. These changes may be interpreted as a consequence of soil water content variations, different stages of growth, as well as crop harvesting effects, which cause false positive errors resulting from similar ΔBrI to burned areas.

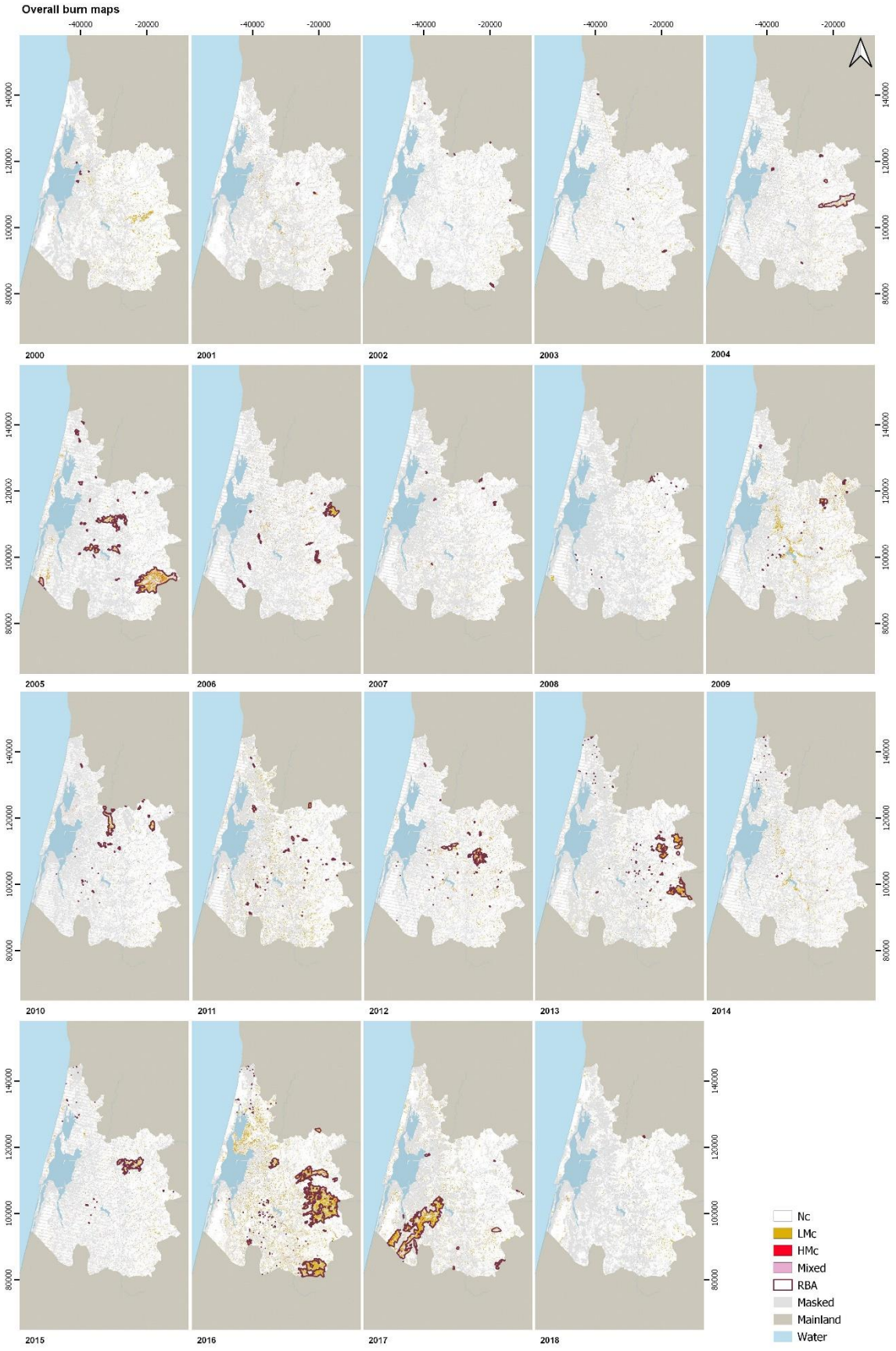

Figure 4.11 – Overall burn maps obtained from MINDED-BA from 2000 to 2018, in comparison to the reference burned areas RBA (ICNF, 2020)(ICNF, 2020) (Coordinate System: PT-TM06/ETRS89)

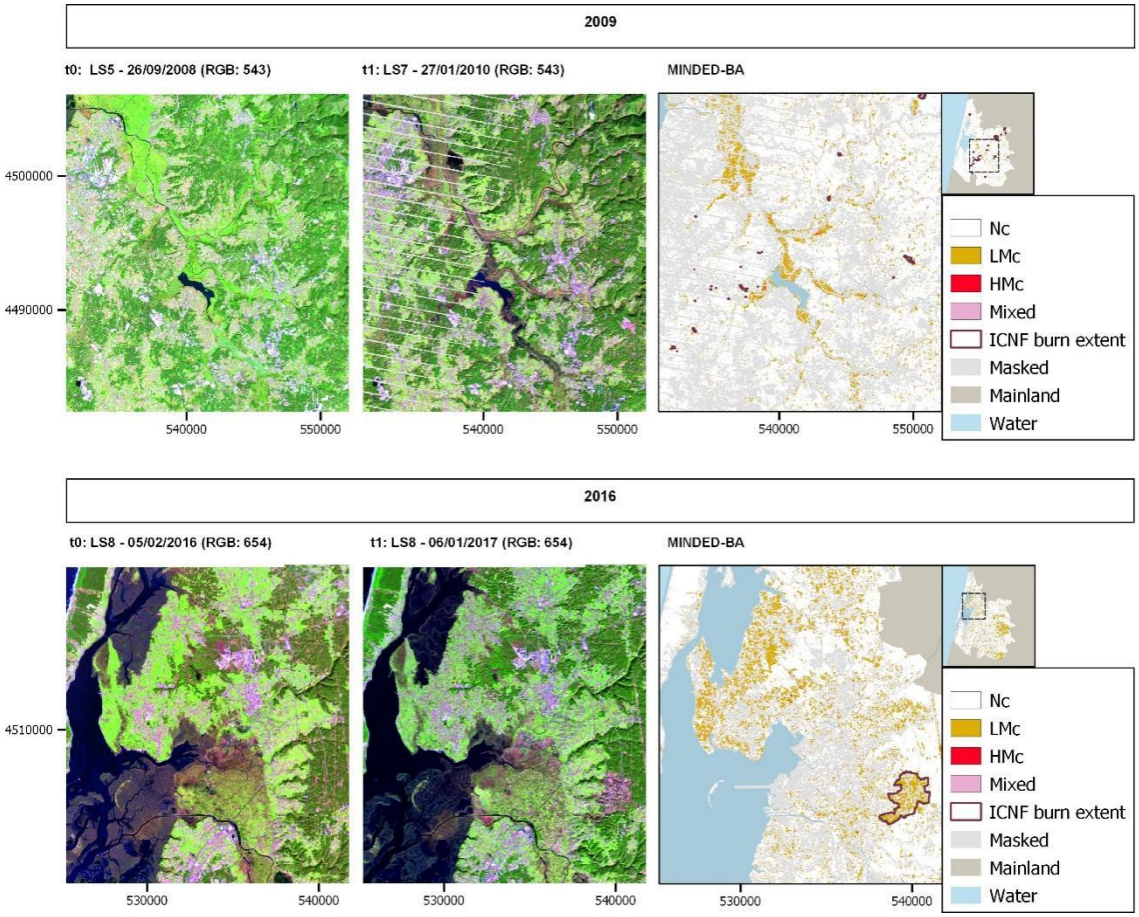

Figure 4.12 – False colour RGB composites (R:SWIR2; G:SWIR1;B:NIR) of t0 and t1, together with MINDED-BA overall burn maps and RBA, for 2009 and 2016 (Coordinate System: PT-TM06/ETRS89).

4.4. Accuracy assessment

The accuracy analysis of the MINDED-BA overall burn maps results was performed with the confusion matrix approach (Congalton, 1991). Table 4.8 and Figure 4.13 summarize the overall statistics, in which the distribution of both LMc and HMc classes (whose sum corresponds to the total changes - TC) were analysed in respect to the yearly reference burned areas (RBA) (ICNF, 2020). For the purpose of summarization, we will be presenting the results of commission errors in respect to the total changes (TC_{CE}), i.e., false positive detections of changes, while omission errors will be presented in terms of burned areas (BA_{OE}), i.e., false negative cases.

Table 4.8 – Confusion matrix statistics between the MINDED-BA overall burn maps results and the yearly reference burned areas (RBA)(ICNF, 2020)(ICNF, 2020), from 2000 to 2018 (Nc – no change; LMc – Low Magnitude change; HMc – High Magnitude change; TC – Total changes (LMc+HMc); Ov– Overall accuracy ; TC_{CE} – TC commission errors; and BA_{OE} – Burned areas omission errors).

	Accuracies (%)					Errors (%)		Total area (ha)		
	Nc	LMc	HMc	TC	Ov	TC_{CE}	BA_{OE}	LMc	HMc	RBA
2000	100.0	0.1	-	0.1	96.4	99.9	74.0	3645	0	8.6
2001	100.0	1.2	-	1.2	97.0	98.8	15.7	2774	0	40.1
2002	100.0	2.3	100.0	2.3	98.6	97.7	23.6	1573	0	47.6
2003	100.0	1.5	-	1.5	98.0	98.5	26.0	2232	0	45.4
2004	99.4	11.8	-	11.8	97.1	88.2	64.9	2572	0	862.0
2005	98.5	54.2	88.2	56.9	96.1	43.1	30.0	4678	403	4134.2
2006	99.7	17.2	79.3	17.2	96.9	82.8	29.6	3186	3	779.6
2007	99.9	0.6	0.0	0.6	97.5	99.4	81.9	2235	0	74.5
2008	99.9	0.9	0.0	0.9	98.3	99.1	81.7	1349	1	68.7
2009	99.9	3.5	17.1	3.6	94.6	96.4	26.7	5074	49	251.6
2010	99.6	27.6	-	27.6	98.1	72.4	42.2	1787	0	853.4
2011	99.8	4.3	-	4.3	93.8	95.7	43.5	5741	0	435.1
2012	99.8	16.9	85.0	20.3	96.9	79.7	22.9	3618	191	1003.7
2013	99.2	38.6	91.8	39.2	96.1	60.8	26.1	4329	52	2327.0
2014	100.0	0.3	0.0	0.3	96.7	99.7	43.6	3253	1	15.5
2015	99.6	20.3	-	20.3	97.7	79.7	43.6	2397	0	862.7
2016	98.9	43.3	84.6	43.6	90.6	56.4	12.7	15974	112	8033.0
2017	99.3	45.5	93.4	47.0	93.9	53.0	11.2	8897	287	4861.4
2018	100.0	1.4	-	1.4	97.8	98.6	8.3	1921	0	30.2
Average	99.7	15.3	58.1	15.8	96.4	84.2	37.3	4064.9	57.8	1301.8

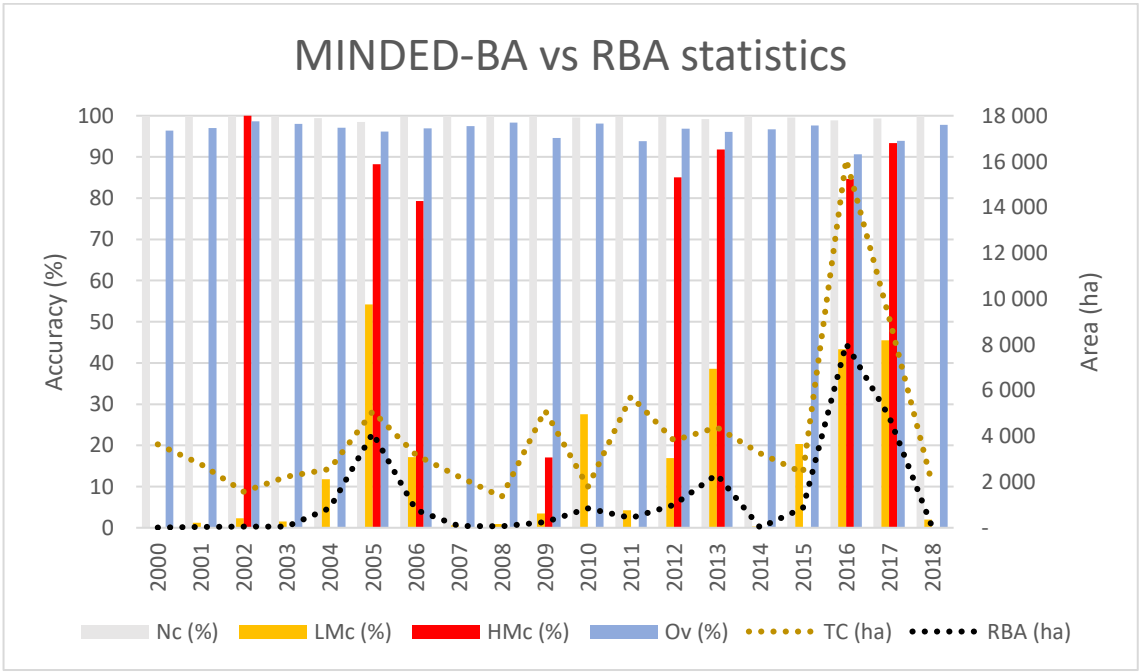

Figure 4.13 – Summary of the confusion matrix statistics between MINDED-BA overall burn maps and the yearly reference burned areas (RBA) (Nc – no change; LMc – Low Magnitude change; HMc – High Magnitude change; TC – Total changes (LMc+HMc); Ov– Overall accuracy).

The results of the confusion matrix show that MINDED-BA has a satisfactory response, reaching an average overall accuracy of 96.4%. We found Nc areas to have the highest average class accuracy (99.7%), followed by HMc (58.1%) and LMc areas (15.3%). The accuracies of HMc areas are the most variable, followed by LMc areas. Such variability is correlated with the total area of yearly RBA, with higher LMc and HMc accuracies occurring in years with larger burned extents (e.g., for those years with over 1000 burned hectares). This correlation seems to be particularly stronger for LMc areas, which have a polynomial correlation with RBA (R^2=0.951) (Figure 4.14). On the other hand, the Overall accuracy seems to be more stable and independent from the RBA extent.

In general, we found TC_{CE} to be clearly higher than the BA_{OE}. This fact is confirmed by TC (i.e., LMc+HMc) being always higher than the RBA (Figure 4.13). Once again, there seems to be a correlation between RBA and error rates, with the lowest errors occurring in years with larger burned extents, particularly for TC_{CE}, which also have a polynomial correlation with RBA (R^2=0.955) (Figure 4.14).

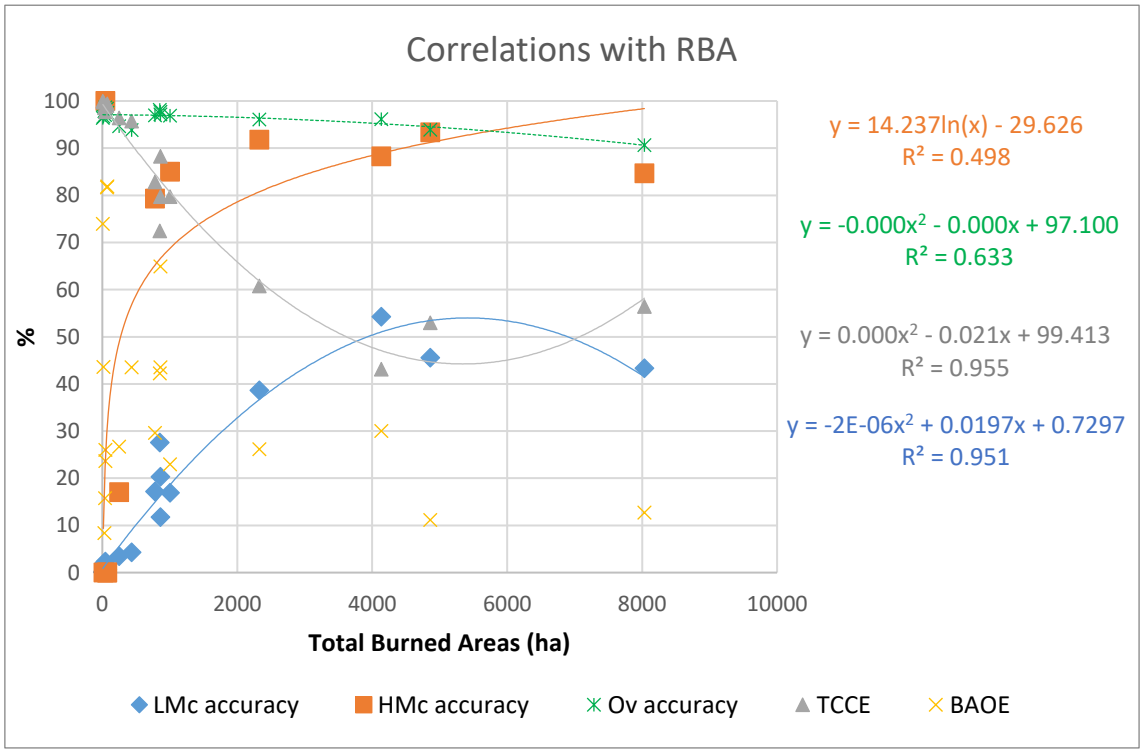

Figure 4.14 – Correlations between different parameters of the confusion matrix of MINDED-BA overall burn maps and the Reference Burned Areas (RBA) (Nc – no change; LMc – Low Magnitude change; HMc – High Magnitude change;); Ov– Overall accuracy ; TC_{CE} – Total changes commission errors; and BA_{OE} – Burned areas omission errors).

To verify the benefits of the multi-index approach, we repeated the confusion matrix analysis for each individual ΔBrI, with the corresponding results being summarized in Table 4.9. In terms of the Nc class agreement, all indexes had similar performances, with ΔNBRl and ΔNBR2, respectively having the best (99.7%) and worst (99.3%) performances. In turn, for the LMc class, ΔNBRl achieved the highest average values (10.9%), with ΔNBRs and ΔNDVI having the lowest agreement rates (9.2%). The results for HMc are more contrasted, with ΔNBRl showing the highest agreement levels (51.0%), while ΔNBR2 being significantly worse than the remaining ΔBrI. Nevertheless, the best overall agreement was obtained for ΔNBR2, with an average of 95.6%, which is still under the MINDED-BA overall agreement (96.4%). In terms of errors, we can verify that TC_{CE} are clearly above the BA_{OE}, confirming the tendency of overestimation of changes by every individual ΔBrI. ΔNBRl results have both the best average TC_{CE} (87.3%) and the best average BA_{OE} (34.7%).

The comparison between Table 4.8 and Table 4.9 allows verifying that in general MINDED-BA outperformed every ΔBrI individual parameter of the accuracy analysis, with the exception of omission errors that are slightly lower for ΔNBRl and ΔNBRs.

Table 4.9 – Summary of the confusion matrix results, between every individual ΔBrI and the RBA, from 2000 to 2018 (Nc – no change; LMc – Low Magnitude change; HMc – High Magnitude change; Ov– Overall accuracy ; TC_{CE} – Total Changes commission errors; and BA_{OE} – Burned areas omission errors).

year	ΔNBRs						ΔNBRI						ΔNBR2						ΔNDVI					
	Nc	**LMc**	**HMc**	**Ov**	TC_{CE}	BA_{OE}	**Nc**	**LMc**	**HMc**	**Ov**	TC_{CE}	BA_{OE}	**Nc**	**LMc**	**HMc**	**Ov**	TC_{CE}	BA_{OE}	**Nc**	**LMc**	**HMc**	**Ov**	TC_{CE}	BA_{OE}
2000	100.0	0.1	0.5	92.8	99.9	41.4	100.0	0.1	-	95.7	99.9	54.7	100.0	0.1	-	99.4	99.9	93.8	100.0	0.0	-	93.8	100.0	80.5
2001	100.0	0.3	20.7	89.2	99.6	10.5	100.0	0.8	0.0	95.2	99.2	17.7	100.0	0.3	-	98.6	99.7	90.9	100.0	0.6	-	93.4	99.4	19.0
2002	100.0	0.8	-	95.4	99.2	18.0	100.0	1.7	57.1	98.0	98.3	24.2	100.0	0.6	-	97.7	99.4	72.5	100.0	0.7	32.8	96.2	98.9	25.9
2003	100.0	0.8	-	95.1	99.2	20.2	100.0	0.8	30.8	95.6	99.1	22.7	100.0	0.5	2.7	97.6	99.5	77.1	100.0	0.8	-	96.3	99.2	38.7
2004	99.4	7.9	-	93.5	92.1	50.4	99.4	8.0	55.6	94.1	92.0	54.2	99.1	3.8	-	96.1	96.2	88.0	99.3	7.4	-	95.2	92.6	68.4
2005	98.5	40.2	94.1	93.6	59.7	29.2	98.4	35.8	81.8	95.6	46.5	31.9	96.7	32.6	-	93.3	67.4	63.8	98.6	24.0	89.3	92.1	64.0	24.9
2006	99.7	9.2	78.3	93.6	90.7	27.6	99.8	4.1	63.0	91.4	92.7	25.2	99.5	7.5	0.0	94.8	92.5	56.7	99.7	15.3	-	96.7	84.7	37.9
2007	99.9	0.3	1.9	92.5	99.7	74.8	99.9	0.4	0.0	95.1	99.6	78.8	99.9	0.4	0.0	97.4	99.6	88.5	99.9	0.4	-	95.8	99.6	81.1
2008	99.9	0.5	0.5	95.2	99.5	70.7	99.9	0.7	-	97.7	99.3	81.3	99.9	0.2	-	98.1	99.8	94.8	99.9	0.7	0.0	97.2	99.3	77.0
2009	99.9	1.0	15.2	91.1	97.6	22.9	99.9	2.6	-	91.8	97.4	25.1	99.8	6.8	0.0	98.5	93.2	68.1	99.9	1.7	34.3	91.6	97.3	27.1
2010	99.6	9.9	-	93.6	90.1	34.2	99.6	19.8	-	97.1	80.2	41.2	99.1	6.4	0.0	96.5	93.6	82.5	99.5	14.0	-	96.1	86.0	44.4
2011	99.8	2.9	-	89.8	97.1	40.7	99.8	3.1	-	90.8	96.9	41.0	99.6	2.9	0.0	95.3	97.1	73.9	99.8	2.9	90.0	90.4	95.9	34.4
2012	99.8	5.0	74.9	92.4	90.5	19.8	99.8	8.9	84.6	96.1	83.0	24.0	99.3	17.4	-	98.0	82.6	73.5	99.8	9.1	-	92.3	90.9	22.5
2013	99.2	21.8	90.1	91.9	77.1	25.0	99.2	36.7	-	95.7	63.3	27.4	98.5	15.9	0.0	91.7	82.8	49.4	99.2	16.1	45.3	93.0	82.4	35.2
2014	100.0	0.1	2.4	91.3	99.9	28.5	100.0	0.2	1.3	94.4	99.8	41.5	100.0	0.1	0.0	97.1	99.9	88.1	100.0	0.2	-	94.8	99.8	46.6
2015	99.6	14.6	-	95.8	85.4	39.1	99.6	15.3	-	95.8	84.7	33.2	99.3	5.5	66.7	92.8	94.5	63.4	99.4	16.5	-	97.1	83.5	57.2
2016	98.8	10.7	58.8	86.5	66.0	12.7	98.8	41.8	91.9	90.3	57.5	14.1	97.5	70.4	44.4	95.6	29.6	30.5	98.9	32.0	0.5	85.4	68.1	11.9
2017	98.2	49.3	91.1	94.5	48.9	30.2	99.5	24.4	95.0	87.5	69.9	8.0	98.1	25.5	4.1	86.6	74.5	28.4	99.1	32.1	0.3	92.1	68.4	18.9
2018	100.0	0.0	0.0	93.1	100.0	100.0	100.0	1.4	-	97.7	98.6	13.4	100.0	0.3	0.0	90.2	99.7	33.0	100.0	0.9	68.1	96.2	98.5	5.8
Average	99.6	9.2	40.7	92.7	89.1	36.6	99.7	10.9	51.0	94.5	87.3	34.7	99.3	10.4	9.8	95.6	89.6	69.3	99.6	9.2	40.1	94.0	89.9	39.9

4.5. Uncertainty analysis

The uncertainty analysis of MINDED-BA consists in analysing the results of the combination among the four coeval ΔBrI thematic maps. For this procedure, we defined a range of uncertainty classes, ranging from 0 to 3:

0 – unanimity (4 identical coeval classifications)

1 – absolute majority (with three identical coeval classifications)

2 – relative majority (with two identical coeval classifications)

3 – no majority (tie between two couples of identical coeval classifications)

The above mentioned pixel-scale values allowed us to obtain the overall uncertainty, which corresponds to the uncertainty class values weighted according to their frequency. Table 4.10 summarizes the results of the uncertainty analysis, where we can verify that MINDED-BA uncertainty values are mostly 0 and 1, which contribute for low overall uncertainties. However, for every year, the highest uncertainty class (i.e., 3) exceeds the intermediate class (i.e., 2). From the entire dataset, we found that 2008 and 2002 have the lowest average uncertainties, while 2017, 2016 and 2011 have the highest average uncertainties.

Table 4.10 – Uncertainty class distribution of yearly overall burn map results.

years	Uncertainty classes								
	0		1		2		3		
	area (ha)	%	area (ha)	%	area (ha)	%	area (ha)	%	Average uncertainty
2000	948900	91.0	73613	7.1	158	0.0	20162	1.9	0.13
2001	823368	85.8	105364	11.0	153	0.0	30975	3.2	0.21
2002	1049771	92.0	76194	6.7	0	0.0	15516	1.4	0.11
2003	1050957	91.3	73423	6.4	13	0.0	26504	2.3	0.13
2004	896207	88.9	84347	8.4	7	0.0	27907	2.8	0.17
2005	778087	85.9	91987	10.2	8282	0.9	27052	3.0	0.21
2006	857233	87.7	80862	8.3	848	0.1	38361	3.9	0.20
2007	832291	89.3	73488	7.9	86	0.0	25883	2.8	0.16
2008	793570	93.4	43421	5.1	2277	0.3	10562	1.2	0.09
2009	837502	87.3	84842	8.8	7194	0.7	30194	3.1	0.20
2010	813525	90.1	71555	7.9	17	0.0	17348	1.9	0.14
2011	795139	83.6	122965	12.9	0	0.0	33116	3.5	0.23
2012	934072	87.8	97178	9.1	3373	0.3	28721	2.7	0.18
2013	718831	84.8	105790	12.5	3093	0.4	19652	2.3	0.20
2014	893693	88.3	87313	8.6	2061	0.2	29480	2.9	0.18
2015	898133	89.7	83251	8.3	0	0.0	19340	1.9	0.14
2016	866092	78.1	174932	15.8	32917	3.0	35384	3.2	0.31
2017	722058	77.7	156027	16.8	1843	0.2	49610	5.3	0.33
2018	740162	84.0	131475	14.9	0	0.0	9527	1.1	0.18

Figure 4.15 shows the uncertainty maps for MINDED-BA, where we can observe that the highest uncertainty classes (i.e., 2 and 3) tend to be located within the limits of RBA. Pixels corresponding to uncertainty values of 1 seem to be either randomly distributed (e.g., 2010, 2018), or are concentrated nearby water bodies (along the lower sections of the Vouga River and around the Pateira de Fermentelos lagoon, for 2000, 2001, 2009, 2014).

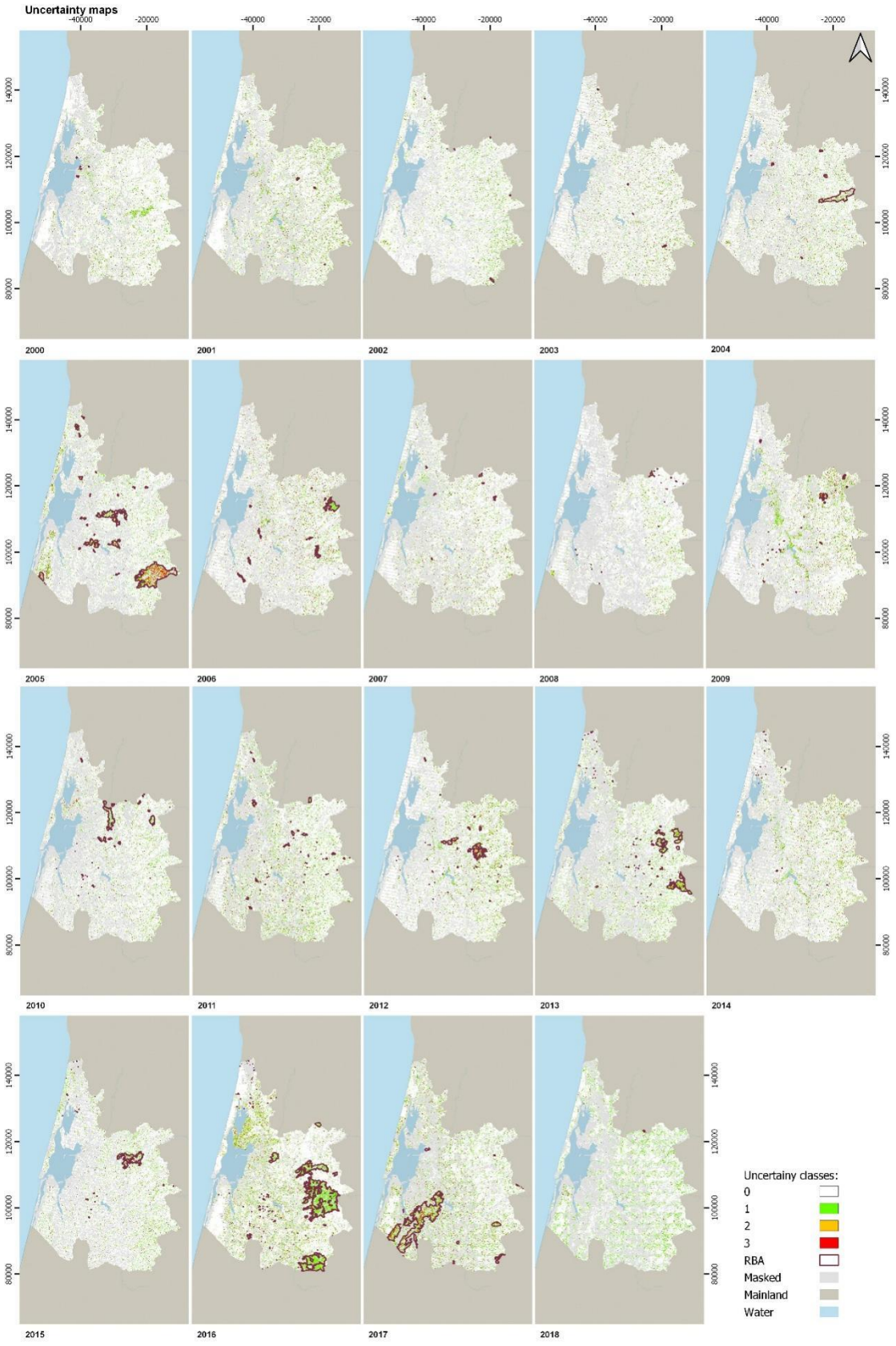

Figure 4.15 –MINDED-BA uncertainty maps, from 2000 to 2018 (Coordinate System: PT-TM06/ETRS89).

5. Discussion

This study presents a change detection model for determining burned extents from wildfires. It consists in the development of a previous model (MINDED), originally designed for determining flood extents (Eduardo R. Oliveira et al., 2019). Despite both being weather-related hazards (Deleu et al., 2011; Lavalle et al., 2005), flooding and wildfires have antagonistic causes and effects. Floods are often the consequence of extreme precipitation events, while wildfires tend to occur and proliferate during dry periods. Nonetheless, this work demonstrates that the same theoretical principles can be applied to determine the extents of both hazardous processes. This can be done by selecting different hazard-specific indices, or by focusing on different sides of the same index-differencing distribution curves. Since MINDED and MINDED-BA share the same theoretical principles, they also share certain advantages and limitations. By combining several indices based on different multispectral regions, both methods allow narrowing the range of types of change, in which burned area detection is also included.

When analysing processes such as wildfires, which have non-Boolean characteristics and result from the interaction with other natural and anthropic processes, it is essential to define an adequate set of procedures to ensure the quality of the modelled results. Figure 4.16 highlights both the advantages of the multi-index approach (Multi-index), and the importance of the pre-processing developments (Masking) introduced in MINDED-BA, in a way that the final result (i.e., the Multi-index + Masking) shows clear improvements when compared to the reference burned areas (RBA) (ICNF, 2020). Nevertheless, as an index differencing-based approach, it is still not completely able to discriminate each type of change.

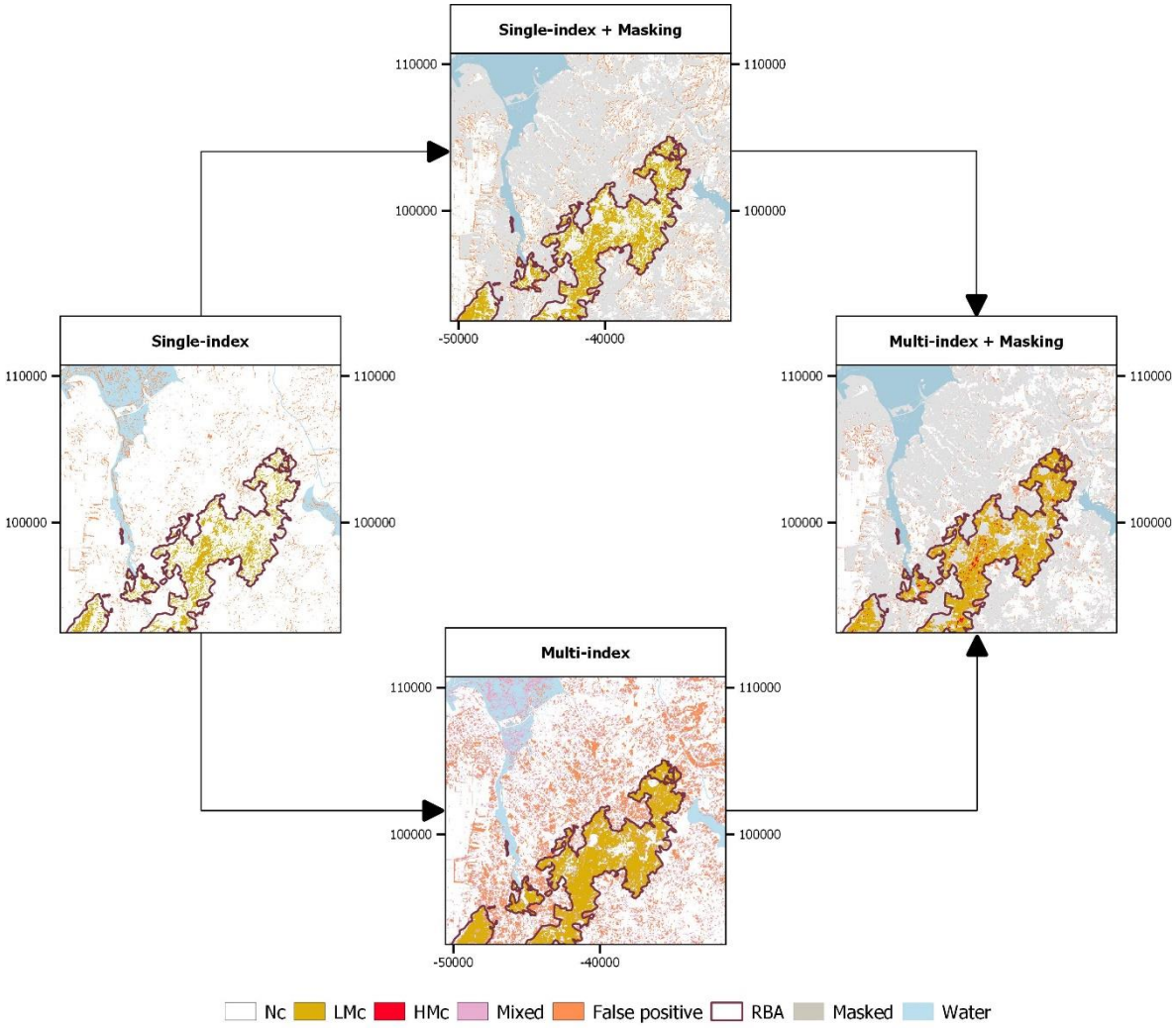

Figure 4.16 – Comparison of results obtained with different processing levels, including those from HRS masking and the multi-index majority analysis (example of the year 2017, with the single index differencing corresponding to ΔNBR2) (Coordinate System: PT-TM06/ETRS89).

As a digital change detection method, MINDED-BA is intrinsically dependent on the quality and quantity of the information conveyed by the images used for both *t0* and *t1* scenes. This means that, for instance, in the temperate Mediterranean climate regions, for estimating yearly burned areas, *t0* and *t1* should be acquired as closest as possible to the end of each year, to ensure that each forest fire season (i.e., from early spring to late summer) has ended. Considering MINDED-BA relies on multispectral images acquired by sensors with revisiting periods of several days, such as those provided by Landsat, this might present additional difficulties. The first difficulty is to find cloud-free images during the wet season, which for particularly rainy years may be hard to obtain, especially for older epochs with a more limited scene availability. For this reason, it was not possible to select images acquired exactly at the same time of every year, ranging from late September to

late January of the following year. This may be considered as an important source of error, since more changes other than burning may become detected by MINDED-BA (e.g., phenological cycles, seasonal agricultural or forestry management practices). Additionally, due to this limited image availability and the total time extent of this study (i.e., 18 years), we had to consider couples of images acquired by different Landsat sensors (Table 4.2). Nevertheless, as referred by Oliveira et al. (2019), using different sensors for *t0* and *t1*, is not expected to affect the accuracy of the model significantly, but instead cause shifting of the ΔBrI modal values, and consequently of the threshold values (as observed in Table 4.5). The second difficulty is that several phenomena other than fires may constitute false positives for every ΔBrI, requiring further pre-processing steps.

Regarding the atmospheric correction of the multispectral images used as *t0* and *t1*, to ensure the replicability and robustness of MINDED-BA results, we considered the Landsat Level 2 products (i.e., given as surface reflectance) which are determined by the USGS algorithm (Ihlen and USGS, 2019; U.S. Geological Survey, 2016). For the same reasons, we also considered the quality assessment bands ('pixel_qa'), which were used to mask clouds, cloud shadows, water and snow features. Nevertheless, considering the relative stability of permanent water bodies within our study area and the ready-availability of spatial thematic data containing their limits, we defined a buffer area with the objective of masking such permanent water bodies. This ensured that none of those pixels remained undetected by the USGS algorithm and avoided any further interference with the MINDED-BA results.

Additional criteria were also necessary to discard other potentially known interferences such as forest/shrubland clearcutting, agricultural crop harvesting, or soil mobilization occurred between *t0* and *t1*.. This might be achieved with pre- or post-processing masking of highly reflective surfaces (HRS), which might occur in *t1*, so resulting in false positive detections. Such task may be implemented by creating a user-defined training dataset, or by considering reference literature values. The first option has the advantage of providing the best correlation with the characteristics of a study area, but may require a-priori knowledge of both bare soil and burned area locations (e.g., using analogous approaches to Cenci et al., 2017c), being more dependent on the end-user expertise and technical skills. On the other hand, classifications based on reference land cover literature values, allows implementing the model in a fully automatic routine without any subjectivity issues. The latest also allows the possibility of being applied as a "black-box" tool, targeted for non-experts in remote sensing techniques. Since the thresholding procedures of MINDED-BA rely entirely on the index differencing statistics, there is a clear advantage in

implementing masking as a pre-processing step (as opposed to post-processing), because by eliminating such interferences, the signal separation between changes and no-changes is also improved (i.e., noise reduction). For these reasons, we adopted the theoretical reference value approach to define a thresholding range applied to those multispectral bands that maximize the separation between burned areas and HRS. Then, we determined sensor-specific Tasseled Cap Brightness (TCB) values for a series of increments within the thresholding range, which were later used to mask HRS from every *t1* scene. In principle, we expected the best masking to correspond to those increments positioned towards the middle of the thresholding range, as their position was likely to maximize the difference towards the HRS theoretical reflectance signatures, and to provide the best trade-off between the Total changes commission errors (TC_{CE}) and the Burned areas omission errors (BA_{OE}). In fact, if MINDED-BA was to be applied without any complementary information or additional analysis, M2 or M3 would likely be the safest alternatives. Instead, we found that the lowest threshold (i.e., M1) was the best option for our case study (see Figure 4.4). This result may be explained by the different spectral characteristics of the burned areas, as well as the reflectivity of HRS due to local pedology and geology. Moreover, we would like to highlight that instead of the TCB, we could have directly integrated the same multispectral bands, as sum or average of reflectance values. After trying such approaches, we verified that despite having similar results, the TCB provided slightly better masking of HRS, allowing obtaining marginal, but consistent improvements (ca. 1%) for every parameter of the confusion matrix.

The optimal bin selection approach introduced in this work is a further development to the MINDED threshold selection procedure. It consists in a conceptual interpretation of the shape for the ΔBrI frequency distribution function, by depicting what are the expected indications are caused by noise and signal variations. Despite the different ΔBrI under analysis being obtained by integrating different multispectral bands combinations and the tested bin number values being characterized by a set of 15 samples in a quite large range (10 – 1259), the obtained range of optimal bin numbers is concentrated in only 3 samples (Figure 4.7; 28,40,56). These findings may be a consequence of the effects of the time span between *t0* and *t1* images, as well as the extent and type of changes. However, further research should be performed to understand truly this behaviour. As for the thresholds T1 and T2, in theory these should fall within the range of ΔBrI values 0 – 2 (as only normalized indices were considered). The results show that T1 is more concentrated in a small range of values (interquartile range 0.10-0.36), while a wider range characterizes T2 (0.45-0.99). We can conclude that the optimal bin number distribution spreads within ca. 20% of the sampled range, while the threshold T1 within ca. 13% of the expected range,

hence suggesting high stability regardless the ΔBrI. On the other hand, T2 spreads within ca. 27%, suggesting higher variability.

Regarding the threshold distribution, there are several factors affecting their magnitude and variability. Such factors should include the types of changes occurring between *t0* and *t1*, as well as the sensors used to detect them, which in some cases are different between the two epochs (Table 4.2). For these reasons, such threshold variations should not be interpreted as an indicator of uncertainty, as they reflect the method's response to a shift of the modal value of the frequency distribution functions. The higher variability observed for T2 should also be more dependent on the optimal bin number value, because the higher the bin number, more intermediate thresholds may be detected (Figure 4.8).

If not addressed correctly, or addressed at all, some of the above-mentioned conditions may still produce effects over the entire MINDED-BA model chain. In those cases, the ΔBrI distribution functions and their corresponding *d1f* and *d2f*, may be affected, triggering the possibility of detecting sub-optimal thresholds and leading to less accurate classification as burned related changes (either as LMc or HMc). Despite all the pre-processing steps, MINDED-BA seems to have a tendency of overestimating burned areas (in comparison to the RBA) (as observed in Figure 4.11, Figure 4.12, Figure 4.13 and Table 4.8). This tendency is likely a consequence of the wide and flat topography of the lower section of the Vouga River Watershed. In some cases, we found several LMc areas to occur nearby river bodies which are prone to flooding (Oliveira et al., 2019) (e.g., for 2000, 2009 and 2014). Moreover, MINDED-BA may be also sensitive to higher differentials of either vegetation greenness or water contents between *t0* and *t1* images, as might be the case for 2016 (see Figure 4.12). This means, that in such cases, *t0* was probably acquired during particularly wetter or even flooded condition. As an alternative, both *t0* and *t1* scenes could have been acquired earlier to the wet season, but with the risk of missing burned areas from those years.

From the initial set of normalized indices, we found ΔNDWI results to have insufficient performances in detecting burned areas (Figure 4.10), so we discarded it from further steps of MINDED-BA. For these reasons, we ended up using four ΔBrI. In general, we found ΔNBRl to have the best individual performance for most parameters of the confusion matrix analysis, while ΔNBR2 achieved the best overall accuracy with the RBA (Table 4.9). These findings, confirm the indications found in the literature (Bastarrika et al., 2011; Pereira et al., 1999), which highlight the benefits of considering both SWIRs and SWIRl to improve the discrimination between burned areas and water. However, as observed in the examples of Figure 4.10, ΔNBR2 seems to underestimate certain

burned areas, probably resulting by reduced fire severity conditions. The majority analysis of MINDED-BA has demonstrated to handle most individual ΔBrI limitations, meaning that the overall maps of Figure 4.11 represent the best combination for most of the confusion matrix parameters (Table 4.8). Moreover, the uncertainty assessment which is enabled by the majority analysis provides additional and relevant information about those locations where MINDED-BA tends to perform with different levels of confidence.

The correlations found between some of the parameters of the confusion matrix and the RBA extents (Figure 4.14) indicate that, as a general behaviour, the larger the burned areas the better the performance of the MINDED-BA. This is likely the consequence of MINDED-BA being a statistically dependent method, requiring that the frequency of pixels corresponding to burn-related changes should be large enough to produce measurable changes on *df1* and *df2* functions. Nevertheless, the method accuracy is also dependent on the occurrence of other types of changes that may lead to detect false-positives, such as those verified in 2016.

Despite being the widest within our study area, wildfires are not exclusive to forests or agricultural areas. In particular, during those years with the largest burned areas, many fires involved other land covers, such as artificial or even wetland areas (e.g., for 2017). Such heterogeneity of burned surfaces increases the difficulty in finding optimal thresholds, which ideally would have to be transversal to detect burned-related changes for every type of land cover.

Regarding the ICNF official burned areas, which were used as our RBA, they are the closest available dataset that may be used as a ground truth alternative. However, this dataset is in practice a product of a multi-source survey, combining fieldwork and remote sensing data interpretation. This means that these are also affected by unknown errors which, as an example, may overestimate the real extent of burned areas (e.g., as seen in Figure 4.4, where the outer RBA polygon seems to be including several non-burned islands), and consequently increase the BA_{OE}. Besides, this ICNF dataset is mostly Boolean in terms of the occurrence of fires, therefore, we have no way of verifying which fire severities are being considered. Nevertheless, for the last years, ICNF has started releasing additional information, such as date, type of fire (e.g., shrubland, agriculture, and forestry), cause of ignition, or source, which seem to demonstrate coordination with multi-level civil protection agents.

The tendency for overestimating is a common issue for any image differencing method based on a bitemporal analysis, particularly when implemented with couples of images with one year or larger temporal separation. However, since MINDED-BA has been completely integrated in an

automatic script, it should be relatively easy to implement it in a systematic routine, in order to analyse different couples of images acquired within a shorter time span (i.e., corresponding to the satellite temporal resolution). This would also enable to assess the yearly-burned areas extents. In fact, if such analysis was to be performed, the user subjectivity errors when selecting the images would no longer persist, and the overestimation issue should be highly minimized. Such higher frequency multitemporal comparisons would also allow to analyse the persistence (or not) of detected changes throughout more than an image couple, which by itself should allow a systematic improvement of burned extent detection.

6. Conclusion

This study presents MINDED-BA, an automatic change detection method based on multispectral optical satellite images, aimed at determining yearly-burned extents. The method was implemented within a study area located on northwest central Portugal, using Landsat data from 2000 to 2018. This work is the development of a previous multi-index differencing method, originally designed to detect flood extents. MINDED-BA allows detecting burned-related changes, based on the analysis of magnitudes of the image differencing statistics. Another relevant point of the method concerns the development and implementation of several pre-processing steps introduced within the modelling workflow, with the objective of discarding some of the most significant sources of error mentioned in the literature. From such developments, we highlight a new procedure to mask highly reflective surfaces, based on land cover-specific multispectral literature reflectance values, which were integrated and implemented in MINDED-BA through the Tasseled Cap Brightness. Moreover, the optimal bin number selection procedure introduced in this work to process the image-differencing statistics, which is on the basis for the threshold selection for the classification of changes, has demonstrated to be a consistent and subjectivity-free approach. The performance of such innovations was verified by comparing MINDED-BA outputs with an official dataset of burned areas. Moreover, MINDED-BA also showed significant improvements compared to the single-index results. In fact, its majority analysis allowed combining the classifications provided by the best performing indices, while reducing noise caused by single-index false positives. Nevertheless, in comparison to the reference burned extents, MINDED-BA tends to overestimate burned areas, being sensitive to changes other than those from burning. This was particularly noticeable whenever the couples of images used to perform index differencing were acquired under significantly changed conditions over about one year (e.g., in terms of water content, seasonal vegetation greenness, or when major land-use changes take place).

The method was implemented through an automatic python script, selecting one Landsat scene per year, acquired after the study area annual fire season. Considering the ease of implementation provided by a GRASSGIS python script, its straightforward theoretical principles and effective results, MINDED-BA has the potential of being useful as a reliable unsupervised method for the preliminary assessment of regional and national level yearly-burned extents. Moreover, if implemented by integrating also other sensors different from Landsat, it should allow to improve the temporal resolution of the input data and to mitigate detection errors.

REFERENCES

Abdollahi, M., Islam, T., Gupta, A., Hassan, Q.K., 2018. An advanced forest fire danger forecasting system: Integration of remote sensing and historical sources of ignition data. Remote Sens. 10. https://doi.org/10.3390/rs10060923

Adab, H., Kanniah, K.D., Solaimani, K., Sallehuddin, R., 2015. Modelling static fire hazard in a semi-arid region using frequency analysis. Int. J. Wildl. Fire 24, 763–777. https://doi.org/10.1071/WF13113

Baig, M.H.A., Zhang, L., Shuai, T., Tong, Q., 2014. Derivation of a tasselled cap transformation based on Landsat 8 at-satellite reflectance. Remote Sens. Lett. 5, 423–431. https://doi.org/10.1080/2150704X.2014.915434

Bastarrika, A., Chuvieco, E., Martín, M.P., 2011. Mapping burned areas from landsat TM/ETM+ data with a two-phase algorithm: Balancing omission and commission errors. Remote Sens. Environ. 115, 1003–1012. https://doi.org/10.1016/j.rse.2010.12.005

Campbell, J.B., Wynne, R.H., 2011. Introduction to Remote Sensing, Fifth Edition, 5th ed, introduction to remote sensing fifth edition.

Cenci, L., Disperati, L., Persichillo, M.G., Oliveira, E.R., Alves, F.L., Phillips, M., 2017. Integrating remote sensing and GIS techniques for monitoring and modeling shoreline evolution to support coastal risk management. GIScience Remote Sens. 00, 1–21. https://doi.org/10.1080/15481603.2017.1376370

Chander, G., Hewison, T.J., Fox, N., Wu, X., Xiong, X., Blackwell, W.J., 2013. Overview of intercalibration of satellite instruments. IEEE Trans. Geosci. Remote Sens. 51, 1056–1080. https://doi.org/10.1109/TGRS.2012.2228654

Chuvieco, E., Aguado, I., Jurdao, S., Pettinari, M.L., Yebra, M., Salas, J., Hantson, S., de la Riva, J., Ibarra, P., Rodrigues, M., Echeverris, M., Azqueta, D., Roman, M. V, Bastarrika, A., Martinez, S., Recondo, C., Zapico, E., Martinez-Vega, F.J., 2014. Integrating geospatial information into fire risk assessment. Int. J. Wildl. Fire 23, 606–619.

Chuvieco, E., Martín, M.P., Palacios, A., 2002. Assessment of different spectral indices in the red-near-infrared spectral domain for burned land discrimination. Int. J. Remote Sens. 23, 5103–5110. https://doi.org/10.1080/01431160210153129

Chuvieco, Emilio, Riaño, D., Aguado, I., Cocero, D., 2002. Estimation of fuel moisture content from multitemporal analysis of Landsat Thematic Mapper reflectance data: applications in fire danger assessment. Int. J. Remote Sens. 23, 2145–2162. https://doi.org/10.1080/01431160110069818

Coelho, C.O.A., Alves, F.L., Ferreira, A., Castanheira, E., Esteves, T.C., 2007. Relatório Final Risco de Incêndio Florestal, Definição das condições de risco de cheia, incêndios florestais, erosão costeira e industriais na área de intervenção da AMRIA. Aveiro, Portugal.

Congalton, R.G., 1991. A review of assessing the accuracy of classifications of remotely sensed data. Remote Sens. Environ. 37, 35–46. https://doi.org/10.1016/0034-4257(91)90048-B

de Luca, G., Silva, J.M.N., Modica, G., 2021. A workflow based on Sentinel-1 SAR data and open-source algorithms for unsupervised burned area detection in Mediterranean ecosystems. GIScience Remote Sens. 58, 516–541. https://doi.org/10.1080/15481603.2021.1907896

Deleu, J., Tambuyzer, H., Stephenne, N., 2011. Multi Risk preparedness supported by Earth Observation. Eurosense Gi4DM Conf. 3-8 May, Antalaya, Turkey.

DGT, 2020. SNIG - Sistema Nacional de Informação Geográfica [WWW Document]. URL https://snig.dgterritorio.gov.pt/

EEA, 2020. Corine Land Cover (CLC) 2012.

EEA, 2010. Mapping the impacts of recent natural disasters and technological accidents in Europe - An overview of the last decade, EEA Technical report. Copenhagen, Denmark. https://doi.org/10.2800/62638

Escuin, S., Navarro, R., Fernández, P., 2008. Fire severity assessment by using NBR (Normalized Burn Ratio) and NDVI (Normalized Difference Vegetation Index) derived from LANDSAT TM/ETM images. Int. J. Remote Sens. 29, 1053–1073. https://doi.org/10.1080/01431160701281072

Giuseppe Mancino, Agostino Ferrara, A.P. and A.N., 2020. Cross-Comparison between Landsat 8 (OLI) and Landsat 7 (ETM+) Derived Vegetation Indices in a Mediterranean Environment. Remote Sens. 12, 20. https://doi.org/10.3390/rs12020291

Hantson, S., Chuvieco, E., 2011. Evaluation of different topographic correction methods for landsat imagery. Int. J. Appl. Earth Obs. Geoinf. 13, 691–700. https://doi.org/10.1016/j.jag.2011.05.001

Hughes, M.J., Hayes, D.J., 2014. Automated Detection of Cloud and Cloud Shadow in 4907–4926. https://doi.org/10.3390/rs6064907

ICNF, 2020. Cartografia de áreas ardidas [WWW Document]. URL http://www2.icnf.pt/portal/florestas/dfci/inc/mapas

ICNF, 2019. Programa Regional de Ordenamento Florestal - Centro Litoral. Caracterização biofísica, socioeconómica e dos recursos florestais.

Ihlen, V., USGS, 2019. Landsat 7 (L7) Data Users Handbook. USGS Landsat User Serv. 7, 151.

JAXA, 2020. ALOS Global Digital Surface Model "ALOS World 3D - 30m (AW3D30)" [WWW Document]. URL https://www.eorc.jaxa.jp/ALOS/en/aw3d30/index.htm

Kavzoglu, T., Erdemir, M.Y., Tonbul, H., 2014. Evaluating performances of spectral indices for burned area mapping using object-based image analysis 1–7.

Keeley, J.E., 2009. Fire intensity, fire severity and burn severity: A brief review and suggested usage. Int. J. Wildl. Fire 18, 116–126. https://doi.org/10.1071/WF07049

Key, C.H., Benson, N.C., 1999. Measuring and remote sensing of burn severity [poster abstract]. Jt. Fire Sci. Conf. Work. Proc. 284–285.

Lavalle, C., Barredo, J.I., De Roo, A., Niemeyer, S., San Miguel-Ayanz, J., Genovese, E., Camia, A., 2005. Towards an European integrated map of risk from weather driven events, Reproduction.

Leblon, B., San-Miguel-Ayanz, J., Bourgeau-Chavez, L., Kong, M., 2016. Remote Sensing of Wildfires. L. Surf. Remote Sens. Environ. Risks 55–95. https://doi.org/10.1016/B978-1-78548-105-5.50003-7

Lillesand, T.M., Kiefer, R.W., Chipman, J.W., 2015. Remote Sensing and Image Interpretation, 7th ed. New York, USA.

Liu, B., Siu, Y.L., Mitchell, G., 2016. Hazard interaction analysis for multi-hazard risk assessment: A systematic classification based on hazard-forming environment. Nat. Hazards Earth Syst. Sci. 16, 629–642. https://doi.org/10.5194/nhess-16-629-2016

Martín, M.P., Gómez, I., Chuvieco, E., 2006. Burnt Area Index (BAIM) for burned area discrimination at regional scale using MODIS data. For. Ecol. Manage. 234, S221. https://doi.org/10.1016/j.foreco.2006.08.248

Matin, M.A., Chitale, V.S., Murthy, M.S.R., Uddin, K., Bajracharya, B., Pradhan, S., 2017. Understanding forest fire patterns and risk in Nepal using remote sensing, geographic information system and historical fire data. Int. J. Wildl. Fire 26, 276. https://doi.org/10.1071/WF16056

McFeeters, S.K., 1996. The use of the Normalized Difference Water Index (NDWI) in the delineation of open water features. Int. J. Remote Sens. 17, 1425–1432. https://doi.org/10.1080/01431169608948714

Oliveira, E.R., Disperati, L., Cenci, L., Pereira, L.G., Alves, F.L., 2019. Multi-Index Image Differencing Method (MINDED) for flood extent estimations. Remote Sens. 11, 1–29. https://doi.org/10.3390/rs11111305

Parker, B.M., Lewis, T., Srivastava, S.K., 2015. Estimation and evaluation of multi-decadal fire severity patterns using Landsat sensors. Remote Sens. Environ. 170, 340–349. https://doi.org/10.1016/j.rse.2015.09.014

Pereira, J.M.C., Sá, A.C.L., Sousa, A.M.O., Silva, J.M.N., Santos, T.N., Carreiras, J.M.B., 1999. Remote Sensing of Large Wildfires, in: Chuvieco, E. (Ed.), Remote Sensing of Large Wildfires. Springer Berlin Heidelberg. https://doi.org/10.1007/978-3-642-60164-4

Riaño, D., Chuvieco, E., Salas, J., Aguado, I., 2003. Assessment of different topographic corrections in landsat-TM data for mapping vegetation types (2003). IEEE Trans. Geosci. Remote Sens. 41, 1056–1061. https://doi.org/10.1109/TGRS.2003.811693

Rouse, J.W., Hass, R.H., Schell, J.A., Deering, D.W., 1973. Monitoring vegetation systems in the great plains with ERTS. Third Earth Resour. Technol. Satell. Symp. 1, 309–317.

Sahana, M., Ganaie, T.A., 2017. GIS-based landscape vulnerability assessment to forest fire susceptibility of Rudraprayag district, Uttarakhand, India. Environ. Earth Sci. 76, 1–18. https://doi.org/10.1007/s12665-017-7008-8

Satir, O., Berberoglu, S., Donmez, C., 2016. Mapping regional forest fire probability using artificial neural network model in a Mediterranean forest ecosystem. Geomatics, Nat. Hazards Risk 7, 1645–1658. https://doi.org/10.1080/19475705.2015.1084541

Schowengerdt, R.A., 2007. Remote Sensing: Models and Methods for Image Processing, Third Edit. ed. Academic Press.

Schroeder, W., Oliva, P., Giglio, L., Quayle, B., Lorenz, E., Morelli, F., 2016. Active fire detection using Landsat-8/OLI data. Remote Sens. Environ. 185, 210–220. https://doi.org/10.1016/j.rse.2015.08.032

Singh, A., 1989. Review Articlel: Digital change detection techniques using remotely-sensed data. Int. J. Remote Sens. 10, 989–1003. https://doi.org/10.1080/01431168908903939

Song, C., Woodcock, C.E., Seto, K.C., Lenney, M.P., Macomber, S. a., 2001. Classification and change detection using Landsat TM data: When and how to correct atmospheric effects? Remote Sens. Environ. 75, 230–244. https://doi.org/10.1016/S0034-4257(00)00169-3

Trigg, S., Flasse, S., 2001. An evaluation of different bi-spectral spaces for discriminating burned shrub-savannah. Int. J. Remote Sens. 22, 2641–2647. https://doi.org/10.1080/01431160110053185

U.S. Geological Survey, 2019a. Landsat 8 Surface Reflectance Code (LASRC) Poduct Guide. (No. LSDS-1368 Version 2.0).

U.S. Geological Survey, 2019b. Landsat 4-7 Surface Reflectance (Ledaps) Product Guide. https://doi.org/10.1016/0042-207X(74)93024-3

U.S. Geological Survey, 2016. Landsat 8 Data Users Handbook. Nasa 8, 97.

USGS, 2020a. Landsat Normalized Burn Ratio 2 [WWW Document]. URL https://www.usgs.gov/core-science-systems/nli/landsat/landsat-normalized-burn-ratio-2

USGS, 2020b. Earth Explorer [WWW Document]. URL https://earthexplorer.usgs.gov/ (accessed 11.12.20).

Vilar, L., Camia, A., San-Miguel-Ayanz, J., 2015. A comparison of remote sensing products and forest fire statistics for improving fire information in mediterranean Europe. Eur. J. Remote Sens. 48, 345–364. https://doi.org/10.5721/EuJRS20154820

Zhu, Z., Woodcock, C.E., 2012. Remote Sensing of Environment Object-based cloud and cloud shadow detection in Landsat imagery. Remote Sens. Environ. 118, 83–94. https://doi.org/10.1016/j.rse.2011.10.028

Zongyi Ma, Yaowen Xie, Jizong Jiao, Linlin li, Xiangqian Wang, Hui, S.R., Liu, Q., Song, Z., Tao, G.H., 2011. Study on the relationship between scirpus planiculmis grow and Soil water content. Procedia Environ. Sci. 10, 2029–2035. https://doi.org/10.1016/j.proenv.2011.09.318

Chapter 5:
GENERAL CONCLUSIONS AND FUTURE RESEARCH

1. Key findings

This thesis is focused on the development and application of remote sensing methods to support the characterization of multiple hazards in a coastal region. To this end, two methods sharing the same theoretical principles, were developed and implemented in the Aveiro Region Study Area.

The first method, Multi-INDEx Differencing (MINDED), is described in Chapter 3, consisting of a change detection approach for determining the extent of flooded areas. MINDED was implemented through a semi-automatic procedure, using GRASS-GIS, a freeware Geographic Information System software which includes a Python language interface. Despite being based on a traditional change detection approach, considering image differencing of Water-related Indices (WrI), the method includes several innovative procedures and showed great potential for being used in regional-scale flood extent estimations. One of its key aspects is the threshold selection step, which can be obtained exclusively from data frequency analysis, without the need of ground truth information. Despite the unimodal characteristics of the image differencing data, which is often problematic for many threshold selection methods (e.g., Ng et al., 2013; Otsu, 1979), MINDED allows classifying different magnitudes of flood-related changes, including those caused by the detection of saturated soils, which may represent traces of recent flood events. In addition, this procedure is particularly useful in reducing user-induced subjectivity issues and allowed to establish the basis for further automatization developments. Moreover, the majority analysis implemented within MINDED allows combining the strengths of each individual WrI and provides estimates of uncertainty. Despite no ground truth data being available, which is demonstrative of the importance of this research, the results of MINDED were compared to an alternative method, the HSBA, which is based on SAR data, highlighting that MINDED is more sensitive to detect changes which may be related to flooding.

The second method, the Multi-Index Differencing Method for Burned Areas (MINDED-BA), is presented in Chapter 4, consisting in the adaptation and development of the original MINDED, with the purpose of estimating burned areas. This subsequent model combines several Burned related Indices (BrI) and an improved workflow suited for the characterization of a different hazard. Particular attention was given to the pre-processing stage of the method, where several procedures were introduced to address those conditions which would likely result in false detection of burned areas. The threshold selection of MINDED-BA also includes a new subjectivity-free procedure for optimal bin number selection, which not only allows finding the best statistical compromise between signal and noise, but also enables the possibility of implementing the method in a fully automatic routine. The results of MINDED-BA were compared to the official annual burned areas provided by the Portuguese Institute of Nature and Forest Conservation, allowing verifying the significant improvements from the newly introduced procedures, as well as the advantages of the multi-index majority analysis over the single-index results. Despite achieving high overall accuracy levels, we found that MINDED-BA tends to overestimate burned related changes, with false positives occurring whenever the method was sensitive to detect other types of change.

Being based on multispectral indices obtained from optical sensors, both MINDED and MINDED-BA have several limitations. Both methods are completely dependent on the availability of images used to characterize both pre- and post-event conditions. In the case of floods, the choice of the post-event image is particularly important, since the effects caused by the presence of water are spatially and temporally more dynamic when compared to the effects of fire. On the other hand, when comparing two epochs separated by several months (i.e., such as in the case of annual burned extent analysis), most change detection methods are also more susceptible of detecting other non-desired types of change. Such changes may result from phenology, land use practices (e.g., agricultural management), or even land cover conversions. Besides, other false positives may arise from the occurrence of clouds and casting of shadows by clouds or topography. For these reasons, we can generally assume that the usability and performance of both methods will be likely better in non-mountainous locations, without long periods of permanent cloud cover, such as in coastal areas like the Aveiro Region. Considering the limitations imposed by the use of medium resolution optical satellite sensors (e.g., Landsat series), the study of flood extents is expected to be easier in large floodplain areas, in comparison to steeper sloped riverbeds. In the case of MINDED-BA, its most straightforward use is to estimate annual burned area extents at regional scales, but it could be implemented also to detect changes over different temporal and spatial scales, particularly by incorporating data from other sensors.

MINDED and MINDED-BA are themselves the main contributions of this thesis, which may be used as two highly automatized tools to support the characterization of two different types of hazards. By being dependent on RS data and techniques, both models are expected to be valuable contributes for low-cost and expedite alternatives, to study locations with scarce data collection availability, and to aid subsequent supervised classifications or fieldwork validations.

Following, the three formulated research questions will be answered considering the work developed in this thesis:

'How can RS data and methods be incorporated in multi-hazard risk assessments, in an effective and efficient way?'

The models developed in this thesis provide a good starting point for multi-hazard risk assessments, since they share a common theoretical base and nomenclature, facilitating their further integration. Considering the concept of 'risk', which is often characterized as a function of 'hazard' and 'vulnerability' (Smith, 2013; UNISDR, 2009), this thesis might be considered as a contribute to the first factor of this function. The 'hazard' concept in turn, is often defined as a function of 'probability' and 'magnitude' (Smith, 2013; UNDRO, 1979), so MINDED and MINDED-BA are more directly contributing to analyse the magnitude of occurred events and may be particularly useful during the initial stages of the hazard risk assessment process chain (e.g., Van Westen, 2013). Such methods may also be relevant to perform frequency analysis (e.g., Meneses et al., 2018; Oliveira et al., 2012), to estimate the probabilities associated with different magnitudes of such phenomena, or to feed and validate other models (Chapter 2). Moreover, they can also contribute for the vulnerability evaluation process, helping to identify which are the elements at risk and how to estimate their value (e.g., as preparation for damage-assessment field interviews).

In the specific case of floods (Chapter 3), by using the precipitation records and remote sensing imagery alone, we estimated the probabilities of such events by assuming the probabilities of floods are the same probabilities of precipitation records. Nevertheless, the probabilities of the events calculated using a Weibull distribution from the precipitation records, may not have a direct correspondence with floods, particularly in more artificialized water bodies and basins. By considering the first images of the Landsat series, which at the time of writing of this thesis are already ca. 40 years old, we should be in principle able to characterize a significant number of events of the recent past. However, we have to highlight the decreased availability and more limited specs of older images, which together with other factors affecting the usability of multispectral optical scenes (e.g., cloud coverage), may significantly reduce the number of

detectable flooding events. Despite the ephemeral characteristics of the presence of water, the high sensitivity of MINDED to detect increases of surface wetness makes this model a useful tool to monitor occurred floods.

Regarding MINDED-BA, we present the results of yearly-burned areas between 2000 and 2018 (Chapter 4), which in principle and depending on the satellite image availability, could also be extended back to the late '70s (Landsat MSS and TM series operation period). Due to the longer lasting effects of vegetation burning in respect to flooding, MINDED-BA is capable of detecting burned-related changes by comparing images acquired with ca. one-year intervals, which in turn allows performing systematic monitoring of wildfire events. Anyway, the same method could be implemented also to map more accurately the extent and intensity of burned areas related to specific known fire events. Such approach could be performed by selecting the closest images prior and after the epoch of the event (similarly to the approach described in Chapter 3).

'What are the main advantages and limitations of using satellite remote sensing methods to monitor weather-related hazards in coastal regions?'

One of the main advantages of the RS methods over other ground-based approaches is related to the synoptic perspective of satellites, which allows surveying wide territorial extents, with little time and resources. If such RS methods incorporate objective decision rules integrated in automatic routines, they ensure highly reproducible and unbiased classifications, which may be harder to achieve when performing fieldwork. Coastal regions, in particular, may include several types of locations of difficult access, e.g., steep slope coastal cliffs, dense wetlands, or high-energy water bodies, which may only be observed from higher fields of view. The use of satellite RS data to characterize weather-related variables is well established in the literature and the literature includes several examples of such methods being used in hazard assessment contexts (Chapter 2). Both MINDED and MINDED-BA are methods capable of detecting hazard-related changes, provided the effects of such occurrences persist by the time of the post-event image acquisition. Besides, without systematic ground-level monitoring data, RS methods may be the only alternative for studying phenomena occurred in the recent past. In particular, the simplicity of MINDED and MINDED-BA is one of their greatest advantages, being less demanding in terms of input data when compared to other more complex RS methods. Besides, MINDED and MINDED-BA are close to the fields of environmental sciences (and further away from applied mathematics, or computational sciences), which may facilitate the understanding by potential end-users about the methodological workflows and enable tweaking according to their needs. More complex methodologies do not

necessarily indicate improved performances, as it is the case of univariate image differencing which have been described to achieve better results in comparison to other more complex change detection methods (Singh, 1989). The fact that MINDED and MINDED-BA may use bi-temporal medium resolution images helps to reduce the computational task times and requirements, and since they were implemented using readily available and free-access data and software also widens their potential of application.

RS methods are nonetheless susceptible to produce detection errors, and ground-level validations are recommended for achieving the truest representations of reality. Besides, we must highlight the effects of the Earth atmosphere, which is always present between satellite sensors and the land surface, being susceptible of introducing artefacts, leading to detect false changes or even entirely block any surface reflectance signal. Since optical satellite sensors are only capable of measuring passive energy, they are usually set up to measure reflected sunlight and to operate for daytime conditions. The changes that may be detected by MINDED and MINDED-BA depend on the spatial, spectral and temporal resolutions of the sensor used for the imagery acquisition. This means that if any given type of change takes place in a very small extent, e.g., over an area several times smaller than the pixel resolution of the acquiring sensor, it may not be detectable by the method. In the same way, if the effects of change do not persist until the post-image acquisition, or if such effects do not have a distinct spectral signature, the methods would also fail due to the sensor insufficient temporal and spectral resolutions. MINDED and MINDED-BA rely on the analysis of the frequency distribution curve of the index image differences to infer what types of changes might occur. However, image-differencing approaches are not conceptually capable of individualizing and classify every type of change. Nevertheless, as seen in Chapter 3 and 4, the methods may include within the automatic procedures complementary steps to mask/isolate likely known interferences.

‘May RS techniques be exclusively used to reliably characterize multiple types of hazards in coastal regions?’

The development of satellite sensors has been remarkably improved during the last decades and the use of remote sensing techniques have followed the same trend. Looking back at a few decades ago, there was only a very limited number of multispectral satellite sensors that could be used for studying hazardous events and other earth processes. Besides, compared to today’s standards, such data was less easily available and considerably more limited in terms of the sensor specs. In the 90s, also with the advent of SAR sensors, other opportunities for RS techniques emerged and

today there is a wide variety of satellites, which allow extracting and integrating different types of relevant data to characterize hazardous processes (Chapter 2). SAR sensors may perform under conditions not accessible to passive multispectral sensors, but they are affected by some limitations that do not allow obtaining the same information as passive sensors (Chapter 3). Another important aspect of multispectral imagery, in particular of more ancient sensors, is that they may be the only way of analysing older events. For this reason, it is important to keep developing methods that are capable of integrating and comparing both older and more recent data, contributing for widening the timeframe of monitored hazardous events and improving the determination of their frequency and magnitude.

The exclusive use of RS data for multi-hazard risk assessments still implies some limitations, so it should ideally be complemented with other ground-level data. For example, the characterization of the 'vulnerability' concept is particularly complicated from the point of view of RS. In a way, the 'exposure' analysis might be partially characterized by incorporating variables derived from DEMs and multispectral imagery (e.g., elevation, slope and land cover). Instead, the characterization of the 'susceptibility' concept, which is often characterized by the preparedness or coping capacity the elements at risk (Adger, 2006; Martini and Loat, 2007), should be a significantly harder task from the synoptic perspective of satellites. Nevertheless, depending on the type of hazard under analysis, several types of information might be extracted from RS techniques in order to analyse socioeconomic aspects (e.g., density of human settlements, discrimination among different types of infrastructures, vegetation health from agriculture/forestry).

In conclusion, at the time of writing of this thesis, ideally RS methods should not be used exclusively to perform hazard assessments, and far less to establish an entire base for complete risk assessment processes. However, every day this gap is becoming narrower and in the future RS data and methods are expected to be progressively more relevant and useful.

2. Future research

Hazard risk assessments will continue challenging spatial planners and decision makers to adopt better practices in usually complex scenarios. Models such as those presented in this thesis can be useful tools to support their decisions. However, given the high diversity of scientific fields involved, further efforts should be taken to improve the comprehension and implementation of such tools. Despite the high automatization levels of both MINDED and MINDED-BA, their replicability would

likely benefit from developing user-friendly interfaces, with direct connections to satellite imagery database catalogues.

The implementation of both models to the Aveiro Region seems to indicate good overall performances, but further developments should be made to better study and manage their limitations, in order to improve their accuracies. Such developments may include alternative pre and post-processing procedures, the incorporation of imagery acquired by different sensors, and to test different data arrangements (e.g., optimize the imagery temporal selection, consider different indices, or test other segmentation techniques). Further research should also include the implementation of MINDED and MINDED-BA in a wider diversity of locations, conditions, and other types of hazards, including those characterized in Chapter 2 (i.e., soil erosion and coastal floods; but also, e.g., landslides, earthquakes). Moreover, the same methodological principles behind these models should also be valid for analysing any other kind of spatio-temporal change, which might be registered in RS imagery. Future research could be applied in monitoring other types of earth surface processes, including as climate change impacts (e.g., glacier melting, shoreline erosion, live coral reef depletion).

REFERENCES

Adger, W.N., 2006. Vulnerability. Glob. Environ. Chang. 16, 268–281. https://doi.org/10.1016/j.gloenvcha.2006.02.006

Martini, F., Loat, R., 2007. Handbook on good practices for flood mapping in Europe. Eur. Exch. Circ. flood Mapp. 60.

Meneses, B.M., Reis, E., Reis, R., 2018. Assessment of the recurrence interval of wildfires in mainland Portugal and the identification of affected LUC patterns. J. Maps 14, 282–292. https://doi.org/10.1080/17445647.2018.1454351

Ng, H.F., Jargalsaikhan, D., Tsai, H.C., Lin, C.Y., 2013. An improved method for image thresholding based on the valley-emphasis method. 2013 Asia-Pacific Signal Inf. Process. Assoc. Annu. Summit Conf. APSIPA 2013 0, 5–8. https://doi.org/10.1109/APSIPA.2013.6694261

Oliveira, S.L.J., Pereira, J.M.C., Carreiras, J.M.B., 2012. Fire frequency analysis in Portugal (1975-2005), using Landsat-based burnt area maps. Int. J. Wildl. Fire 21, 48–60. https://doi.org/10.1071/WF10131

Otsu, N., 1979. A Threshold Selection Method from Gray-Level Histograms. IEEE Trans. Syst. Man. Cybern. 9, 62–66. https://doi.org/10.1109/TSMC.1979.4310076

Singh, A., 1989. Review Article: Digital change detection techniques using remotely-sensed data. Int. J. Remote Sens. 10, 989–1003. https://doi.org/10.1080/01431168908903939

Smith, K., 2013. Environmental hazards: Assessing risk and reducing disaster, Environmental Hazards: Assessing Risk and Reducing Disaster. https://doi.org/10.4324/9780203805305

UNDRO, 1979. Office of the United Nations Disaster Relief Co-ordinator (UNDRO).

UNISDR, 2009. 2009 UNISDR Terminology on Disaster Risk Reduction. Int. Strat. Disaster Reduct. 1–30. https://doi.org/978-600-6937-11-3

Van Westen, C.J., 2013. Remote Sensing and GIS for Natural Hazards Assessment and Disaster Risk Management, in: Schroder, J.F., Bishop, M.P. (Eds.), Treatise on Geomorphology. Elsevier Inc., San Diego, USA, pp. 259–298.

SUPLEMENTARY MATERIALS

Appendix A

Table A.1 - General information about free access satellites (Sources: Chander et al., 2009; ESA, n.d.; Kolecka and Kozak, 2014; Kunte et al., 2014; Roy et al., 2014; USGS, n.d.)

Mission	Launch date	Decommission	Sensor	Bands spatial resolution	Revisit time
Landsat 1	July 23, 1972	January 7, 1978	MSS and RBV	Multispectral 4-7: 68x83m (resampled to 60m); TIR 8: 68x83m (resampled to 60m)	18 days
Landsat 2	January 22, 1975	February 25, 1982	MSS and RBV	Multispectral 4-7: 68x83m (resampled to 60m); TIR 8: 68x83m (resampled to 60m)	18 days
Landsat 3	March 5, 1978	March 31, 1983	MSS and RBV	Multispectral 4-7: 68x83m (resampled to 60m); TIR 8: 68x83m (resampled to 60m)	18 days
Landsat 4	July 16, 1982	June 30, 2001	MSS and TM	Multispectral 1-5; 7: 30m; TIR 6: 120m	16 days
Landsat 5	March 1, 1984	June 5, 2013	MSS and TM	Multispectral 1-5; 7: 30m; TIR 6: 120m	16 days
Landsat 7	April 15, 1999	Operational (SLC-off since May 31, 2003)	ETM+	Multispectral 1-5; 7: 30m; Panchromatic 8: 30m; TIR 61-62: 60m	16 days
Landsat 8	February 11, 2013	Operational	OLI and TIRS	Multispectral 1-7, 9: 30m; Panchromatic 8: 15m; TIR 10-11: 100m (resampled to 30m)	16 days
Earth Observing-1	November 21, 2000	Operational	ALI	Panchromatic PAN: 10m; Multispectral 1-7: 30m	16 days
Terra (EOS AM-1)	December 18,1999	Operational	ASTER	VNIR 1-3, 3B; 15m; SWIR 4-9: 30m; TIR 10-14: 90m	16 days
Terra (EOS AM-1)	December 18,1999	Operational	MODIS	Multispectral 1-2: 250m; 3-7: 500m; 8-36: 1km	1-2 days
Aqua (EOS PM1)	May 4, 2002	Operational (failure on Band 6 shortly after launch)	MODIS	Multispectral 1-2: 250m; 3-7: 500m; 8-36: 1km	1-2 days
SPOT-5	May 4, 2002	March 31, 2015	SPOT-5	Panchromatic PA-1 PA-2: 5m; Multispectral 1-3: 10m; SWIR: 20m	2-3 days
STS-99	February 11, 2000	February 22, 2000	SRTM	Band C and X: Worldwide DEM of 1 arc-second (30 m)	NA
Suomi NPP	28 October, 2011	Operational	VIIRS	Multispectral M1-M16: 750 m; Imagery I1-I5: 350m; Low-light Day-Night-Band: 750 m	1-2 times a day
ERS-1	July 17, 1991	March 10, 2000	RA, ATSR, MWR, SAR, WS, PRARE	ATSR IR: 1km, MWS: 20hm; MWR: 20km; SAR: 30m; WS: 50km;	35 days
ERS-2	April 21, 1995	September 5, 2011	RA, ATSR, MWR, SAR, WS, PRARE GOME	ATSR IR: 1km, MWS: 20hm; MWR: 20km; SAR: 30m; WS: 50km; GOME: 5km vertical, 40-320km horizontal	35 days
ENVISAT	March 1, 2002	April 8, 2012	ASAR, MERIS, AAT SR, RA-2, MWR, GOMOS, MIPAS, SCIAMACHY, DORIS, LRR	MERIS Band 1-15: RSR 1.2km, FSR 300m; ASAR: 30m, WSM 150m, GMM 1km; AATSR: 1km; GOMOS: 1.7km vertical	3 days
SENTINEL-1	April 3, 2014	Operational	SENTINEL-1A	SAR Band C – SM: 5x5m; IW: 5x20m; EW: 20x40m; WV: 5x5m	12 days
	April 25, 2016	Operational	SENTINEL-1B		12 days
SENTINEL-2	June 23, 2015	Operational	SENTINEL-2A	Multispectral B1, B9, B10: 60m; B2-B4, B8: 10m; B5-B7, B8A, B11, B12: 20m	10 days
	March 7, 2017	Operational	SENTINEL-2B		10 days
SENTINEL-3	February 16, 2016	Operational	SENTINEL-3A	SLSTR – S1-S6: 500m; S7-S9, F1-F2: 1km; OLCI – 21 spectral bands: 0,3 - 1.2km; SARL: Ku-band (~300m), C-band (~300m)	SLSTR, OLCI: 1-2 days; SRAL: 27 days
	April 25, 2018	Operational	SENTINEL-3B		

Table A.2 - Single hazard methods for Wildfires (MT: Model type – DD: Data-Driven, Pb-D: Physically based – Deterministic, Pb-P: Physically based – Probabilistic; RS: Satellite Remote Sensing data incorporation)

Method	Year	What does it do?	Data requirements	Scale	Geographical scope	Advantages	Disadvantages	Sources	MT	RS
Fire Weather Index	1977	Combination of an Initial Spread Index and Buildup Index, resulting in a Fire Danger Index based on meteorological data.	Temperature, relative humidity, wind speed, rain, vegetation cover	Variable	Forests	Good indicator of the potential of ignition, fire extension and extinction capacities; Well consolidated and used by most national agencies	Demanding in terms of meteorological data	(Bedia et al., 2015; IPMA, 2015; Van Wagner, 1987)	DD	✓
Fuel moisture content	2001	Fuel moisture content correlation with Landsat optical bands	Landsat imagery (1-7)	Regional	Mediterranean	Correlation of FMC with NDVI / NDII / LWCI / Relative greenness	Not a risk assessment model.	(Emilio Chuvieco et al., 2002)	Pb-D	✓
Wildfire risk	2007	GIS based risk model, combining 4 intermediate indices: fire detection probability, ignition risk, propagation risk and suppression probability	Elevation data, buildings, roads, land use and watchtower locations.	Regional	Mediterranean (maritime influence)	User friendly; built around easily available data; potential for semi-automatic routines (allowing updates);	Although the FWI was taken into consideration, no meteorological factors where included due to lack of data	(C. O. A. Coelho et al., 2007)	Pd-D	✓
Framework for fire risk assessment	2009	Fire risk assessment method based on fire occurrence probability and potential damages. .	FMC (Terra-MODIS, NOAA-AVHRR images); Land cover/use; Lightning statistics; DTM; Degradation potential data; Landscape value;	Regional/ Local	Mediterranean	Emphasis on potential damages of fire, rather than ignition and propagation potential (most common); Complete description of input factors (including human negligence, arson, recreation and land-use)	Very demanding in terms of data requirements (socio-economic; erodibility; vegetation response ability); no validation to vulnerability components due to lack of estimations on fire effects	(Chuvieco et al., 2010)	Pd-P	✓
Vulnerability assessment indicators	2014	Identifies a set of indicators to determine the vulnerability of forest fires and coastal erosion	Many socio-economic variables, land cover/use, habitats, geomorphology	Regional/ Local	Mediterranean	Includes a list of exposure, susceptibility/fragility and lack of resilience indicators for coastal erosion and wildfires, applied to Portuguese study sites	Not a risk assessment model; Complexity resulting from too many indicators and corresponding data requirements; Lack of detail on the indicators description.	(Tedim et al., 2014)	-	-

Table A.2 (continuation) - Single hazard methods for Wildfires (MT: Model type – DD: Data-Driven, Pb-D: Physically based – Deterministic, Pb-P: Physically based – Probabilistic; RS: Satellite Remote Sensing data incorporation)

Method	Year	What does it do?	Data requirements	Scale	Geographical scope	Advantages	Disadvantages	Sources	MT	RS
MODIS/ EFFIS	2015	Analysis of agreement between MODIS and the European Forest Fire Information System between 2000 and 2009	MODIS	Global/ Regional	Europe	Analysis in terms of number of active fires and burned area by means of linear and quantile regressions.	Not a risk assessment model	(Vilar et al., 2015a)	-	✓
MMT / FlamMap	2016	Pixel-based LiDAR canopy fuel characterization that uses that uses the MTT algorithm to model burn probability (pixel burns/total number of fires), conditional flame length (fire intensity estimate) and fire size.	Topography, geospatial information on fuels, data on weather, fuel moisture content and fuel characteristics.		Mediterranean	Preliminary exposure analysis for risk mapping and mitigation.	Not a complete risk assessment methodology; No available LIDAR for our study area (besides the Aveiro Lagoon).	(Alcasena et al., 2016)	Pb-P	✓

Table A.3 - Single hazard methods for Soil Erosion (MT: Model type – DD: Data-Driven, Pb-D: Physically based – Deterministic, Pb-P: Physically based – Probabilistic; RS: Satellite Remote Sensing data incorporation RS: Satellite Remote Sensing data incorporation)

Method	Year	What does it do?	Data requirements	Scale	Geographical scope	Advantages	Disadvantages	Sources	MT	RS
USLE	1978	Soil erosion estimation in croplands on gently sloping topography	Rainfall and runoff factor, Soil erodibility factor, Topography, Land cover and management, Support practice	Local	Gentle slope croplands - USA	Widely studied; Useful for local conservation planning at an individual property level	Fails to properly distinguish between soil and climatic conditions in the infiltration process	(Wischmeier and Smith, 1978)	DD	-
Morgan-Morgan-Finney	1984	Empirical model for predicting annual soil loss	Rainfall energy, overland flow, plant height, ground cover, rainfall interception, evapotranspiration, hydrologic depth of soil, top soil layer bulk density, soil surface cohesion, slope	Local	Mediterranean	Some of the simplicity of USLE/ RUSLE models but has a more consolidated physical structure, separating the Soil Erosion Process into a water phase and sediment phase	Extremely data demanding (introducing sources of error and uncertainty)	(Vieira et al., 2014, 2010)	DD	-
RUSLE	1997	Calculates annual soil loss	Precipitation, soil properties, topography, land cover, experimental factor	Regional / Local	USA / Mediterranean	Less demanding in terms of data requirements; widely studied	Tendency to overestimate runoff and soil erosion rates; still depending on soil properties and experimental factor	(D. Lu et al., 2004; Renard et al., 1997, 1994; Vieira et al., 2014, 2010)	DD	✓
ERMIT	2006	Provides a distribution of post -fire erosion rates with likelihood of their occurrence	Topography, vegetation cover, soil texture and burn severity	Regional / Local	USA / Mediterranean	Suited to simulate the early stages of the disturbance window in post-fire scenarios; Predicts the probability of sediment delivery from the base of a hillslope	Doesn't provide average annual erosion rates	(Robichaud et al., 2007; Vieira et al., 2014)	Pb-P	-
PESERA	2012	Estimation of runoff and erosion rates: constructed around a central water balance, separating precipitation into possible pathways;	Relief, soil and vegetation characteristics, climate data	Regional / Local	Europe	Consistent and objective estimates of soil erosion rates with regional applicability; Model flexibility; Capable of providing long-term average values; Possibility of using scenarios; Ability to isolate fire-induced from 'background' erosion	Data demanding, particularly rainfall; dependent of national spatial soil data (uniformity and harmonization issues); Concentrated on dominant processes but poorly estimating the remaining; Over-estimation of post fire soil erosion in thin stony soils	(Esteves et al., 2012; Kirkby et al., 2008)	Pb-D	✓

Table A.4 - Single hazard methods for Floods (MT: Model type – DD: Data-Driven, Pb-D: Physically based – Deterministic, Pb-P: Physically based – Probabilistic, Va: Variable; RS: Satellite Remote Sensing data incorporation RS: Satellite Remote Sensing data incorporation)

Hazard type	Method	Year	What does it do?	Data requirements	Scale	Geographical scope	Advantages	Disadvantages	Sources	MT	RS
Fluvial	**Empirical Curve Number**	1972	Estimation of runoff volume from watershed	Land use, soil types, DEM, average annual precipitation, average annual temperature	Local / Regional	USA	Usable for the design of water control structures	Not intended for reproducing hydrographs of actual floods; Little quantitative information; Developed to be used in the USA	(Mockus et al., 1972)	DD	✓
	HBV	1976	Semi-distributed rainfall-runoff conceptual model, which simulates discharge using rainfall, temperature and estimates of potential evaporation	Daily temperature, precipitation, evaporation, land use, geology, elevation	Local / Regional	River basins	Usable with different climatic conditions; Has many applications, including flood forecasting	Large number of parameters need to be found through calibration; cannot simulate high resolution flood plain processes	(Bergström, 1976; Grillakis et al., 2010; Lindström et al., 1997)	DD	✓
	TOPMODEL	1979	Semi distributed conceptual model; Purely topographic interpretation, measuring the capacity to accumulate water	Catchment topography, soil transmissivity	Local / Regional	River basins	Can also be considered as a physical model as its parameters can be theoretically measured; can be used in single or multiple sub catchments; Allows to calculate water depth or storage deficit at any location	Large number of parameters need to be found through calibration; cannot simulate high resolution flood plain processes	(Beven and Kirkby, 1979)	DD	✓
	WEPP	1989	Continuous simulation to predict soil loss and deposition, rather than average net soil loss; Contains its own process-based models for hydrology, water balance, plant growth, residue decomposition and soil consolidation;	Daily rainfall data; Daily discharge data; Soil map; DEM, Landsat images; Toposheets;	Local / Regional	River watersheds	Capable of predicting spatial and temporal distributions of net soil loss/gain for entire hillslopes; Simulates the effects of vegetation in individual storms;	Too complex and data-demanding to be used as simple management tool and as a screening model	(Tiwari et al., 2000; Verma et al., 2010)	Pb-P	✓

Table A.4 (continuation) - Single hazard methods for Floods (MT: Model type – DD: Data-Driven, Pb-D: Physically based – Deterministic, Pb-P: Physically based – Probabilistic, Va: Variable; RS: Satellite Remote Sensing data incorporation RS: Satellite Remote Sensing data incorporation)

Hazard type	Method	Year	What does it do?	Data requirements	Scale	Geographical scope	Advantages	Disadvantages	Sources	MT	RS
Fluvial	**SWAT**	1993	Physical model that breaks an entire catchment into sub sections	Daily rainfall data, topography, land use, vegetation and soil characteristics	Local / Regional	River basins	Useful to simulate water sediment circulation, agriculture production and pollutants in ungauged basins; efficient for long term simulations	Complexity and highly dependent on data;	(Gassman et al., 2007)	Pb-P	✓
	LISFLOOD	1999	Simple raster-based model for flood inundation simulation due to extreme rainfall	DEM; land use; Manning Roughness Coefficients	Local / Regional	Fluvial and coastal floodplains	Accounts for influences of topography, precipitation, antecedent soil moisture content, land use type and soil type; Useful for flood extent/depth maps in large river basins	Lacks consideration about ground water flow or other to revert the water to go back into the river channel.	(Bates and De Roo, 2000; Lavalle et al., 2005; Van der Sande, 2001)	Pb-P	✓
	Planar water surface	2000	Static flood extension maps obtained from DEM overlaid with a planar surface. All areas below that surface are considered flooded	LIDAR / DEM	Local/ Regional	River floodplain	Simplistic approach with very few data requirements	Completely dependent on DEM resolution; Absence of channel/floodplain routing, surface penetration or any other flow dynamics;	(Priestnall et al., 2000; Rathjens et al., 2016; Sangwan and Merwade, 2015)	DD	✓
	Remote sensing based flood extent estimation	2002	Flood inundation extent obtained from a combination of Landsat and DEM	M Radarsat-1, Landsat TM	Regional	Coastal floodplain	Reliable results for coastal floodplains with larger spatial extents and low relief; Complementary use of DEM to Landsat for dense canopies	Errors resulting from lower DEM resolution	(Wang et al., 2002)	DD	✓
	Multi-attributes semantic partitions	2006	Integration of urban growth, vulnerability and dispersion flow layers, obtained with RS and using a fuzzy integral	ESR-SAR, SRTM-3, SPOT4	Local	Urban areas	Application in urban growth contexts, where there is no monitoring of food hazards	Experimental results; Methodological complexity	(Onana et al., 2008)	Pb-D	✓

Table A.4 (continuation) - Single hazard methods for Floods (MT: Model type – DD: Data-Driven, Pb-D: Physically based – Deterministic, Pb-P: Physically based – Probabilistic, Va: Variable; RS: Satellite Remote Sensing data incorporation RS: Satellite Remote Sensing data incorporation)

Hazard type	Method	Year	What does it do?	Data requirements	Scale	Geographical scope	Advantages	Disadvantages	Sources	MT	RS
Fluvial	**Risk Map Germany**	2006	Regionalization approach for flood peak discharge; Statistical analysis of ungauged areas and very long recurrence intervals; Hydrodynamic simulations for hazard and risk mapping; GIS-based software; Multifactorial approach for damage estimation	Gauge data; (Inundation depth; flow velocities); DTM; land use; precipitation; damage functions	Local/ Regional	River basins	Allows to map the extent of inundation zones and water depths for different return periods, including ungauged areas;	Requires long series of gauge data	(Büchele et al., 2006)	DD / Pb-P	-
	Topographic index / Topographic wetness index	2007	Modified version of TOPMODEL for the delineation of flood prone areas based on topography	DTM (e.g., ASTER, SRTM)	Regional	River Basins	Good performance for broad resolutions and basins with higher slope ratios	Not a complete risk assessment method (probabilities are not considered); Doesn't consider the influence of artificial structures	(Jalayer et al., 2014; Kirkby et al., 2008; Manfreda et al., 2014, 2011, 2008; Qin et al., 2011)	DD	✓
	HEC-HMS/HEC-RAS flood risk analysis	2010	Flood risk analysis based on HEC-HMS (Hydrologic Modelling System) and HEC-RAS (River Analysis System); HEC-HMS simulates rainfall losses and runoff from a single rainfall event or a continuous rainfall; HEC-RAS used to obtain flood extent and depth.	SAR, Digital Contour Maps, Spot heights, land use, LiDAR, rainfall gauge data, stream flow gauge data; demography; building construction materials; household vulnerability survey	Regional	River Basin	Production of hazard maps corresponding to different return periods; Consideration of vulnerability of population and buildings	Dependent on gauge data (rainfall and stream flow) and surveys; Difficult to determine appropriate cross section locations where they are not explicitly represented; Increased computational cost	(Brunner, 2016; Samarasinghe et al., 2010; Scharffenberg, 2013)	Pb-D	✓
	Static flood inundation model	2011	Simple static flood inundation model performed by filling global DEMs with water;	SRTM, HYDRO1K, field observation of watermarks	Local / Regional	Coastal floodplain	Simple approach; vertical accuracy assessment of global datasets on a local scale	Some ambiguity in radar measurements; questionable accuracy and resolutions of global DEMs	(Karlsson and Arnberg, 2011)	DD	✓

Table A.4 (continuation) - Single hazard methods for Floods (MT: Model type – DD: Data-Driven, Pb-D: Physically based – Deterministic, Pb-P: Physically based – Probabilistic, Va: Variable; RS: Satellite Remote Sensing data incorporation RS: Satellite Remote Sensing data incorporation)

Hazard type	Method	Year	What does it do?	Data requirements	Scale	Geographical scope	Advantages	Disadvantages	Sources	MT	RS
Fluvial	**Flood prone areas identification based on RS elevation data**	2012	Pattern classification techniques for the delineation of flood-prone areas and hazard graduation	Existing flood hazard maps; Void filled and Hydrological condition elevation models (HydroSHEDS); distance from nearest stream, elevation to the nearest stream, surface curvature, contribution area, local slope	Regional	River basins	Allows to distinguish areas subject to flood hazard with a return time greater than the used based on relative elevation and distance from the nearest stream; DEM resolution enough to describe local terrain morphology; Recommended for primary assessments, to identify flood-prone areas and hazard grading in large regions	DEM resolution not enough for the recognition of flood control structures	(Degiorgis et al., 2012)	Pb-D	✓
	Probabilistic GIS-based method for delineation of urban flooding risk hotspots	2013	Combines the Topographic Wetness Index, Urban morphology types and census data, using maximum likelihood to estimate the threshold to identify flood-prone areas	DEM, rainfall annual maxima, Population density	Local	Portions of river basins/ Cities	Uses Bayesian parameter estimation for the characterization of uncertainties in delineating the potentially flood-prone areas (by calculating the complementary probability of false values)	Uncertainties of TWI threshold lead to considerable differences in the results	(Jalayer et al., 2014)	DD	✓
	Flood susceptibility mapping	2016	Delineation of flash-flood prone areas through integration of catastrophe theory and analytical hierarchy process in a GIS;	Ground surface elevation, slope angle, curvature, topographic wetness index, stream power index, curve numbers, and distance from intermittent streams	Regional	Arid regions	Few data requirements; application in vast remote areas; sensitivity analysis for each factor is provided; the catastrophe theory does not involve the decision maker's opinion in assigning weights for the causative factors (decreased subjectivity)	Standardized and normalized data;	(Al-Abadi et al., 2016)	DD	✓

Table A.4 (continuation) - Single hazard methods for Floods (MT: Model type – DD: Data-Driven, Pb-D: Physically based – Deterministic, Pb-P: Physically based – Probabilistic, Va: Variable; RS: Satellite Remote Sensing data incorporation RS: Satellite Remote Sensing data incorporation)

Hazard type	Method	Year	What does it do?	Data requirements	Scale	Geographical scope	Advantages	Disadvantages	Sources	MT	RS
Coastal	**DSAS**	early 1990's	Rate-of-change statistics for a time series of shoreline vector data	Optical/Microwave imagery	Regional	Coastal areas	Allows the use of shoreline proxies which can be obtained exclusively with RS techniques	Not applicable on urban/artificial shorelines	(Cenci et al., 2017b, 2015, 2013; Himmelstoss, 2009; Virdis et al., 2012)	DD	✓
	Coastal Vulnerability Index	2005	Coastal Vulnerability Index based on relative risk variables;	Geomorphology (RS data); Shoreline change rate (RS data/DSAS), Coastal slope (Bathymetries); Relative Sea-Level change (tide gauges); Mean significant wave height; Tidal Range (e.g., WXTide software)	Regional	Coastal areas	Allows the possibility of aggregating data obtained from diverse sources (including. RS data); Objective assessment of natural factors contributing to the evolution of the coastal zone; Useful for management purposes	Dependent on gauge data information (Tidal Range); Subjectivity associated to data ranking	(Kumar et al., 2010; Pendleton et al., 2005)	Pb-D	✓
	DIVA	2006	Dynamic and Interactive Vulnerability Assessment tool. Quantitative coastal vulnerability indicators. Database of biophysical and socio-economic coastal data; Sea level and socio-economic scenarios; Integrated model with several interacting modules and a graphical interface.	80 biophysical and socioeconomic parameters (access to a pre-defined database)	National / Regional / Global	Coastal areas	Freely available; Intuitive and user-friendly graphical interface; Allows basic and advanced level interactions (using own scenarios and alternative algorithms); Modelling framework and semi-automated development process.	Not designed for local scale applications or to be used as a decision support tool; Local data inconsistencies; Does not provide expert level GIS functionality; Several relevant drivers and processes were not included	(Hinkel and Klein, 2009)	Pb-D	-

Table A.4 (continuation) - Single hazard methods for Floods (MT: Model type – DD: Data-Driven, Pb-D: Physically based – Deterministic, Pb-P: Physically based – Probabilistic, Va: Variable; RS: Satellite Remote Sensing data incorporation RS: Satellite Remote Sensing data incorporation)

Hazard type	Method	Year	What does it do?	Data requirements	Scale	Geographical scope	Advantages	Disadvantages	Sources	MT	RS
Coastal	**Coastal Hazard Wheel**	2012	Generic framework for coastal hazards assessment	Google Earth, Bing maps, Satellite imagery	Sub-regional to national	Coastal areas	Hazard screening in areas with limited data availability; Covers ecosystem disruption hazards, gradual inundation, salt-water intrusion, erosion and flooding.	Based on a geological layout with unknown certainty; Qualitative assessment; No integration between hazards	(Appelquist, 2013; Appelquist and Balstrøm, 2015)	Pb-D	✓
	THESEUS	2014	Exploratory tool for integrated coastal risk assessment, including the effects from different scenarios	DEM, hydraulic structures and infrastructures position and geometry; land use; socio-economic indicators; habitats and species	Regional	Coastal areas	Freely available; Preliminary risk assessment, identification of threatened areas and mitigation solutions; Multi-criteria analysis; Expert weighting of indicators	Limited in terms of the inclusion of the resilience concept; Experimental tool	(Simcic et al., 2014)	DD	✓
	XtremRisk	2015	Integrated risk analysis to coastal floods. Storm surge generator, joint probability analysis, reliability and breach analysis, damage assessment	Tidal gauge and wind records; damage functions;	Local / Regional	Estuary/Open coast	Uses a storm surge generator to reproduce storm surge curves	Complexity; Requires large record series	(Oumeraci et al., 2015)	DD	-
	CERA	2016	Tool for assessing risk of coastal erosion (QGIS plugin); Incorporation of weighted coastal vulnerability and consequence parameters; Risk matrix.	Distance to shoreline, topography, geology, geomorphology, land cover, anthropogenic actions, maximum significant wave height, maximum tidal range, erosion/accretion rates, population, employment, ecology status, historical heritage	Local	Coastal areas	Low data requirements, fast tool, easy application, open software, weighting of vulnerability parameters based on expert judgement and multi-criteria analysis	Dependent on data obtained from other methods; No account of probabilities	(Narra et al., 2017)	Va	✓

Table A.5 - Multi-hazard methods (AG: Aggregation; MT: Model type – DD: Data-Driven, Pb-D: Physically based – Deterministic, Pb-P: Physically based – Probabilistic, Va: Variable; IN: hazard interactions; RS: Satellite Remote Sensing data incorporation)

Name	Year	What does it do?	Data requirements	Scale	Geographical scope	Advantages	Disadvantages	Sources	Results	MT	AG	IN	RS
Community Risk	1999	Comparison of single hazard risk ratings, calculated from the exposure of elements according to scenarios of exceedance of risk acceptability and hazard vulnerability rankings	Historical event records, gauge data, building characteristics and road data, land cover, DEM	Local	Tropic community	Quantitative comparison between multiple hazards	No overall multi-hazard classification; overall vulnerability index assuming equal contribution from all hazards; Results provided as suburb-by-suburb ranks; Empirical assumptions introduce errors and uncertainties	(Granger et al., 1999)	Element-oriented	DD / Pb-P	✓	-	-
Munich Reinsurance company	2003	Risk as the combination of Hazard exposure and vulnerability. Hazard Exposure: Average annual losses combined with probable maximum loss; Vulnerability: Building class and regulations/ planning in respect to hazards	City statistics, building data, historical loss data, demography	Local	Megacities	Absolute approach; Hazard weighting calculated from historical loss data; Determination of probable maximum loss (1000 year);	Limited application (megacities); The index is highly influenced by the exposure values, while vulnerability plays a secondary role; Vulnerability is highly dependent on the quality of available data comparability issues); Lack of detail in method description	(Munich Reinsurance Company, 2003)	Absolute potential loss values (per megacity)	DD / Pb-P	✓	-	-
Disaster Risk Index	2004	Sum of single hazard assessments extracted from EM-DAT. Provides hazard frequency per country and hazard-specific vulnerability indicators. Cluster analysis and PCA per country.	EM-DAT	Global	World	Worldwide application	Only represents primary hazard events recorded in global disaster databases (even when the majority of loss is associated other different hazards triggered by the primary event); Refers exclusively to loss of life.	(UNDP, 2004)	Loss of life	DD	✓	-	✓

Table A.5 (continuation) - Multi-hazard methods (AG: Aggregation; MT: Model type – DD: Data-Driven, Pb-D: Physically based – Deterministic, Pb-P: Physically based – Probabilistic, Va: Variable; IN: hazard interactions; RS: Satellite Remote Sensing data incorporation)

Name	Year	What does it do?	Data requirements	Scale	Geog. scope	Advantages	Disadvantages	Sources	Results	MT	AG	IN	RS
HAZUZ-MH	2004	Step-by-step software guide to establish multi-hazard risk assessments. Includes different levels of analysis and its own provided database (optional). Works with deterministic or probabilistic scenarios for loss estimation	Optional data regarding population, structures and vulnerability	Census tract	USA	User friendly but still customizable; Includes its own database.	Designed for the USA; Only provides aggregated estimations of lost, without identifying which specific elements will be affected; no aggregation for multi-hazard interactions	(FEMA, 2004)	General application	DD / Pb-D / Pb-P	✓	-	-
European integrated map of risk from weather driven events	2005	Incorporation of vulnerability, exposure and hazard, into one risk layer, specific for each hazard type; the multiple hazards were not aggregated into a unique representation	DEM, Land cover , European Soils Map, EFAS flood forecasts, Satellite imagery (post-fire), EFIS, Temperature, Humidity, Socio-economic statistics, mitigation measures	NUTS 3	European Union	Vulnerability and exposure specific for each hazard; Configurable risk-scenarios by modifying the hazard, exposure or vulnerability; Employs validated models and homogeneously generated data	Impossible to include return period calculations (data unavailability); simplified procedures and assumptions were applied; Two-dimensional flood modelling; Damage assessment not including cars	(Lavalle et al., 2005)	General application	Pb-D	-	-	✓
Global multi-hazard analysis	2005	Mortality/Economic loss risks (weighted values of population/GDP); Exposure according to vulnerability coefficient (20-year historical mortality/economic losses). Multi-hazard index as a sum of individual hazard estimates	GDP (World Bank Classification), Population, EM-DAT;	Country	World	Compares the global multi-hazard analysis with regional/ local case study examples	Data inconsistency: Broad representation of global loss estimations which vary unevenly in the EM-DAT records; coarse resolution of global data on socioeconomic and vulnerability variables (if any exist)	(Dilley et al., 2005)	General application	DD	?	-	-

Table A 5 (continuation) - Multi-hazard methods (AG: Aggregation; MT: Model type – DD: Data-Driven, Pb-D: Physically based – Deterministic, Pb-P: Physically based – Probabilistic, Va: Variable; IN: hazard interactions; RS: Satellite Remote Sensing data incorporation)

Name	Year	What does it do?	Data requirements	Scale	Geog. scope	Advantages	Disadvantages	Sources	Results	MT	AG	IN	RS
ESPON	2006	Integrated hazard and risk overview on the European territory. Application of the Delphi method to weight several hazard assessments	Combination of hazard-specific indices with historical records.	NUTS 3	EU	First integrated approach in Europe; Case study testing	Preliminary approach based on preliminary data sets;	(Schmidt-Thomé et al., 2006)	General application	Pb-D	✓	-	-
Urban multi-hazard risk analysis using	2006	Characterization of hazard susceptibility and elements at risk	Building footprint, aerial photographs, field surveys, economic and demographic data; IRS LISS III - PAN and ASTER images	Local	Urban	Alternative to restricted data access situations; Element-oriented (buildings)	Does not quantify risk - qualitative combination of multi-hazard susceptibility; General approach	(Khatsu and Van Westen, 2005)	Element-oriented	-	-	-	✓
Multi-risk assessment	2006	Individual hazard assessments determined from exceedance probabilities of potential events and damages (distribution functions). Estimation of loss with damage functions	Time series of hourly wind speeds, averaged over a sampling period of 10 min; gauge discharge data; seismic records; official topographic-cartographic system (land register)	Local	Cities	Risk curves with exceedance probabilities and direct monetary losses, provide valuable information for disaster mitigation	Uncertainties where not considered (which are expected to be high);	(Grünthal et al., 2006)	Monetary economic losses	DD	-	-	-
Total estimation of risk	2009	Empirical approach to select factors for hazard, vulnerability and elements at risk exposure. Distribution according to classes based on experience of authors. Total estimation of risk determined as a sum of both hazards, population and land use	Topography, aerial photos, soil map, geohydrology map, irrigation area map, climate map, slope map, watershed classification map, geological map, district map, field survey	Regional	River basin	Possible stakeholder and public acceptability of results (easy to understand)	Simplistic empirical approach; No details about the application of RS methods; No hazard interaction is considered.	(Wipulanusat et al., 2009)	General application	Pb-D	✓	-	✓

Table A.5 (continuation) - Multi-hazard methods (AG: Aggregation; MT: Model type – DD: Data-Driven, Pb-D: Physically based – Deterministic, Pb-P: Physically based – Probabilistic, Va: Variable; IN: hazard interactions; RS: Satellite Remote Sensing data incorporation)

Name	Year	What does it do?	Data requirements	Scale	Geog. scope	Advantages	Disadvantages	Sources	Results	MT	AG	IN	RS
Principles of multi-risk assessment	2009	General procedure for multi-hazard risk assessments. Comparison between single-risk assessments and a long-term scenario of triggering events, using the Bayesian event structure principle	Single-hazard annual risk for human life; Historical event records	Local	Mediterranean municipality	Accounts for weighting and merging of multi-hazard interactions; Describes the general steps to be used in MRA	Generic real case example without the aim of providing real estimations; Only one scenario of hazard interactions	(Marzocchi et al., 2012; Marzocchi and Woo, 2009)	Element-oriented (Human life loss)	Pb-P	✓	✓	-
Regional RiskScape	2011	Software with components of a risk model: hazards, assets (elements at risk) and vulnerability models (or fragility functions)	Customizable parameters according to each module (hazard, assets and loss)	Local	Urban centres and small communities	Allows function calls of external hazard computer models, or surfaces from pre-computed hazard or observed scenarios	Lack of uncertainty quantifiers; generic approach; does not allow modelling the interaction between multiple hazards and assets in a risk scenario	(Schmidt et al., 2011)	Element-oriented (economic loss)	Va	✓	-	-
Generic multi-risk approach	2014	Generic probabilistic framework based on sequential Monte Carlo Method for coinciding and triggered events (Markov chain), time-variant vulnerability and exposure.	Generic data (e.g., hazard intensity, long-term occurrence rate, damage ratio)	Variable	Variable	Probabilistic assessment of losses; Recognition of more or less probable risk paths; Introduction of risk migration matrix	Complexity; Lack of real-word application and capability of dealing with uncertainties, domino effects in socioeconomic networks, climate change, infrastructure ageing and exposure changes	(Mignan et al., 2014)	Conceptual/ General application	DD	✓	✓	-

Table A.5 (continuation) - Multi-hazard methods (AG: Aggregation; MT: Model type – DD: Data-Driven, Pb-D: Physically based – Deterministic, Pb-P: Physically based – Probabilistic, Va: Variable; IN: hazard interactions; RS: Satellite Remote Sensing data incorporation)

Name	Year	What does it do?	Data requirements	Scale	Geog. scope	Advantages	Disadvantages	Sources	Results	MT	AG	IN	RS
Three-level framework for multi-risk assessment	2015	Multi-risk assessment framework which includes a decision-tree flow chart for qualitative, semi-quantitative (matrix) or quantitative assessments (Bayesian networks)	Pre-assessment of: single hazards (e.g., rate of occurrence, pathway, intensities), vulnerabilities (e.g., people, buildings) and consequences (loss of life, economic losses, environmental degradation)	Variable	Variable	Flexible structure; Quantitative assessment of hazard interactions and dynamic vulnerability; Includes a theoretical example of Bayesian networks to estimate the probability of triggering/cascade effects; Capable of treating uncertainties of hidden geodynamic variables	Requirements of pre-assessment of single hazards, vulnerabilities and consequences; More suitable to geo-dynamic hazards; No real-case application	(Liu et al., 2015)	Conceptual / General application	DD	✓	✓	-
Hazard forming environmental analysis	2016	Multi-hazard risk assessment based on the analysis of stable and trigger factors. Includes 4 classes of hazard interaction trigger analysis: independent, murex, parallel and series	Stable factors (river basins, landform,	County	River basin	Comparison of stable and trigger factors according to multiple hazards; Trigger factor analysis considers hazard interactions besides domino effects; Vulnerability addresses multiple hazards as a group	Unable to cope with hazards without obvious environment characteristic (e.g., storm); Limited knowledge about triggering factors can induce additional relationships between natural hazards; generic case study application	(Liu et al., 2016a)	Conceptual / General application	Va	✓	✓	-

Table A.5 (continuation) - Multi-hazard methods (AG: Aggregation; MT: Model type – DD: Data-Driven, Pb-D: Physically based – Deterministic, Pb-P: Physically based – Probabilistic, Va: Variable; IN: hazard interactions; RS: Satellite Remote Sensing data incorporation)

Name	Year	What does it do?	Data requirements	Scale	Geog. scope	Advantages	Disadvantages	Sources	Results	MT	AG	IN	RS
Comparative performance of MHRA methods	2016	Comparison of two types of approaches in multi-hazard risk assessment: risk index and mathematical statistical method	General statistics (e.g., demography, economy), disaster history (EM-DAT)	National	Country	Presents the relative merits of both approaches resulting from a general case study application	Generic examples using simplified approaches	(Liu et al., 2016c)	Conceptual / General application	DD / Pb-P	✓	✓	-
MmhRisk-HI	2016	Calculates possible loss and exceedance probability of multiple hazards, including their interactions. Uses a Bayesian Structure. Treats multiple hazards as a group with corresponding vulnerability-related indicators.	Environmental data (meteorological), Disaster data (type, time place direct economic loss), Socioeconomic data (GDP, income, population density, gender ratio, age structure, telecommunication infrastructure, transport route, medical provision, social dependency)	Province	Regional	Addresses hazard interactions; Possibility of integration in a GIS environment to map risk areas; benefits from a Bayesian structure to select indicators and exceedance probability calculation; Effective estimation in a real loss situation;	Unable to provide loss per individual hazard; Based on a limited set of actual hazard-interaction; Absence of uncertainty quantifiers	(Liu et al., 2016b)	Economic losses provided	DD	✓	✓	✓
Clustering and analytical hierarchy process applied to multi-hazard risk assessments	2016	Clustering of monuments based on parameters obtained with RS. Addressing of individual and unique characteristics using the Analytical Hierarchy Process. Overall risk hazard map determination.	Clustering into groups followed by AHP for each class. Interpolation of weight factors and application into an overall risk map.	Regional	Regional	Allows the integration of several single-hazard assessments in an overall hazard risk; Objective methodology for hazard aggregation	Hazard interaction is not taken into consideration; AHP lacks the ability to cope with data uncertainty and imprecision	(Agapiou et al., 2016)	Element-oriented	DD	✓	-	✓

Appendix B

Table B.1 - Fifty largest precipitation events, from 23 meteorological stations located in the Vouga River watershed (between 1979/12/30 and 2017/09/12); Corresponding availability of satellite images: LS—Landsat; S—Sentinel; This table is ordered according to the maximum return period (descending).

Date	**Maximum Daily Precipitation (mm)**	**Maximum Return Period (Years)**	**Available Satellite Images**		**Flood Event Records** (Alves et al., 2010; CMI, 2016)
			t1	**t2**	
1995/12/25	180.0	32.7	-	-	Águeda, Albergaria-a-Velha, Aveiro, Murtosa
2007/06/14	85.0	29.3	LS5 (2007/06/04)	LS5 (2007/06/20) *	Ovar
#2003/01/19	80.6	26.5	LS7 (2002/12/07)	LS7 (2003/01/24)	Estarreja, Oliveira do Bairro, Vagos, Murtosa
2008/04/10	96.1	24.9	-	LS7 (2008/04/11 *)	Estarreja , Murtosa, Mira, Vagos, Oliveira do Bairro
1993/10/09	124.9	24.2	-	-	-
1995/12/26	114.5	23.6	-	-	Águeda, Albergaria-a-Velha , Aveiro, Murtosa
1983/11/22	97.0	23.4	-	-	-
1985/02/09	120.0	23.1	-	-	-
2004/12/01	90.0	22.9	LS7 (2004/11/26)	LS7 (2004/12/12 *)	-
1989/12/21	120.0	19.8	-	-	-
2001/01/27	150.1	19.6	-	LS7 (2001/02/03) *	Albergaria-a-Velha, Aveiro , Estarreja, Ílhavo, Sever do Vouga, Vagos, Mira , Murtosa
#2016/02/13	128.9	16.4	S1 (2016/02/06); LS8 (2016/02/05)	LS7 (2016/02/29)	Águeda
1984/10/19	121.0	16.4	-	-	-
1998/09/28	85.0	14.6	-	-	Águeda, Vagos
2003/01/03	98.8	12.4	-	-	-
2015/09/16	129.4	12.1	LS7 (2015/09/06); LS8 (2015/09/14 *); S1A (2015/09/10, 2015/09/15)	LS7 (2015/09/22 *); LS8 (2015/09/30 *); S1 (2015/09/16)	-
#2004/03/12	78.5	11.8	LS7 (2004/02/12)	LS7 (2004/03/15)	-
1996/02/06	125.7	11.8	-	-	Murtosa
1980/11/12	85.5	11.5	-	-	-
2006/11/24	96.1	11.4	-	-	Estarreja, Ílhavo
2016/01/04	133.3	9.8	LS7 (2015/12/27 *); S1 (2016/01/02); S2 (2015/12/22)	S1A (2016/01/08); S2 (2016/01/11 *)	Águeda

Table B.1 (continuation) - Fifty largest precipitation events, from 23 meteorological stations located in the Vouga River watershed (between 1979/12/30 and 2017/09/12); Corresponding availability of satellite images: LS—Landsat; S—Sentinel; This table is ordered according to the maximum return period (descending).

Date	**Maximum Daily Precipitation (mm)**	**Maximum Return Period (Years)**	**Available Satellite Images** t1	t2	**Flood Event Records** (Alves et al., 2010; CMI, 2016)
1994/01/06	116.1	9.8	-	-	Águeda, Murtosa
1982/11/07	73.2	9.8	-	-	-
1996/05/18	67.0	9.0	-	-	Murtosa
2005/12/02	111.3	8.8	LS7 (2005/11/29)	LS7 (2005/12/15)	-
2008/04/08	93.5	8.3	-	LS7 (2008/04/11 *)	-
1993/09/17	99.5	8.1	-	-	-
1986/11/11	73.5	7.9	-	-	-
1983/04/22	110.0	7.9	-	-	-
1984/11/16	117.0	7.8	-	-	-
1991/03/06	82.5	7.8	-	-	-
2005/10/30	80.0	7.7	-	-	-
2003/08/29	71.5	7.3	-	-	-
#2009/10/07	119.0	6.8	LS7 (2009/09/21)	LS5 (2009/10/15)	-
2001/02/06	73.3	6.6	-	-	Ovar
1989/02/26	87.5	6.6	-	-	-
1987/09/26	99.0	6.5	-	-	-
1997/01/09	108.7	6.5	-	-	Murtosa
2002/10/01	67.1	6.2	-	-	Mira
1992/01/08	67.0	6.0	-	-	-
2009/12/07	73.2	5.9	-	-	-
1994/10/05	63.3	5.9	-	-	Ovar
2002/11/19	73.0	5.9	-	-	-
2004/10/27	67.3	5.7	-	-	-
2006/12/08	125.9	5.4	LS5 (2006/10/12)	-	-
1996/01/09	66.4	5.0	-	-	Murtosa
1988/01/25	80.0	5.0	-	-	-
2015/01/31	127.8	4.9	LS8 (2015/01/01); S1(2015/01/30; 2015/01/31)	LS7 (2015/02/10) *; LS8 (2015/02/18)	-
1997/12/22	77.5	4.9	-	-	Murtosa
2009/10/22	63.9	4.7	-	-	-

Selected precipitation event, * Significant cloud percentage (>15% of the overall scene).